Processing strategies optimization and error mitigation of geodetic measurements

by
Martina Coccia

M.S., University of Rome, 'La Sapienza', Rome (ITALY), 2009

Submitted in partial fulfillment of the requirements for the degree of

Doctor of Philosophy
At the
MASSACHUSETTS INSTITUTE OF TECHNOLOGY

June 2017

Signature of Author Signature redacted
Department of Earth Atmospheric and Planetary Sciences
Massachusetts Institute of Technology
May, 30th, 2017

Certified by Signature redacted
Thomas Herring
Professor of Geophysics, Massachusetts Institute of Technology
Thesis Supervisor

Accepted by Signature redacted
Robert D. van der Hilst
Schlumberger Professor of Earth and Planetary Sciences
Head, Department of Earth Atmospheric and Planetary Sciences

Processing strategies optimization and error mitigation of geodetic measurements

by
Martina Coccia

Submitted to the Department of Earth Atmospheric and Planetary Sciences,
Program in Geophysics and Seismology
on May 30th, 2017 in partial fulfillment of the requirements
for the degree of Doctor of Philosophy

Abstract

This doctoral thesis focuses on the application of geodetic techniques and finite element modeling to studying crustal deformation and other processes. In particular, it focuses on optimizing standard processing strategies, reducing the noise in the measurements and mitigating the effects of external processes in order to extract the signal of interest. Geodetic techniques, such GPS and InSAR, are still affected by major sources of errors, such as multipath, atmospheric effects, snow, blockage of the signal by infrastructure that can make difficult the detection of geophysical signal. In this thesis, I analyze three sets of data for which I have used different approaches to estimate the displacement and to investigate the sources of deformation that contribute to the signal.

The first project consists of studying the deformation caused by the seasonal cycle of injection/withdrawal of gas in a depleted gas reservoir using InSAR measurements and Finite Element modeling techniques. In this project, I present a method to reduce the atmospheric signal, using statistical techniques and filtering and to estimate the error on the measurements. I compare the estimates with Finite Element modeling of the reservoir, using an elastic rheology.

The second project analyses the unrest of Katla volcano in Iceland using GPS observables. GPS stations on top of the volcano register a complex signal, caused by the concurrence of different processes, such as snow on the antenna, multipath, earthquakes, volcanic deformation and hydrological events. In this project, I explore methods to detect the effects of snow/ice on top of antennas and to separate the different sources of the signal in order to extract the volcanic deformation component. I then compare the GPS measurements with a finite element model of snow/ice load on the volcano to validate the source of the estimated deformation.

The third project involves the analysis of long term deformation and determination of vibrations of the Al-Hamra tower in Kuwait, using 24-hours averaged, 6-hours averaged and 1Hz GPS measurements. The signals of GPS stations mounted on buildings are often affected by multipath due to reflective objects on the roof and suffer from reduced accuracy due to the partial masking of the sky by infrastructures on the roof. I explore different ways to mitigate the multipath, assessing an optimal GPS processing strategy for building installation. As the resulting

deformation observed by the GPS instruments is highly correlated to variations in temperature, I present a finite element model of the building, where the major source of deformation is caused by a differential heating of the external walls. I also discuss the effects of the winds on the structure of the building, analyzing the high rate GPS measurements.

Thesis Supervisor: Thomas Herring
Title: Professor of Geophysics

Acknowledgements

This dissertation concludes a long journey at the Massachusetts Institute of Technology and I would like to thank everyone who helped me reach this goal. I wouldn't make it without the support, guidance and friendship of many.

First, I would like to deeply thank my advisor Prof. Thomas Herring whose invaluable advice and support throughout these years made possible to complete this thesis. I am very grateful to Prof. Bradford Hager, Prof. Taylor Perron and Prof. Brendan Meade for serving as members of my committee and for their help and comments. I would like to extend my thanks to Prof. Oral Buyukozturk, Dr. Kunal Patil and all the colleagues from Kuwait for letting me be part of their Signature Project. I would like to express my gratitude and appreciation to Dr. Benedikt Ofeigsson at the Icelandic Meteorological Institute for making the internship possible and for helping me gain experience in volcano monitoring.

I would also like to thank my many friends and colleagues that accompanied me throughout this journey. First of all, my dear friend Sedar, whose exceptional kindness, hearth and humor, made me feel the support of a brother; my friend Nasruddin Nazerali for great conversations about life, art and science and Helen Shaw-Feng with whom I shared many experiences, nights of Spaghetti-westerns and fun times on the Cape. I would like to thank all my officemates Kang Hyeun Ji, Junlun Li and Abdulaziz Almuhaidib for making the 8th floor office an interesting and enjoyable place to work at.

I would also like to deeply thank everyone outside MIT that helped me overcome difficulties and grow as a person: Stefanie for an invaluable friendship and good hearth and for sharing with me the incredible journey that is horsemanship; all my friend from Italy that made me always feel close to home: Carmine, Carolina, Alice and Vania.

I am forever indebted to my family for their unconditional support and love, my parents Anna and Renato and my sisters Valentina e Camilla, and my 'new' family for accepting me and supporting me, Karen and Jude, Misa and Gabriel. Finally, I am deeply thankful to my husband Josh for his love and support and for a wonderful life together.

TABLE OF CONTENTS

LIST OF FIGURES

LIST OF TABLES

LIST OF ABBREVIATIONS

GPS	Global Positioning System
Envisat	Environmental satellite
RADARSAT	Radar satellite
IGS	International GNSS Service
InSAR	Interferometric SAR
SAR	Synthetic Aperture Radar
SNR	Signal to Noise Ratio
DEM	Digital Elevation Model
3D	Three Dimensional
RMS	Root Mean Square
N	North
E	East
S	South
W	West
T	Temperature
LOS	Line of Sight
PSD	Power spectrum density
STFT	Short Time Fourier Transform
DFT	Discrete Fourier Transform
MPH	Miles per Hours

Chapter 1

Noise analysis and downsampling of InSAR measurements to constrain surface deformation in a gas reservoir

Abstract

In this chapter, I present a methodology for the study of a deformational sequence in a gas reservoir (Beta reservoir), using a combination of geodetic data analysis and finite element modeling. The project was part of the of the Multiscale Reservoir Science Project, lead by Dept. of Environmental and Civil Engineering (Prof. Ruben Juanes group), by Earth Atmospheric and Planetary Science Dept. (Prof. Brad Hager and Thomas Herring groups) at MIT and ENI S.p.A., E&P division (Italy). The overall project had the purpose of characterizing the properties of the reservoir (porosity and permeability), by inverting the deformation field measured by InSAR observation. In this chapter I develop the analysis of the geodetic measurement and a forward model to be compared with the measured field. InSAR data were processed using a PS scatters technique (Hooper et al. 2004) that ensure a better estimate of the motion when ground conditions change on the scale of the radar wavelength between different acquisitions. I present a method to estimate noise covariance of InSAR data, taking into account the spatial correlation of noise between individual data points for each interferograms. I show a method to average and filter InSAR data in order to reduce the numbers of points to be compared with the model and the noise in the data. I simulate the ground motion caused by injection/withdrawal of gas in the reservoir with a finite element model: pressure changes inside the reservoir are input to the geomechanical model to obtain the ground displacement. From the analysis, we measure a ground displacement up to 15 mm of subsidence and 5 mm of uplift on top of the reservoir and we conclude that the observed deformation is a result of seasonal pressure changes in the reservoir, due to injection/withdrawal cycles of natural gas.

1.1 Introduction

Differential interferometric synthetic aperture radar (InSAR) is a satellite-based technique that allows to measure the surface motion with high resolution and spatial continuity. The interferometric procedure consists in interfering two overlapping SAR images acquired from similar viewing geometry and subtracting geometrical phase contributions using satellite ephemeris data and a reference topography model (Ferretti et al. 2007). Although high accuracy is theoretically achievable with this technique, several errors can still affect the observed interferometric phase, such as topography model errors, atmospheric delay and satellite state vector (Ferretti et al., 2007). Therefore, to better characterize the deformation models in these data sets and to resolve them properly, it is important to assess and quantify the noise affecting them. Many classical geophysical applications of InSAR have been successfully applied to study deformation without quantifying the error (Massonet et al. 2005; Fialko and Simons, 2001).

However, in some cases error estimation is required to model the deformation. In fact, some inversion methods, such as Kalman filtering, require an error model to be incorporated in the inversion.

In this chapter, I estimate the covariance structure of the InSAR data with specific application to the inversion of ground deformation in response to gas storage in a depleted reservoir. Inversion techniques can be computationally costly if the number of points to be inverted is large. Previous studies (e.g. Jonsson et al. 2002; Simons et al. 2002) have shown that proper spatial sampling and averaging of interferogram can effectively reduce the computational cost while retaining as much information as possible.

In this chapter I explore methods to reduce the number of points in the dataset through spatial filtering and I discuss their effectiveness in reducing the error and extract the signal of interest.

Previous efforts using this approach to investigate the deformation history of the reservoir (Teatini et al, 2011) had resulted in a qualitative agreement in sign and amplitude between the InSAR data and the forward model of the reservoir but quantitative discrepancies in magnitude and spatial scale.

In this study, I apply a procedure to improve Teatini et al. approach, using ENVISAT data with a broader coverage in order to detect regional trends and asses the quality of the data. I model the deformation using a finite element model, built in the Pylith software (Aagaard et al., 2008).

Funding for this project was provided by Eni S.p.A. through the *Multiscale Reservoir Science Project.*

Some of the concepts described in this chapter are published in: '*Reservoir characterization in an underground gas storage field using joint inversion of flow and geodetic data*', Jha et al. 2015.

1.2 InSAR data: processing and error estimation

1.2.1 PS scatter processing

Differential interferometric SAR is a methodology where two SAR scenes acquired over the same area at different times provides radar phase information that allows for the detection and measurements of sub-centimeters-scale ground movement in the form of phase change interferogram (Burgmann et al. 2000; Hassen, 2001). The radar signal is scattered back from an object on the ground toward the receiver. The amplitude, polarization and phase of the scattered signal changes depending on the characteristic of the object. Comparisons of the received signal characteristics to the transmitted signal allows the properties of the object to be inferred (fig. 1.2.1 *left*). In the standard methodology for InSAR processing, measurements of the radar phase change are made on a pixel-resolution basis. Although standard processing has been successfully applied in various deformation studies, this methodology can generate largely incoherent results when ground conditions change on the scale of the radar wavelength between data acquisition. In fact, the phase value for each pixel is given by the sum of the signal scattered by different objects within the pixel. If the scatterers move with respect to each other, the phase sum changes between different acquisitions, resulting incoherent phase distribution in time (fig.1.2.1). The permanent scatter (PS) methodology is instead based on the identification of individual radar reflectors that

are smaller than the pixel resolution and remain coherent over long time intervals (Ferretti et al. 2001) (fig. 1.2.1 *right*). The algorithm involves removing the residual topographic component of

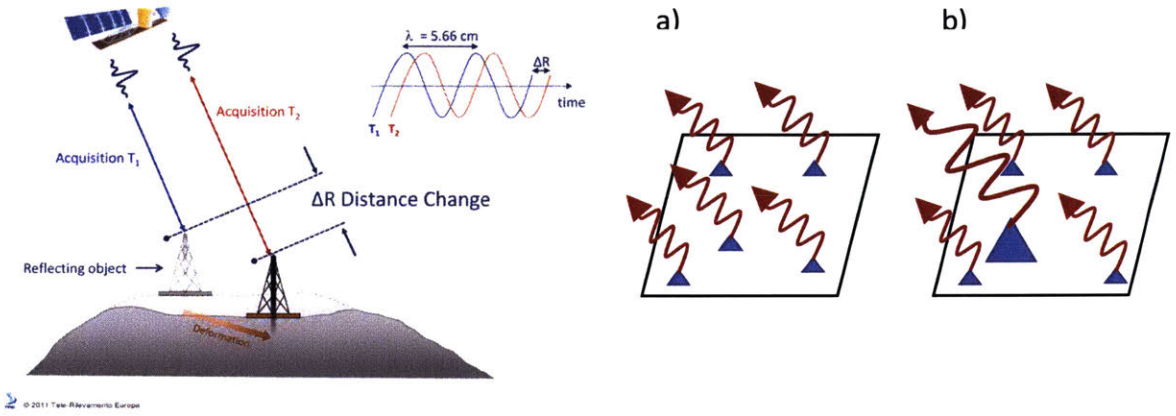

Figure 1.2.1 Scheme of Aperture Radar interferometry (InSAR) on the *left* (Courtesy of *Telerilevamento Europa*). Sketch for different InSAR processing procedures: standard (*right a)* and with PS scatters methodologies (*right b*).

flattened interferogram phase for each PS, then unwrapping the PS phases both spatially and temporally. The scatterers are chosen with stable phase characteristics and generally correspond to persistent, bright radar reflectors, such as buildings, poles, metallic structures, rocks or similar objects. PS InSAR technology has been successfully used to detect ground motion in oil reservoir (Stancliffe and Var der Kooij, 2001; Vasco et al., 2008; Mathieson et al., 2009).

For this study, we used EnviSAT InSAR data, that were processed by Noa Bechor using the PS identification method (StaMPS) as described in Hooper et al. (2004) to study the seasonal deformation in the Beta gas field (Northern Italy). StaMPS method identifies pixels with phase stability that are not identified by the existing amplitude-based algorithm. It uses the spatial correlation of the phases rather than a well-defined phase history so that temporally-variable processes are successfully detected (e.g., volcanic deformation, injection/removal cycle in oil field). In table 1.2.1 the main features of the processing are reported. A director is the vector describing the satellite direction (table 1.2.1). The total number of PS points used in the processing are 99314. In the previous work of Teatini et al. (2011), the seasonal deformation of the BETA field has been detected using RADARSAT-1 images from 2003 to 2007 processed with PSInSAR™ analysis (Ferretti et al. 2001). RADARSAT is the Earth observation satellite operated

by the Canadian Space Agency and was active from 1995 to 2013. The satellite observes in the C-band wavelength (5.6 cm) and has an HH polarization of the signal (horizontal transmit and horizontal receive), a resolution from 8 to 100 m and a repeat cycle of 24 days. EnviSAT satellite, operated by the European Space Agency and active from 2002 to 2012, also acquires in C-band and has 5 polarization modes, a spatial resolution beween 30 and 150 m and a repeat cycle of 35 days. Figure 1.2.2 shows the comparison between EnviSAT and RADARSAT-1 data: RADARSAT data are more scattered and have a smaller mean amplitude compared to the EnviSAT, as expected for different methodologies used. In fact, the two methods (PSInSAR™ and StaMPS) mainly differ on the PS selection: the first one relies on the model of the temporal behavior of the PS (PSInSAR™), while the second is based on the spatial correlation of the PS, with the assumption of the spatial smoothness of the deformation signal. This results in different PS selected for the analysis with different density (table 1.2.1) and different phase behavior.

	EnviSAT		***RADARSAT***	
Feature	*Ascending*	*Descending*	*Ascending*	*Descending*
First scene	5-Jun-2005	5-Jun-2005	7-Mar-2003	28-Apr-2003
Last scene	25-Feb-2007	23-Feb-2007	12-Oct-2007	16-Oct-2007
Number of scene	13	13	63	58
Number of PS	99314	99314	4995	5923
Director	[0.5566 -0.1034 0.8243]	[-0.5161 -0.1052 0.8501]	[0.8500 -0.5160 -0.1052]	[0.8243 0.5566 -0.1035]

Table 1.2.1 Main features of the ENVISAT dataset used in the processing (*Courtesy of Noa Bechor*) and of the RADARSAT dataset processed by *Teatini et al. (2011).*

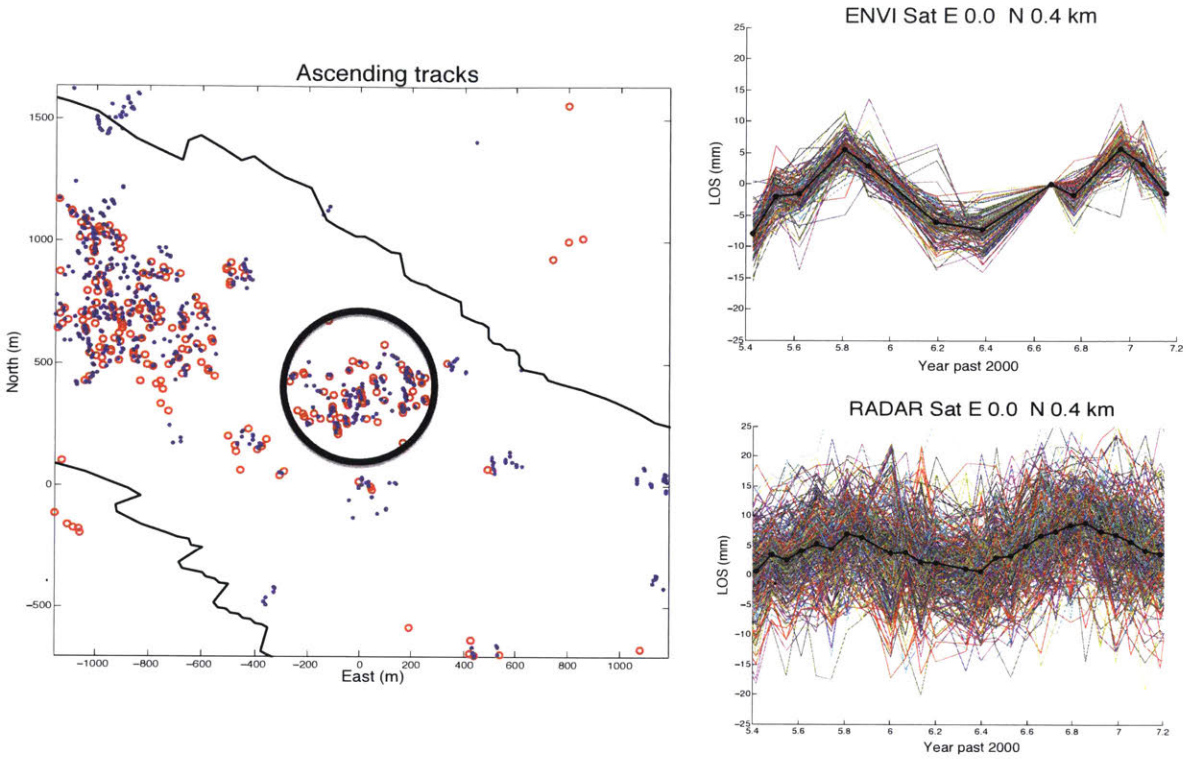

Figure 1.2.2 Comparison between the ENVISAT (*top right)* and RADARSAT (*bottom right)* dataset at the center of the reservoir. The RADARSAT data results in a more scatter and lower amplitude LOS deformation compared to ENVISAT.

In figure 1.2.3 the time series for ascending tracks of the ENVISAT dataset are shown. Thirteen dates spanning from 2005 to 2007 have been processed and seasonal variations of the deformation can be observed in the time series. The magnitude of LOS (Line-of-Sight) displacement observed ranges between -40 mm and 20 mm. Negative and positive motion indicate that the PS point is moving respectively away and towards the satellite. The phase has been converted in displacement, multiplying it by $56.2\ mm/(4\pi)$. The reference date used for the processing is September, 3rd 2006. In the following section, a methodology to filter and smooth the results to reduce the number of data points and an analysis of the error will be discussed.

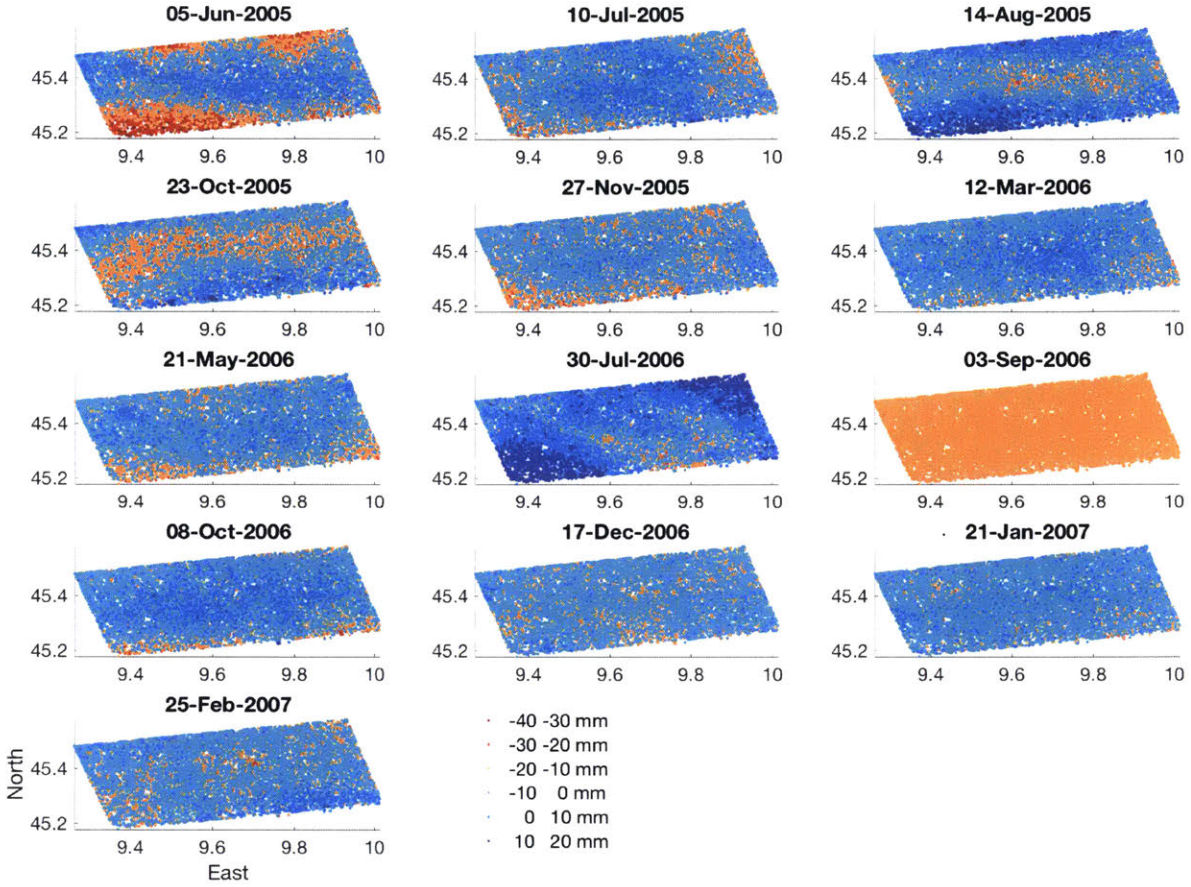

Figure 1.2.3 Time series for the ascending tracks of ENVISAT dataset, processed with StaMPS methodology (Hopper et al., 2004). The reference date for the processing is September, 3rd 2006. Deformation varies between -40 mm to 20 mm. Large deformation, possibly related to regional processes or atmospheric errors, occurs at different times of the year.

1.2.2 Covariance analysis and error model on InSAR interferograms

InSAR interferograms can contain spatially correlated signals, mostly related to atmospheric and ionospheric structures that are commonly coherent over length scale of tens to hundred km (Hanssen, 2001). Vertical variation of the refractivity index in the atmosphere, due to changes in pressure, temperature and water vapor content can results in correlation between range change and

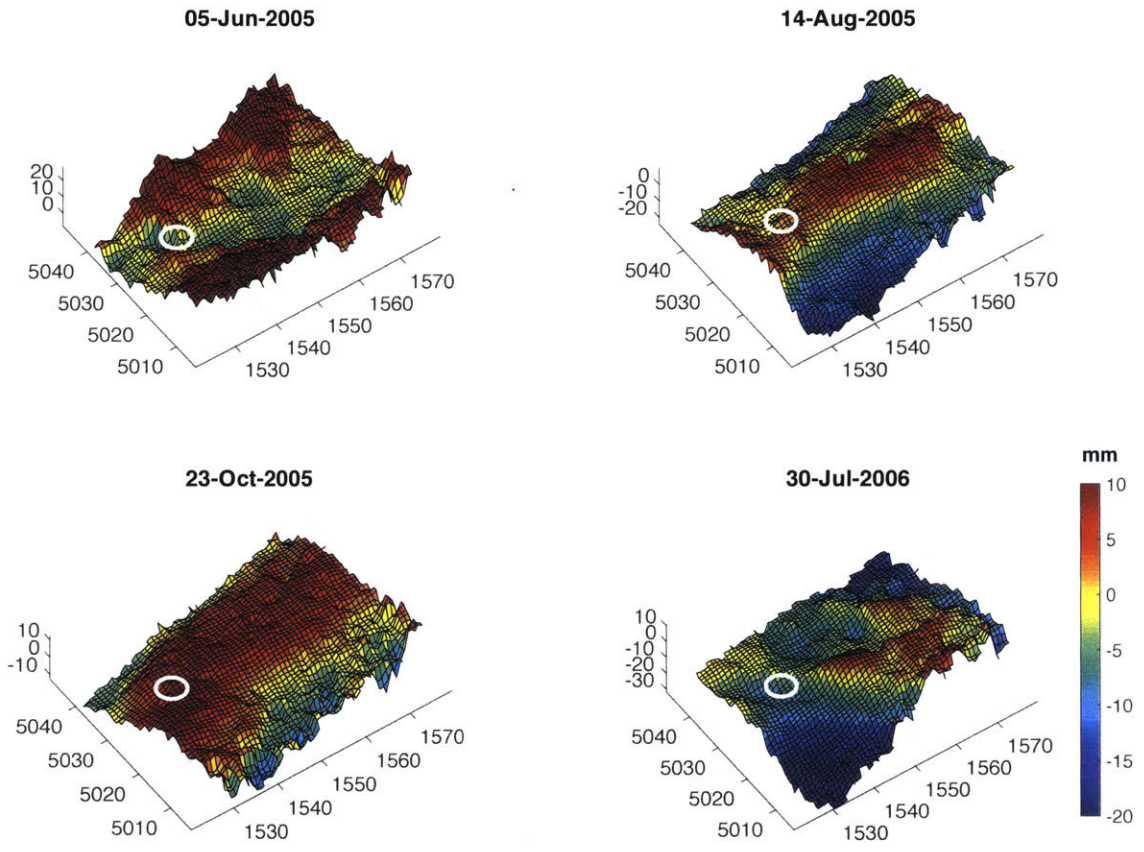

Figure 1.2.4 Interferograms of the ENVISAT data, showing spatially correlated signals affecting the observed deformation. Measures of the displacement are shown in Line-of-Sight (LOS) direction and are in mm. White circle shows the location of Beta reservoir. The horizontal coordinates are in Gauss-Boaga geographic projection.

topography between two SAR acquisitions (Hanssen, 2001). As the resulting phase patterns typically mimic the topography, it is difficult to discriminate between atmospheric and

deformation signals is particularly in areas where topography and deformation are correlated (Beauducel et al., 2000). Two main methodologies have been previously applied to mitigate the effect of the atmosphere on SAR interferograms: statistical (Zebker et al. 1997; Emardson et al. 2003) and calibration (Delacourt et al. 1998, Williams et al. 1998, Wadge et al. 2002). The statistical methodology consists in stacking and averaging several independents interfeograms to mitigate the noise with the assumption that the atmospheric delay is white noise. However, this methodology requires a large number of interferograms to obtain a precise average of the noise value and spatial and temporal variation are lost in the averaging of the images. In the calibration methodologies, the phase delay is estimated from external data, such as zenital delay estimation from GPS (Global Positioning System) data (Williams et al., 1998; Webley et al., 2002; Li et al., 2006a; Onn and Zebker, 2006), local atmospheric data collection (Delacourt et al., 1998) and assimilation of meteorological data in atmospheric models (Wadge et al., 2002; Puysségur et al., 2007; Doin et al., 2009). Although these methods are proved to be accurate in mitigating part of the atmospheric phase delay, they rely on local data which are often sparse (therefore not suitable to model turbulence in the atmosphere) or not available at all. GPS data were not available in the area of study.

In this analysis, the atmospheric phase errors are estimated by applying temporal and spatial filtering. The contributions of these errors are determined by filtering first unwrapped phase values in time using a high pass filter (HP), then the resulting values in space with a low pass filter. This is based on the characteristic of these errors of being highly correlated in space, but uncorrelated in time. This filtering technique allow a partial reduction of the noise due to atmospheric structures but there are still contributions, especially when turbulence is present. These contributions are considered as noise in the signal and they need to be quantified in order to assess the significance of the source model inferred from the data. In this study, I estimated the covariance structure of noise in the interferograms to understand the contribution to the deformational signal, following a similar approach as described in Lohman and Simmons (2005).

To estimate the noise covariance matrix, $\mathbf{C_n}$, Lohman and Simmons (2005) assume that the covariance between any two points depends only on the distance between, under the assumption that the noise is isotropic and spatially stationary. The covariance between two points at r distance is therefore:

$$C_n(r) = Cov(\boldsymbol{x}, \boldsymbol{x}+\boldsymbol{r}) \quad (1)$$

$$= E[f(\boldsymbol{x})f(\boldsymbol{x}+\boldsymbol{r})] \quad (2)$$

where $r=|\mathbf{r}|$, $f(\mathbf{x})$ is the measurement at position $\mathbf{x}$, where the averaged noise value is assumed to be zero. I also calculated the structure function as the variance of the difference between two points separated by a distance r (Hanssen, 2001; Jonsson, 2002; Lohman and Simmons, 2005),

$$S(r) = E\left[\left(f(\boldsymbol{x}) - f(\boldsymbol{x}+\boldsymbol{r})\right)^2\right] \quad (3)$$

such that

$$C_n(r) = \sigma^2 - \frac{S(r)}{2} \quad (4)$$

where σ^2 is the variance of noise. A sample variogram is used instead of the explicit covariance formulation as the calculation of autocorrelation between any possible pairs of points within the image would be computationally costly. Lohman and Simmons (2005) demonstrate that choosing a large number of random pixels binned by distance in the sample variogram ensure an accurate estimate of the covariance.

Sample covariance function can be calculated in a similar way as the sample variogram and describes the spatial relation between data pairs at $\boldsymbol{x}_i$ and $\boldsymbol{x}_i+\boldsymbol{r}_i$:

$$C(r) = \frac{1}{P(r)} \sum_{i=1}^{P(r)} f(x_i) \cdot f(x_i + r_i) - (m_i \cdot m_r) \quad (5)$$

where $\boldsymbol{m}_i$ and $\boldsymbol{m}_r$ are local means of $\boldsymbol{f}$ at $\boldsymbol{x}_i$ and at $\boldsymbol{x}_i+\boldsymbol{r}_i$, respectively and $\boldsymbol{P(r)}$ the number of sample of each length r. Assuming second order stationarity the local mean within the image is constant and the equation above simplifies to:

$$C(r) = \frac{1}{P(r)} \sum_{i=1}^{P(r)} f(x_i) \cdot f(x_i + r_i) - \bar{f}^2 \quad (6)$$

Thus, in this case I can relate the variogram $\gamma(\boldsymbol{r})$ and the covariance function with:

$$\gamma(r) = C(0) - C(r) \qquad (7)$$

I calculated experimental variogram and covariance for each image, using all the data that do not contain known deformation (reservoir area). I then subtracted the best-phase fitting plane to remove potential error ramp caused by inaccurate orbital information. For this deformation-free image, I calculated a sample variogram and a sample covariance function as follow. For each distance r I randomly several locations (x_i, y_i) within the image and many random direction θ_i and compared the value at (x_i, y_i) and $(x_i + r\cos\theta_i, y_i + r\sin\theta_i)$. I calculated the sample variogram as in **(6)** and the covariance function as in **(7).** I fitted then the variogram with normalized Gaussian function, from which I estimated the correlation length for each interferogram (fig 1.2.5) as follow:

$$\frac{1}{\sigma\sqrt{2\pi}}\, e^{-\frac{(x-\mu)^2}{2\sigma^2}} \qquad (8),$$

where μ is the mean and σ the standard deviation. I found that the correlation length for different interferograms varies from 5 km to 10 km (as shown in fig. 1.2.6).

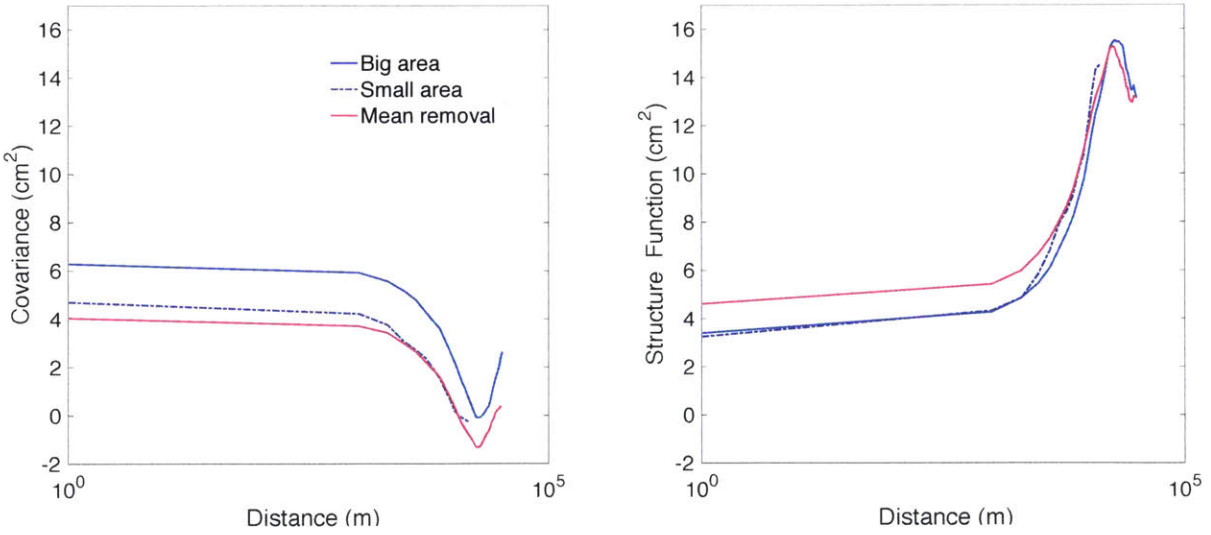

Figure 1.2.5 Covariance (*left)* and structure function (*right*) dependence on the window size of the image and the mean removal. The calculation is carried for 5-Jun-2005 interferogram. The covariance and structure functions are determined by variogram and calculated for the full image (*solid blue line*), for a quarter of the size of the image (*dotted blue line*) and removing the mean from the full image (*magenta line*).

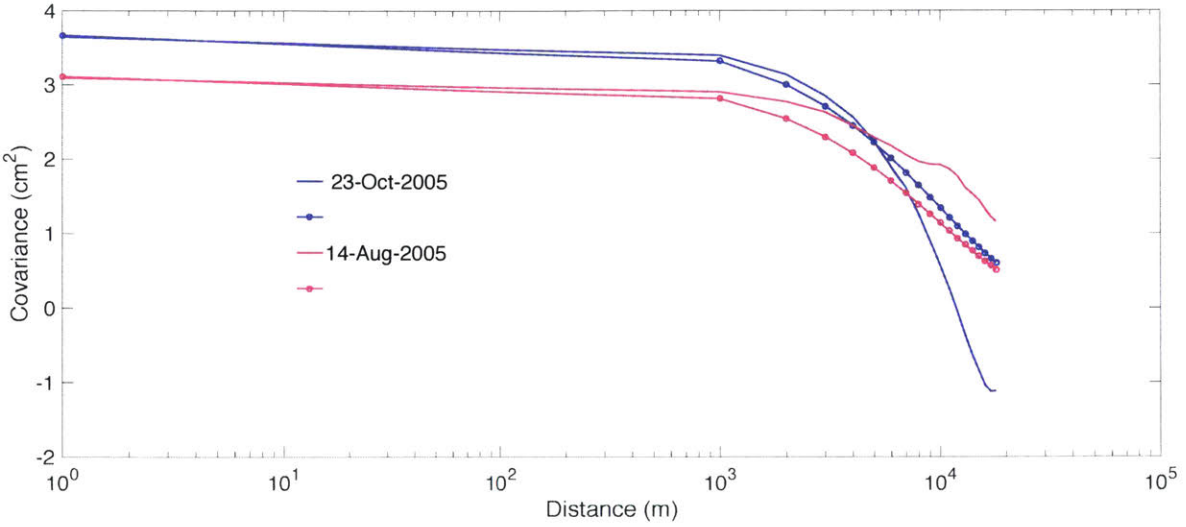

Figure 1.2.6 Variogram calculated for interferogram at date 14 August 2005 (bold purple) and 23 October 2005 (Bold blue) and their respective fitting (point and line). The correlation length inferred for the first interferogram is 5 km, while for the second interferogram is 11 km.

1.2.3 InSAR data resampling

The high spatial density of the InSAR measurements can be not ideal when inversion or comparison with a forward model of the deformation source is required. It is possible to reduce the number of data points without losing significant information by taking appropriate spatial averages. In order to do that, I first removed the deformation at the borders of the reservoir. In fact, a preliminary model of injection/withdrawal into a reservoir indicate that the deformation due to the pressure changes drops to zero outside the reservoir. Therefore, any motion detected by InSAR

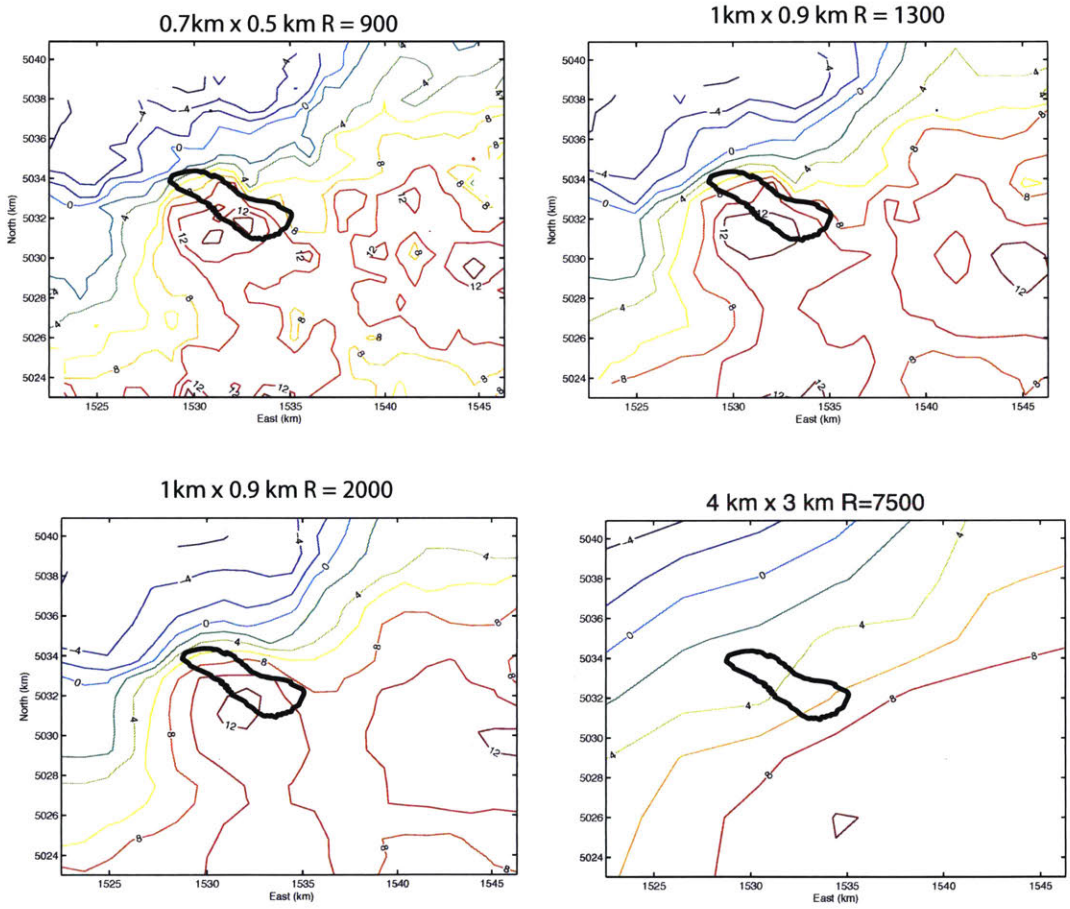

Figure 1.2.7 Filtering and averaging for different cell sizes. Deformation is shown in LOS and in mm. The horizontal coordinates are in Gauss-Boaga geographic projection. Black line shows the shape and location of the reservoir. A larger grid *(bottom right)* reveals regional processes underlying the reservoir.

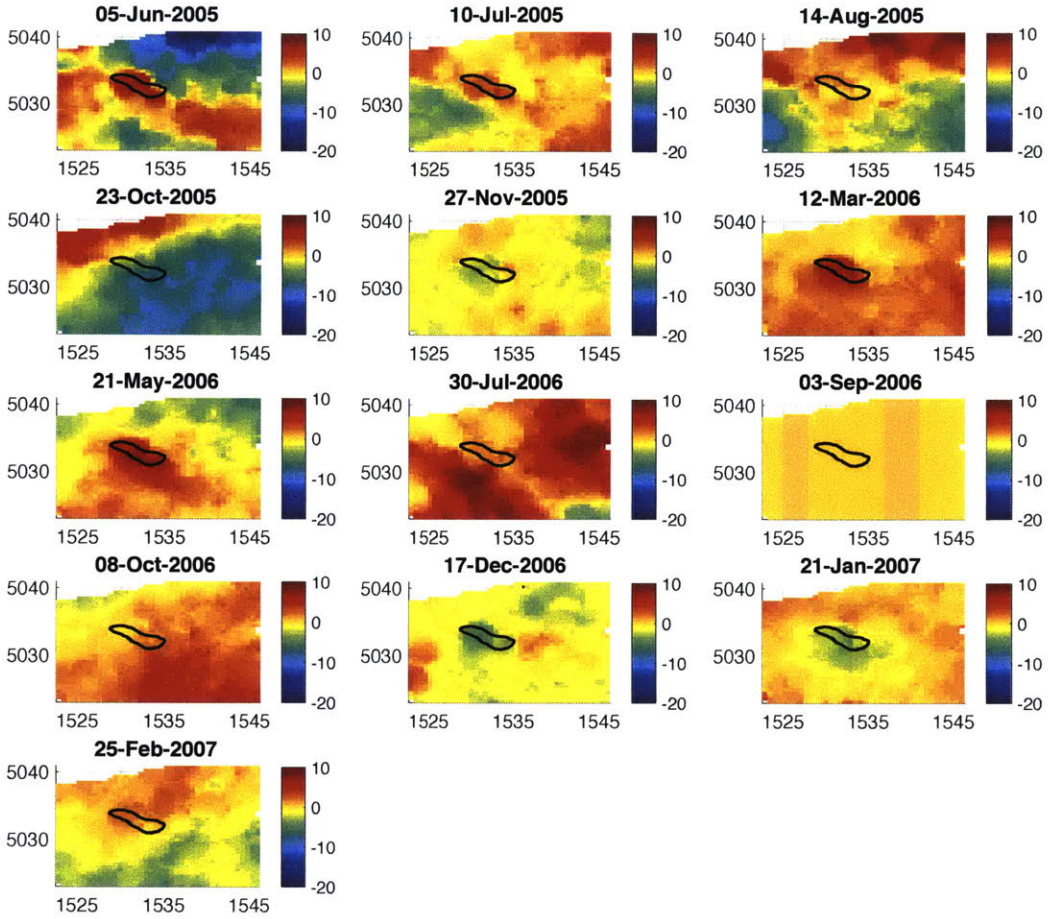

Figure 1.2.8. Smoothed time series of the INSAR dataset. The grid used was 470x350m with a smoothing radius of 750m. The LOS displacement ranges from -20 to 15 mm. The horizontal coordinates are in Gauss-Boaga geographic projection and the units are km.

data outside the reservoir has no contribution from the reservoir itself but it relates to regional deformation trends or correlated noise. Regional deformation in the area is related to both natural (tectonic, hydrologic) and anthropogenic processes (gas extraction, water use). In particular, the subsidence in Po river basin controlled by the Appennines subduction ranges from 0.7-1 mm/yr (Doglioni, 1993). The magnitude of deformation associated with other processes has not been established yet.

In this section I investigated how different averaging grids affect the signal and how they can be related to the deformation into the reservoir. I performed the averaging dividing the image in a regular grid and applying the Gaussian filter to the measurements inside the grid cells. I also included some of the points from the neighbor cells to obtain smoother results. In Figure 1.2.7 an

example of different grid averaging for a single interferogram is shown. A coarse grid averaging removes higher frequency contributions to the signal, showing a deformation that is likely not related to the local field of the reservoir, but to regional processes. A finer grid includes instead smaller contributions, very likely related to noisy data. The number of data points drops off from 10^4 in the finer grid to 10^2 in the larger grid. In following section, I compared different smoothing results with the deformation field inferred from the forward model.

In Figure 1.2.8 a complete cycle of injection/withdrawal is shown. The motion is projected in line-of-site direction (LOS), meaning that the surface moves towards or away from the satellite. Separating the horizontal component from the vertical in InSAR data can be difficult and not accurate, introducing errors that can compromise the correct estimation of the deformation. For that reason, I decided to maintain the data in the line-of sight and project the FEM model results in the satellite direction for comparison.

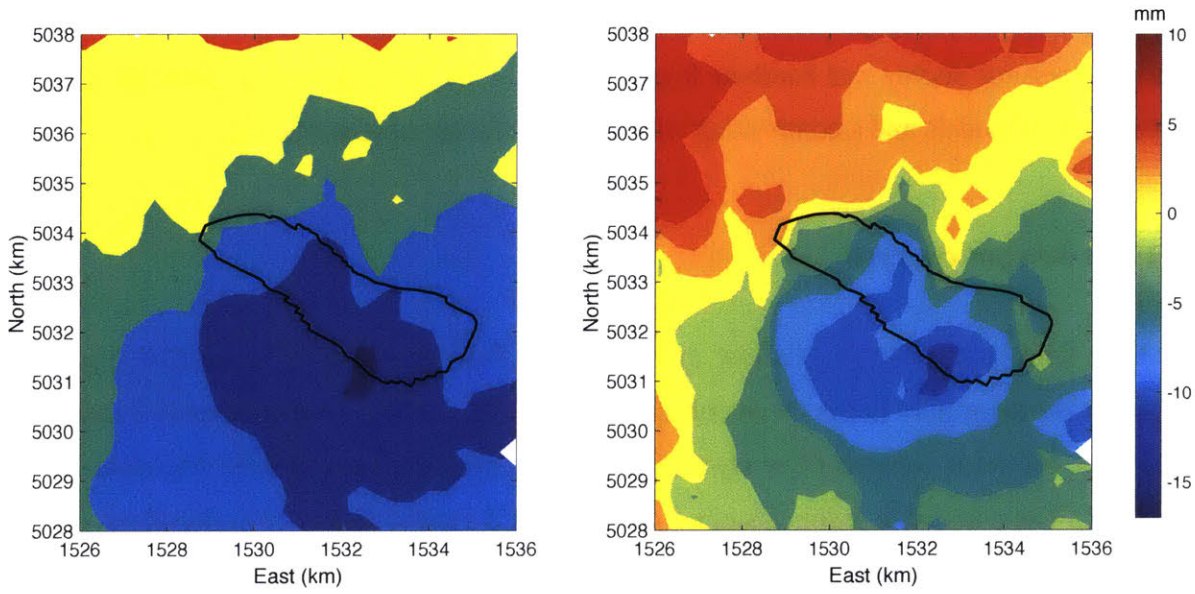

Figure 1.2.9 Comparison the original deformation field (*left*) and the effect of the regional deformation field removal (*right*). The LOS displacement inside the oil field is reduced on average of about 4 mm. The horizontal coordinates are in Gauss-Boaga geographic projection.

The large motions can be related to regional processes and correlated noise and are removed from the reservoir deformational field (fig. 1.2.9). The removal of the regional deformation reduced the displacement inside the oil field of about 4 mm on average. The comparison between the different filtering/sizing models and the finite element model of the oil field will be discussed in next section.

1.3 Forward model of Beta gas reservoir

1.3.1 Introduction

A forward model allows to predict quantities of interest for a specific set of the model parameters. In this study, the forward model is a one-way coupled flow and geomechanics model of the Beta field. Three different steps are involved in the model realization: the geological model, the flow model, and the geomechanical model. A geological model allows to build the geometry of the study area with its structural (faults, folds, pinchouts, etc.) and stratigraphic (sand-shale layering, lithology etc.) characteristics. These features are important to model as they can act as impermeable barriers to flow and may have deformational behavior significantly different from the surrounding medium. It becomes necessary to implement an accurate geological model for the realization of the flow and geomechanical models. A geological model of the Beta field is realized from a 3D seismic survey and borehole logs available in the field. Below I present the flow and geomechanical models and a comparison with the geodetic measurements.

1.3.2 The Beta gas reservoir

The Beta field is an onshore, shallow multilayer gas field operated by Stogit-ENI S.p.A. and located in Northern Italy in the Po river basin (Stogit S.p.A. 2008). As described in Teatini et al. (2011), the reservoir consists of sandy sediments onlapping the partly folded Messianian basin (fig. 1.3.1). The permeable sediments pinch out northward against the impermeable clays, creating stratigraphic gas traps. The reservoir is 1050-1350 m deep and is divided in three gas-bearing pools (San P/E, San P/C and San P/B) that are vertically separated by 20-30 m thick clay layers (Teatini et al. 2011). The reservoir is connected to an aquifer in southward direction.
Primary production started from San P/E from 1981 to 1986 and a minor production occurred over the period 1988-1996 in San P/B and San P/C. UGS (*Underground Gas Storage*) started soon after.

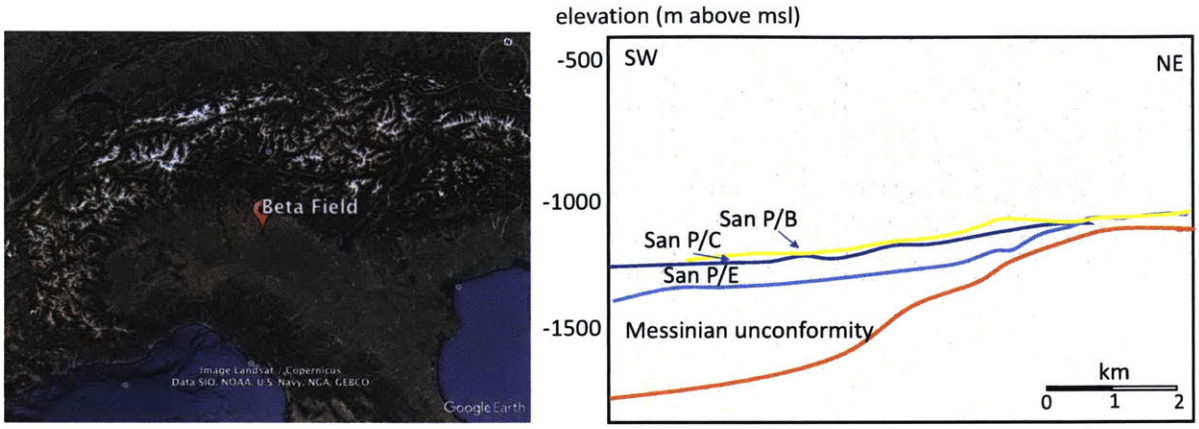

Figure 1.3.1 *Left:* location of the 'Beta' reservoir (Google Earth image: 45°28'10.81''N; 9°31'26.47'' E; elev 236 m; eye alt 521.45 km; date 05/07/2017). *Right:* Cross section of the geometry of the reservoir based on vertical seismic cross section through field along a southwest-northeast direction. The geological units of major interest are shown. *Modified after Teatini et al. 2011.*

1.3.3 Flow model

The Beta gas field is composed by three gas bearing layers that have been harvested at different times. The first deposit (layer San P/E) was in production from 1981 to 1986, with a cumulative volume of gas of 2701 MSm^3 (*Mega-standard cubic meter*). The layer is today used to store natural gas between April and November and to withdraw from it the rest of the year. The other two layers (SanP/C and San P/D) were exploited from 1988 to 1996, producing respectively 204 and 104.5 MSm^3 of gas. STOGIT S.p.a. has developed a dynamic flow model for Beta field, using *Eclipse™* software (Schlumberger, 2007). The model simulates the time variation of pressure in the reservoir and two scenarios with a maximum injection pressure of 107% and 120% of the initial pressure for San P/E layer in November (at the end of the injection cycle). The flow equations are solved in the standard conditions for a two-phase gas (CH_4 in the present case) and water system (the so called 'black oil' model). The flow simulation was then calibrated with a "history match" procedure based on the pressure and production measurements collected over the time interval from 1981 to 2007.

The aquifer, extending 20 km southwest of the reservoir, is included in the model to ensure that the pressures propagate correctly in the nearby areas. The aquifer model was also calibrated, assuming a value for the horizontal permeability that would allow a volume of water compatible with the amount of gas produced. However, the lack of dynamic well data and lack of prior well log data in the aquifer region to determine aquifer pore volume and permeability introduce a

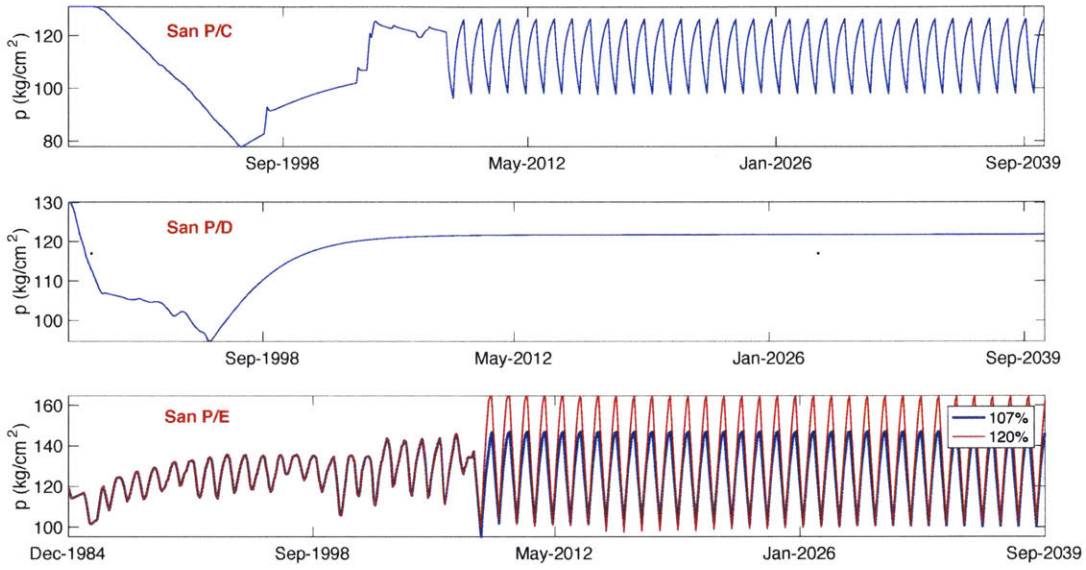

Figure 1.3.2 Time series of the pressure variation in San P/C., San P/D and San P/E layers. For San P/E two scenarios are shown:107% and 120% pressure in blue and red respectively (data are *courtesy of ENI-Stogit S.p.a.)*.

relatively large uncertain in the pressure variation effects on the aquifer. The areal extension of the model, covering both the gas-bearing region and the aquifer region, is 56x54 km^2.

The resulting simulation shows that the pressure variations are larger in San P/E layer with values between 105 kg/cm^2 and 140 kg/cm^2 and between 100 kg/cm^2 and 160 kg/cm^2 in the 107% and 120% scenarios respectively (fig.1.3.2). The simulation also suggests that the effects of the pressure variation for cycles of injection/withdrawal are limited to an area of about 4km radius from the edges of the reservoir (fig. 1.3.3).

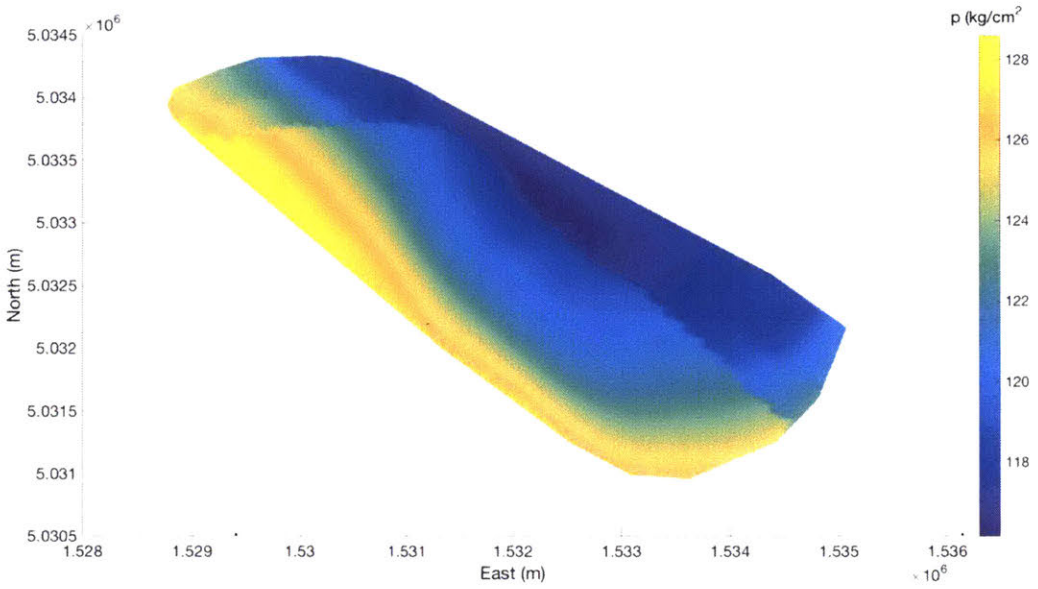

Figure 1.3.3 Map of pressure distribution in San P/E layer at the end of the production (1986). The pressure field affects only a radius of about 4 km from the reservoir (pressure data are *courtesy of ENI-Stogit S.p.a.)*. The sharp line on the northern side of the reservoir, representing a pressure contrast, is related to the presence of the aquifer.

1.3.4 Forward modeling

The surface deformation related to periodical fluids injection and withdrawal into an underground reservoir depends primarily on the field geometry (i.e., depth, thickness, areal extent), geomechanical properties of the gas- bearing and surrounding porous medium, and pore pressure changes induced by fluid storage and removal. The process is theoretically described by the 3-D fully coupled poroelasticity model, originally developed by Biot (1941). Based on the classical poroelastic theory, the equilibrium equations governing the deformation of a mechanically isotropic medium are

$$G\nabla^2\boldsymbol{u} + (G+\lambda)\nabla(\nabla\cdot\boldsymbol{u}) = \alpha\nabla p + \boldsymbol{b} \quad (9)$$

where ∇^2 is the Laplace operator; G and λ are the shear modulus and Lame' constant of the medium

respectively; **u** is the displacement vector; α is the Biot coefficient; p is the in situ pore pressure variation; and **b** is the vector of the body forces. Within the gas reservoir, p has to take into account the pressure of both the water (p_w) and the gas (p_g) component according to the relationship (Bishop, 1959):

$$p = S_g p_g + S_w p_w \quad (10)$$

with S_w and S_g the saturation index of water and gas respectively. The water saturation is the fraction of the pore space occupied by water. Most reservoirs are water wet and contain connate water. Water saturation may range from 10% to 50% for an oil or gas reservoir and is 100% for an aquifer. The gas saturation is the fraction of the pore space occupied by gas (S_g) and can vary from 30% to 90%.

In a fully coupled model, porosity is function of pressure and temperature. This means that stresses into the rocks caused by changes in fluids pressure modify the porosity. As the software used for the geomechanical simulation doesn't allow coupled physics, I created a preliminary model solving the flows equations first and passing the resulting pressure field to the geomechanical simulator. One-way coupling doesn't update the pressure and displacement back and forth, between the flow and geomechanics calculations at each time step. The limitation of this type of model is that the dependence between the two equations is not well represented.

The geomechanical simulation is performed using the software *Pylith*, which is a finite element simulator for crustal deformation. I assumed a linear-elastic rheology, defined by Young's modulus (E) and Poisson's ratio (ν). I also performed a simplified geometry simulation to conduct sensitivity tests. The complete model has an areal extent of 20 km x 16 km and a depth of 5 km. Boundary conditions with zero displacement in normal direction on the side and zero displacement on the bottom boundaries are prescribed, while the top surface is a free boundary. The geomechanical grid has been rotated by 24° in order to align with the reservoir and its extent is large enough to assure no effects at the boundaries. The reservoir has been modeled as a rectangular shape including the aquifer area at 1100 m depth below the surface. Neumann boundary conditions ('loads' on the right-hand side of the system of equations) are prescribed for the boundaries of the reservoir where the simulated gas pressures are input as tractions on the boundary surface. The 3D mesh performed with *Cubit™* (Sandia National Laboratories, 2010) is

formed by 200,000 hexahedral elements with a resolution of 200 m with a refinement on the reservoir boundaries to be consistent with the element dimension used in Eclipse for the fluid flow simulation (about 50 m grid size). The deformation has been computed for 13 time steps (from 1 October 2003 to 1 Jun 2006). The complete geometry (courtesy of ENI-Stogit S.p.a. in fig 1.3.4) has an areal extent of 149x92x35 km with 479780 hexahedral elements. The grid is refined at the reservoir. Boundary conditions are the same as in the simplified model and pressure changes in the reservoir are simulated from *Eclipse ™*.

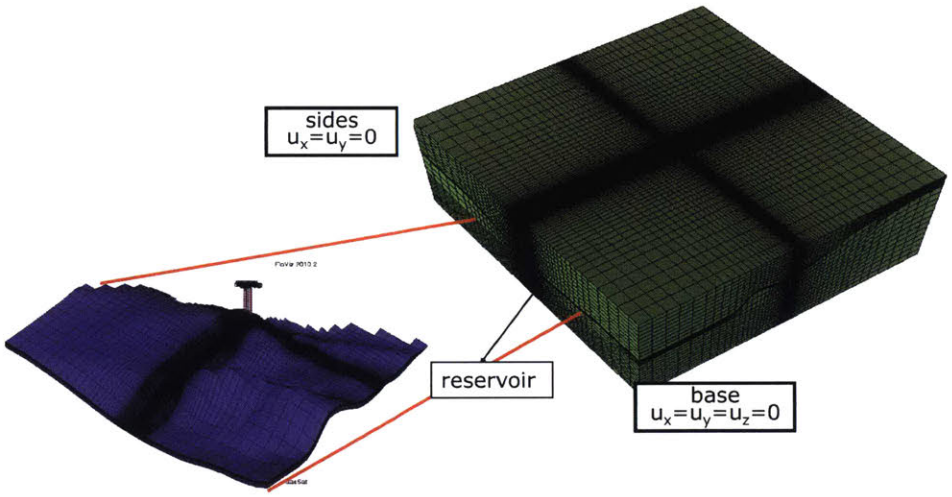

Figure 1.3.4 Full geometry of the FEM model (*courtesy of E.N.I-Stogit S.p.A.*). Mesh and boundaries condition are shown. A close up of the reservoir geometry is shown on the left.

1.3.4 Sensitivity analysis

To assess how sensitive the ground displacement is to the variation of mechanical properties, several test models were run, varying subsurface properties both in horizontal and vertical direction and pressures into the reservoir. These simulations are also intended to establish how well the displacement caused by the pressure field can be resolved by InSAR measurements. The model geometry has been rotated to align the major axis of the reservoir with E-W direction. In the first case, I modeled several cycles of injection/withdrawing into the reservoir, using the pressure changes simulated with *Eclipse™* and properties as shown in figure 1.3.5. *P*- and *S*-waves velocities from a seismic survey of the area were available at few depths (courtesy of ENI-Stogit S.p.a.) to calculate the elastic moduli of the reservoir. For the sensitivity run, the elastic moduli and densities were calculated from the linear interpolation of V_p and V_s with depth (fig. 1.3.5). The properties are uniform in horizontal direction. In figure 1.3.6 the vertical displacement

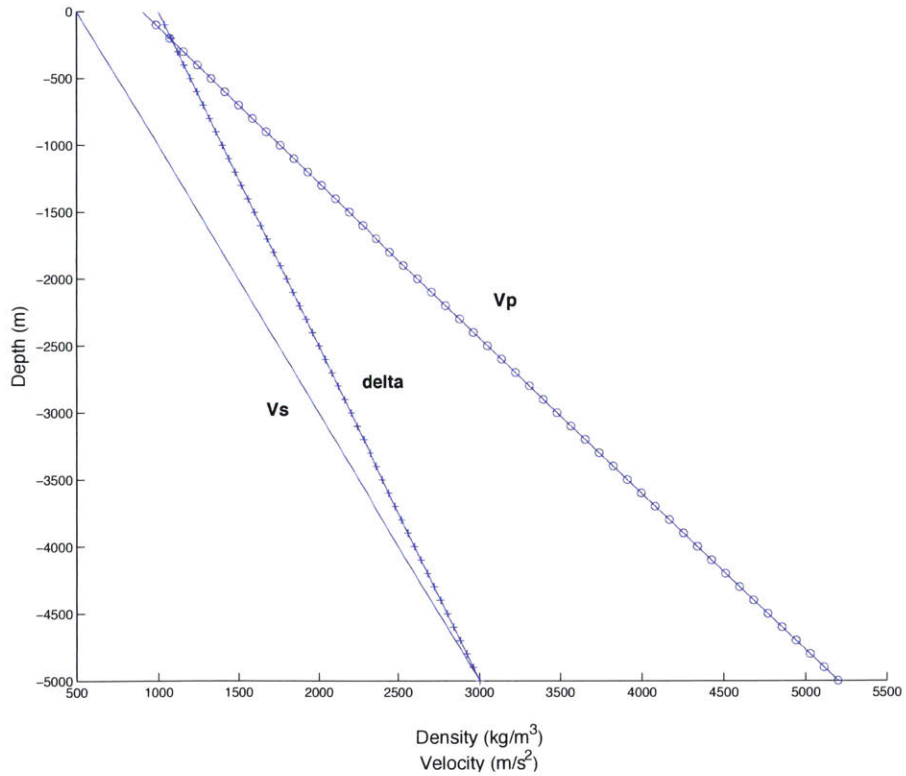

Figure 1.3.5 P- and S-waves velocities and density (delta) linear variation with depth.

simulations for several cycles of injection/withdrawal is shown. The vertical deformation field has

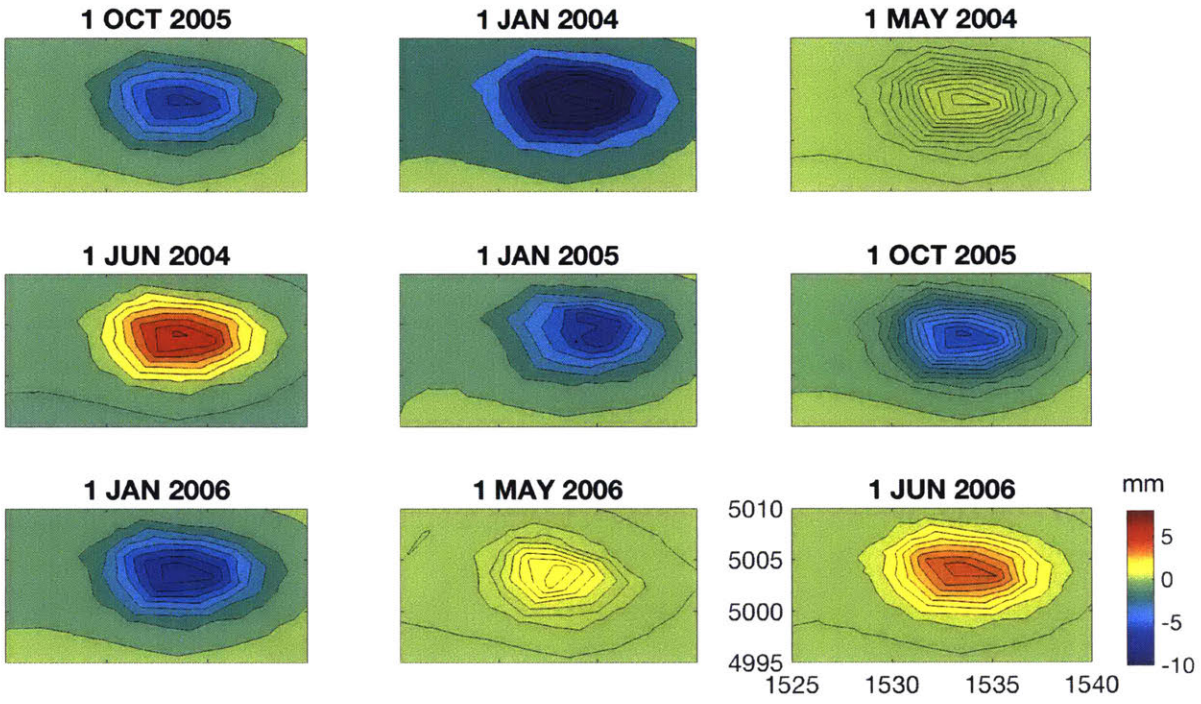

Figure 1.3.6 Close up of the displacement for a cycle of injection/withdrawal in the reservoir with linearly varying elastic properties. Deformation varies from -10 to 7 mm. The horizontal coordinates are in Gauss-Boaga geographic projection and the units are km.

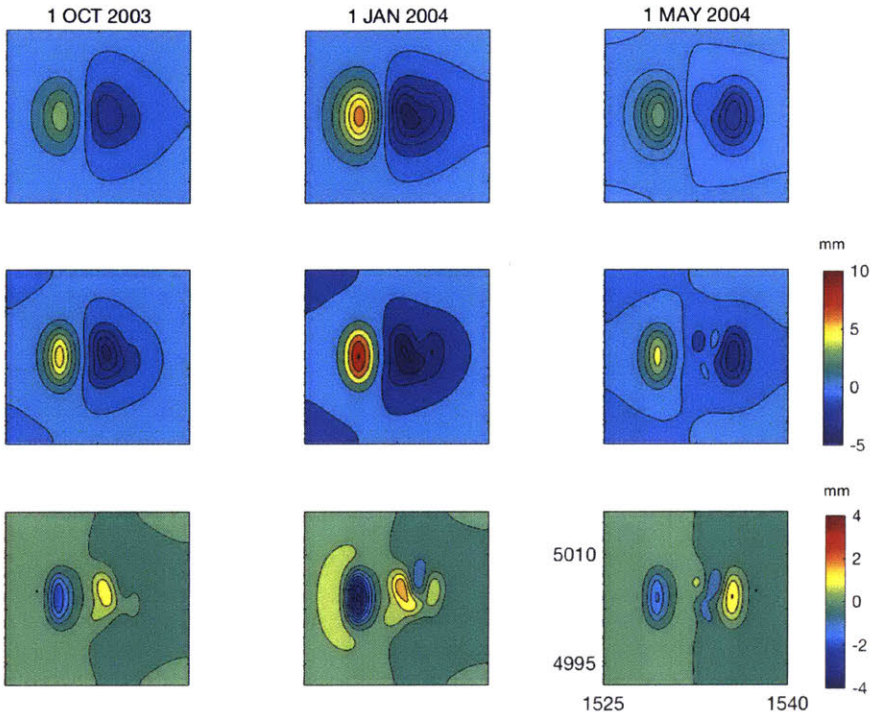

Figure 1.3.7 Close-up of the x-direction displacement for a cycle of injection/withdrawal in the reservoir with linearly varying elastic properties.

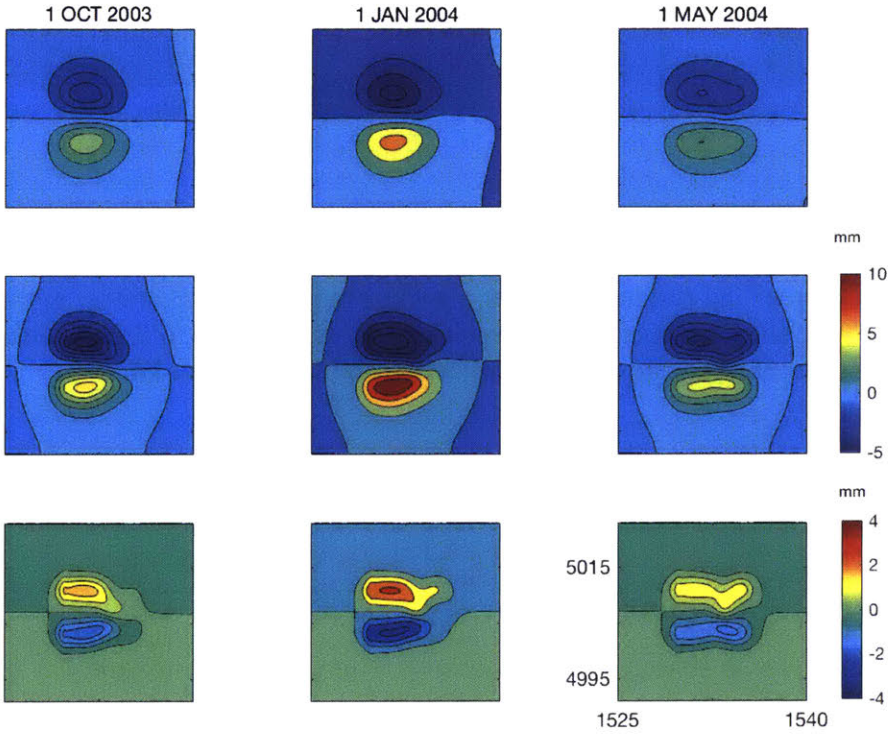

Figure 1.3.8 Close-up of the y-direction displacement for a cycle of injection/withdrawal in the reservoir with linearly varying elastic properties.

an elliptic shape elongated in E-W direction (along the major axis of the reservoir) in some months

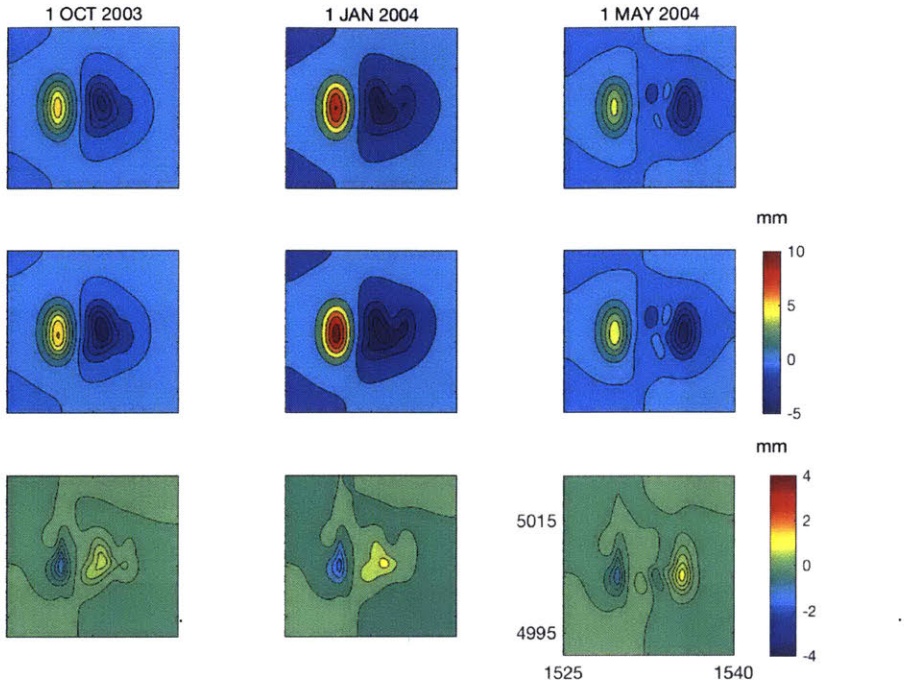

Figure 1.3.9 Close up of X displacements (in mm) at three different times. Top row has elastic moduli varying linearly with depth. Middle row has elastic moduli varying with depth but the north half is 10% more compliant than the south half. Bottom row is the difference between the top ones.

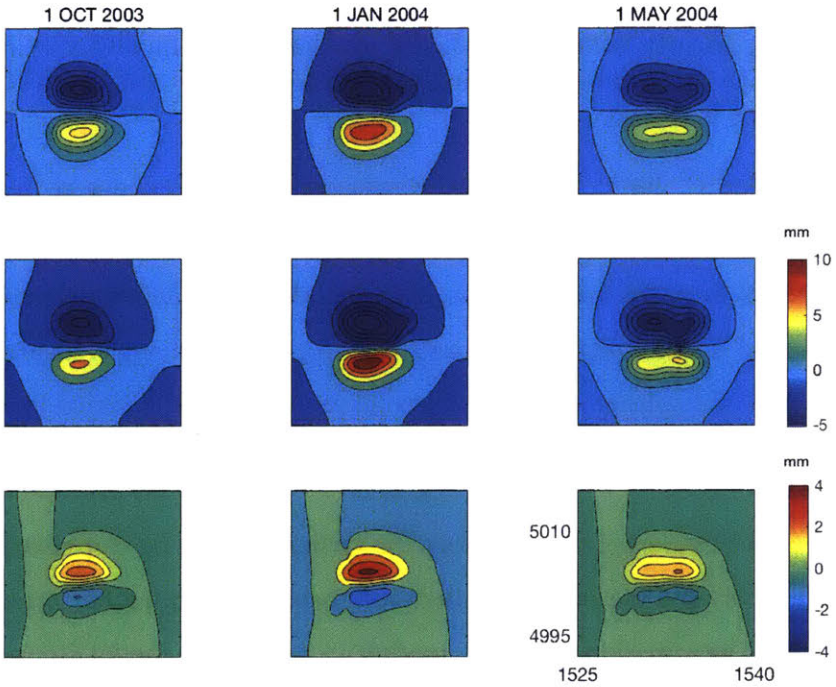

Figure 1.3.10 Close up of Y-displacements (in mm) at three different times. Top row has elastic moduli varying linearly with depth. Middle row has elastic moduli varying with depth but the north half is 10% more compliant than the south half. Bottom row is the difference between the top ones.

The deformation is characterized by general subsidence relative to the initial condition

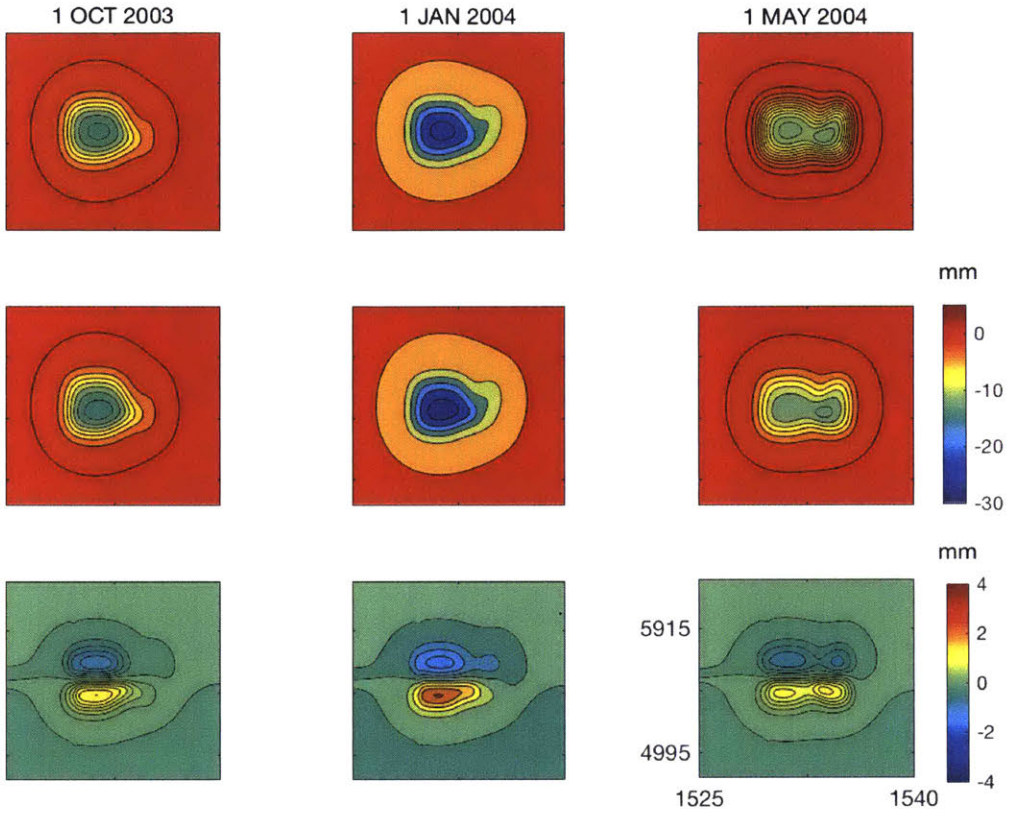

Figure 1.3.11 Close up of vertical displacements (in mm) at three different times. Top row has elastic moduli varying linearly with depth. Middle row has elastic moduli varying with depth but the north half is 10% more compliant than the south half. In the bottom row the difference between the two models is shown.

corresponding to October 1st 2003. The highest displacement values occur at the center of the reservoir, varying from -5 to -8mm, while the motion is null at the boundaries. In May 2006, the deformation field differs from the other months, showing almost no deformation at the center of the reservoir. Horizontal displacement is less sensitive to pressure changes inside the reservoir, producing only few mm of displacement. In the second sensitivity test, I varied the elastic moduli horizontally, making the north half 10% more compliant of the south half.

In figures 1.3.9 to 1.3.11 I the comparison between the vertical linear case (top row), the horizontal varying case (middle row) and the difference between them for both the horizontal and vertical components is shown. The variation of elastic moduli in half of the model shifts the maximum subsidence northward, towards the compliant region with differences respect to the linear case of about 10%. The difference between the two models ranges from -2 to 2 mm, -3 to 3 mm and 0 to 4mm for X-, Y- and Z- direction respectively. I demonstrated that the model is sensitive to the

variations of pressure inside the reservoir as well as the horizontal and vertical variations of the elastic moduli. The resulting deformation field is comparable in magnitude to the displacement measured by the InSAR data. In the next section, the extended model will be compared with the InSAR measurements.

1.3.5 Comparison between InSAR data and the forward model

In this section, I compare the InSAR averaged data with the extended model simulations results. In paragraph 1.2.3 I showed how different degree of filtering and smoothing can affects the deformation field measured by InSAR. In figure 1.3.12, a comparison between different data gridding is shown for May 2006: a finer grid (on the right) introduces more details inside the reservoir, fitting the InSAR measurements better compared to a coarser grid (*left*). In fact, the estimated RMS (*Root Mean Squares)* drops from 8 mm (larger grid) to 6 mm (finer grid). Outside the reservoir where the aquifer is located, both models cannot reproduce the deformation field measured by InSAR. This suggests that either the model doesn't correctly simulate the aquifer deformation or other deformation processes that are not taken into account in the FEM modeling occur around the reservoir.

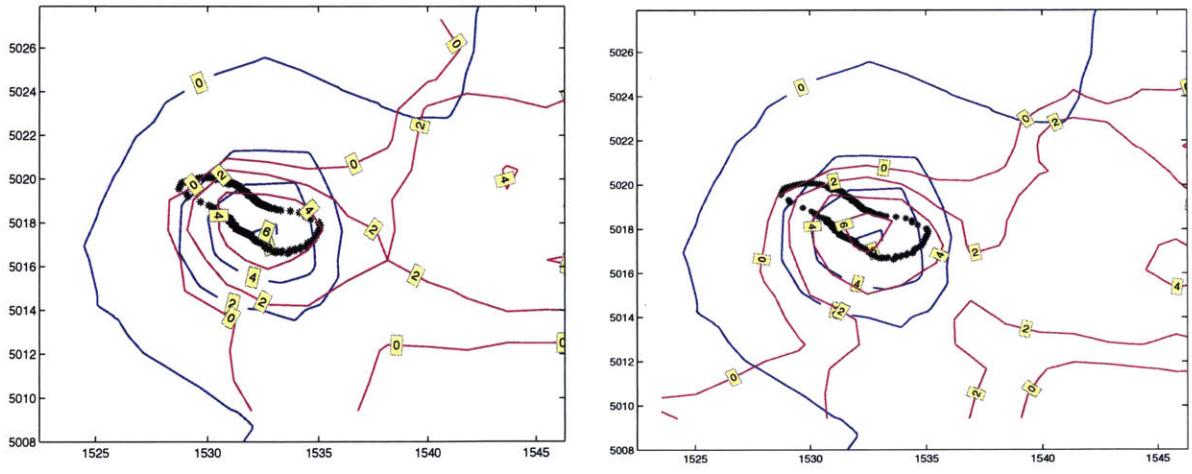

Figure 1.3.12 comparison between the FEM model (*blue*) and InSAR data *(magenta*) with different gridding and smoothing. *Left:* a finer grid (R = 1.7 km) and lower degree of smoothing. *Right:* a coarser grid (R = 2.1 km) and a higher degree of smoothing.

It can generally be concluded that a grid sizing around 1 to 1.7 km with a medium smoothing factor (20% of the number neighboring points) can better reproduce the FEM results, without losing too much detail.

As seen in the previous section, a horizontal and vertical variation in the elastic moduli can produce different results depending on the amount of the variations. In figure 1.3.13 a comparison between a model with uniform (*right*) and linear varying elastic properties (*center*) is shown. In the first model the resulting displacement is lower compared to the second model. The RMS is 6 mm for the uniform simulation and 4 mm for the linear simulation. Therefore, it can be concluded that a rheology with variation of the properties with depth simulates more accurately the observed displacement field. It can be also noted that the deformation field has a more complex pattern than the one simulated in the finite element model.

As suggested by the previous comparisons, I performed the complete simulation for 19 dates between 2003 and 2007 with a depth varying elastic rheology. An example of cumulative displacement obtained from the simulations is shown in figure 1.3.14, where is compared with

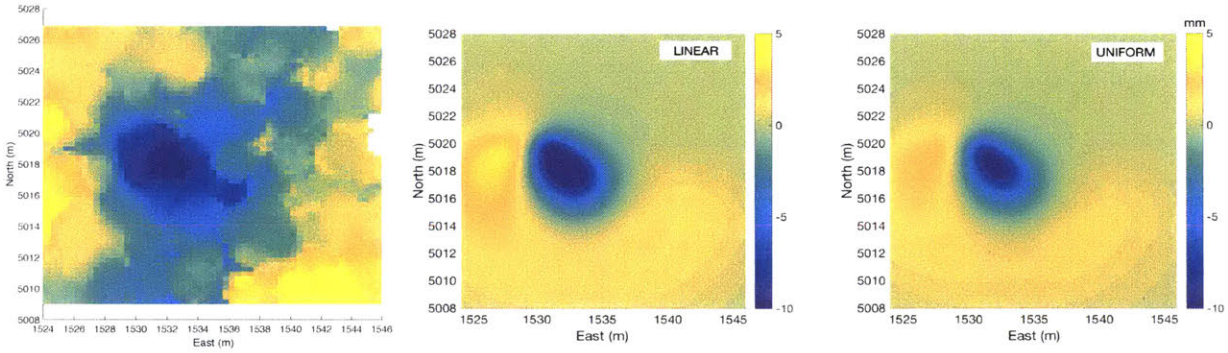

Figure 1.3.13 comparison between InSAR (*left*) data, linear varying properties model (*center*) and uniform properties model (*right*). The rheology with elastic properties varying with depth (*center*) better represent the deformation field measured by InSAR (*left*).

InSAR data smoothed at 1.2 km and for three different time periods: 05-June-2005/23-Oct-2005, 23-Oct-2005/21-May-2006 and 3-Sept-2006/17-Dec-2006.

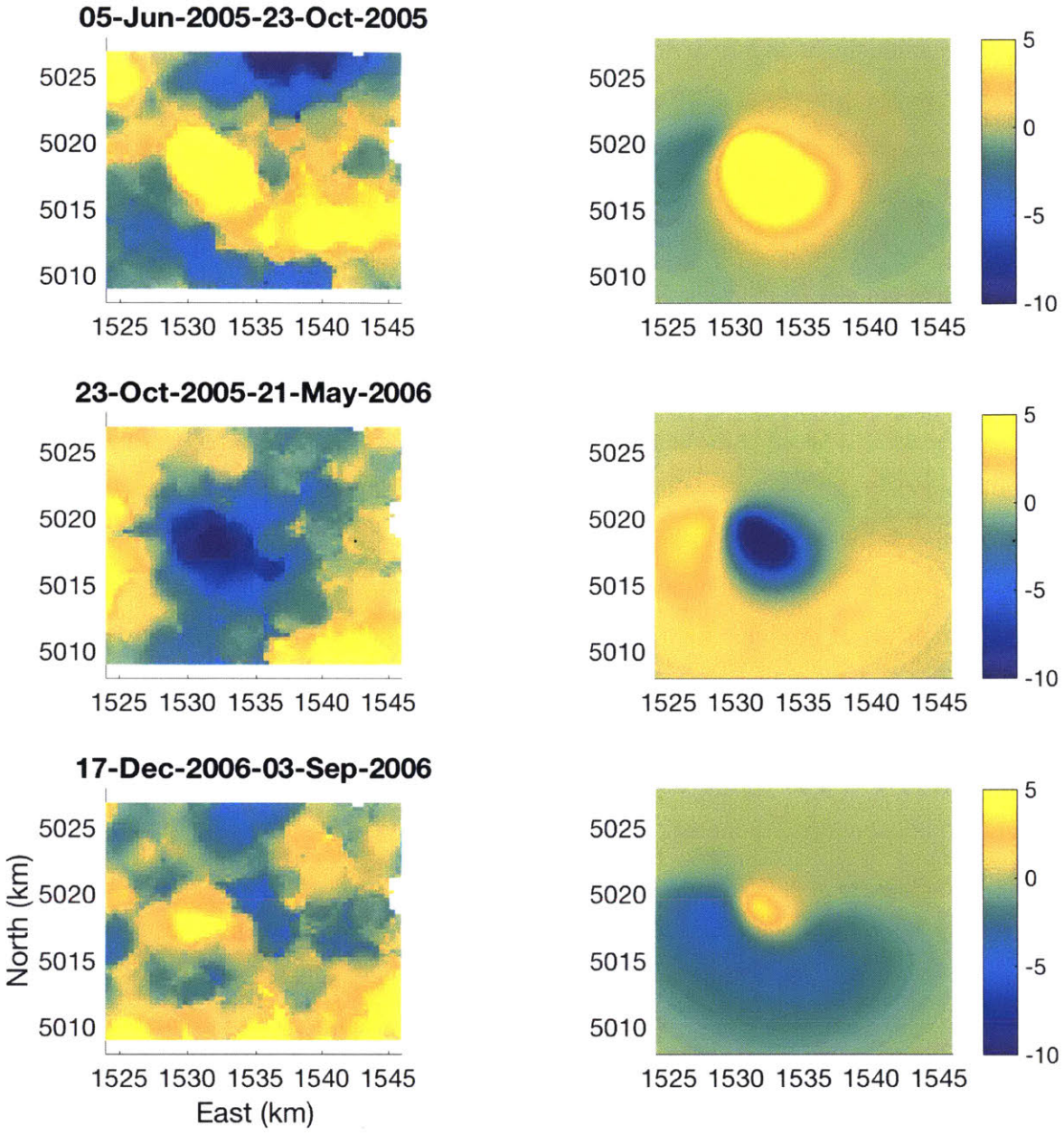

Figure 1.3.14 Comparison between InSAR (*left*) data and extended model with Z-varying elastic properties (*right*) cumulative deformation at three different time periods. The displacement is shown in mm. The RMS varies between 4 and 6 mm.

The RMS varies between 4 to 6 mm depending on the time and the position within the interferogram. Outside the reservoir, the complex pattern of deformation is not captured by the finite element model. That can be related to noisy InSAR data that are not averaged or an incomplete model of the deformation processes around the reservoir and in the aquifer.

In figure 1.3.15, time series of the displacement for the extended model and the models with no deformation outside the boundary at different locations inside and outside the reservoir are shown. The errorbars on the InSAR data are calculated as variance of the data inside each grid cell and they are on average 2-4 mm. A closer look at the time series reveals that generally the peaks of the displacement in the InSAR data are delayed compared to the simulation inside the reservoir and overestimated of about 2 to 5 mm. This suggests that the elastic response to the pressure changes in the finite element model is faster than the consequent displacement measured by InSAR data. The effect of boundary removal from the InSAR displacement field is more relevant outside the edges of the reservoir as no contribution from the Beta field deformation is expected (point 4- fig.12.15). The south-eastern part outside the reservoir (point 5- fig.12.15) is where the aquifer is located and therefore is affected by the pressures changes in the reservoir. The motion in this area is comparable with the deformation field inside the reservoir.

Generally, it can be concluded that the spatial distribution of the predicted deformation is comparable in terms of modulus with the measured field with differences especially outside the edges of the reservoir. A fully coupled simulation as well as an elastoplastic rheology can likely improve the fit between data and model. Generally, the removal of displacement field at the boundaries improves the fitting for the areas outside the reservoir and the aquifer. It is also clear that slightly perturbations of the elastic parameters in horizontal and vertical directions can produce important changes in the deformation field and need to be taken in account for modeling. Especially the lateral changes can be properly modeled only with an accurate rheology that encompasses also horizontal variations of the elastic moduli. In particular, a more accurate model of the aquifer is necessary to ensure the correct propagation of the pressure in the south-eastern part of the reservoir.

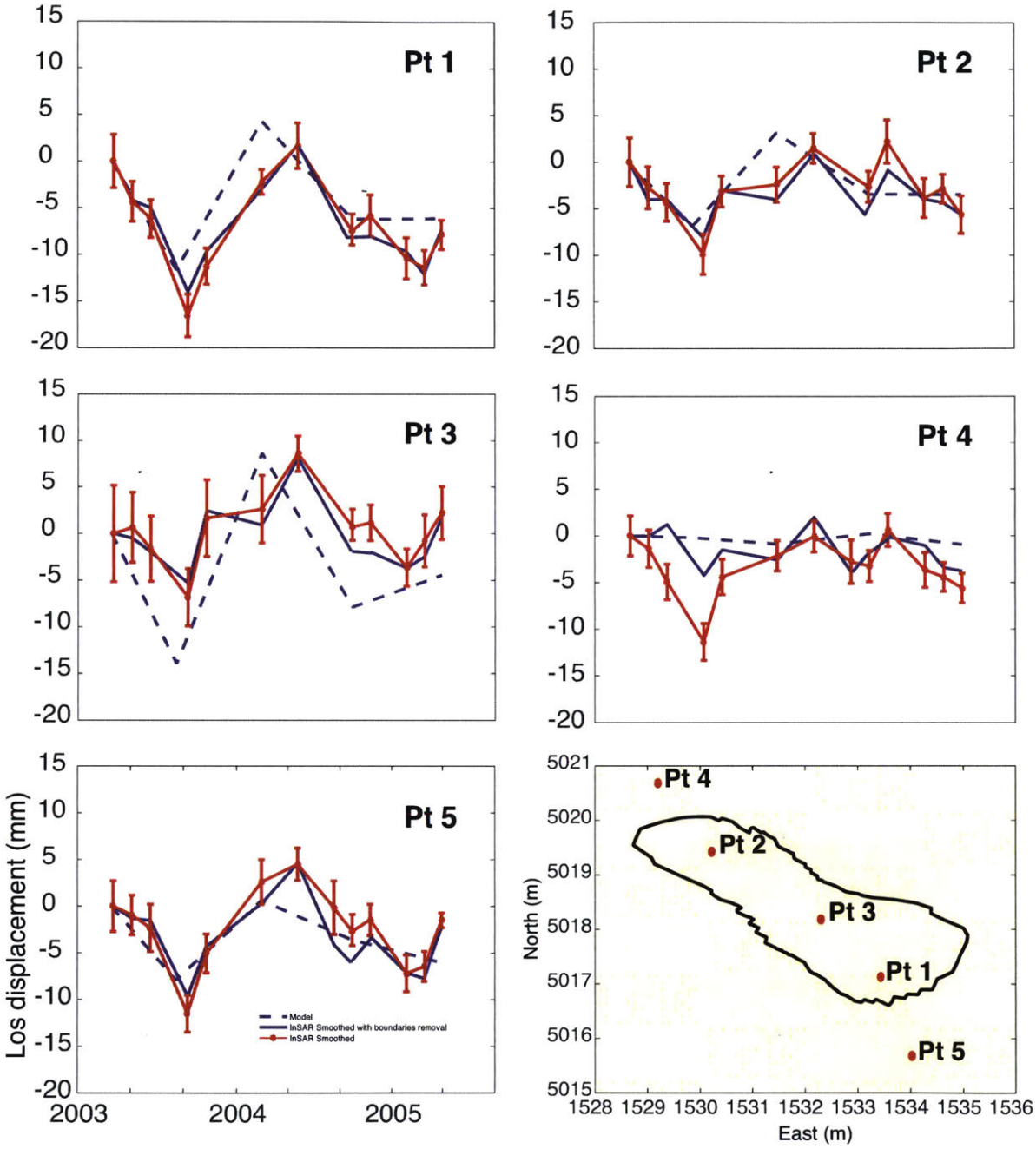

Figure 1.3.15 Times series for the 5 points within and outside the boundaries of the reservoir. Dotted blue line represents the forward model; blue line represents the InSAR data with boundaries removal and red line represents InSAR data smoothed with errorbars. The plots are in LOS direction. At the top right, a map with the location of the points is shown.

1.4 Conclusions and future work

In this study, I presented a methodology to model the deformation in the Beta gas reservoir, resulting from seasonal injection of natural gas during the summer months and withdrawal during the winter months.

I demonstrated that PS scatter technique used to process the InSAR data produced more accurate results compared to standard processing techniques presented in previous studies (Teatini et al. 2008). I presented a method to estimate noise covariance of InSAR data, taking into account the spatial correlation of noise between individual data points in the interferograms.

I showed that InSAR covariance structure can be different varying the spatial aperture of an InSAR scene and taking into account satellite orbital errors. I calculated the correlation length for each interferogram imaging the Beta gas field, fitting a Gaussian curve. I found that the correlation length for different interferograms varies from 5 km to 10 km. I showed a method to average and filter InSAR data in order to reduce the numbers of points and the noise in the data. Comparison with the forward model have shown that the averaging with a grid size between 1 and 1.7 km has the best trade-off between noise reduction and retaining enough data points that contribute to the reservoir deformation.

The flow model was provided by ENI-Stogit S.p.A. (2008) and it provided two model after the production of the field: 107% and 120% of initial pressure scenarios. The modeled pressure variations inside the reservoir ranged between 105 kg/cm^2 and 140 kg/cm^2 and between 100 kg/cm^2 and 160 kg/cm^2 in the 107% and 120% scenarios respectively.

I simulated the geomechanical response of the reservoir subject to fluid injection/production with a three-dimensional elastic model and vertical varying properties. Sensitivity test showed that the deformation field is sensitive to pressures changes inside the reservoir and to variation of elastic moduli in all three directions. I compared the model predictions with InSAR measurements. From the comparison between the finite element model I concluded that InSAR time series are delayed in time respect to the model predictions. This issue can be addressed using a different rheology as well as mechanical properties.

Deformation maps show a complex spatial distribution of the deformations that is not reproduced by the FEM model. These patterns in the deformation are likely related perturbations of parameters in horizontal directions. The two-way coupling can also improve the fit between simulations and

InSAR measurements, characterizing more accurately the dependence between the flow model and the geomechanical calculations.

Finally, I suggest the addition of GPS data to complement the InSAR measurement as they can be used to estimate the atmospheric contribution to the InSAR signal, which still represent a large source of uncertainty during the processing. The continuity of GPS data will also improve the time coverage of the geodetic data.

Chapter 2

Deformation at Katla Volcano (ICELAND) using continuous GPS measurements.

Abstract

The advancements of the techniques for detection of crustal deformation and the rising number of GPS stations installed on volcanoes have tremendously impacted our understanding of the magmatic processes, giving us a more detailed view on the magma dynamics and interactions within the substrate. Despite these advancements, the long-term forecast of volcanic eruptions still represents a challenge and thus volcanic monitoring is still an open field. This is often related to concurrence of processes happening on and around the volcanic edifice at different time scales, such as snow loads, geothermal fluid circulation and hydrological processes. In this chapter, I process and analyze four years of continuous GPS measurements in the southern volcanic zone in Iceland. I analyze the 2010 Eyjafjallajökull event, whose deformation is very well measured by the GPS data. I conduct a spectral analysis of the SNR (Signal-to-Noise ratio) of AUST GPS station (Austmannbunga) on the rim of Katla volcano to explore the effects of the snow on the antenna. I analyze the seasonal motion on the rim of Katla and construct a finite element model to test the hypothesis of seasonal deformation controlled by snow loading on the volcano. I conclude that snow loading cannot solely explain the motion observed on the rim of the volcano and finally suggest a freezing/melting fractured rock model to be tested in order to explain the magnitude and phase of the observed deformation at Katla station.

2.1 Introduction

This study was part of an internship with the Icelandic Meteorological office in Iceland that took place in the summer of 2013. The main goal of this project was to have a closer look to the GPS monitoring data of Katla volcano, located in the south-western part of the island.

After the 2010 eruption of Eyjafjallajökull volcano that caused exceptional disruption to air traffic, closing airspace over much of Europe for days, numerous efforts were put to gain a deeper understanding of volcanic eruption dynamic and forecasting (e.g. FUTUREVOLC project). In addition to that, a lot of attention was driven towards the neighboring volcano Katla (west) as the past eruptive history has showed a link between the two, being the eruption of the first being followed by the eruption of the latter short after. Despite the history, Katla volcano hasn't erupted since 2010, suggesting the need to review the available data to determine its current activity and consequent hazard.

For this project, I processed continuous GPS data and other available data (seismic and weather data) to analyze 4 year of history of Katla volcano after 2010 Eyjafjallajökull eruption.

GPS time series as well as seismic data between September 2009-2010 reveal a clear inflation around the Eyjafjallajökull caldera, with uplift up to 38 mm before the eruption. I then analyzed the GPS time series on the Katla volcano to study the unrest of the volcano. Austmannbunga station, located on the rim of the volcano, shows a complex pattern of seasonal processes.

GPS raw data were provided by IMO (Icelandic Meteorological Office) in Reykjavík, Iceland, during the 2013 summer internship.

2.2 The area of study

2.2.1 Tectonic setting and volcanism in Iceland

Iceland is part of the Mid-Atlantic Ridge (MAR), where the Eurasian plate separates from the North-American plate. The spreading center starts in the Reykjanes peninsula in the southwestern portion of the Island and ends in the Tjörnes fracture zone in the northern portion of the island.

The ridge is not continuous but it deviates mid-way of about 150 km eastwards, due to the interaction with the Icelandic hotspot. This complex tectonic setting produces a highly active volcanism that can be divided in two distinct types (Sigmundsson, 2006): the volcanic flank zones where little spreading occurs and the volcanic rift zones where the spreading is extensive. The latter can have distinctive characteristics depending on its obliquity respect to the MAR.

In Iceland over thirty active volcanoes have been recognized, with eruptions occurring every few

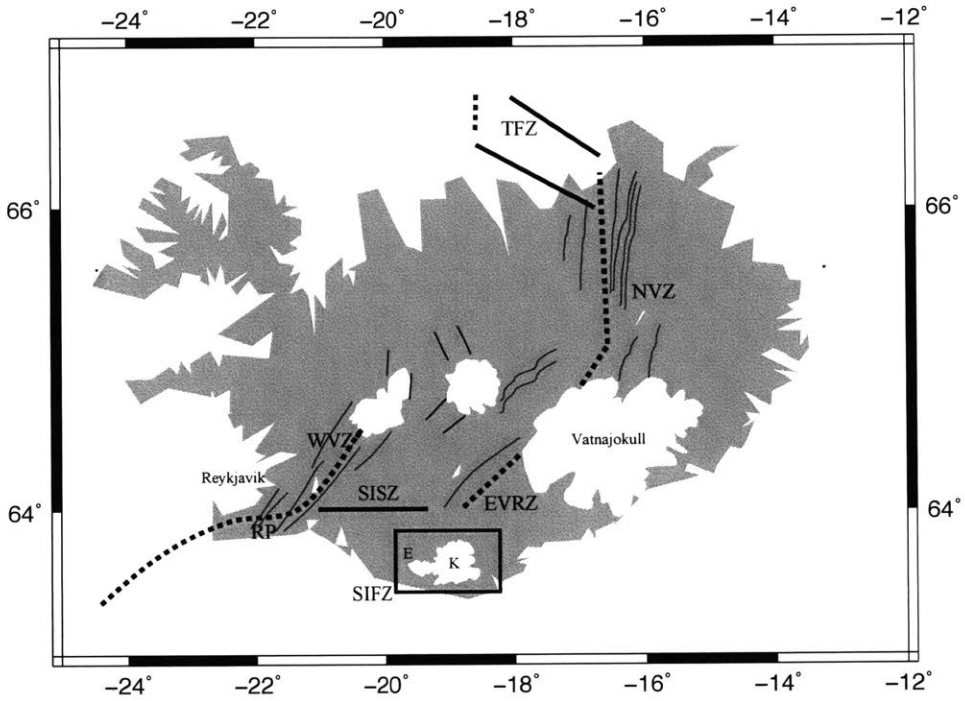

Figure 2.1.1 Map of Iceland showing the principal tectonic features: spreading axis in dashed gray line that runs from the Rekyanes Peninusula (RP) to the Western Volcanic Zone (WVZ) and terminates at the Langjökull icecap; the eastern part of the spreading center begins at the Eastern Volcanic Rift Zone (EVRZ) and it transitions to the Northen Volcanic Zone at the Vatnajökull icecap; two transform zones, the Icelandic Seismic Zone (SISZ) and the Tjornes Fracture Zone (TFZ) that accommodate the spreading. *Modified after Albino et al. 2010*

years. Most of the volcanoes are characterized by a central edifice and a fissure swarm zone where extensive fracturing occurs (Sigmudsson, 2006). Many volcanoes lie underneath an icecap, whose interaction with the eruptions causes instant flooding (*jökulhlaups*) and phreato-magmatic products. These icecaps are also gradually melting, causing a viscoelastic response of the asthenosphere. This phenomenon is called GIA (Glacial Isostatic Rebound) and it results in a general uplift of Iceland in response to the reduction of the ice masses. Furthermore, the gradual removal of icecaps on top of the volcanoes causes changes in the stress field around the magmatic

chambers, causing a variation in magma production (for depressurization) and therefore influencing the amount of eruptions and the severity of them (Albino et al., 2010). The complexity of the tectonic setting in Iceland makes it difficult to distinguish volcanic signals from other sources of deformation.

2.2.2 Eyjafjallajökull volcano

Eyjafjallajökull is a strato-volcano, located west of the Katla volcanic system and situated in a propagating rift outside the main plate spreading center, at the southern termination of the eastern rift zone (EVRZ). The area is characterized by central volcanoes but lacks typical rift structures, resulting in magma generation different from the one produced in rifting zones. Lava flows occur on both side of the volcano through fissuring systems, but are more prominent on the western side. Although the volcano has known eruptions in historical times, it has been less active compared to other volcanoes in the same zone (Gudmundson et al., 2008). Previous eruptions of Eyjafjallajökull include a radial fissure eruption around AD 920, a small summit eruption in AD 1612 or 1613, and another summit eruption in AD 1821–23. A short phreato-magmatic phase in December 1821 was followed by a year-long period of intermittent magmatic/ phreato-magmatic activity and flooding. An intrusion beneath the S flank occurred from July to December 1999 and was registered by an increased seismic activity and deformation captured by tilt, GPS and InSAR measurements (Pedersen and Sigmundsson, 2006). The last historical activity is the 2010 eruptive event, which will be discussed in the following sections.

2.2.3 Katla volcano

Katla Volcano is one of the most active volcanoes in Iceland with 20 eruptions since the 9th century (Sturkell at al. 2008). It is located on the South-Iceland flank and is thus away from the extensive rifting areas. Katla is then identified as an intra-plate volcano, located on the Eurasian tectonic plate. Some interaction with the EVZ to the North however occurs. The volcano is partly covered by the Myrdalsjökull icecap, which has a mean diameter of 30 km and is up to 750 m thick. Katla's

eruptions are therefore phreato-magmatic and tend to be accompanied by jökulhkaups (glacial outburst flood). Katla caldera has an elliptical shape and is breached in three points, where water floods can discharge.

Seismic studies detect the presence of low-velocity P-waves and S-waves shadow zone below the Katla caldera, which indicated that the magmatic chamber is below the volcano. The last major eruption was in 1918, which was accompanied by a massive flood. Then in 1955 a small event

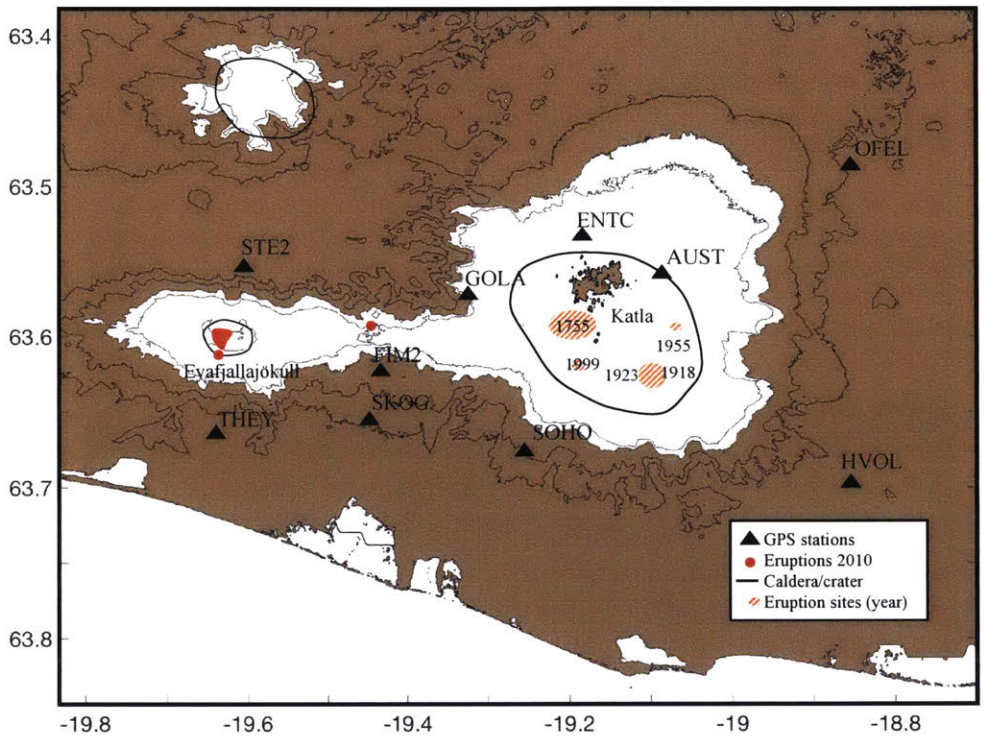

Figure 2.2.1 Historical eruptions map of Katla volcano and 2010 event locations of Eyjafjallajökull volcano. *Modified after Bjornsson et al. 2000.*

occurred with the formation of ice cauldrons. The most recent activity was in 1999, with a consequent flood and proceeded by seismic tremor and relatively small earthquake under the icecap.

Different signals detected at the Katla Volcano suggest a complex pattern of the deformation and interaction between different processes. Katla is dominated by elevated background seismicity with periods of elevated activity concentrated within the rim and the western flank of the volcano.

InSAR data processed in previous study show that there is no detectable inflation signal around the glacier. However, the GPS observations at AUST station (on the rim of Katla) and to a lesser extent on ENTC and GOLA station (north-western flank of Katla), suggest a complex interaction between the magmatic-, the geothermal-systems and the pressure variations at the base of the ice cap.

2.3 GPS time series processing and analysis

2.3.1 GPS time series processing and seismic data

Continuous GPS measurements from 23 stations in the southern part of Iceland between 2009-2014 along with 20 ITRF stations have been processed using GAMIT/GLOBK software v 10.5

Figure 2.3.1 Continuous GPS stations in the south-western part of Iceland

(see Herring et al, GAMIT *Reference Manual,* 2012).

Data were provided by Icelandic Meteorological Office (IMO) and University of Iceland (UI) in Reykjavík, Iceland. I estimated the daily position of the stations using International GNSS Service (IGS) 2008 absolute phase center corrections for receiver antennas and ocean-loading model

FES2004. Linear and annual trends were estimated with *tsfit* to detrend the time series. Twenty reference stations were used to determine the ITRF08-Eurasia fixed reference frame.

The missing data in the times series are related either to power issue at the stations or missing data collection by the Icelandic Meteorological Office (IMO).

The seismic data were obtained from the online catalog from the South Iceland Lowland Seismic network (SIL) operated by IMO. For the analysis of the 2010 volcanic eruption, the seismic events were selected as following: they were encompassed between -20 and -18.63 degree of longitude and 63.5 and 63.8 in latitude; they were occurring between August 2009 and 31 March 2010; the local magnitude $M_L \geq 0.8$.

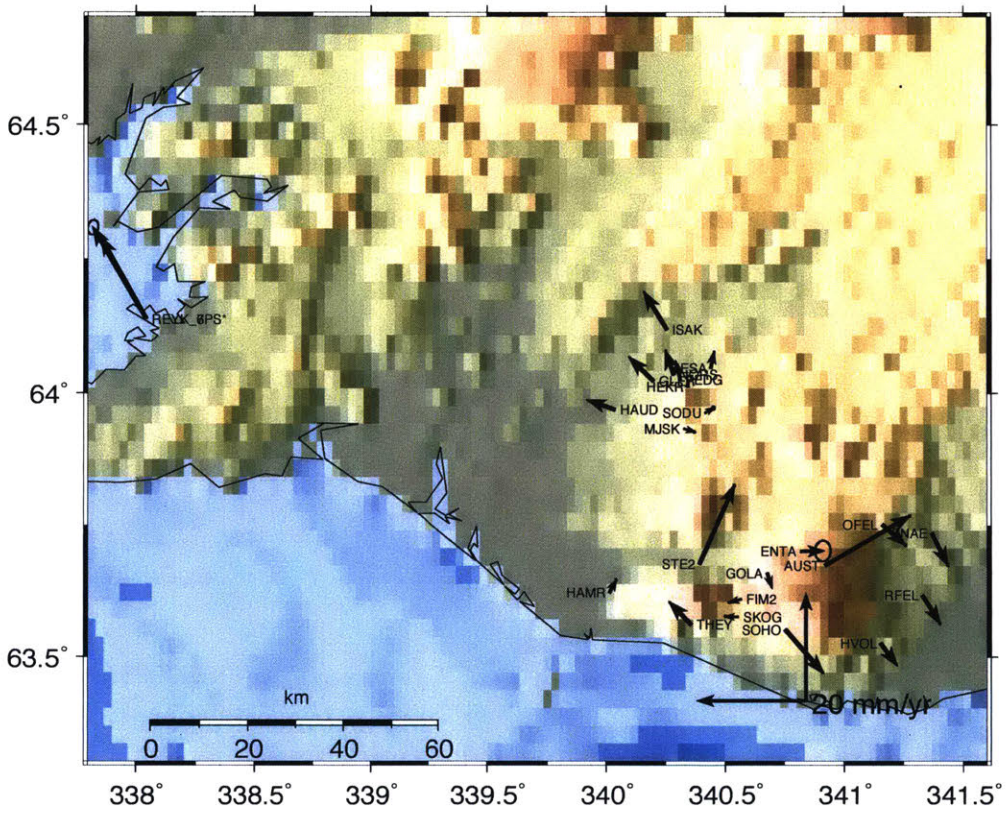

Figure 2.3.2 Horizontal GPS velocities of the Icelandic GPS stations in the southern volcanic zone relative to stable Eurasia for the time interval 2009-2014. The ellipsoids on the arrow indicate the error on the estimates with 95% confidence interval. The uncertainties on the velocities are estimated as Random Walk noise.

2.3.2 Eyjafjallajökull volcanic system time series

Eyjafjallajökull volcano is mainly monitored by four continuous GPS stations: Þorvaldseyri (THEY) on the south side, Steinsholt (STE2) on the north side, Hamragarður (HAMR) on the western side and Fimmvörðuháls – Baldvinsskáli (FIM2) and Skógaheiði (SKOG) on the eastern side bording the Katla volcanic system.

Data available for this project, spanning from 2009 (only THEY data) until end of 2013, show little deformation prior to January 2010 (fig.2.3.3 and 2.3.4). THEY time series is dominated by

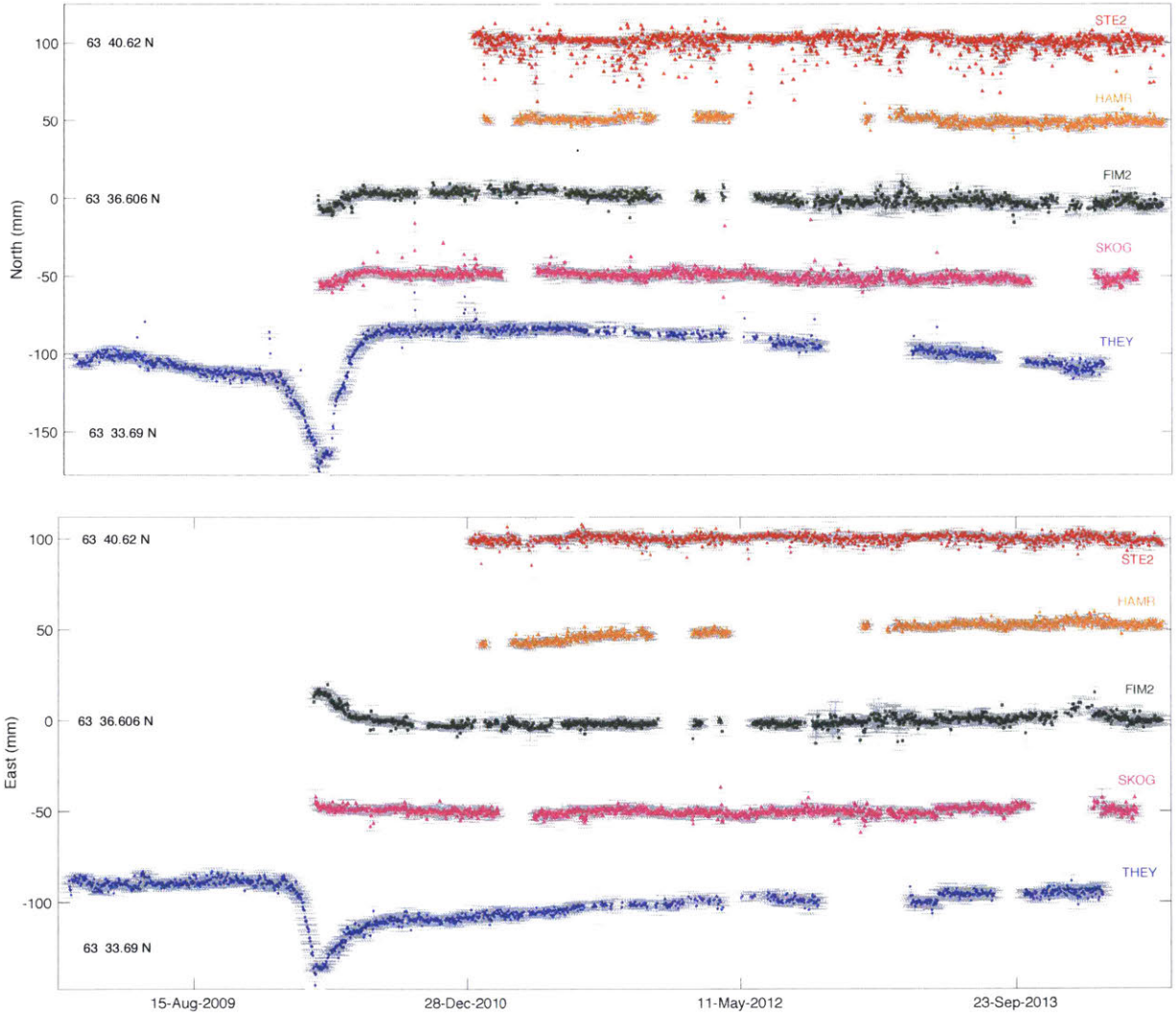

Figure 2.3.3 North (*top*) and East (*bottom*) components of the time series for Eyjafjallajökull GPS stations (THEY, SKOG, STE2, HAMR, FIM2). The time series have been spaced out for clarity and displayed from the northernmost (STE2) to the southernmost (THEY) stations. HAMR is on the western side of the volcanic edifice, while FIM2 and SKOG are located on the eastern side.

the 2010 event with ~ 7 cm of displacement in south and west direction (away from the center of the caldera) at the time of the main eruption. The pre-eruptive phase is characterized by nearly undetectable motion in E-W direction and ~15 mm of south displacement accumulated from beginning of 2010 until the 4 of March when the eruption took place. The uplift during the eruption is ~ 40 mm, while after the event a deflation of 70 mm is detected at the station during one-month period. The co-eruptive phase is detected also by SKOG and FIM2 on the eastern side of the volcanic edifice with few mm of displacement in all three components (fig. 2.3.3 and 2.3.4). The post-eruptive phase is characterized by few mm of displacement for the three components at

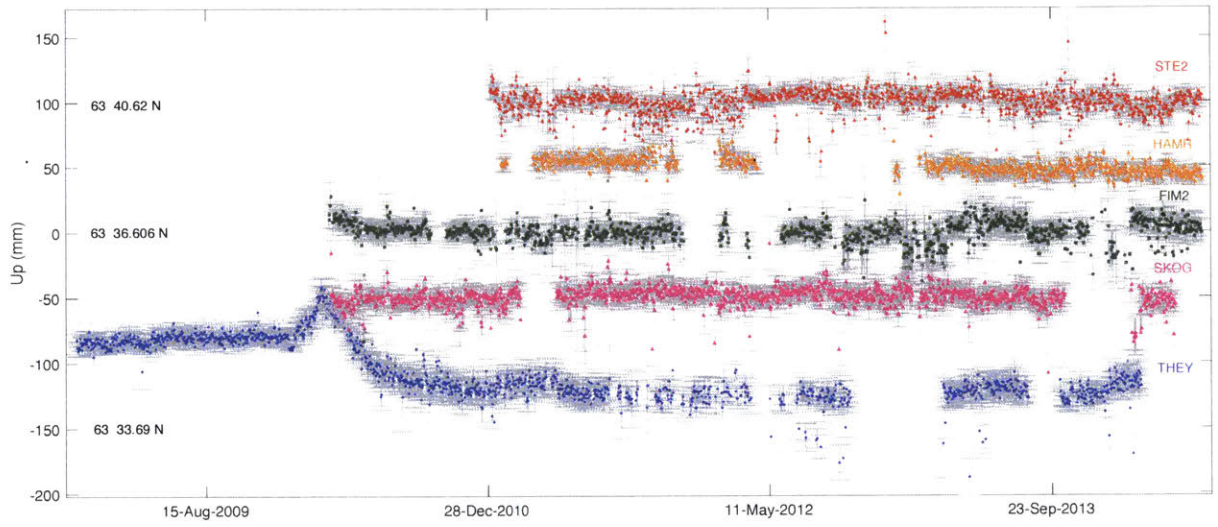

Figure 2.1.4 Up components of the time series for Eyjafjallajökull GPS stations (THEY, SKOG, STE2, HAMR, FIM2). The time series have been spaced out for clarity and displayed from the northernmost (STE2) to the southernmost (THEY) stations. HAMR is on the western side of the volcanic edifice, while FIM2 and SKOG are located on the eastern side.

SKOG station and few mm of displacement in N-S and Up component and 13 mm in the E-W component at FIM2 station. After the 2010 event at Eyjafjallajökull, the GPS stations haven't detected any major deformation processes related to the volcano activity. An event is visible at the beginning of May 2013 at THEY, SKOG and FIM2 stations that is likely related to seismic events.

2.3.3 Katla volcano time series

Katla volcano is monitored by several GPS stations: Austmannsbunga (AUST) is located on the

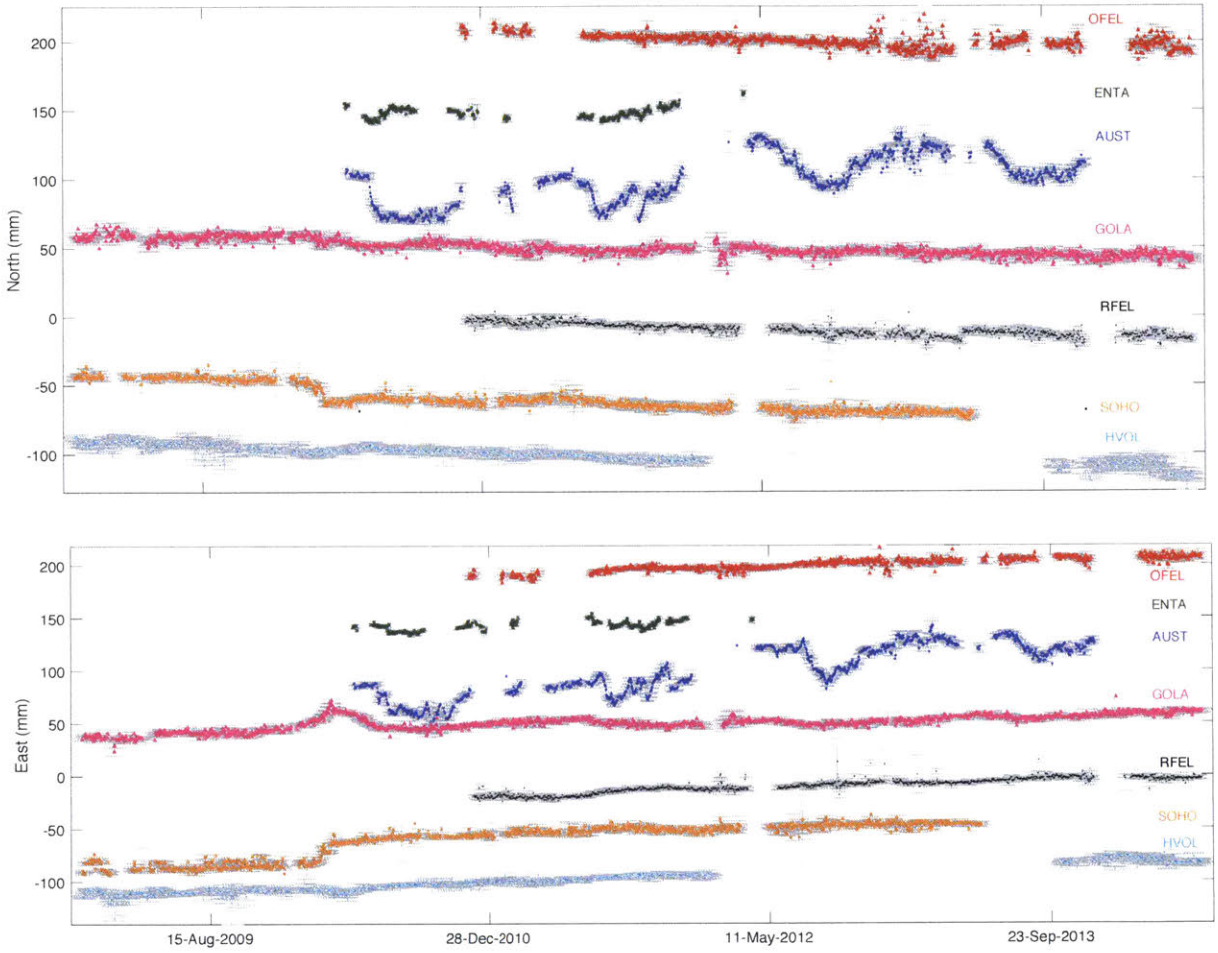

Figure 2.3.5 North (*top*) and East (*bottom*) components of the time series for Katla GPS stations (OFEL, ENTA, AUST, GOLA, RFEL, SOHO, HVOL). The time series have been spaced out for clarity and displayed from the northernmost (OFEL) to the southernmost (HVOL) stations. SOHO is on the western side of the volcanic edifice, while OFEL and RFEL are located on the northeastern side.

rim of the caldera at an altitude of 1438 m and has been operating since 2010; Goðabunga (GOLA) is located on the north-western flank of the volcano and has been operating since 2006. Enta (ENTA) is on the northern flank of the volcano while Sólheimaheiði (SOHO) and Láguhvolar

(HVOL) monitor the southern flank; Öldufell (OFEL), Snæbýli (SNAE) and Rjúpnafell (RFEL) are on the northeastern part, outside the volcano edifice.

Katla GPS time series from 2009 to 2014 reveals a complex interaction between deformation processes. SOHO and GOLA stations and HVOL to a lesser extent detected the 2010 eruption of the neighboring volcano Eyjafjallajökull (fig.2.3.7). Before March 4th 2010, SOHO and GOLA stations begins moving respectively southeast by about 16 mm and east by about 15 mm. Immediately after March 4th 2010, the two stations move 5 mm north and then rapidly southeast by 16 mm and 10 mm respectively. After the flank eruption took place and during the summit eruption, the two stations didn't register any visible deformation. The uplift is slightly detectable in the GOLA station but none is present in SOHO.

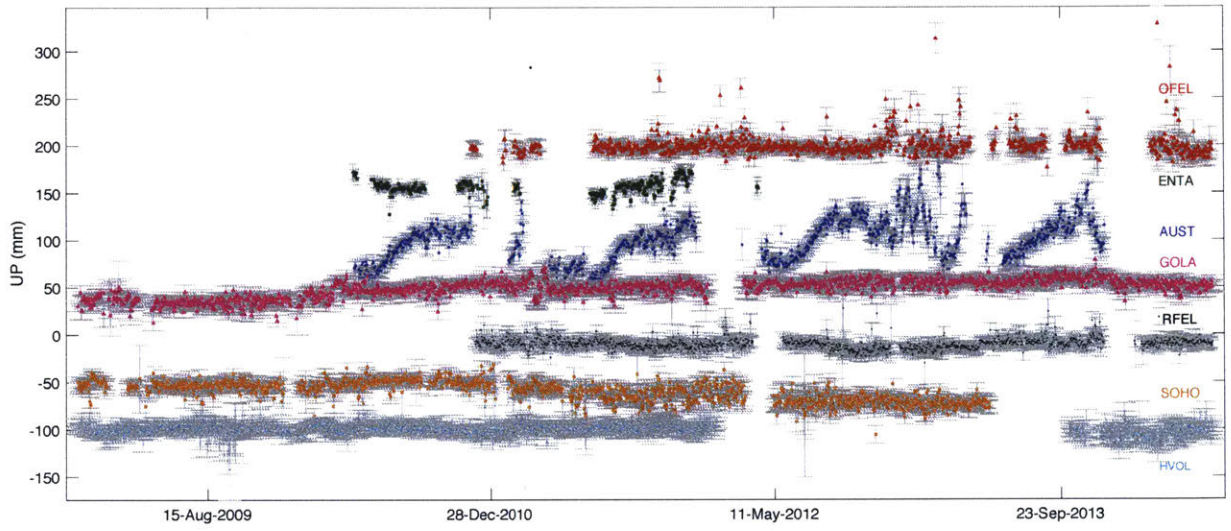

Figure 2.3.7 Up components of the time series for Katla GPS stations (OFEL, ENTA, AUST, GOLA, RFEL, SOHO, HVOL). The time series have been spaced out for clarity and displayed from the northernmost (OFEL) to the southernmost (HVOL) stations. SOHO is on the western side of the volcanic edifice, while OFEL and RFEL are located on the northeastern side.

The movement of the two stations very likely the combination of the inflation happening at the Eyjafjallajökull volcano and the displacement on the local faults, activated by changes in stresses caused by the volcanic event.

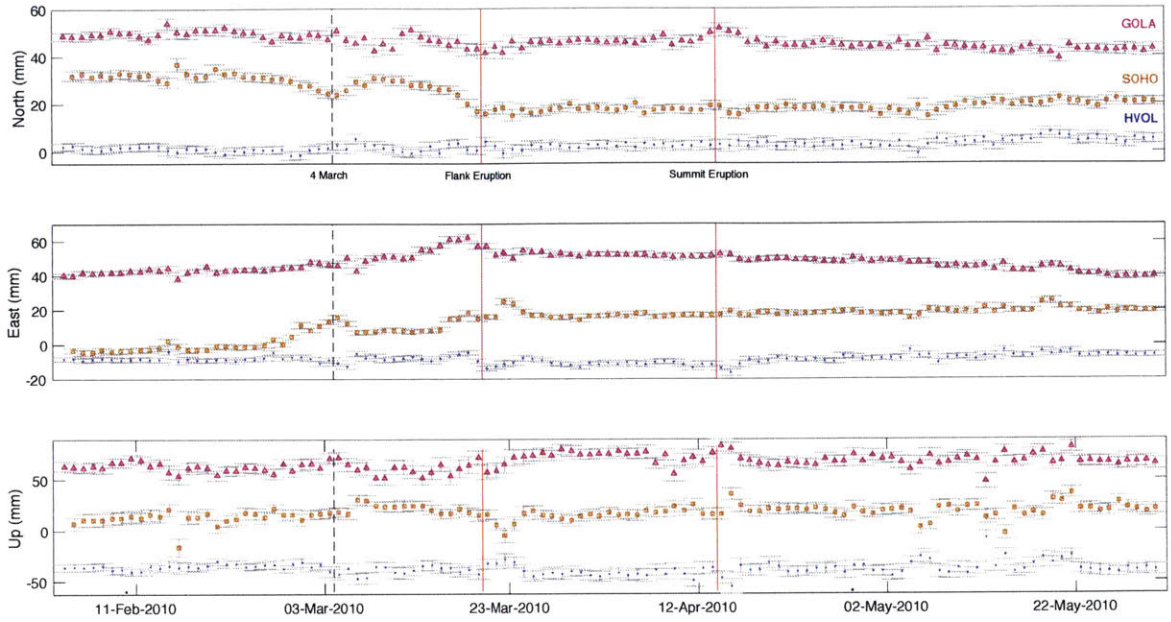

Figure 2.3.6 SOHO (*southwest*), GOLA (*northwest*) and HVOL (*southeast*) time series close up for the 2010 Eyjafjallajökull event. All the stations show a complex pattern of deformation at Katla that can be mostly explained with the inflation of the neighboring volcano. However, the complexity of the motion reveals the presence of a secondary source of deformation.

2.3.4 2010 Eyjafjallajökull event

On 20 March 2010, a major eruption from a 500-meter long fissure on the Eyjafjallajökull's western flank (Fimmvörduháls pass) took place after nearly 190 years of intermittent unrest (Swindles et al. 2011). This event was followed by a larger eruption at the summit on April 14th that continued until late May 2011 (Sigmundsson et al. 2010). Signs of deformations were detected at the GPS stations monitoring the volcano as well as an increase of the seismic activity. At the beginning of 2010, THEY station started moving southward with a displacement of 12 mm (fig. 2.3.8) and the seismic events become more frequent (several earthquakes per day), indicating the starting of the inflation. Although data pre-eruption was not available for SKOG and STE2 stations, other studies (Sigmundsson et al. 2010) indicate SKOG station started to move southeastward a few weeks after THEY with a displacement of ~ 4 cm. On March 4th, the seismic

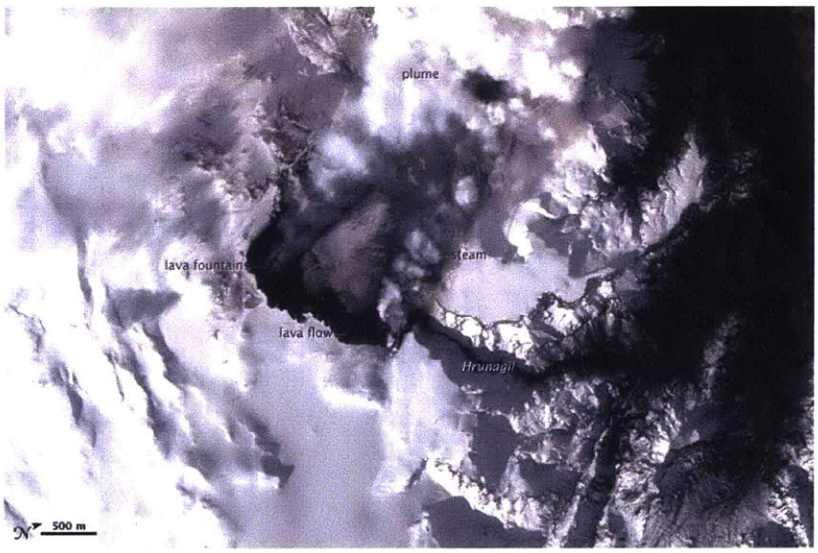

Figure 2.3.8 The image was acquired on March 24th by the Advanced Land Imager (ALI) aboard NASA's Earth Observing-1 (EO-1) satellite. The image shows lava fountains, lava flows, a volcanic plume, and steam from vaporized snow.

activity increased drastically with depth of 7-13 km and location along the western flank of the volcano (fig. 2.3.6); STE2 on the northern side of the volcanic edifice started moving westward (time series from www.gps.vedur.is) and both THEY (fig. 2.3.7) and SKOG station (Sigmundsson

et al. 2010) started deforming at a higher rate. Pre-eruptive phase is also detected by GOLA station on the eastern flank of Katla volcano (fig. 2.3.9). Since the beginning of 2010, the station moved by about 10 mm eastward and after March 4th the rate of deformation picked up, as the station moved 10 mm in about 16 days until the flank eruption.

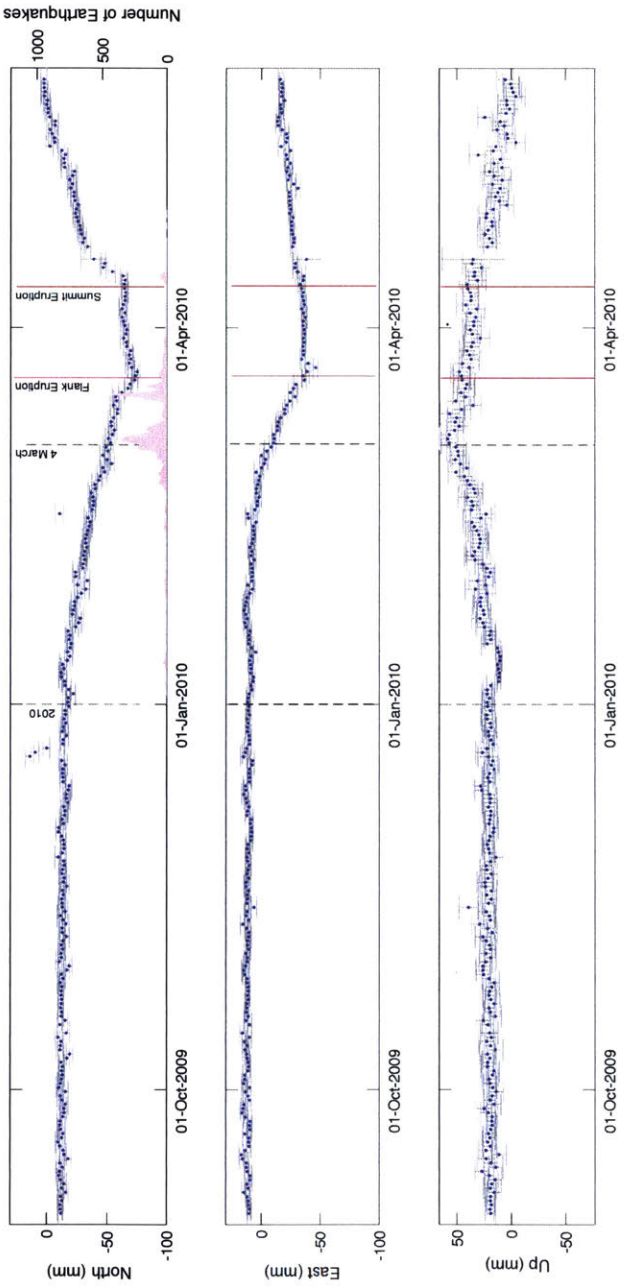

Figure 2.3.9 Close up of THEY GPS time series between mid 2009 and mid 2010. Dotted lines indicate the timing of the volcanic activity: beginning of the activity (2010), increase of the deformation (March 4th), flank eruption (March 20th) and summit eruption (April 9th). Pink shadings indicate the daily rate of earthquakes.

The pattern of the deformation during the pre-eruptive phase reveals a complex placement of the magma within the volcanic chamber with higher rates of deformation after March 4th. On the late evening of March 20th, the opening of an effusive fissure on the side of the volcano's flank marked the beginning of the eruptive activity. During this stage, THEY didn't show any detectable changes while FIM2 and SKOG moved of a few mm eastwards. The opening of the vents caused the momentarily cease of the deformation and the volcano stayed in an inflated state until the

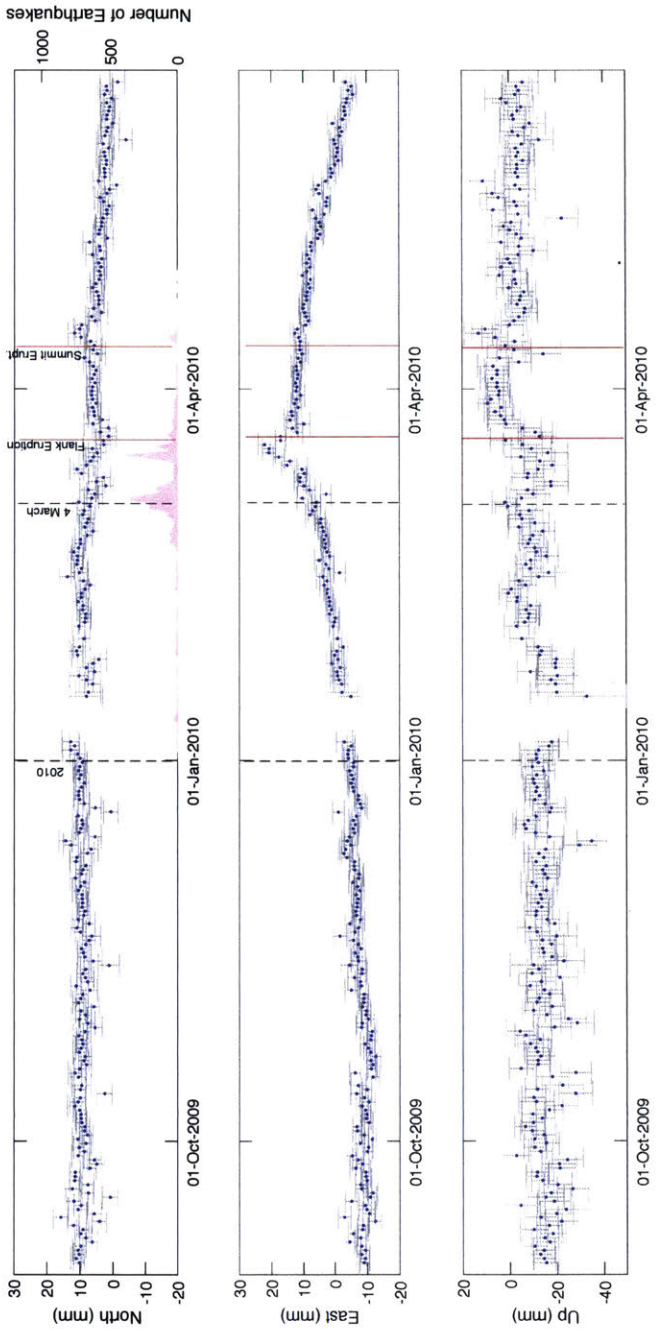

Figure 2.3.10 Close up of GOLA GPS time series between mid 2009 and mid 2010. Dotted lines indicate the timing of the volcanic activity: beginning of the activity (2010), increase of the deformation (March 4th), flank eruption (March 20th) and summit eruption (April 9th). Pink shadings indicate the daily rate of earthquakes.

beginning of April. On April 14th, an explosive eruption took place in the summit of the volcano and the activity remained sustained until the beginning of May. The pattern of the seismicity revealed a change in the magma migration: the direction moved from E-W (until March 20th) to NE-SW and at shallower depths (5 km). After the summit event, all the stations registered a continuous deflation of the volcano with different rates of deformation.

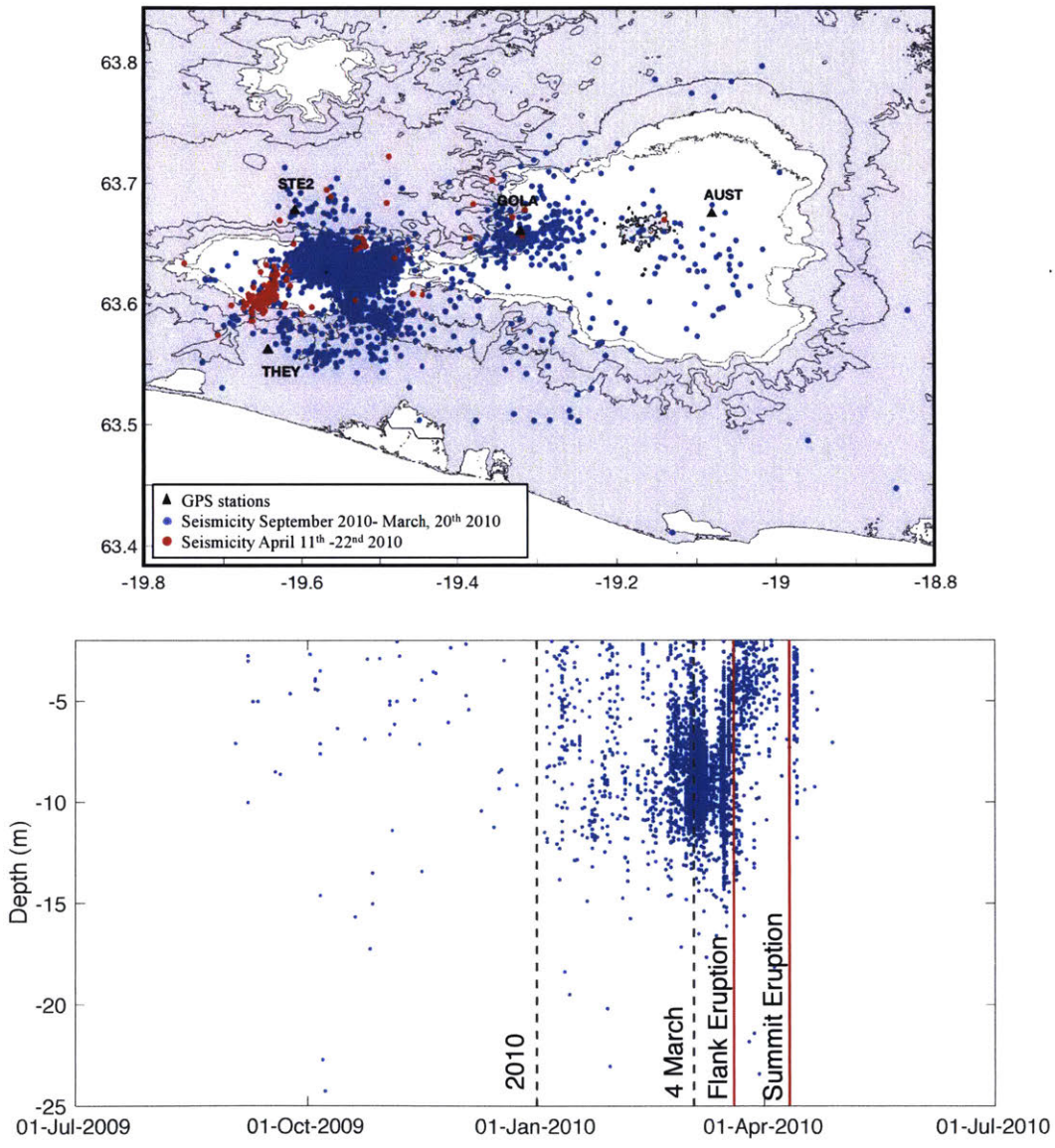

Figure 2.3.11 *Top:* map of the seismicity between September 2009 and March 20th and between April 11th and April 22nd. The pattern shows two different phase of the eruption: on the flank and on the summit. *Bottom:* change with the time of the depths of the earthquakes around Eyjafjalljökull volcanic edifice.

The 2010 eruptive event can be described in three principal phases: a *pre-eruptive* phase with beginning of the inflation starting in January 2010 and an acceleration of the deformation after March 4th; *co-eruption* phase with a flank eruption on March 20th and a summit explosive event on April 14th, characterized by a cease of the deformation; a *post-eruption* phase, starting in April the 20th and characterized by a deflation of the volcanic edifice and sustain activity until late May.

2.3.5 Effect of snow and ice on GPS measurements

The GPS stations monitoring the Katla and Eyjafjallajökull volcanic system are characterized by the presence of snow during the winter months. Snow packs can affect the GPS measurements as they act as smooth reflection surfaces (multipath), resulting in systematic errors in pseudo-range and carrier phase measurements (Braasch, 1996). When monitoring volcanic activity, the presence of multipath can be detrimental as the affected measurements can mask the volcano signal or be mistaken for it. Therefore, it is necessary to analyze the multipath environment of the station to determine how it affects the final position estimates when snow is present. For this study, I analyzed the fluctuations in signal power (SNR, *signal to noise ratio*) caused by reflections. The reflected signal from the snowpack results in a sinusoidal SNR signal whose frequency depends on the height of the snow layer if the surface is flat.

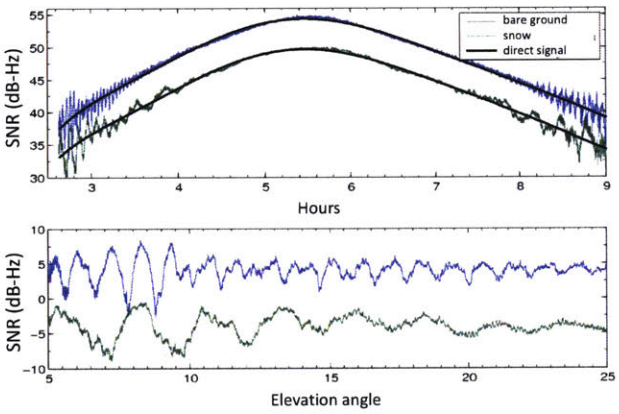

Figure 2.3.11 *Top:* SNR data on L2 frequency for antenna at different distances from the ground. In black it is the direct signal. *Bottom:* SNR residuals plotted as a function of the elevation angle. The two signals are sinusoid with different frequencies: the signal closer to the ground has lower frequency. *Modified after Bilich et al. (2007).*

The GPS stations in this study are affected by the presence of snow to different extent. The analysis of the time series suggests that the most affected stations by the periodical fluctuations of the snow layer on the ground are AUST and OFEL. The jumps in the position estimates at the two stations, mostly affecting the vertical component, are correlated in time and more often appearing during the winter months with some variation from one year to another (fig. 2.3.13). The winter of 2013 has the major effect on the estimates. The temporal characteristics of these jumps and the correlation between the two stations suggests that the multipath caused by the presence of snow is affecting the position estimates at the two stations. A visual analysis of available pictures at AUST

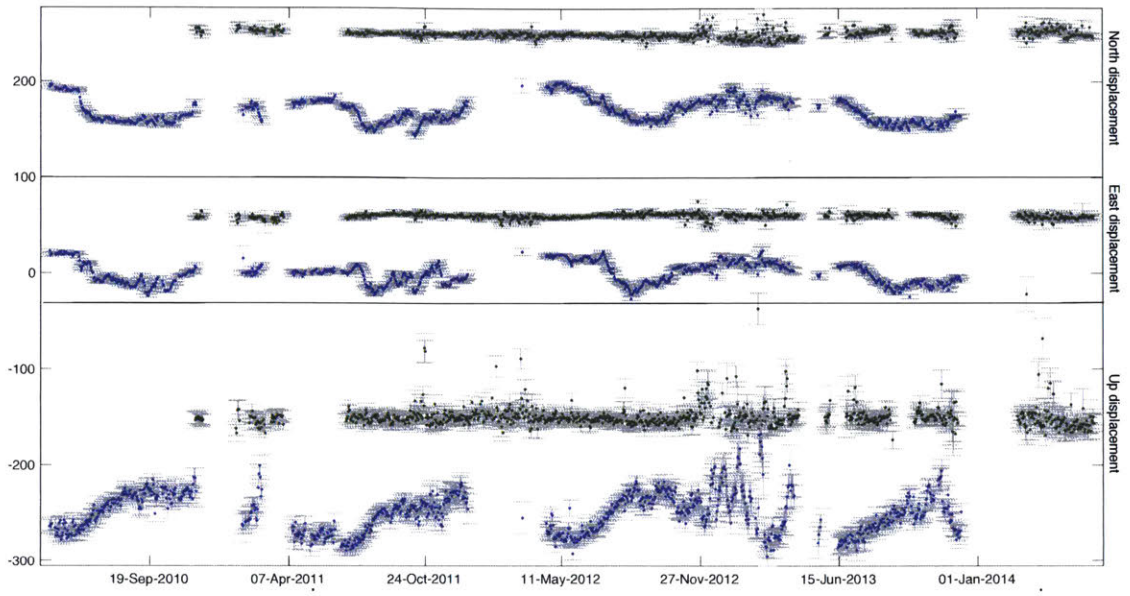

Figure 2.3.12 Time series for AUST (*blue*) and OFEL (*green*). The three components (north, East, Up) are in mm.

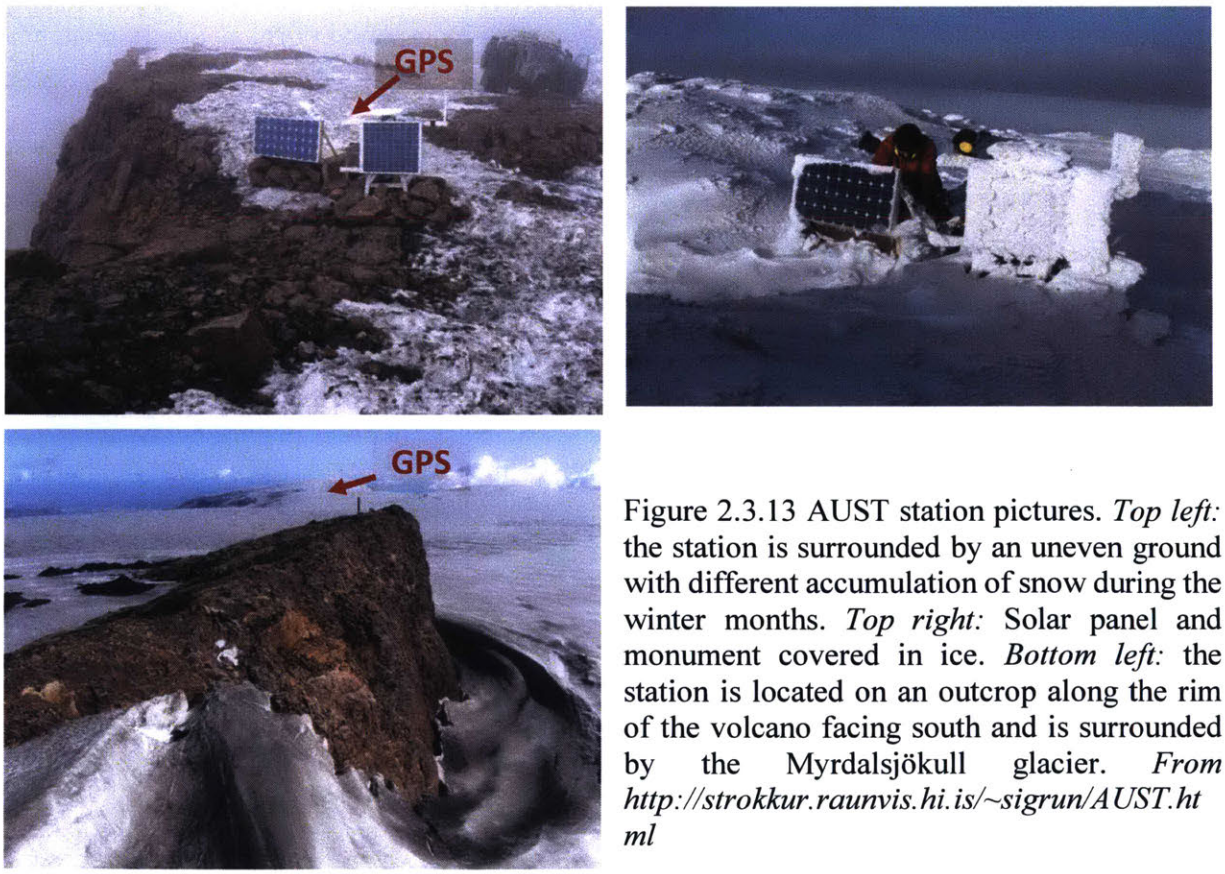

Figure 2.3.13 AUST station pictures. *Top left:* the station is surrounded by an uneven ground with different accumulation of snow during the winter months. *Top right:* Solar panel and monument covered in ice. *Bottom left:* the station is located on an outcrop along the rim of the volcano facing south and is surrounded by the Myrdalsjökull glacier. *From http://strokkur.raunvis.hi.is/~sigrun/AUST.html*

station (fig. 2.3.13) suggested that the multipath effects is complicated and difficult to interpret

due the presence of solar panel on one side of the antenna monument that can be subject to frost during the winter and can act as vertical reflector with varying reflective index when covered in ice (fig. 2.3.13 *top right*). In addition, the station is located on top of an outcrop, part of the volcanic rim, that slopes in north direction and has a drop in the south-west part (fig, 2.3.13 *bottom left*). As the reflecting surface is uneven, the snow accumulation will be different (fig. 2.3.13 *top left*) and the reflections will affect differently the satellite tracks depending on their direction. Although pictures for OFEL station monument weren't available for a visual analysis, the satellite image from Google Earth suggest a flatter ground on which the station is standing. Snow data at the locations were not available for comparison.

To understand the multipath environment, I analyzed the SNR for days of 2013 and 2012. For each day, SNR measurements were extracted by the *svsnr* program of the *GAMIT/GLOBK* software and fit with a low-degree polynomial to remove the direct signal contribution (fig. 2.3.14). The particular location of AUST station made it necessary to perform a spatial analysis, separating the satellite tracks in quadrants to spatially locate the source of reflections in the signal. The frequency content was analyzed using the Lomb-Scargle periodogram, that allows the calculation of the spectrum of not-uniformly sampled data without boosting long-period noise as the more standard Fourier analysis could do. Once performed the analysis of the multipath environment for each day, I compared the spectral peaks over a year period and I developed a detection algorithm to separate the peaks that can be related to snow (*snow index)*, rain (*rain1 index*) and possible atmospheric effects (*rain2 index*).

To select satellite tracks suitable for the comparison, I analyzed the Lombard-Scargle spectrograms for the all tracks in each day and selected those tracks that satisfied the following requirements: the satellite track should be mapping a good portion of the sky and the spectral peak should be at least 4 times stronger than the average noise. The prominent peaks for AUST station in 2013 were found in satellite PRN 2 3 4 7 20 23 24 25 26 31 32.

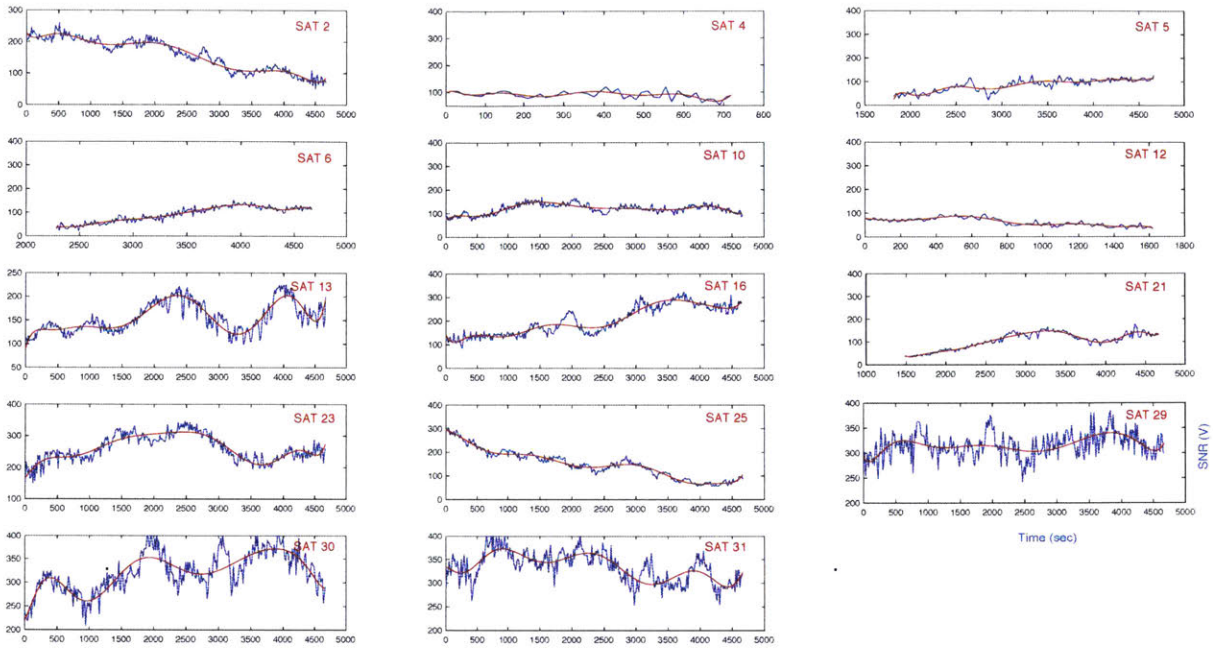

Figure 2.3.14 SNR direct signal fit with a 6th degree polynomial for each satellite track.

The spatial analysis of the SNR reveals a complex signal with contributions from sources at different locations and with frequency ranging from 0.14 to 1.2 mHz. The highest spectral peaks are found in the SE portion of the sky and more prominent in the descending track of the satellites, while secondary peaks can be seen in all the other parts of the sky (fig. 2.3.16). The spatial distribution of the spectral peaks is directly related to the uneven ground around the station and the irregularities of the top of the glacier as well as far-away elevated structures (e.g. hills,

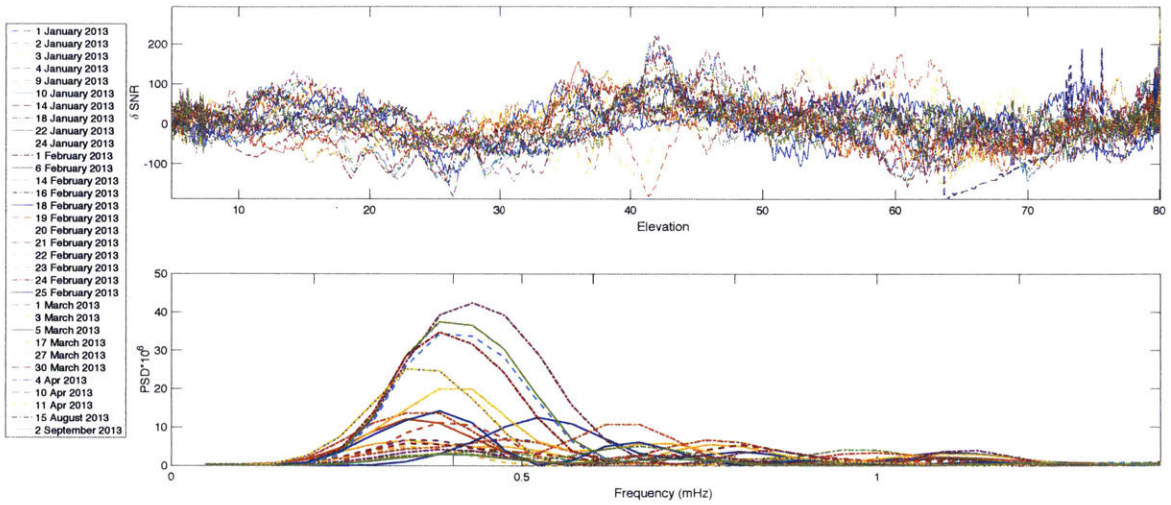

Figure 2.3.15 Example of the descending tracks for satellite PRN 26 at sampled days during year 2013 for AUST station. *Top*: SNR ratio at different elevations for sampled days. *Bottom:* spectrum of the SNR signal. The spectral peak with frequency around ~ 0.4 mHz changes with time in frequency and magnitude.

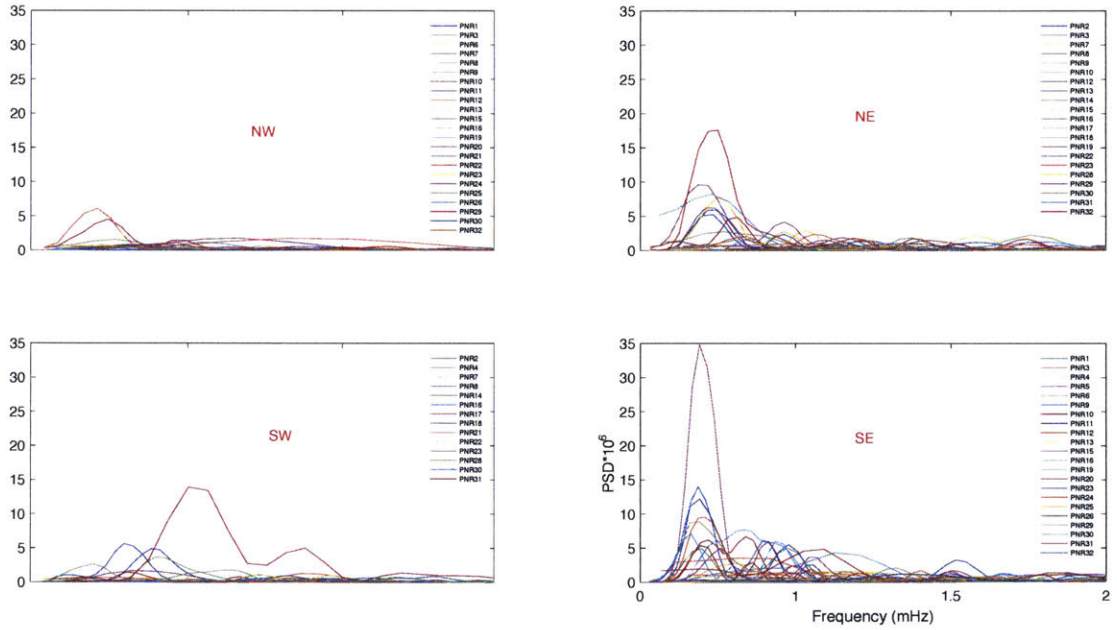

Figure 2.3.16 Example of quadrant analysis for desceding tracks for day '24-February-2013'. The highest peak is located in the SE quadrant for both ascending and descending tracks but its spectral density value doubles in the descending track. For the other quadrants, the peaks have comparable values with slightly differences in the frequency.

outcrops). More detailed photographs of the surrounding glacier were not available to locate the

possible sources of long period multipath signal.

The spectral content of the SNR during the course of the year 2013 at AUST reveals that the peaks in the spectrum are stronger during the winter months, showing a correlation with the jumps in the up component estimates (fig. 2.3.17). In the summer months some variability is present, likely due to the change of reflective index of the ground (e.g. rain) or atmospheric effects. To correlate the variability of the spectrum with the position estimates, I performed the spectral analysis on single satellite tracks, selected following the criteria previously described.

Once the satellites with stronger spectral peaks were selected, I examined the spectrum variations in frequency for each day and found three to four principal peaks corresponding to different periods and different values of spectral density. I then applied an algorithm that selects peaks for three period ranges and separates them in three different classes depending on their relative prominences in a particular frequency frame. For 2013 data of AUST station, the peaks are divided in three periods: ~15 minutes, ~30 minutes and ~1 hour. I then compared the detected peaks with the up component estimates and the relative error, as the presence of snow also affects the error on the estimates. The results are shown in figure 2.3.17. For the shorter period signals (~15 minutes), the highest peaks detected are January 1st, January 17th, January 19th to 26th and February the 19th, 22nd, 23rd, 24th. These days are correlated to the highest jumps in the vertical component estimates as well as the largest errors (fig. 2.3.17). The largest peaks are not present in the second half of the year, where the jumps in the estimates less dramatic. Secondary peaks (*rain1*) are present throughout the year (more in the first half) and are correlated with smaller jumps in the position. The third class of spectral peaks is correlated to minor jumps in the vertical displacement and are visible throughout the year. The peaks are not detected for a few days March and several days in the summer and the fall, where the daily positions show a linear temporal trend. There are few days in the winter (February 8th, February 14th, April 4th and 6th and May 15th through 19th) that are characterized by large errors but no spectral peaks, suggesting that they are related to another process that doesn't affect the SNR. The 30 minutes period analysis (fig. 2.3.17) reveals that the snow peaks are still detected in the same days range as for the shorter period signals, with slight variations. Overall there is a lower number of peaks detected in this frequency range, especially for the second half of the year and the peaks are generally consistent with the jumps in the vertical estimates. The less disturbed days in the time series don't have prominent spectral peaks, as for the shorter period spectral component.

The long time period analysis (~1hr) reveals similar distribution of the peaks, although some variations occurs. The results for the year 2013 show that there is a good correlation between the spectral peaks, the error on the estimates and the jumps in the vertical displacement. In particular, the highest peaks are found in the winter where the largest jumps occur. The prominent peaks occur at different frequency range with different magnitude of spectral density. The summer and fall days of 2013 are characterized by lower peaks that correspond to minor jumps in the vertical component and lower errors on the estimates. Overall, the less disturbed days of the time series have no visible peaks, suggesting that on those days the SNR ratio variability is low.

The analysis has been applied also to 2012 measurements, where the vertical component estimates appear less affected by the multipath. The results (fig. 2.3.18) show again that the detected peaks are correlated with the jumps in the vertical estimates and these signals generally occur in the winter months, while the summer and fall are less affected. In this case, the errors are smaller with some variability and the strongest peak are found only on one day in December 29th for a 30 period range. The least affected positions have low SNR ratio variability, with no detectable spectral peaks, as in 2013 analysis.

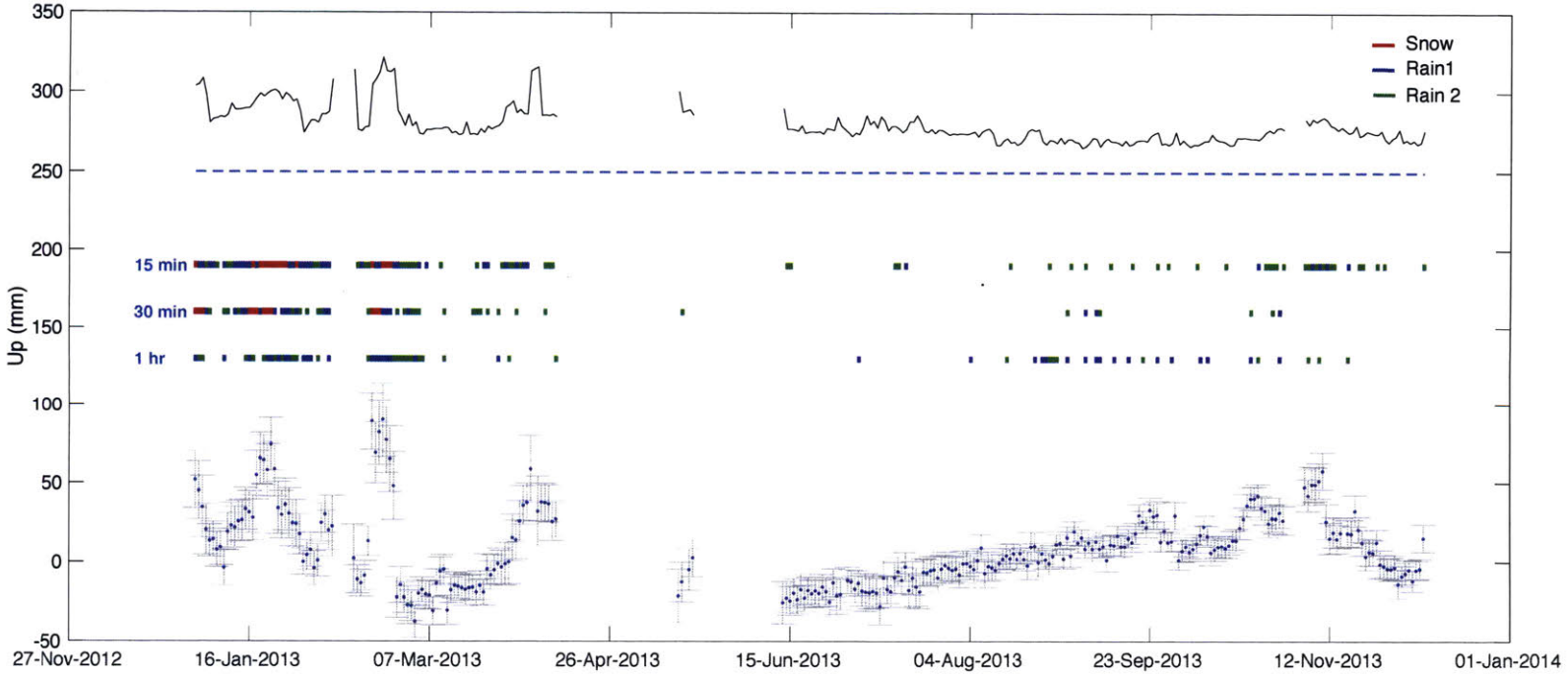

Figure 2.3.17 Snow and rain peak detection for spectral component with ~ 15 minutes (top), 30 minutes (middle) and 1 hour period at Austmannbunga station (AUST) for year 2013. The black curve on top is the standard deviation estimate of the vertical component, exaggerated (x 3) for plotting purposes. Dashed line in blue represents the 0 value for the standard deviation. Red lines are the largest peaks detected, correlated to the larger errors and larger jumps in the estimates. The blue lines are the secondary peaks that can be correlated with secondary jumps in the estimates and smaller errors. The green lines are the smallest peaks (but still distinguishable from the background noise). At the bottom, the time series of the vertical component of the displacement is shown with the respective error bars.

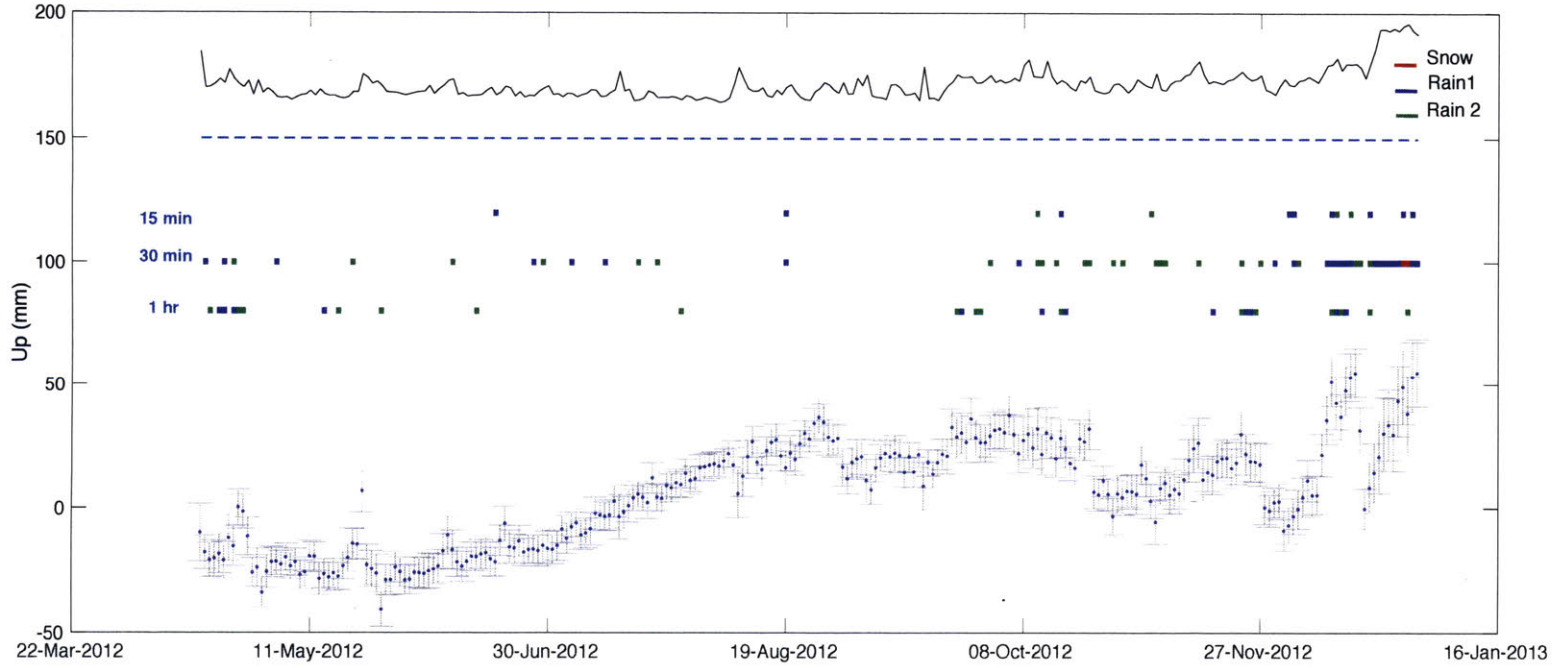

Figure 2.3.18 Snow and rain peak detection for spectral component with ~ 15 minutes (top), 30 minutes (middle) and 1 hour period at Austmannbunga station (AUST) for year 2012. The black curve on top is the standard deviation estimate of the vertical component, exaggerated (x 3) for plotting purposes. Dashed line in blue represents the 0 value for the standard deviation. Red lines are the largest peaks detected, correlated to the larger errors and larger jumps in the estimates. The blue lines are the secondary peaks that can be correlated with secondary jumps in the estimates and smaller errors. The green lines are the smallest peaks (but still distinguishable from the background noise). At the bottom, the time series of the vertical component of the displacement is shown with the respective error bars.

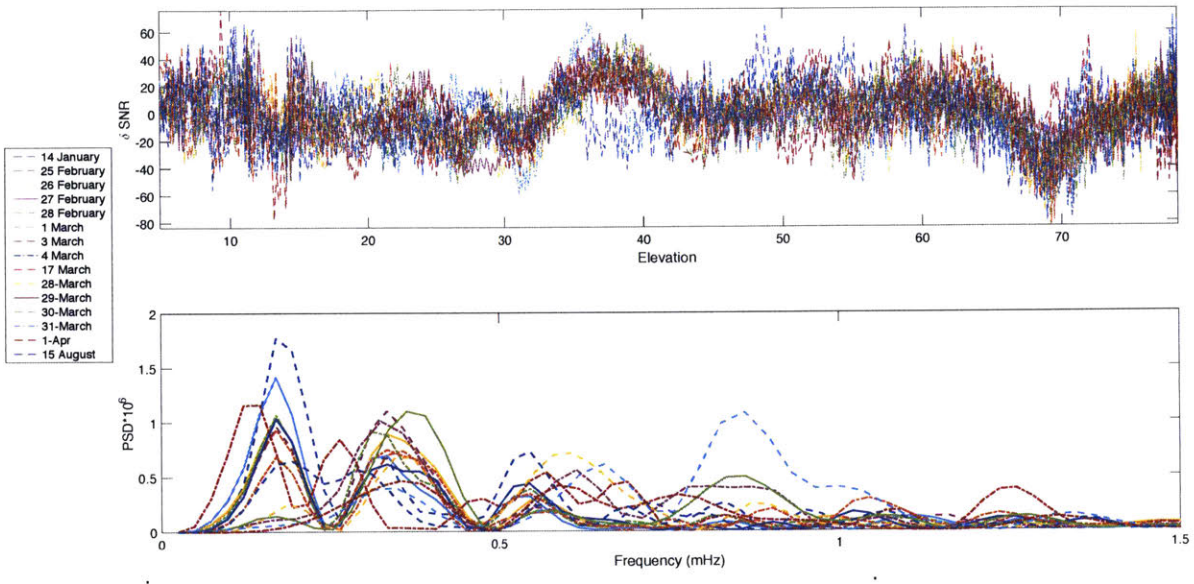

Figure 2.3.19 Example of the descending tracks for satellite PRN 19 at sampled days during year 2013 for OFEL station. *Top*: SNR ratio at different elevations for sampled days. *Bottom:* spectrum of the SNR signal. There are several peaks with similar power density at various frequency ranges.

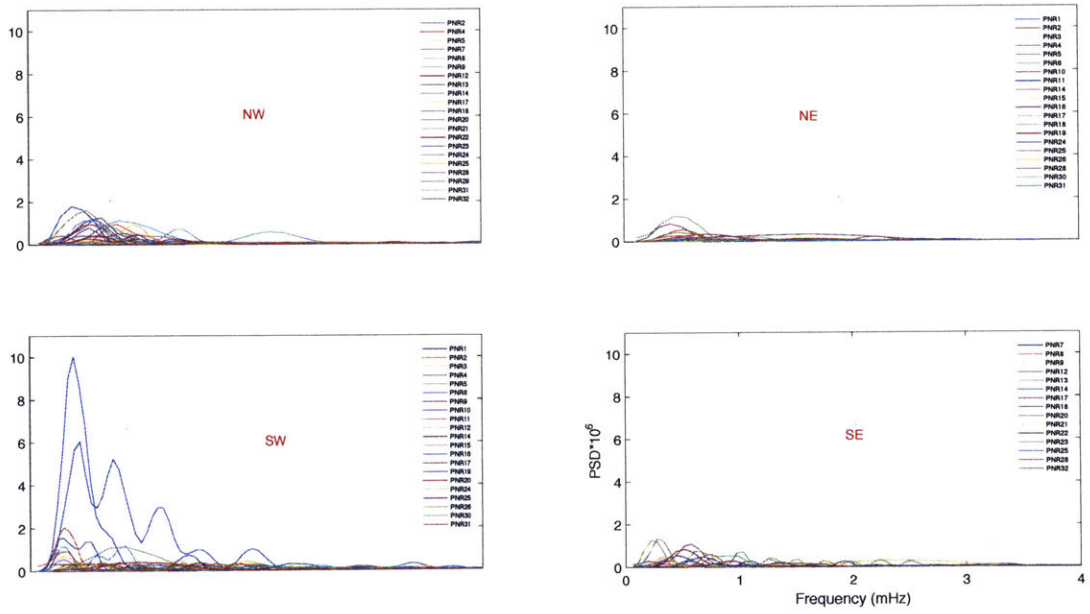

Figure 2.3.20 Example of quadrant analysis for ascending tracks for day '19-February-2013' at OFEL station. The highest peak is located in the SW quadrant for both ascending and descending tracks but its spectral density value higher for the ascending tracks.

The snow detection algorithm has been applied to OFEL station in the NE part of the volcano

winter months. The spectral analysis of OFEL station reveals a variability of the SNR throughout

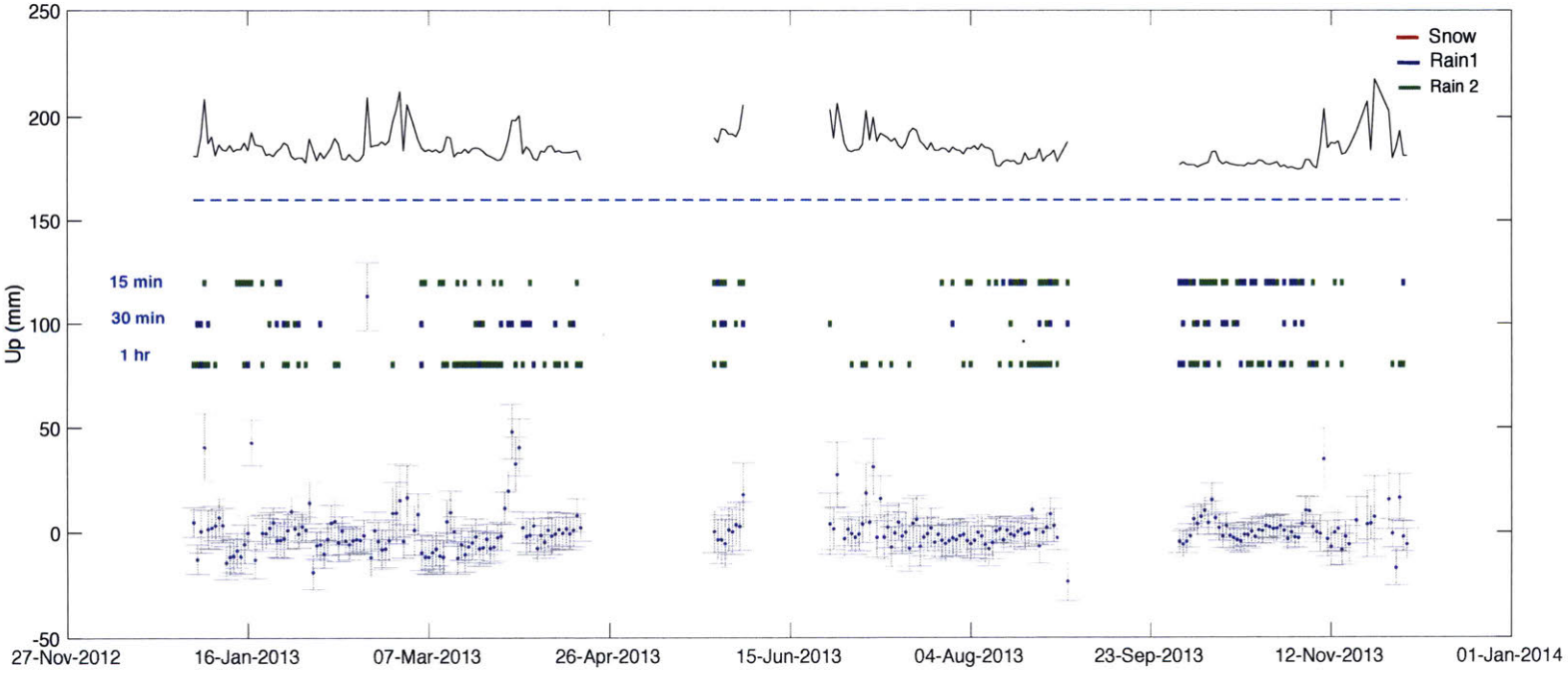

Figure 2.3.21 Snow and rain peak detection for spectral component with ~ 15 minutes (top), 30 minutes (middle) and 1 hour period at Oldufell station (OFEL) for year 2012. The black curve on top is the estimated standard deviation of the vertical component, exaggerated (x 3) for plotting purposes. Dashed line in blue represents the 0 value for the standard deviation. Red lines are the largest peaks detected, correlated to the larger errors and larger jumps in the estimates. The blue lines are the secondary peaks that can be correlated with secondary jumps in the estimates and smaller errors. The green lines are the smallest peaks (but still distinguishable from the background noise). At the bottom, the time series of the vertical component of the displacement is shown with the respective error bars.

the year, with spectral peaks occurring throughout the year (fig. 2.3.19).

Unlike AUST station, the peaks are of comparable magnitude and no prominent peaks (with few exceptions) are present. The separation in quadrants of the satellite tracks (fig. 2.3.20) reveals that the highest peaks appears in the SW portion of the sky, suggesting the possibility uneven ground. The spectral analysis show that secondary peaks can be detected throughout the year at different frequency range. There is a lack of distinctive peaks, with a signal overall noisier and the correlation between spectral peaks, error and estimates jumps is less evident (fig. 2.3.11). Only in few cases (as at the end of March) the secondary peak can be correlated to a jump in the vertical component. The time series is also characterized by a higher number of outliers, suggesting that the station is overall noisier.

This analysis suggests that Austmannbunga (AUST) station at the top of the volcanic edifice is affected by reflections, likely caused by accumulation of snow on top of the antenna and in its surrounding. The reflections on snow produce a complex signal, with spectral peaks visible at different frequency ranges and variable magnitude. This suggests that different objects at various distances are reflecting the signal and the variability of the peaks between frequency ranges demonstrates how the snow accumulates differently depending on the surface of the reflector. The higher frequency signals have larger impact on the estimate of those days where the snow accumulates. The lower frequency signals (>1hr period) have instead effects on several days throughout the year, suggesting the reflective index of the distant reflector changes during the year. Due to the temporal behavior of these reflectors, I suggest that objects close to the antenna reflect the signal, with a large impact on the estimates during few days of the winter months, when consistent snow accumulation occurs. These close range objects have a secondary effect on the estimates throughout the year with different intensities related to the reflective index variations (rain or dry conditions). Distant objects reflections affect instead several days of the year with variable intensities, suggesting that the conditions on these far range reflectors change seasonally. In this case, the top of the glacier is very likely to be the source of reflections and, as the conditions on the surface change throughout the year (snow, ice, water) as well as the height and the shape of the reflector, the resulting spectral peaks are different during the year.

The analysis of Oldufell station (OFEL) shows that reflections are affecting the signal throughout the year with less intensity than AUST station and only in two cases is there a correlation between

estimates and spectral peaks, suggesting that snow is not corrupting the signal; but these effects are probably results of atmospheric effects.

The snow detection algorithm appears to successfully detect spectral peaks variability throughout the year. The interpretation of these results is for now based on speculation on temporal and spatial characteristics of the spectral peaks, as snow data are unavailable at the location. A more robust analysis will also involve the elevation dependency of the signals.

In order to account for the presence of snow in the time series, it is necessary to correctly estimate the RMS on the positions. Current algorithm in the GAMIT/GLOBK software calculated also a 10-points averaged RMS to a more realistic estimate of the standard deviation. However, the error is still underestimated in days when the snow is present (fig.2.3.22). Future work will include a more robust RMS estimates to account for the noise due to snow on the antenna.

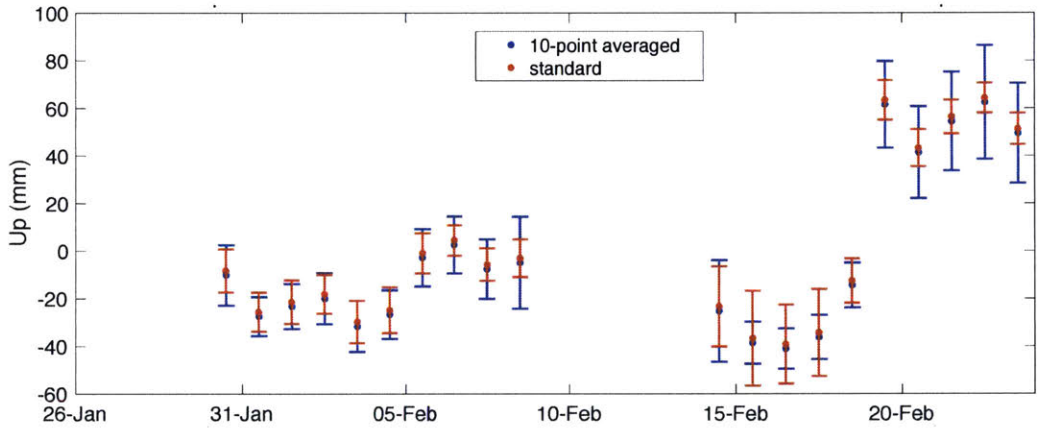

Figure 2.3.22 Example of the standard RMS and 10-point averaged RMS for snowy days at AUST station.

I recommend the installation of a camera and a meteorological station at the GPS location to capture snow accumulation and weather data to compare with the spectral analysis of the SNR. Finally, for the detection algorithm validation, I suggest this analysis to be applied to stations at different location where similar behavior is observed.

2.4 Model of the deformation source

2.4.1 Introduction

Studying the unrest for subglacial volcanoes is often a difficult task as there are many contributing processes to the detected deformation signal that can suggest an unrest of the volcano. It has been observed in various studies (Pinell et al. 2007, MgGuire et al. 2012, Spaans et al. 2015) that the observed motion can be partially or overall attributed to the changing ice-cap. In the past few years with the rise of global temperatures, these glaciers have melted at different rate, resulting in a general shrinking of the ice sheets on top of subglacial volcanoes and contributing to the deformation observed around these volcanoes. In addition to the loading/unloading effects, the mass variations of the ice cap on these volcanoes can influence the distribution of stresses in the crust around the magma chamber, affecting therefore the migration of the magma to the top. The isostatic adjustment to the glaciers retreat affects the long term motion observed at the stations and it has been studied extensively in order to discriminate the loading induced deformation with magma induced deformation (Arnadottir et al. 2009, Auriac et al. 2013).

GPS stations in Iceland, especially the ones located close to the icecaps, are characterized by strong seasonal signals with variations at different periods, suggesting that the observed deformation is the results of several seasonal processes, such as snow, atmospheric and ocean loads.

Snow accumulation during the winter months can result in vertical displacement of several cm (Heiki, 2001) as well as it can play a role in the mass glacier mass balance, contributing to the observed seasonal signal (Grapenthin et al. 2006).

Atmospheric loading (ATML) can also affect the signal at the station, introducing time correlated noise and periodic terms at annual and semiannual periods to the position estimates (Tregoning and Watson, 2009). In addition to ATML, ocean tidal loading is also known to introduce short term variations in the time series and current models used in the processing to take into account of these variations (FES2004, etc) do not consider long term and non-tidal variation in the ocean load. In addition to these seasonal signals, local processes like water reservoir discharge and geothermal processes can affect the deformation, introducing annual and semi-annual terms.

The peculiar location of Katla volcano (high elevation, underlying icecap) suggests that potentially all these processes might affect the deformation observed at the volcano at different time scales. In this chapter I will apply a coherence analysis to the GPS signal with available data of pressure, temperature, precipitation and I will compare my results to other studies to discuss the possible processes causing the observed deformation.

2.4.2 Seasonal deformation through GPS measurements

As seen in the previous paragraph (2.3.15), the short-period variation the position estimates for AUST station can be partially attributed to the presence of snow during the winter months and a combination of rain and atmospheric loading effects during the rest of the year. The signal is also characterized by an annual seasonal variation, suggesting that additional processes have to be taken into account for the analysis of the deformation recorded at the station.

The evaluation of the seasonal component of the time series was carried with *tsview,* a matlab routine that allows us to clean time series (outliers, jumps, earthquake) and evaluate the trends observed in the time series. The displacement at the station can be written as a combination of linear and seasonal term (annual and semiannual period sinusoid):

$$x^i = x_0^i + v^i(t - t_0) + A_0^i \cos\left(\frac{2\pi(t-t_0)}{T_0} - \tau_0\right) + A_1^i \cos\left(\frac{2\pi(t-t_1)}{T_1} - \tau_0\right) + \varepsilon, \quad (11)$$

where x_0^i is the initial position, $v^i(t - t_0)$ is the velocity term (linear) and $A_0^i cos$ is the annual period sinusoid, $A_1^i cos$ is the semi-annual period sinusoid, τ_0 is the phase lag in radians and ε is the noise. The linear and sinusoidal components are evaluated through a least-square solution.

After removing outliers and jumps due to change of the antenna from the time series, the seasonal components were evaluated for all the stations around the volcano.

In figures 2.3.3, 2.3.4 and 2.3.5 are shown the time series of the GPS stations around Katla volcano. Stations on each side of the volcano (GOLA, SOHO, HVOL, RFEL, SNAE, OFEL) show a consistent deformation with velocities of less than 10 mm/year in SSE direction. Evaluation of the seasonal variation for these stations is complicated by the lower magnitude of the variations and by the deformation caused by the Eyjafjallajökull volcanic event on some of the stations as well as the presence of gaps in the data. However, a seasonal component for these stations (GOLA,

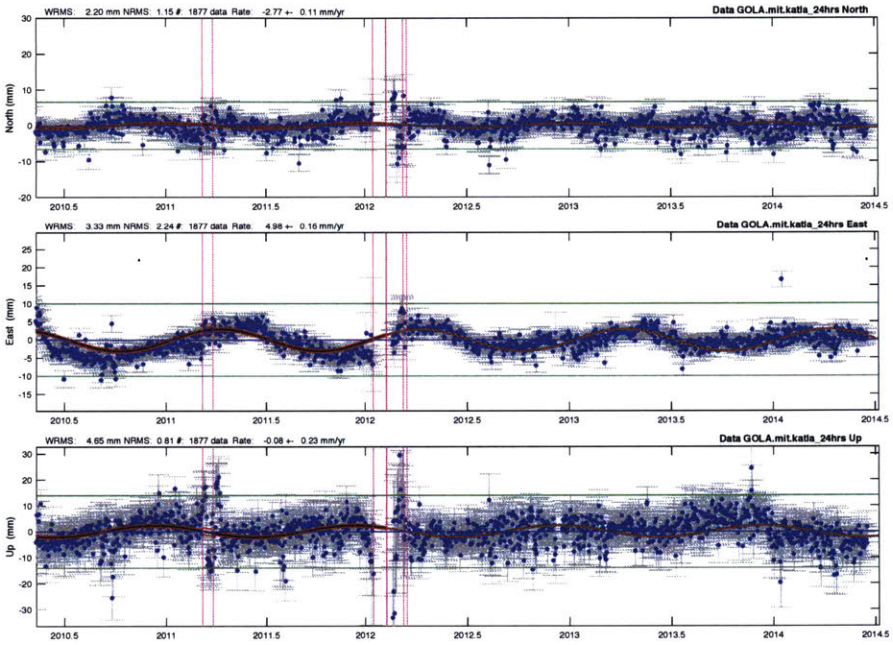

Figure 2.4.1 Detrended time series after the 2010 Eyjafjallajökull event at GOLA station on the western side of the volcanic edifice. *Top:* N-S component; *middle:* E-W component; *bottom:* vertical component. Red lines represent the annual variation at the station. The vertical lines in magenta are corrected jumps for the change of the antenna and/or earthquakes.

SOHO, HVOL, RFEL, SNAE, OFEL) can still be observed (fig. 2.4.1, 2.4.2). The magnitude of the variation is only few mms and is more prominent in the east and up components. During the summer months, the horizontal components reach the maximum peak (NE motion), while the vertical component reaches a minimum; during the winter the stations appear to move in the

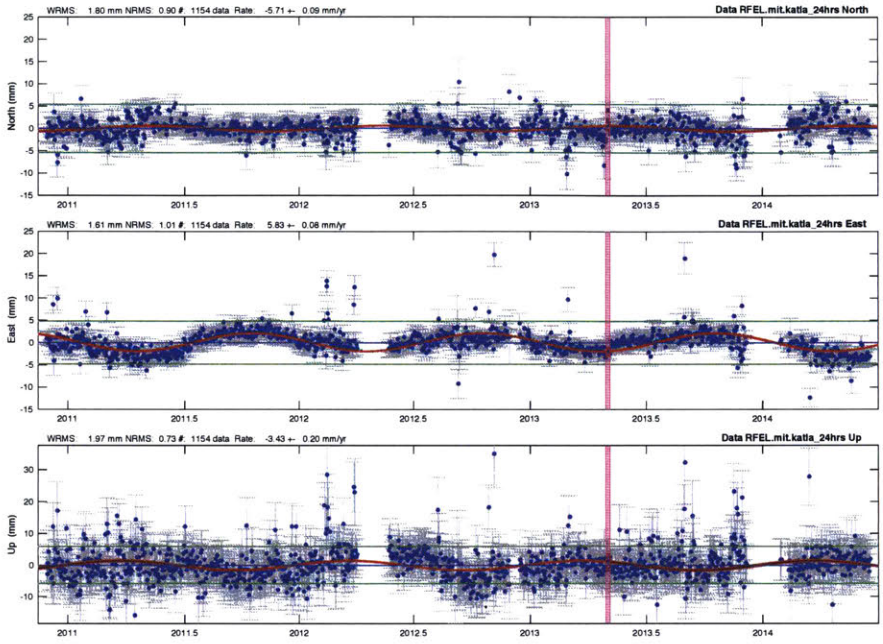

Figure 2.4.2 Detrended time series at RFEL station on the eastern side of the volcanic edifice. *Top:* N-S component; *middle:* E-W component; *bottom:* vertical component. Red lines represent the annual variation at the station. The vertical lines in magenta are corrected jumps for the change of the antenna and/or earthquakes.

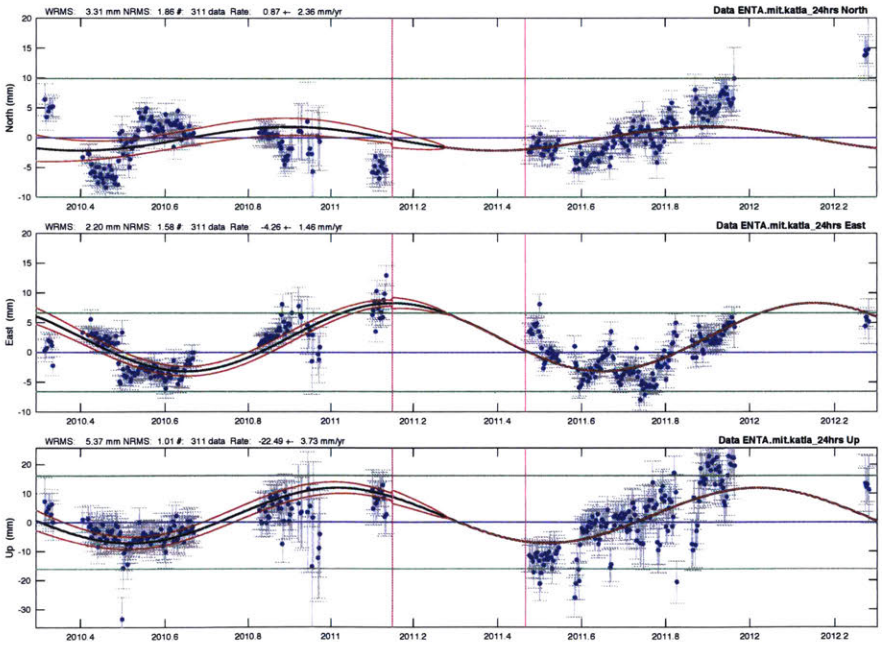

Figure 2.4.3 Detrended time series at ENTA station on the NW side of the volcanic edifice. *Top:* N-S component; *middle:* E-W component; *bottom:* vertical component. Red lines represent the annual variation at the station. The vertical lines in magenta are corrected jumps for the change of the antenna and/or earthquakes.

opposite direction with an uplift and SW motion. These results are only indicative as the

extrapolation of seasonal motion for these stations is complicated by the volcanic deformation of the neighboring volcano and the motions are small in magnitude.

The velocity measured at ENTA station has a different direction (mostly E) that is due to the limited amount of data available for the processing. However, it is still possible to detect a seasonal variation at the station (fig. 2.4.3).

At AUST station located on the volcanic rim these seasonal signals are prominent and complicated by higher frequency variations. In particular, as shown in fig. 2.4.4, the station moves of about 2-2.5 cm on average in SW direction (toward the caldera) during the winter with the minimum value reached in March/April and it moves of about 2-2.5 cm in NE direction (away from the caldera) in the summer with maximum reached late August. The rate of displacement in the summer is higher than the winter, meaning that the deformation measured by station is faster during the summer months. The vertical displacement of AUST station has a phase lag with the horizontal estimates, as the station moves of 4 cm on average in the up direction during the winter months

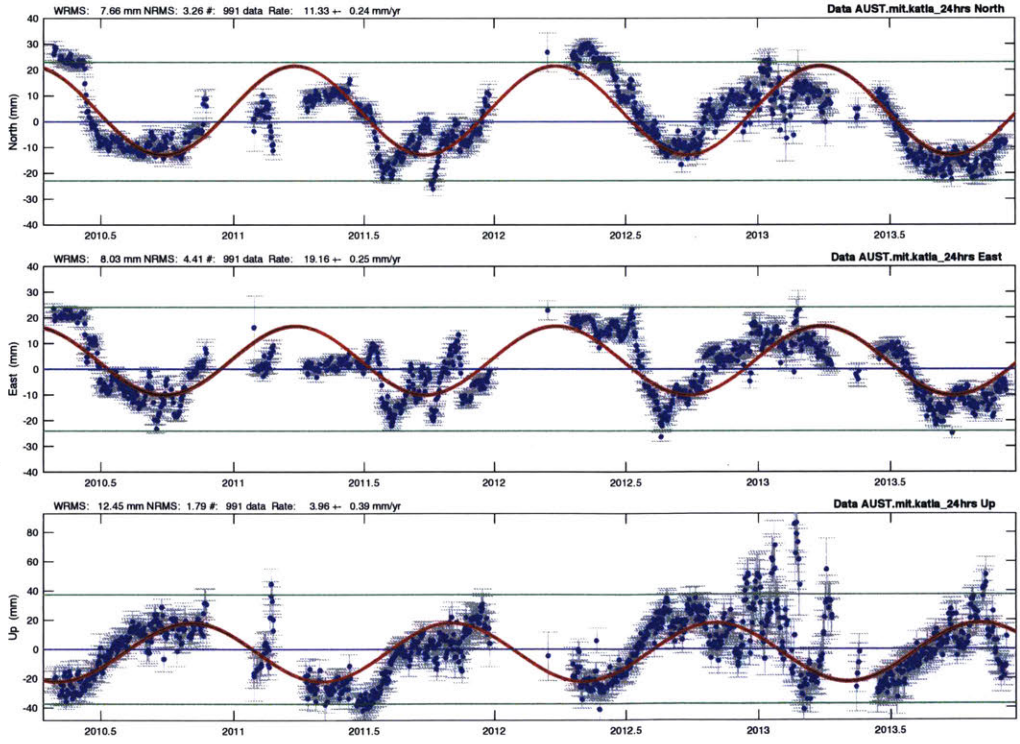

Figure 2.4.4 Detrended time series at AUST station. *Top:* N-S component; *middle:* E-W component; *bottom:* vertical component. Red lines represent the annual variation at the station.

with maximum value reached in November/December and about the same magnitude but in down direction during the summer months with the minimum reached in June. The lag is about 4 months. The position estimates of the station have been compared with available data of temperature and number of seismic events to constrain the characteristics of the seasonal signal. In figure 4.1.4 we show the spectral coherence of the vertical position estimates with the average temperature data. It should be noticed that the weather station ISKAFTRH2 (from www.wunderground.com) is located ~27 km east of the GPS station and that the temperature data likely differ from the actual temperatures at the GPS location. The analysis shows higher coherence for periods of ~ 2, 32, 51 and 128 days with phase lag of -0.5, 0.2, -0.5 and 0.5 radians. Similar results for the horizontal components are obtained, with the maximum of the magnitude-squared coherence of 0.6 for periods of ~2.5, 5, 10 and 128 days with a phase lag respectively of 0, 0.4, 0.78 and -0.7 radians. It is overall clear that the deformation signal is somewhat correlated with the temperature and the time lag calculated is 42 days for north, 53 days for east and 71 days for vertical components. This indicates that there is a correlation between the air temperature and the periodic signal observed at the station, but further investigations with data acquired at the GPS locations are needed to better

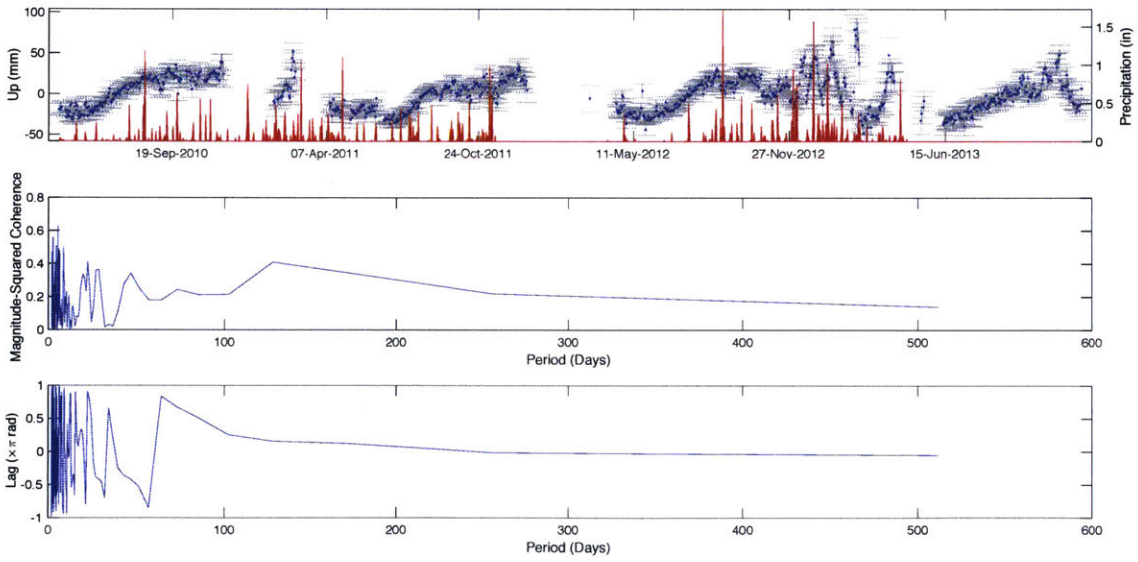

Figure 2.4.5 Coherence estimate for the Up components. *Top:* position estimates are shown in blue and precipitation in red. Magnitude squared coherence for different period (*middle)* and corresponding lag in radians (*bottom*).

constrain the dependence of the seasonal deformation with the temperature.

The same analysis has been carried also for the precipitation data, measured at the weather station.

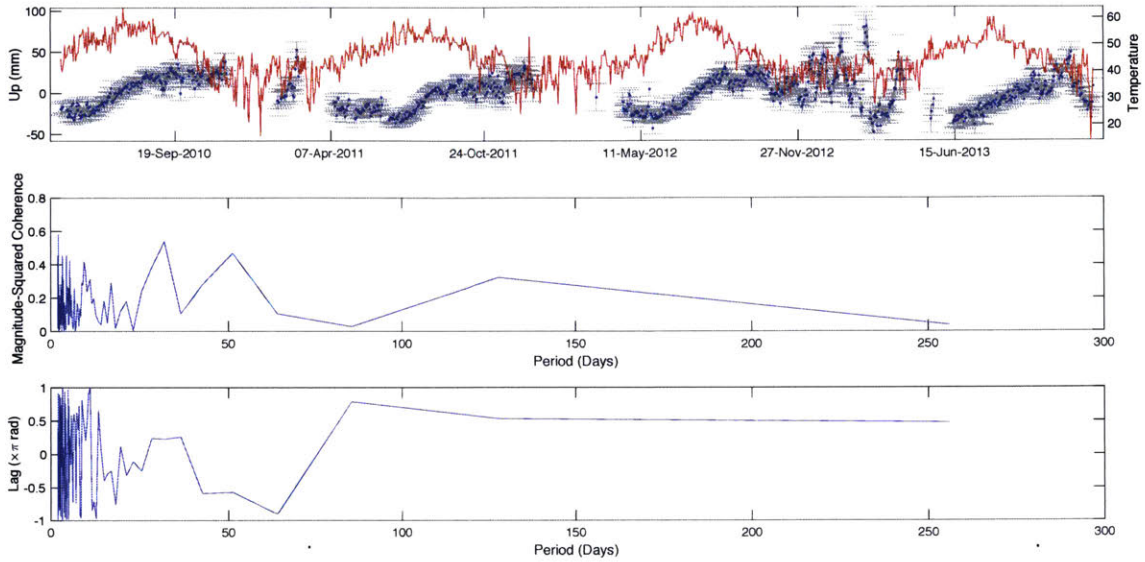

Figure 2.4.6 Coherence estimate for the Up components. *Top:* position estimates are shown in blue and average temperature in red. Magnitude squared coherence for different period (*middle)* and corresponding lag in radians (*bottom*).

The results shown in figure 2.4.6 suggest that the seasonal variations have an evident yearly correlation with precipitation measurements and some of the peaks in the estimates correspond to peaks in precipitation. The highest coherence is found for 3, 5, 10 and 128 days. This result is only indicative because as previously stated the actual precipitation at the GPS location might differ from the data measured at the weather station.

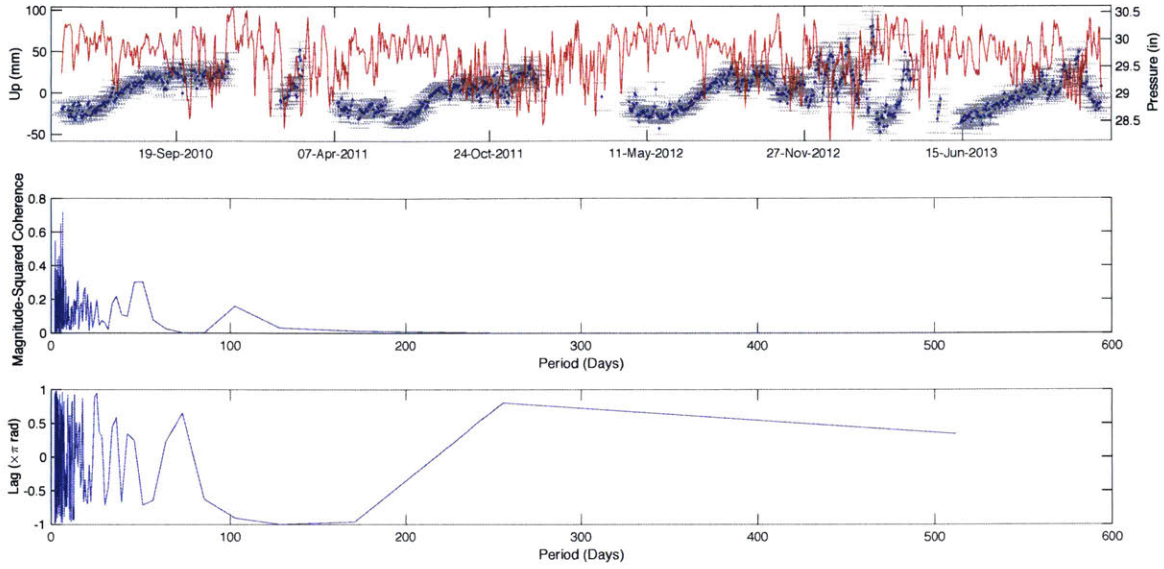

Figure 2.4.7 Coherence estimate for the Up components. *Top:* position estimates are shown in blue and atmospheric pressure in red. Magnitude squared coherence for different period (*middle)* and corresponding lag in radians (*bottom*).

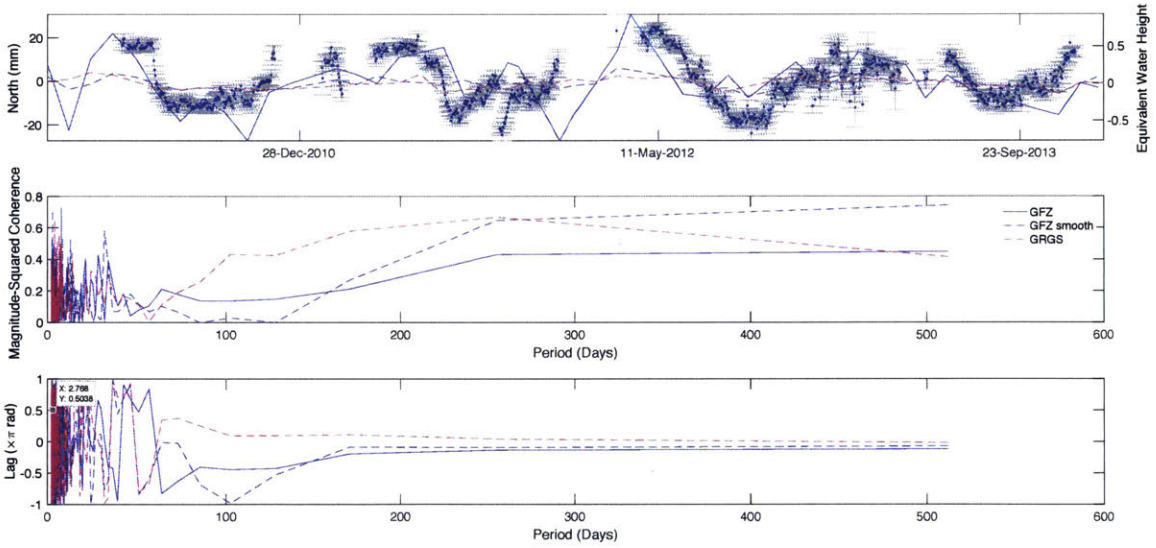

Figure 2.4.8 Coherence estimate for the North components, GFZ gravity solutions (blue), GFZ smoothed solution (red) and GRGS solution (magenta). *Top:* position estimates and gravity field variations expressed in EWH (Equivalent Water Height). Magnitude squared coherence for different period (*middle)* and corresponding lag in radians (*bottom*).

The coherence estimate has been also calculated for the atmospheric pressure data to take into account of the effects of atmospheric loading on the GPS positions.

In figure 2.4.7 the results are shown: the two signals are coherent for short periods (2 to 6 days), suggesting that the atmospheric loading can impact the short term variation of the position

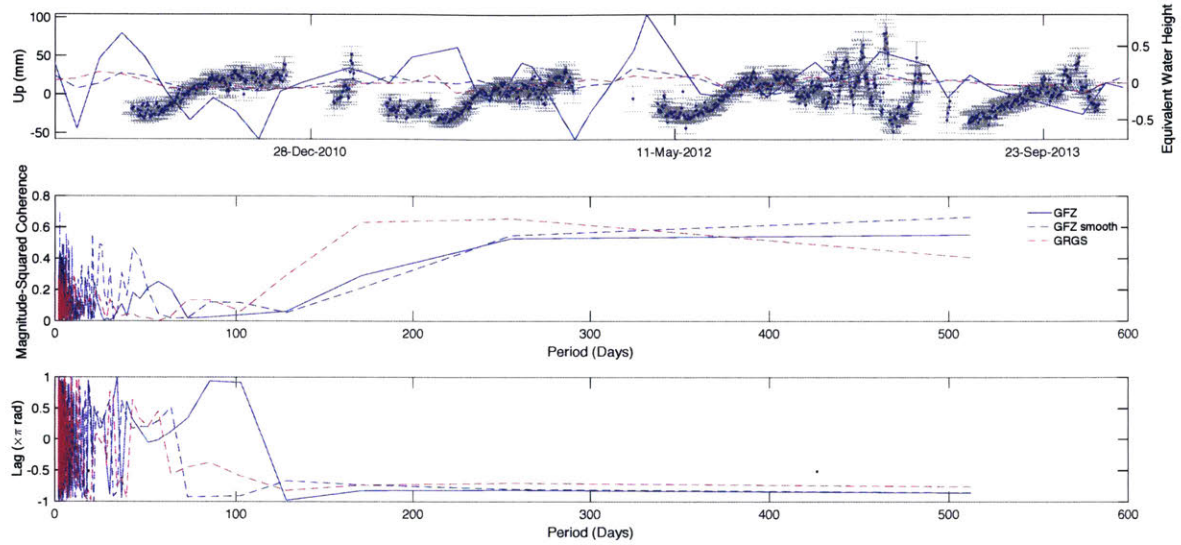

Figure 2.4.9 Coherence estimate for the Up components, GFZ gravity solutions (blue), GFZ smoothed solution (red) and GRGS solution (magenta). *Top:* position estimates and gravity field variations expressed in EWH (Equivalent Water Height). Magnitude squared coherence for different period (*middle)* and corresponding lag in radians (*bottom*).

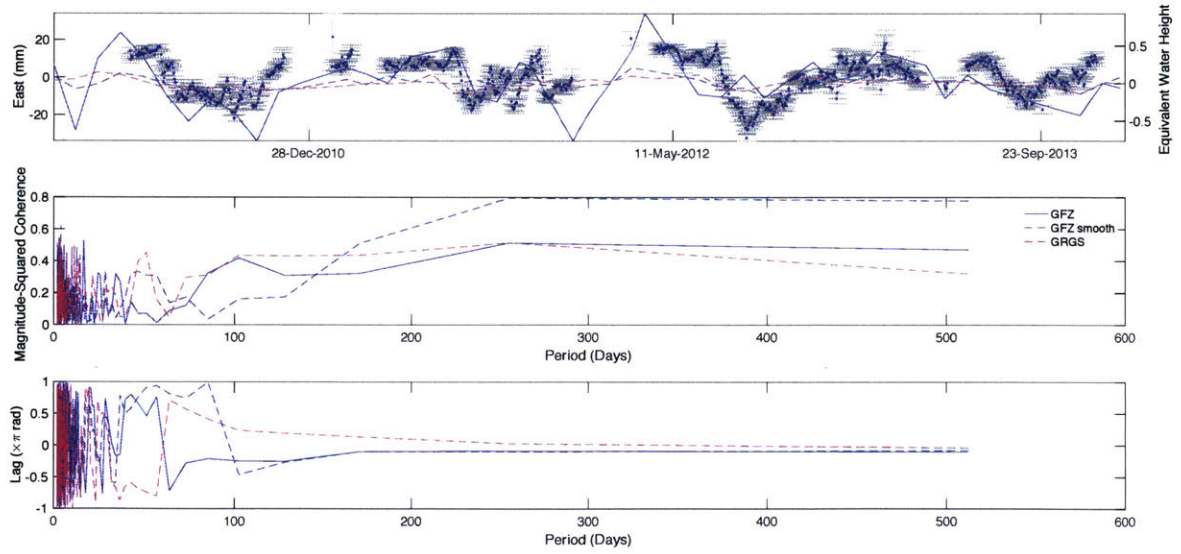

Figure 2.4.10 Coherence estimate for the East components, GFZ gravity solutions (blue), GFZ smoothed solution (red) and GRGS solution (magenta). *Top:* position estimates and gravity field variations expressed in EWH (Equivalent Water Height). Magnitude squared coherence for different period (*middle)* and corresponding lag in radians (*bottom*).

estimates.

In order to consider other possible contributions to the detected signal, I analyzed the variations of the gravity field, that can be related to different processes, such as hydrology loads, snow cover variations, baroclinic ocean signals, etc. I used the three different solutions from GRACE satellite gravity data (LEVEL-2, Release 5) processed by ICGEM (International Center for Global Earth Models) for the first two solutions and by GRGS (Groupe de Recherche de Geodesie Spatial) for the third solution. The first solution (GFZ) has a Gaussian filter applied (50 km) and a maximum degree of spherical coefficients cut-off equal to 60. This solution has a finer spatial resolution but a higher noise level. The second solutions (GFZ smooth) has a standard filter applied (DDK5) and the same cut-off, resulting in a smoother solution (less noisy) but with less spatial resolution. The third solution has a higher degree of spherical coefficients (≤ 80). Gravitational variation such as Earth tides, ocean tides, 3D atmospheric pressure fields and barotropic ocean response have been modelled in the gravity field solutions. The resulting field is therefore related to other unmodeled effects, such as hydrology loads, snow cover, baroclinic ocean signal and glacial rebound.

The analysis shown in fig 2.4.8 reveals that the North and East components of the position estimates are highly coherent for period 32, 102, 170 and 265 days with phase lag respectively of

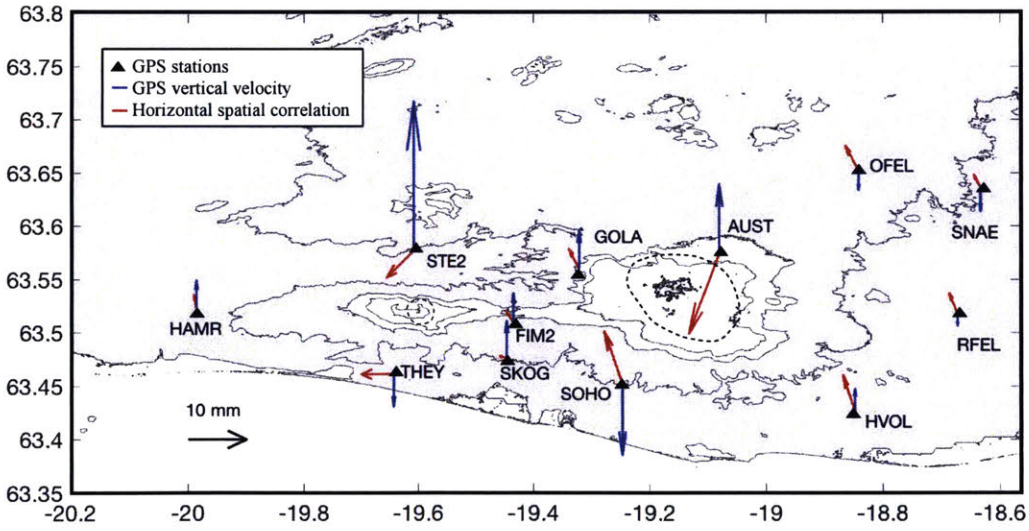

Figure 2.4.11 Direction of the horizontal spatial correlation (in *red*) for the GPS stations and vertical velocity (in *blue*).

0.7, -0.4, 0 and 0.2 lags. The vertical component is instead coherent with the gravity variation for

period of 42, 170 and 256 with phase lags of respectively 0.17, -0.8 and -0.7. The yearly signals in the gravity variation solutions matches very well the horizontal estimates.

In order to indicate the location of the source of deformation, I estimated the spatial correlation between the horizontal components of the GPS stations. The results, shown on the map (fig. 2.4.11), suggest that the stations around the edges of the two volcanic systems (HAMR, OFEL, SNAE, RFEL, HVOL) are mainly affected by the Mid-Atlantic-Ridge tectonics in the northeastern part of the volcanoes. Motion at THEY, STE2, FIM2 and SKOG is instead related to the post-eruptive deformation at the Eyjafjallajökull volcanic system. GOLA and SOHO stations located on the western flank of Katla volcano are influenced by the general deformation field of the area, characterized by the presence of the MID ridge. The horizontal correlation at AUST station indicates instead that the source of deformation is located towards the center of the volcanic caldera. Vertical velocities indicate generally an uplift on the two volcanic edifices, with magnitudes varying between 3 to 15 mm/yr; the two stations at the southern sides of two volcanoes reveal instead a subsidence of respectively 3 mm/yr at Eyjafjallajökull (THEY) and 10 mm/yr at Katla (SOHO). The southeastern side of Katla volcano is instead characterized by down-lift of few mm/yr. The pattern of vertical deformation can be mostly attributed to the glacial rebound as result of the retreat of the ice-caps due to global warming. In fact, previous GIA models have predicted velocities of about 10 mm/yr in uplift and 1-2 mm/yr of horizontal motion (Spaans et al. 2016) for a 65 cm/yr thinning rate for the icecap which is generally in agreement with the velocities estimated in this study. However, a more robust model of the GIA at the Myrdalsjökull icecap is needed to explain local deviation from the general deformation pattern and include more updated mass balance calculation.

If the deformation at the Eyjafjallajökull-Katla volcanic system can be interpreted as result of post-2010 volcanic deformation and glacial retreat, the behavior at AUST station cannot be explained with the same deformation field and other source of deformation have to be taken into account.

Although the coherence analysis for AUST position estimates gives an indication of the possible correlation between the variation of air temperature, barometric pressure, precipitations (shorter periods) and gravity (longer period) and the observed deformation and the spatial correlation, the causality of the different processes cannot be established. In previous studies (Spaans, 2015; Auriac, 2013), the observed deformation has been mostly attributed to the elastic response to

ice/snow loading processes. In the next section, I developed a finite element model to test the hypothesis of seasonal variations as result of ice/snow melting.

2.4.4 Ice/Snow load model

I developed an elastic finite element model using *COMSOL Multiphysics*© to estimate the deformation due to snow load. Under this hypothesis, the accumulated snow would cause the upper layer to bend during the winter, causing the station to move downward and towards the load (SW); while it would cause the opposite motion during the summer months when the load is removed due to melting (fig. 2.4.12).

A 2D seismic survey has shown traveltime anomalies at shallow levels, interpreted as a 5 km-wide magma chamber with a bottom at 3 km below the surface (Gudmundsson et al., 1994). The magma chamber has been simplified and modeled as an ellipsoid with 2.5 km horizontal semi-axes and 350 m vertical semi-axes, centered at 1.5 km below the surface. The elastic properties for the crust around the magma chamber were calculated from the seismic velocities survey and the results of

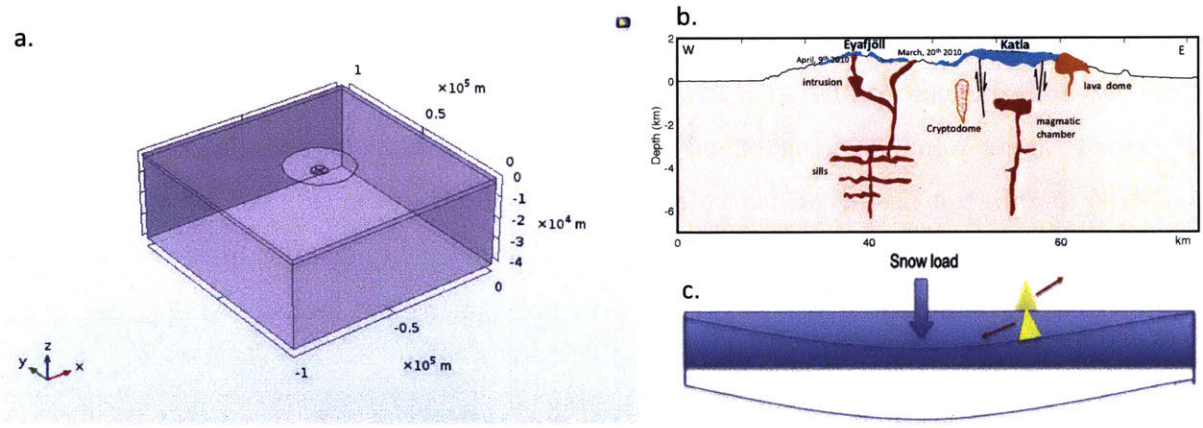

Figure 2.4.12 *a):* Finite Element model geometry. The lengths are in m. The top circular boundary represents the extension of Myrdalsjökull icecap, while the ellipsoid represents the magmatic chamber. *b):* cross section of the Eyafjöll and Katla volcanic systems (*modified after Gudmundsson et al. 1994*). *c)* Sketch of the snow loading mechanism.

the calculation are shown in figure 2.4.13. The anomaly that has been interpreted as the magma chamber of the volcanic system has velocity of 2.5 km/s for V_p. The Myrdalsjökull icecap has been

modeled as a circle of 30 km diameter on top of which the pressure caused by snow accumulation has been applied. The snow accumulation data at ISKAFTRH2 weather station registers value up to 1.5 cm in 2013.

However, as it is likely that snow accumulation at higher elevations is greater than at a lower elevation, for this model I considered a maximum accumulation of 6.5 m of snow, value reported in other studies (Jonsdottir et al. 2007).

The mesh consists of 101883 tetrahedral elements and the element size ranges from 500 to 4000 m, with finer elements around the magma chamber. The upper boundary is free to move in any direction, the bottom is fixed and the side boundaries have a roller condition, as the can move only

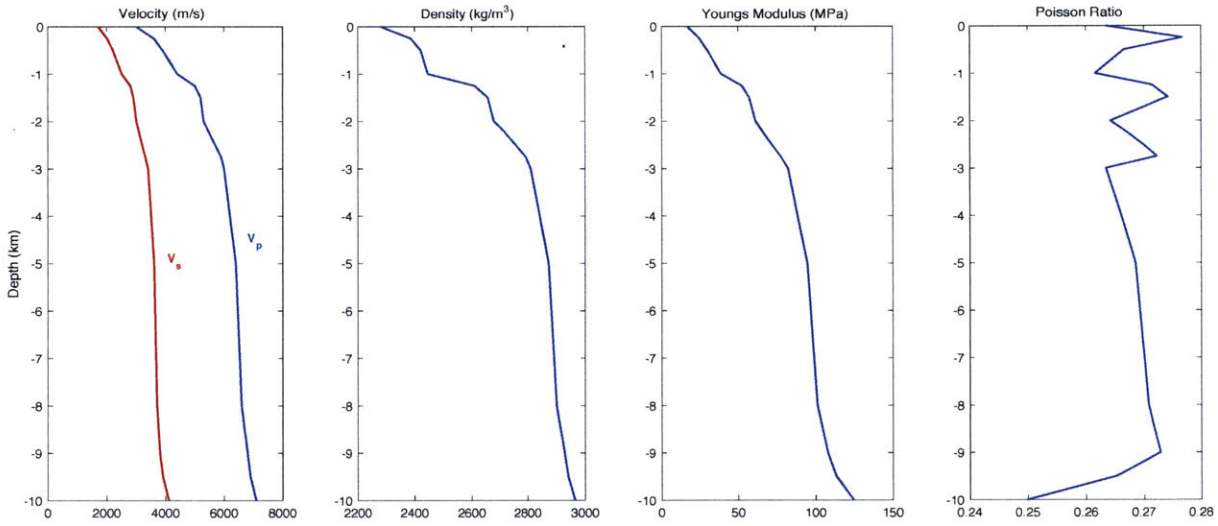

Figure 2.4.13 *From left to right:* V_p and V_s velocities variation with depth (*from Gudmundsson et al. 1994*) in the crust around the magma chamber; Calculated elastic moduli (density, Young's Modulus and Poisson Ratio.

in the xz- or yz-plane (depending on the position of the face). Also, a poroelastic layer of 2 km on the top of the model has been included to explore the effects of a porous material to the deformation field. The porous model has been developed using *COMSOL Multiphysics*© module *Poroelasticity* that solves the Darcy equations. Values for the porosity, permeability and Biot coefficient are respectively 0.5, 10^{-16} m^2 and 0.45 and are obtained from averaged values for volcanic rocks.

Table 2.4.1 Elastic moduli used for the snow load simulation. Young's modulus and Poisson ratio for the magma chamber are inferred from V_p *and* V_s *values.*

	Density	*Young's modulus*	*Poisson ratio*
Magma chamber	2700 kg/m^3	10-15e9 Pa	0.3-0.2
Ice	917 kg/m^3	8.7e9 Pa	0.31
Snow	650 kg/m^3	8.7e9 Pa	0.31

The results of the simulation indicate that the snow loading can only account for a maximum of -8.8 mm of vertical deformation, 0.8 mm of horizontal deformation (fig. 2.4.13-2.4.14). The presence of a partially melted magma chamber as well as variations of the elastic moduli of the latter don't influence the results as the difference in deformation between different models is less

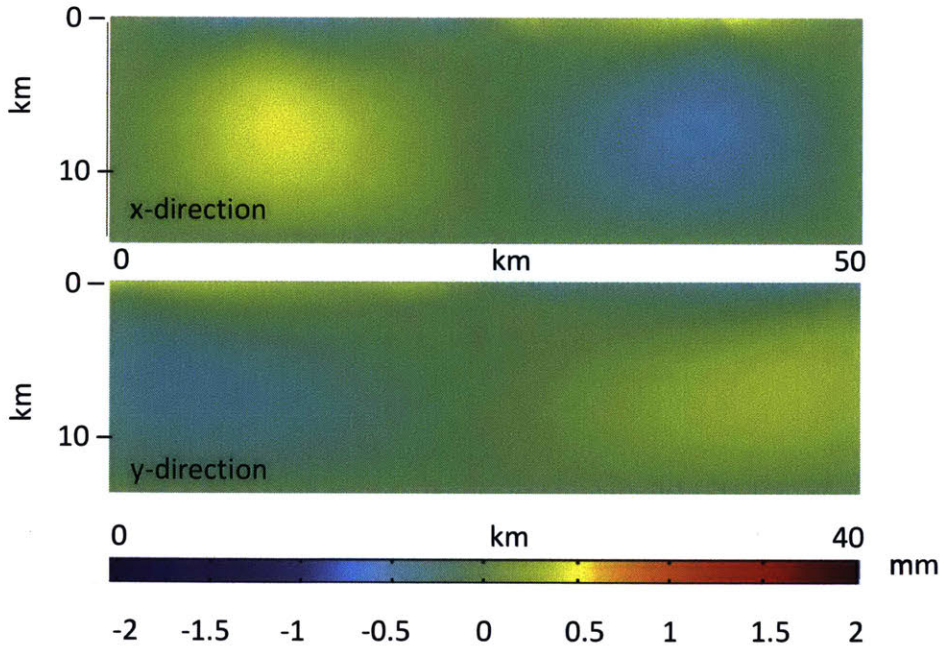

Figure 2.4.13 Close up of the X-direction(*top)* and Y–direction (*bottom)* displacement for a load of 6.5 m thick-snow layer. The displacement is shown in mm. The ellipse in the center represent the magmatic chamber. The model shown has E = 10e9 MPa and ν = 0.31.

than 1 mm (fig. 2.4.15). Also, the addition of a 2-km thick porous layer on the top doesn't change

the ground deformation. To obtain a deformation of 4 cm in the vertical component, as measured at AUST station, the loss of snow/ice from the ice-cap should be of about 40 m.

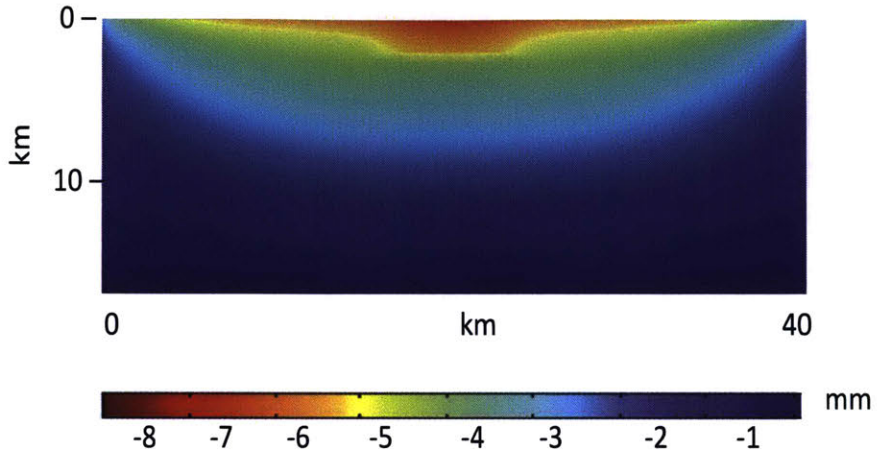

Figure 2.4.14 Close up of Z–direction displacement for a load of 6.5 m thick-snow layer. The displacement is shown in mm. The ellipsoid in the center represents the magmatic chamber. The elastic moduli for the results shown are E = 10e9 MPa and ν = 0.31

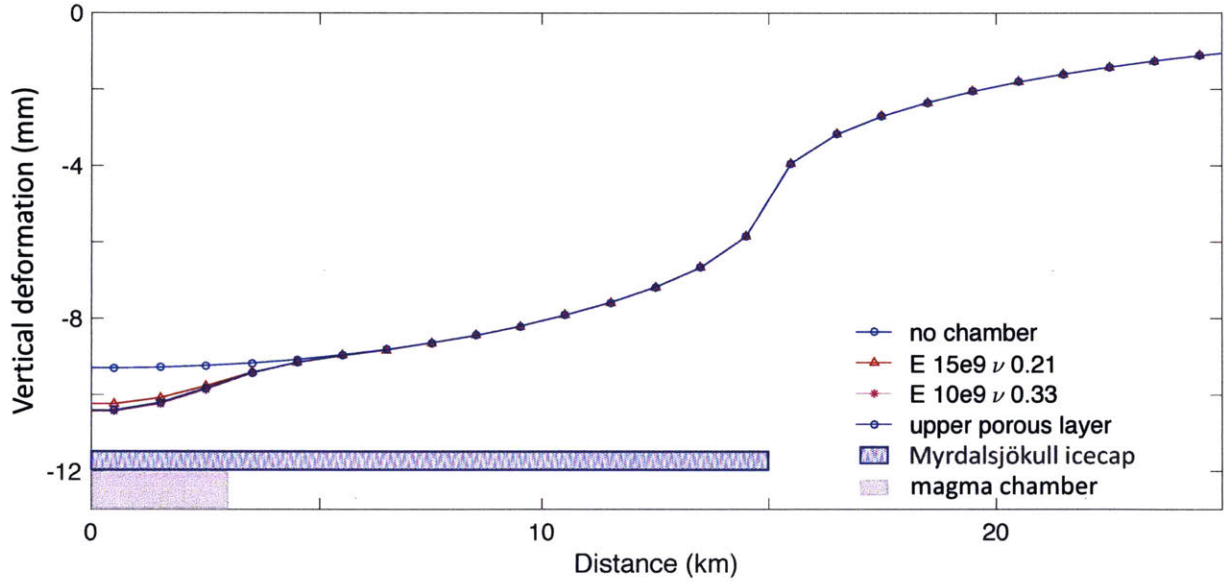

Figure 2.4.15 Comparison of vertical displacement between two different models of the elastic properties of the magma chamber, poroelastic model and no magma chamber model. The deformation is shown for the top layer along the one half of the X-axis (Y = 25 km) as the model is symmetric in x and y. Only the first 25 km of the model are shown. The differences between the three models are less than 1 mm. The extension of the Myrdalsjökull icecap and the magma chamber are shown at the bottom.

Ice/snow mass balance calculations for the Myrdalsjökull icecap account for only a few meters of snow accumulation during the winter months (up to 6.5 m from Jonsdottir et al. 2007) and ice thinning rate of about 65 cm/yr (Schmidt et al. 2012a) for climate change. In addition to that the deformation on the horizontal and vertical is not out of phase as shown in the GPS time series, In fact, there is a 4 moths lag between the horizontal and vertical motions. Therefore, this study suggests that the ice/snow loading deformation model cannot explain the magnitude nor the phase of the seasonal deformation observed at AUST station, as hypothesized in other studies (Spaas, 2015; Auriac, 2013). Although melting/freezing cycles cannot produce a load to explain the observed deformation on the rim of the volcano, they can concur to another phenomenon that has been often linked with deformational processes in sub-zero temperature: freeze fracturing of porous media. In fact, large pressure can develop inside water-saturated media at freezing temperatures. In particular, pore pressure can cause fracturing of pre-existing faults, degradation of rocks and soils and ground displacement. In fact, as pore water freezes, it expands by about 9% in volume. The consequent deformation is function of different variables: permeability of rock, the size of the pores and the existing connections between cavities. In addition, the melting of the icecap on top of the volcano would reduce the overburden pressure and therefore the pressure inside the pores, allowing also the circulation of geothermal fluids and gasses. Jonsdottir et al. (2007) have observed low velocities underneath the Katla caldera, suggesting an intense fracturing of the bedrock and hydrothermal circulation. Moreover, studies on the geochemical signature of the meltwater at Katla volcano have suggested that water composition is driven by hydrological reconfiguration. In particular, in the summer season the reduced overburden pressure due to the melting of snow and ice on the caldera allows the subglacial drainage system to expand, connecting the geothermal areas of the volcano and changing the chemical composition of the melting water. The reduced overburden pressure enhances also geothermal activity and volatile release as well as an increase in low-frequency seismic activity observed in the summer (Jonsdottir et al. 2009). This evidence suggests that the mechanism of freeze/melting in pores and fractures underneath the volcano can concur to explain the observed deformation at Katla volcano and a model of this process should be developed to test this hypothesis.

2.5 Discussion and conclusions

The deformation observed at Katla volcano is characterized by a long-term motion that can be partially attributed to glacial rebound in response to the melting of the icecap and partially attributed to tectonic deformation of the EVRZ and the Icelandic hotspot. The deformation is also characterized by a strong seasonality that has been studied using different type of measurements (seismic, hydrology, GPS). The peak of these seasonal cycles differs depending on the measurements.

As observed by Jonsdottir et al. (2007), earthquakes occur in two distinct areas, one within the caldera and around Goðabunga (corresponding to the location of GOLA GPS station), and seismicity differs between the two areas. Earthquakes occurring at Goðabunga are low frequency and shallow and they increase in number in the fall with the maximum occurring in October whereas earthquakes beneath the caldera are deeper and with a maximum occurring in July-August.

Hydrological discharge and water chemistry show seasonal variations as well (Wynn et al. 2015): in particular, in the winter months, the high oxygenation of the discharged waters suggests a limited contribution of geothermal processes; while in the summer months the presence of $\delta^{18}OSO_4$ is considered as a result of a strong geothermal contribution. Wynn et al. (2015) also hypothesized a spring season configuration of the draining system underneath the ice-cap, characterized by a discrete channelized subglacial hydrology limited to the lower portions of the glacier, a large ice and snow overburden pressure and limited connectivity to the zones of geothermal activity. The summer season configuration is instead characterized by a well-developed channelized subglacial hydrological system, which accesses the geothermal zone. In addition to that, the reduced overburden pressure enhances geothermal activity, heat exchange and volatile release.

In addition to hydrological processes, loads of the Myrdalsjökull icecap have two types of variations (Pinel et al. 2007): an annual one variation of the snow cover in the central part of the volcano with an amplitude up to 6.5 m and a long term decrease of ice thickness, around 4 m/yr due to global warming.

Previous studies have concluded that GIA model could partially explain the long-term velocities observed at the volcano with some deviation from the rebound model due to variations of melting

rate at different altitude to (Spaans et al. 2014). In particular, the latter has been proposed as a possible explanation for the erratic behavior of AUST station. In other studies, (Drouin et al. 2016), the seasonal behavior has also been observed for 71 continuous GPS stations (1997-2014) around Iceland and different sources of deformation have been discussed. In particular, it has been observed that two type of signals are clearly visible in the time series, especially in the vertical component. The first one is a yearly seasonal cycle, with a peak-to-peak amplitude of the cycle ranging from 4 mm near the coast line up to 27 mm in the middle of Vatnajokull icecap. The other is a long-term motion that again can be attributed to glacial adjustment to the icecaps retreat.

Although several studies have observed a seasonal deformation (seismic, GPS, InSAR, hydrology) of volcanic areas in Iceland, there is no common conclusion on the source of the deformation.

In this chapter, I showed that the signal measured around the Katla volcanic system is complex and is characterized not only by a long-term motion and a seasonal variation of the GPS position estimates but also short-term variations that can be attributed to snow accumulation on the antenna. In section 2.2 I proposed a method to detect snow accumulation through the spectral analysis of the signal-to-noise.

AUST station reveals also a strong year-modulated signal, moving of about 2-2.5 cm on average in SW direction (toward the caldera) during the spring with the minimum value reached in March/April and it moves of about 2.5-3 cm in NE direction (away from the caldera) in the winter with maximum reached in late August/September. The rate of displacement in the summer is higher than the winter, meaning that the deformation measured by station is faster during the summer months. The vertical displacement of AUST station is out of phase of about 4 months, as the station moves of 4 cm on average in the up direction during the winter months with maximum value reached in November/December and about the same magnitude but in down direction during the summer months with the minimum reached in June.

I estimated the coherence of the seasonal deformation with different data and the analysis indicates that there is a correlation between the variation of air temperature, barometric pressure, precipitations (shorter periods) and gravity (longer period) and the observed deformation.

In section 3, I modeled the snow/ice loads as a possible source of deformation with depth varying properties of the crust and low-velocity magma chamber and a 2km thick porous layer. To fit the observed deformation of 4 cm in the vertical and 2 cm in the horizontal components, as measured at AUST station, the loss of snow/ice from the ice-cap should be of about 40 m. The current

estimates of mass balance at the Myrdalsjökull icecap only account for up to 6 meters in snow accumulation during the winter months and up to 65 cm/yr for the glacier retreat. I therefore concluded that ice/snow loading cannot explain the magnitude nor the phase of the deformation observed on the volcanic rim. I also suggested an alternative mechanism to explain the observed deformation: the freeze/melting cycles inside the pores and fractures of the rock beneath the volcano can cause change in pressure and ground deformation as well as reconfiguration of the hydrological system, with consequent circulation of geothermal gasses and fluids.

This study stresses the difficulties of interpreting the deformation of sub-glacial volcanoes, as different sources of deformation contribute to the measured signal. It then becomes necessary to carry out a thorough analysis of the observed deformation pattern at different time scales to separate different contributions and with a variety of measurements.

For future work, I recommend the installation of a camera and a meteorological station at the AUST station location to capture snow accumulation and measure weather data to compare with the spectral analysis of the SNR. And for the detection algorithm validation, I suggest this analysis to be applied to stations at different locations where similar behavior is observed.

I also suggest a poroelastic model to study the effects of melting/freezing of water inside the pores and fractures of the rocks beneath Katla volcano.

Chapter 3

Effect of multipath and obstructions on GPS observables and its application to the study of Al-Hamra tower (Kuwait) deformation

Abstract

The third project had the main goal of studying the deformation of the Al Hamra tower in Kuwait caused by thermal excursion, winds and crustal processes (e.g. seismic waves), using GPS observations. In order to detect horizontal and vertical deformation of the building, a GPS station needed to be installed near the top of the building. However, the peculiar shape of the top makes it difficult to obtain useful results. In fact, a wall of ~ 44.6 m (147 ft) height on the northern side of roof not only masks the view of satellites transiting the northern side of the sky, decreasing the accuracy in the results, but it also acts as reflector for the signal, causing a complex pattern of interferences (multipath) in the GPS measurements. While in the long-term estimates, the complexity of the signal might have a less dramatic impact, in the sub-daily estimates the loss of accuracy is significant, making difficult to detect signals coming from earthquakes or hourly motions of the building (thermic effect, wind vibrations, etc.). In January 2016, a GPS station (ALHR) has been installed on the tip of the curtain wall away from obstructions in order obtain results with reduced multipath.
In this project, we also explore the possibility of recovering the loss of accuracy due to the masking of portions of the sky and investigate different methods to mitigate the multipath in order to study the deformation of the building.

3.1 Introduction

Tall buildings are subject to different sources of deformation, such as earthquakes, wind, thermic stress that can compromise their long-term structural stability. The structural assessments of the buildings are mostly carried in the pre-construction phase through modeling, but very rarely is there a post-construction assessment to monitor the long-term behavior of these structures. This is mostly due to the difficulties and expenses of the instrumentation of these high-rise buildings. In particular, GPS instrumentations in an urban setting can be complicated by sky blockage as well as reflections of the signals from the surrounding structures, that can introduce large errors in the position estimates. In this project, the deformation of Al-Hamra tower is analyzed through 24-hours averaged GPS measurements for long term variations and though 1-Hz measurement for sub daily variations. The effects of the multipath on the GPS measurements is discussed and technique to mitigate their effects are explored. A thermal finite element model is proposed to explained the seasonal variation observed in the daily position estimate. The effect of the building will be explored, with a spectral analysis of the high rate GPS data.

3.2 GPS measurements of Al-Hamra tower

3.2.1 Al Hamra tower design and GPS installation

Al-Hamra tower is the tallest sculptured building in the world with a height of 413 m (1354 Ft) and a floor area of 195000 m^2, designed by architectural firm Skidmore, Owings and Merrill and Callison. Finished in 2011 in the central district of Sharq in Kuwait City, the tower has become an icon for the city and a symbol of innovative design, recognized as the Best Inventions of 2011 by Time Magazine. The structure consists of a square-based concrete core, framed by twisting ribbons of torqued walls, defining the iconic form of the tower. The twisting wall was primarily design to sustain an extensive glass use on the north façade to allow primary gulf views for the office tenants. The architectural design of the Al-Hamra tower was carefully considered in response to site-specific environmental and urban conditions. High-rise buildings stability is in fact affected by numerous factors, among them the response of the structure to gravity loads, creep and shrinkage

after construction, degradation of the construction material and environmental elements, such as geology of the site, seismicity, wind and thermal stresses due to solar radiation. Although some of those factors were taken into account during the planning phase and construction, others were not modeled in the original design. In particular, the effects of earthquakes and solar stresses were not considered in the structural analysis of the building (Agarwal et al., 2007).

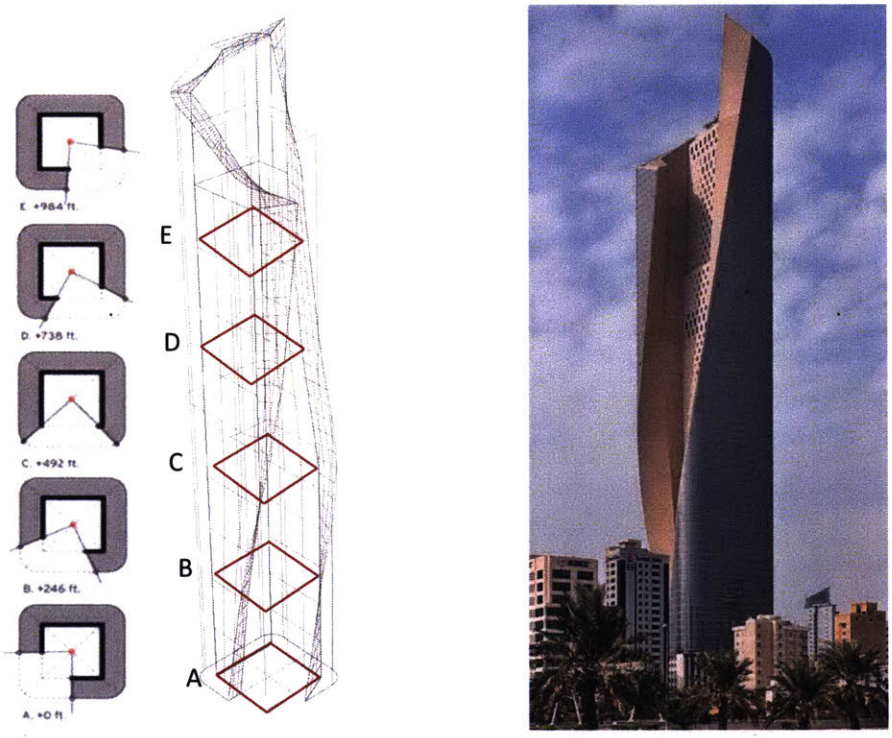

Figure 3.2.1 Al-Hamra tower floor plan and design. Modified after Haney G., 2012

In order to detect the effects of these forces on the building, we installed two GPS stations on top of the Al-Hamra tower. However, the peculiar shape of roof of the building make it difficult to obtain useful results. A wall of ~ 44.6 m (147 ft.) on the northern side of roof not only masks the view of satellites transiting the northern side of the sky, decreasing the accuracy in the results, but it also acts as reflector for signals from the south, causing a complex interference pattern (multipath) in the GPS measurements.

The setting of the GPS stations on the tower has been affected by different reasons. From a technical point of view, the best GPS configuration would have been in a setting free of

Figure 3.2.2. Al-Hamra terrace GPS sites (TER2 and TERR) located at different distances from the western wall to investigate the effects of multipath. Photos by *Thomas Herring.*

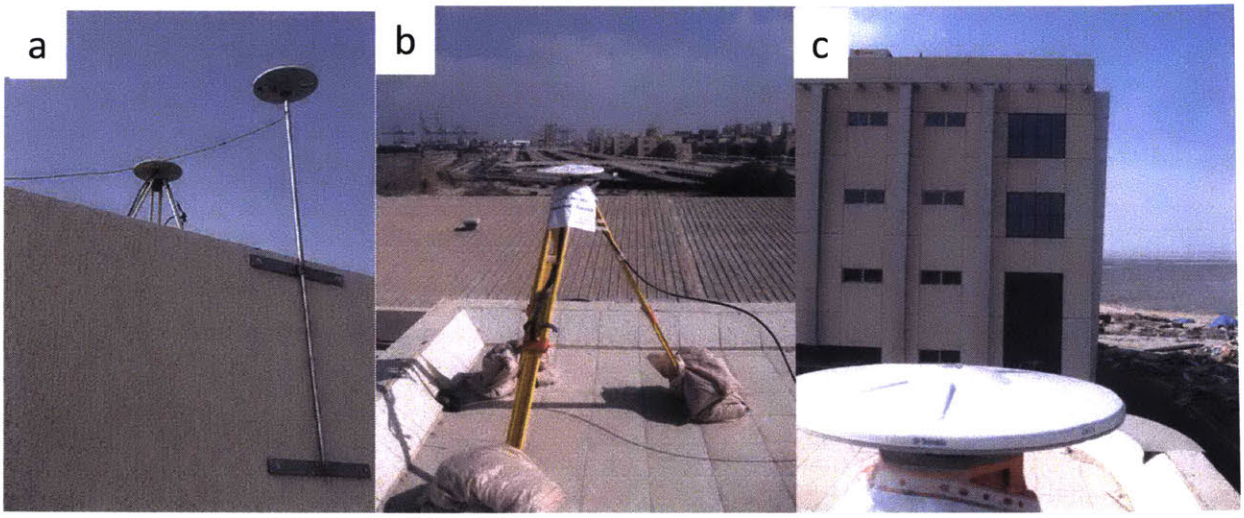

Figure 3.2.3. KISR GPS site located on the roof of the *Kuwait Institute for Scientific Research.* The site is partially obstructed on the north side by another building (*c*). KISR site was installed as a reference station for the high frequency GPS analysis. Permanent installation (*a*) and temporary installation (*a, b*). Photos by *Thomas Herring.*

obstructions, with a solid monument able to prevent the falling of the antenna caused by high winds at the top levels of the building and with the possibility to set up telemetry to avoid manual download of the data and to run long cables for power. Considering all these factors, the area proposed to set the GPS antenna was the tip of the building, which would have required an

installation of a long rod fixed to the wall and long power cables. However due to esthetic reasons, the Al-Hamra tower management didn't initially agree to install one of the GPS at the very tip of the wall (where there were no obstructions). Only a temporary installation at the 80th floor terrace with tripods was initially allowed.

In November 2014, one station was set on the 80th floor with a tripod and one on the roof of the mall (first floor) to test differential GPS, used to obtain the 1Hz solutions for high frequency responses. Afterwards the second GPS was moved to the top terrace at a distance of ~ 5 m from the other antenna to investigate the effects of the interference from the wall at different distances from it. In January 2016, the Al-Hamra management agreed with the top wall installation and one of the GPS station was moved on the edge of the curtain wall, while the other remained at the 80th terrace with a temporary installation (fig. 3.2.4). The ALHR site is mounted on top of 1'' diameter and 4.5 m long stainless steel rod, bolted to the wall façade by four clamps at 1 m distance intervals. Both Al-Hamra sites were later equipped with telemetry. The 80th floor site is now being moved to the top of the mall, located on the ground floor of Al-Hamra tower and will allow direct measurement of the differential motion between the bottom and top of Al-Hamra in the event of a large earthquake. The mall site was tested for two weeks at the beginning of the project.

Another GPS antenna was installed on the roof of KISR building as reference site. Unlike for the terrace site, the sky view at this site is clear except for some obstructions from a building to the North-West (fig 3.2.3, right). Also this station, initially sitting on a tripod, was later fixed to the

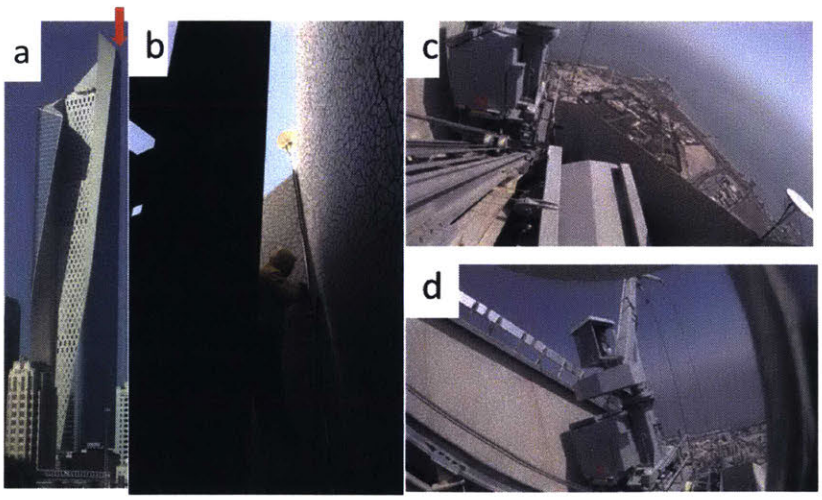

Figure 3.2.4. ALHR GPS installation site. (a) location on the tower (b) the 86th floor Al-Hamra installation with (c) and (d) showing views from the level of the Al-Hamra 86th floor site. Photos by *Thomas Herring.*

building with a permanent monument in November 2016. For the analysis, a permanent station run by the Kuwait University has been used (KUWT gps site).

3.2.2 GPS processing and results

Three separate analyses have been performed to detect different sources of deformations. The processing has been performed using the software package GAMIT/GLOBK to analyze 30s data and the TRACK module to analyze the 1Hz data (Herring et al., GAMIT and GLOBK *Reference Manual, 2015)*.

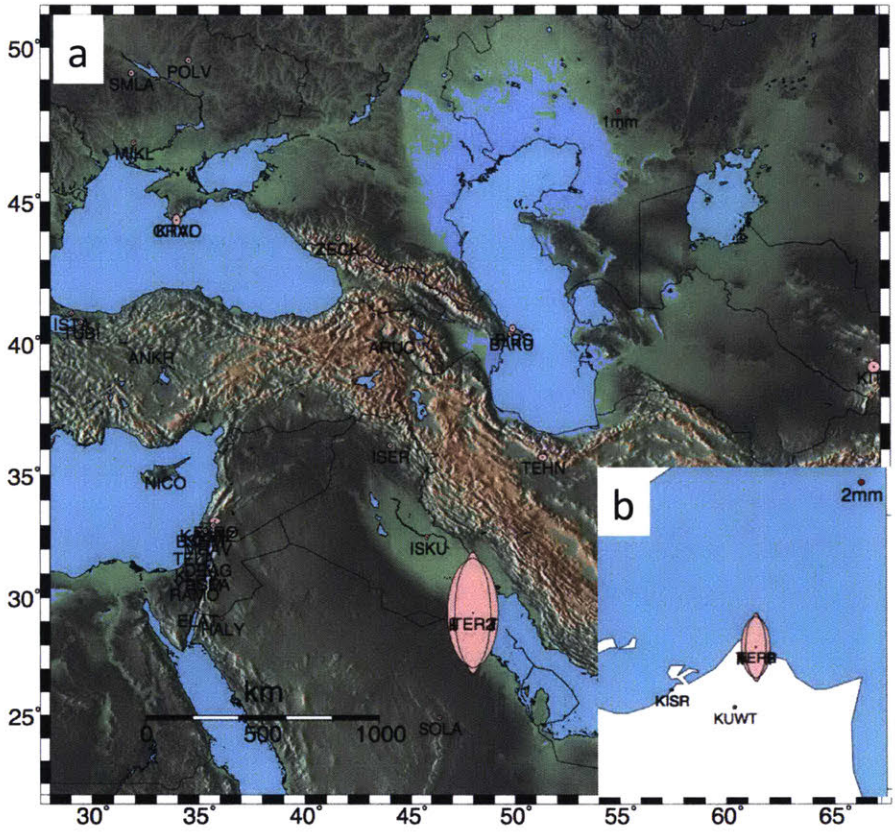

Figure 3.2.5 (a) RMS scatter map of the 20 GPS stations around the Gulf area. Pink ellipses show the RMS scatter of 24 hrs-averaged position estimates. The red circle is the measure unit of 1 mm. While most of the stations used in the analysis show an RMS of about 1 mm, the main terrace sites show a larger scatter. (b) Close-up of the Kuwait GPS stations: TERR has a larger scatter compared to KISR and KUWT stations.

Two approaches have been used to process the 30s data: (a) 24 hrs averaged analysis in which a single position is estimated for the GPS antenna from 24 hours of data and is used to model the

long-term seasonal variations of the building; (b) 6 hrs averaged analysis in which the position is estimated from 6 hours of data with 3 hours of overlap and is to detect sub-daily variations. Both analyses account for the sub-daily tidal motions of the sites. As regional framework, 20 stations from around the Gulf area and Europe have been used in the daily and sub-daily analysis.

The four stations of the Kuwait area have very different performance: while the Kuwait University sites and the KISR sites have good RMS after processing, the two main terrace sites (TERR and TER2) have larger errors due to the obstructed sky view and multipath signature in the signal due to the proximity of reflection surfaces. In fact, the phase residuals of these stations are larger and present high frequency patterns, as expected by reflected signals. A sky map of the residuals shows

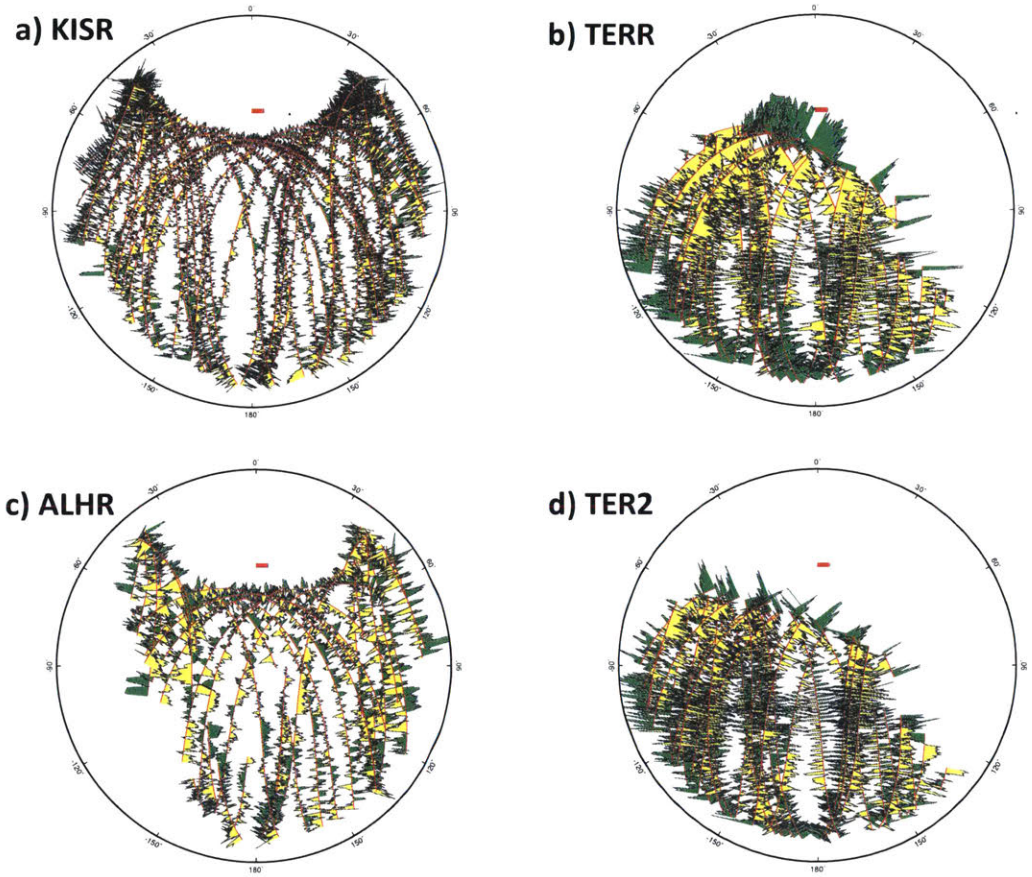

Figure 3.2.6 Sky plots of the phase residuals of the four Kuwait stations for Feb 22nd, 2016. (a) KISR, (b) TERR, (c) ALHR and (d)TER2. The RMS are respectively 7.8 mm, 17.7 mm, 10.8 mm and 15.5 mm. TERR and TER2 phase residuals are characterized by high frequency signals, resulting from reflections on the surrounding walls. Red bar indicates 20 mm.

also the partially obstructed sky (fig.3.2.6). The empty spaces on top of the sky plots represent an

unmapped portion of the sky, due to the inclination of the satellite orbits (55° inclined plane). In ALHR site (fig. 3.2.6-c), no signal is present on the west side due to sky masking by the edge of the curtain wall; while in TERR and TER2 the signal is mostly masked on the east portion and to a less extent on the west portion of the sky (fig. 3.2.6-b and d). The RMSs for day Feb 22nd 2016 are larger in TERR and TER2 (respectively 17.7 mm and 15.5 mm) compared to ALHR site (10.8 mm) and KISR site (7.8mm).

3.2.3 Daily GPS position estimates

Almost two years of data from the Al-Hamra terrace (temporary) sites and reference stations (KISR and KUWT) and one year for Al-Hamra top site (ALHR) were processed for the daily position estimates and they are shown in the figures below. Al-Hamra terrace experiences very strong winds that have disturbed the GPS antennas by blowing it over and tilting it against air conditioning vents near the antennas. In the following figures (3.2.7-3.2.11), the green vertical lines show the times when the antennas were partially blown over. The position offsets in the time series are of the order 10-20 cm and have been removed from the time series. The gaps in the data were due to either the equipment being removed or due to power failures in the circuit delivering power to the receiver. TERR and TER2 measurements are partially affected by multipath and sky blockage, as it is clear from the RMS compared to the other sites and the motion compared to the new site (ALHR). These data indicate that the terrace level, approximately 370 m above ground level is moving abut ±15 cm North-South with an annual frequency. The furthest south motion coincides with late January while the height of the building is its biggest and the western motion is furthest. KISR site performance has been inconsistent: the quality of the data was good at the beginning of the acquisition with low errors on the estimates and then it degraded for most of 2015. After a hard reset, the quality of the data has improved again. It has been established that the poor performance was related to power issues, which has been avoided with a permanent installation in November 2016. The KISR site shows also a seasonal motion, but lower in magnitude compared to ALHR and TERR sites.

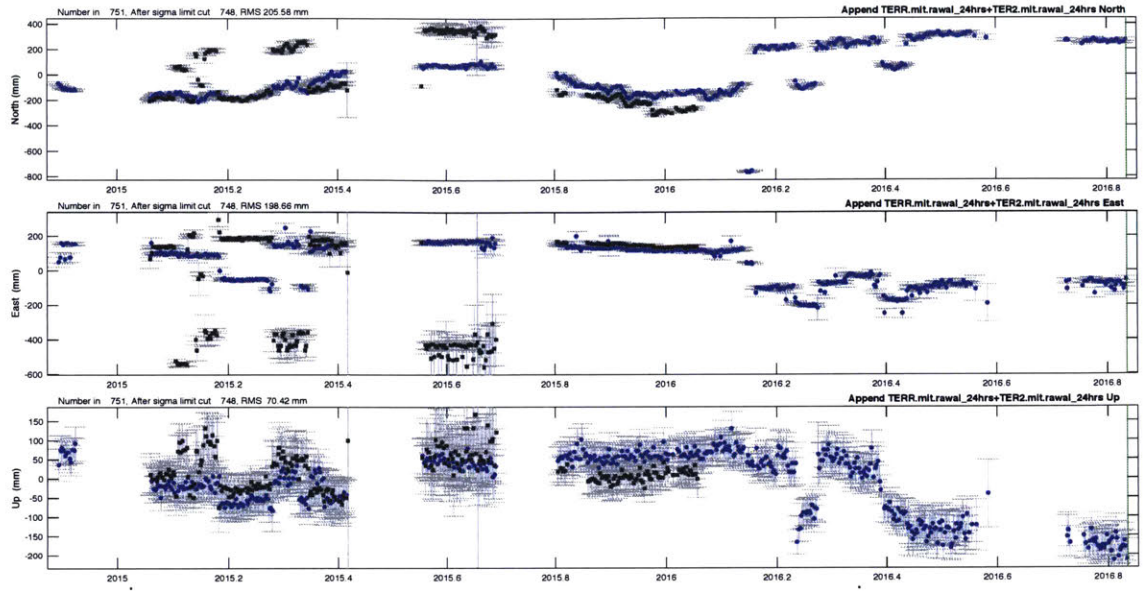

Figure 3.2.7: TERR and TER2 sites 24-hr averaged results. The numerous gaps are consequent to the blowing of the antenna by the wind or by power failure. The panels show (*top*) North (*middle*) East and (*bottom*) height position estimates with mean values removed. One standard deviation error bars are shown.

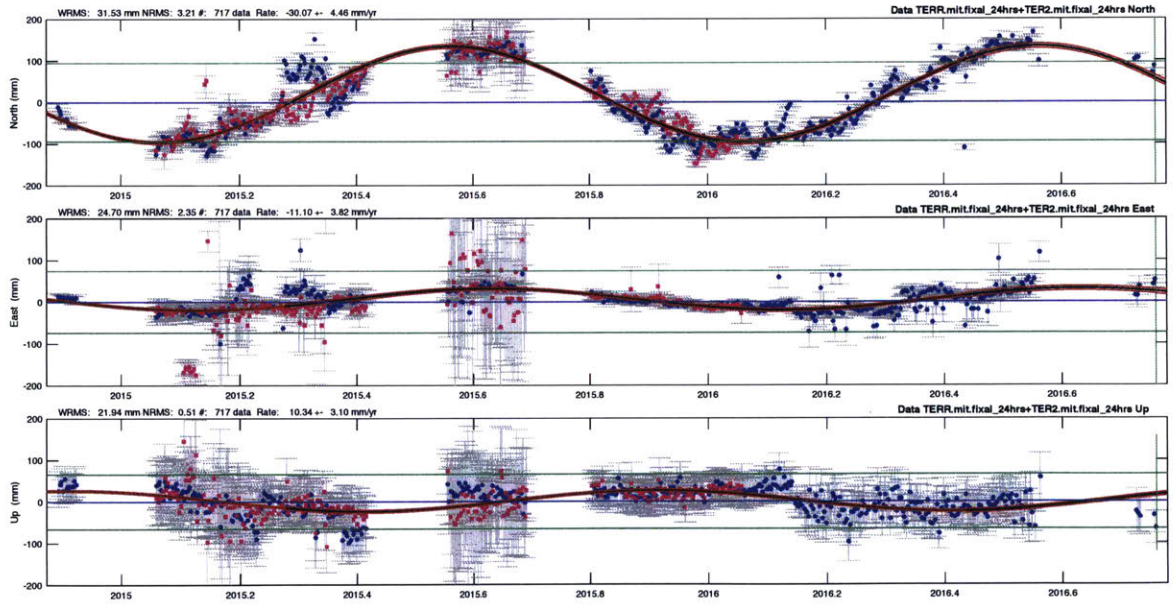

Figure 3.2.8: Estimate of the daily-averaged position for TERR (*blue*) and TER2 (*magenta*) with estimates of the offsets removed. The panels show (*top*) North (*middle*) East and (*bottom*) height position estimates with mean values removed. One standard deviation error bars are shown.

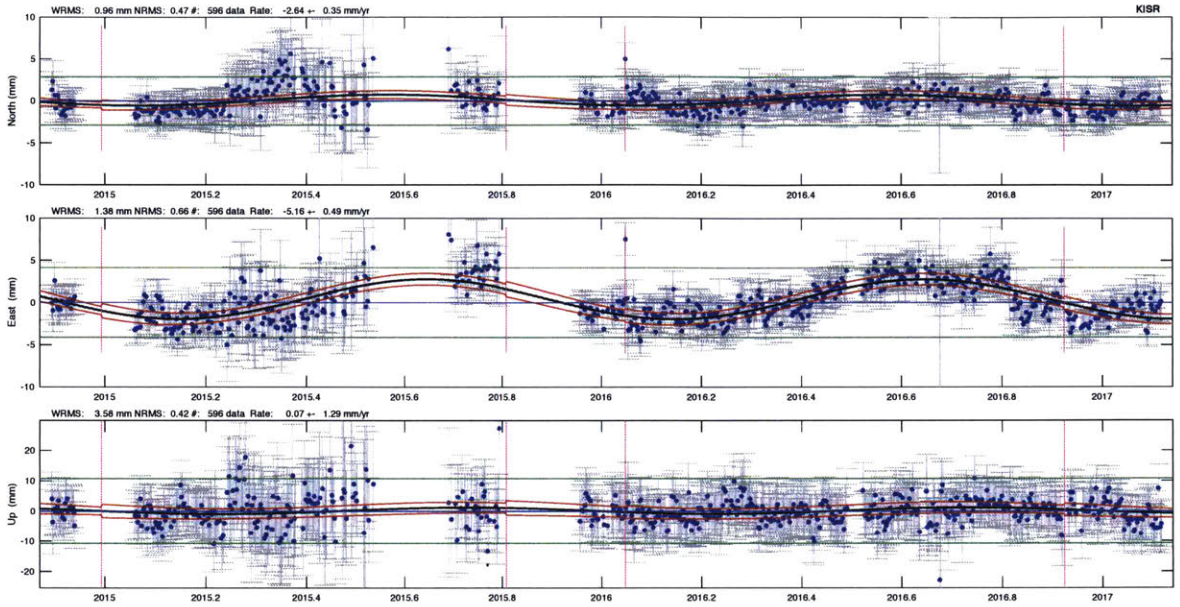

Figure 3.2.9: Estimate of the daily-averaged position for KISR reference site. The panels show (*top*) North (*middle*) East and (*bottom*) height position estimates with mean values removed. One standard deviation error bars are shown.

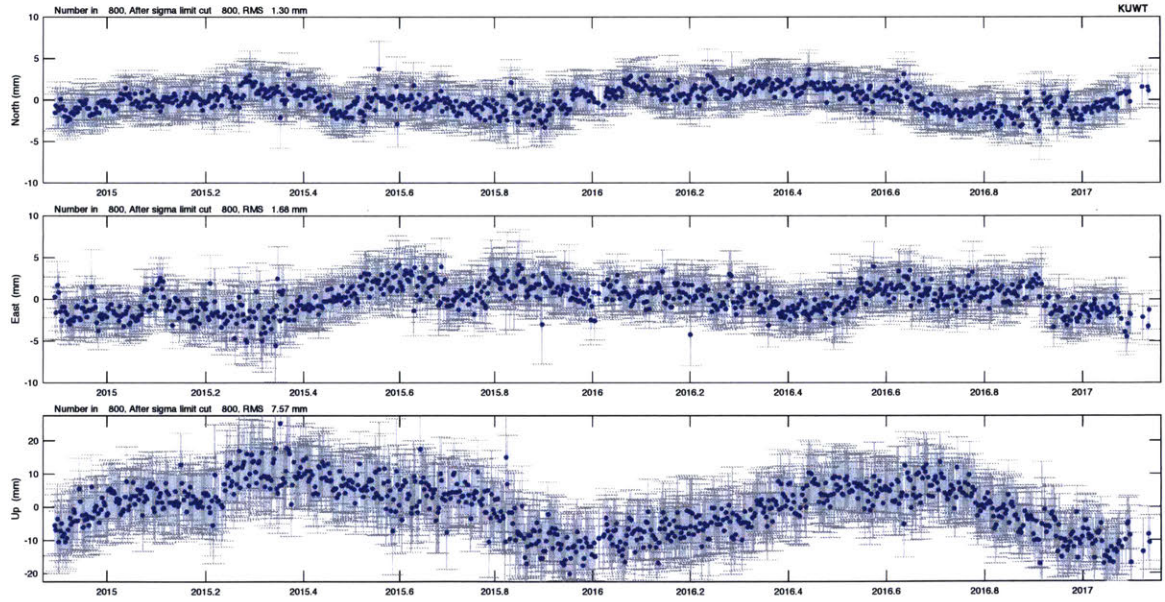

Figure 3.2.10: Estimate of the daily-averaged position for KUWT reference site. The panels show (*top*) North (*middle*) East and (*bottom*) height position estimates with mean values removed. One standard deviation error bars are shown.

Data from the Kuwait University site (KUWT) have been processed. At the beginning of 2016 the station has stopped transmitting data and started transmitting again in April, making the processing more difficult due to the low number of nearby stations. The missing data have been recently retrieved and included in the processing. KUWT site has a permanent monument and the quality of data is good (fig. 3.2.10), with low RMS on the position estimates. KUWT also shows a seasonal motion of few mm (10 mm N and E components and 15 mm Up component).

Data from the newly installed site ALHR have been processed starting on January, the 22nd 2016. The 24-hrs averaged solutions for ALHR station present a better RMS scatter compared to the main terrace sites (TERR and TER2), as the multipath effect is significantly reduced. Also ALHR shows a seasonal motion with southernmost motion in mid-winter and lowest height of the building. The results show a seasonal motion generally in agreement with the main terrace sites estimates, confirming that the position variations are largely an estimate of the true motion of the building. However, a comparison between the Al-Hamra sites shows that there are differences in

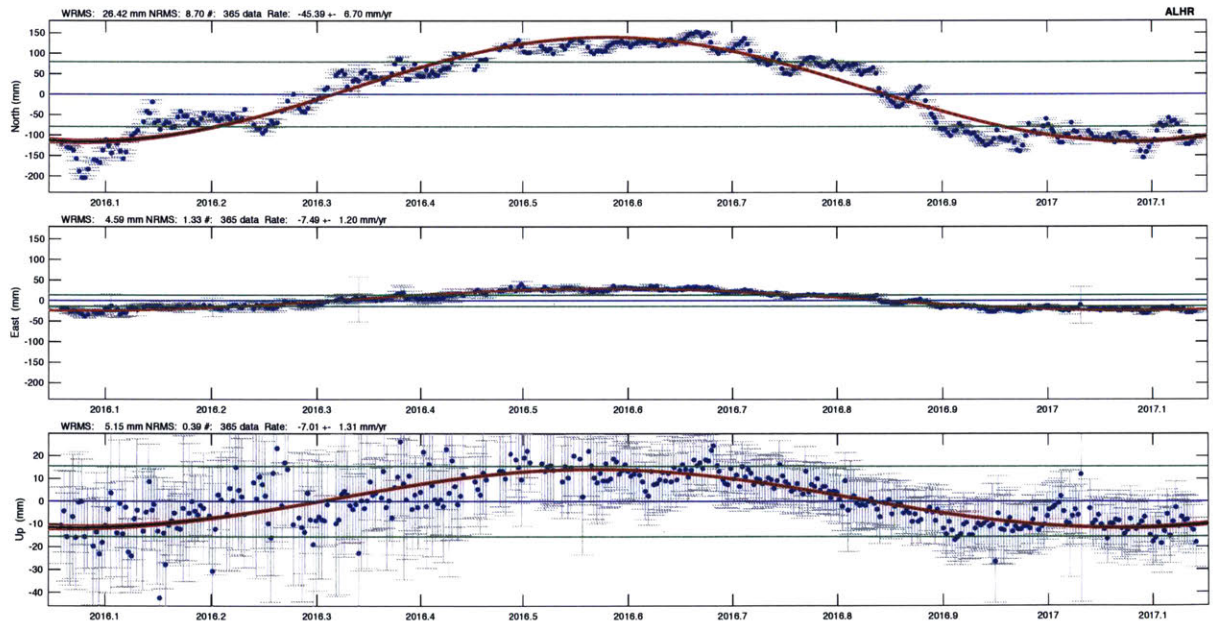

Figure 3.2.11: Estimate of the daily-averaged position for ALHR. The panels show (*top*) North (*middle*) East and (*bottom*) height position estimates with mean values removed. One standard deviation error bars are shown.

the measured deformation: the peaks are in NS (fig. 3.2.12) and EW motions are earlier in ALHM sites, while the Up component is inverted.

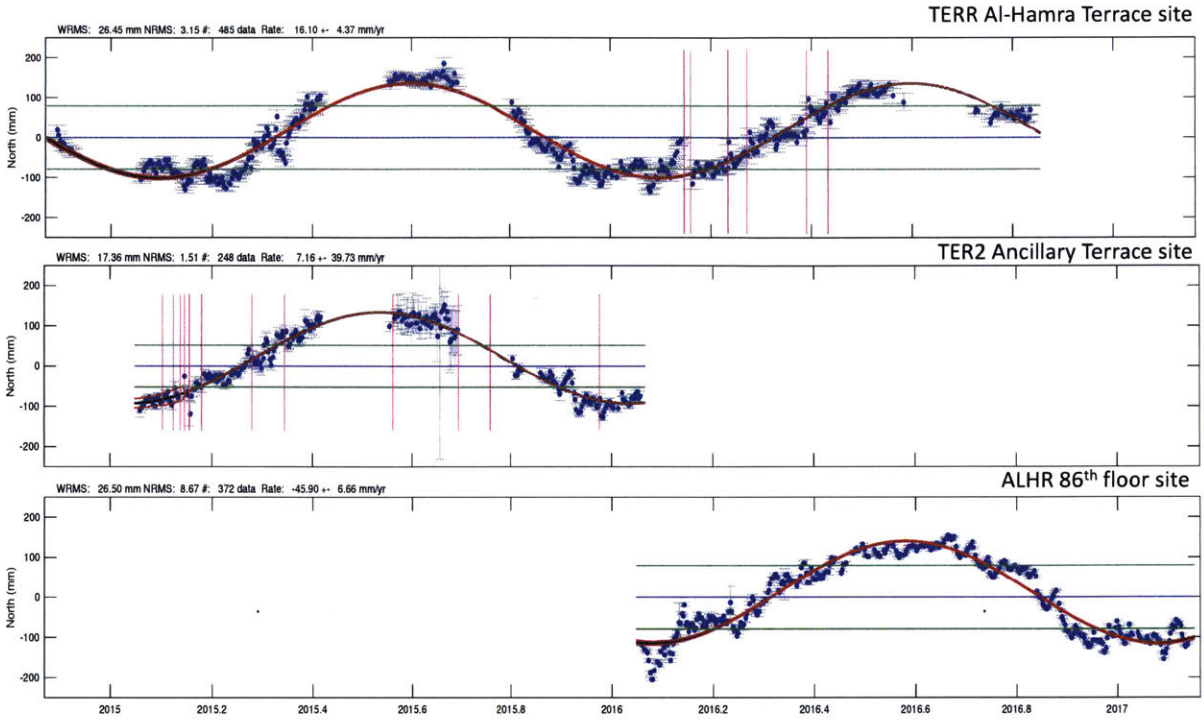

Figure 3.2.12: Comparison between the north component of TERR (*top*), TER2 (*middle*) and ALHR (*bottom*). TER2 was moved to the semi-permanent installation on the 86th floor (ALHR).

3.2.4 Sub-Daily GPS position estimates

For sub-daily motion estimates, the data were averaged over 6 hours period with overlaps of 3 hours to include enough data in the hourly position, therefore an acceptable RMS scatter in the solution. The sub-daily estimates are more heavily affected by the multipath and sky blockage. In fact, the GPS position presents larger errors on the estimate at a specific time of the day for the TERR and TER2 site. The TER2 site has a better RMS compared to TERR, being further away from the reflective surfaces. The new site ALHR on the tip of the building gives better accuracy, being less affected by the surrounding reflectors.

On a closer look to the 6-hours solution for the main terrace site, it can be noted that the position estimate has a larger error at specific moment of the day (specifically around noon and on a lesser extent at midnight for east and north component and at midnight for the up component) and occasionally over an extended period, if the weather conditions change. This can be due to both multipath and to a poor sky configuration of the satellites. After shifting the positon of 6 months

and 12 hrs, it can be noted that most of the larger errorbars coincide, suggesting a poor sky configuration at that time of the day (fig. 3.2.12). The signature of the multipath will be discussed in a later section.

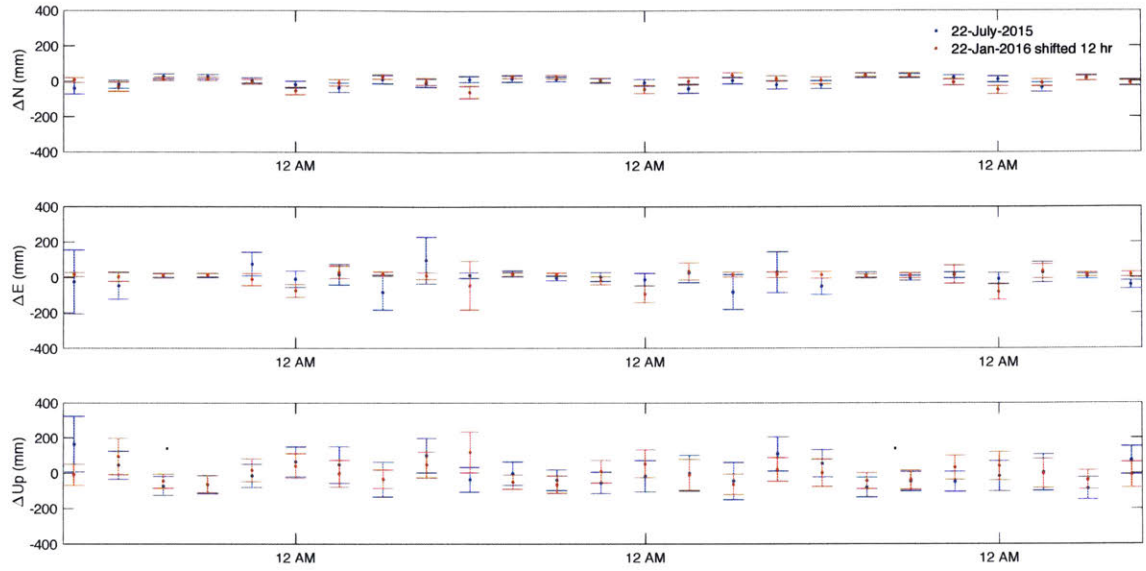

Figure 3.2.12: TERR 6hr solutions on 22-July-2015 at 8:58:59 and six month later (22-Jan-2016 at 8:58:59). Some of the larger error bars repeat after 6 months and12 hours shift as it would be expected it they were result of the satellite configuration.

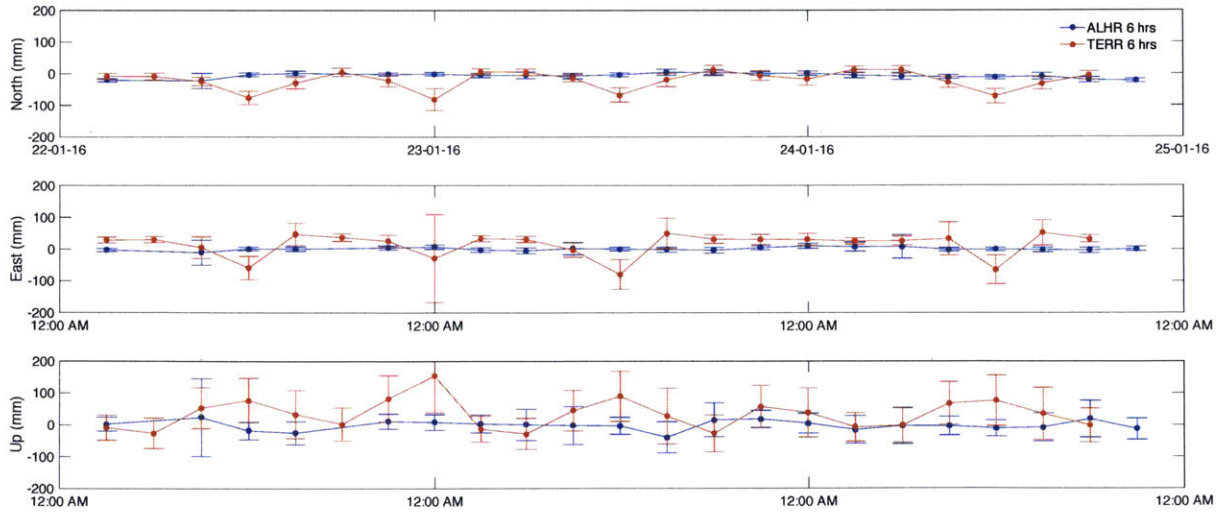

Figure 3.2.13: Comparison between ALHR (*blue*) and TERR (*orange*) 6-hours averaged solutions. TERR solutions are affected by larger errors in all three components, due to the effects of multipath and blockage of sky at certain times of the day.

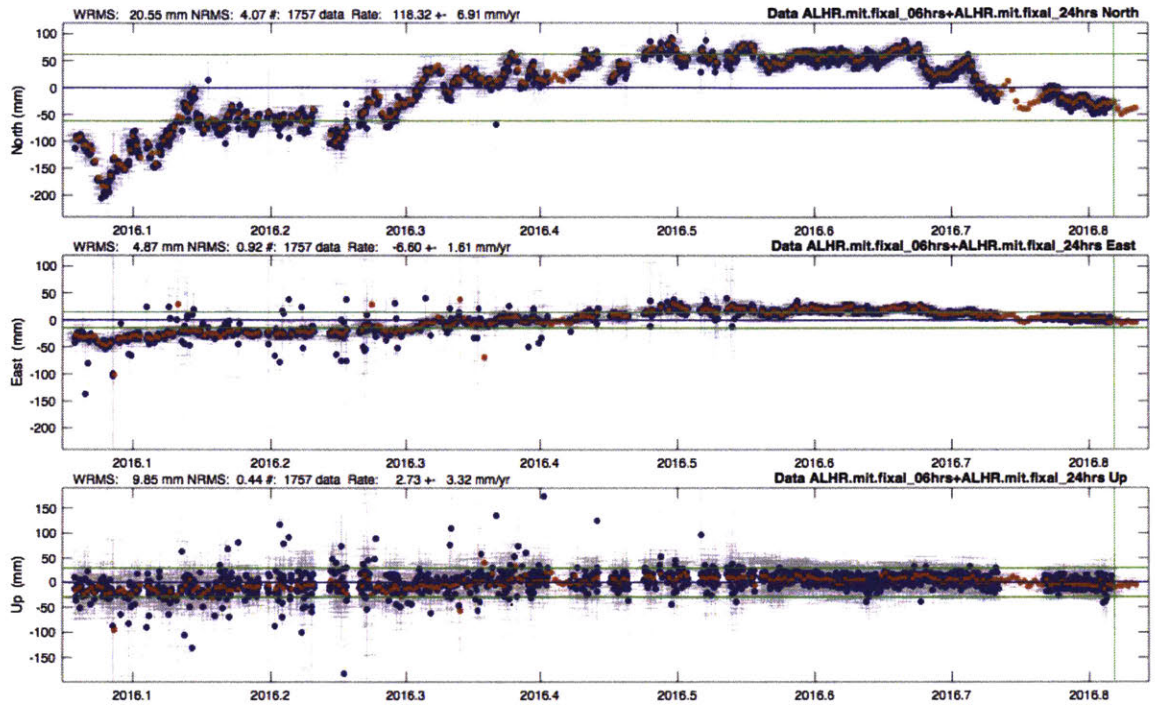

Figure 3.2.14: ALHR 6-hours (*blue*) and 24-hours (*orange*) averaged solutions, showing a distinct sub-daily deformation pattern overlapped by a seasonal pattern. Prior to August 2016, ALHR data show large gaps for unclear reasons. A hard reset of the receiver fixed the issue.

Although a comparison between the TERR and ALHR sites shows that for a sub-daily estimate a better solution can be achieved when the surrounding is free of obstacle or reflective surfaces, both stations reveal a distinct sub-daily deformation pattern, overlapped by the seasonal pattern showed by the daily-averaged solution.

3.2.5 1Hz estimates

In order to detect high frequency components in the GPS signal, such as earthquakes or wind, 1Hz data have been collected and processed using a kinematic technique with the module TRACK from the GAMIT/GLOBK package. The technique is based on the use of carrier measurements and the transmission of corrections from the base station, whose location is well known, to the rover, so

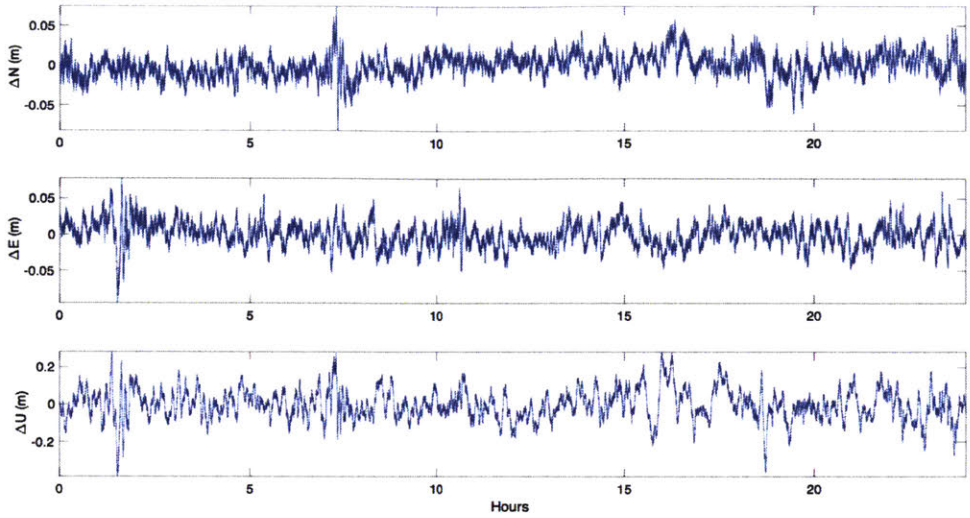

Figure 3.2.15: ALHR 1Hz solution for doy 215 year 2016. The north and east component moves few cm through the day, while the vertical component shows larger displacement. The Up component is 4 times the horizontal components.

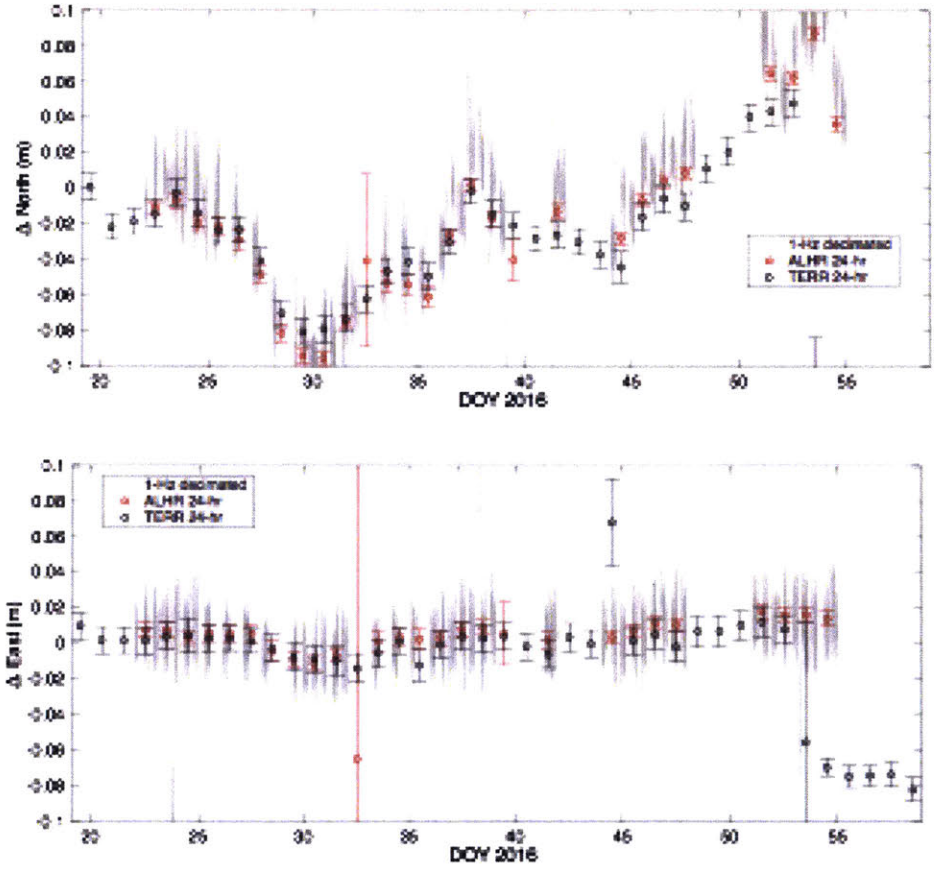

Figure 3.2.16: ALHR 1Hz solution overlapped by the 24hr solution and TERR 24hr solution for North and East components. The high frequency solution track the same deformation as the daily-averaged one.

that the main errors that drive the stand-alone positioning cancel out. In our analysis, we used

KISR site as base station, as relatively stable, and the Al-Hamra stations and Kuwait University stations as rover stations. As the stations are relatively closed to each other (<2-3 km), ionospheric delay can be treated as zero and L1 and L2 ambiguity can be resolved separately. The results from 1Hz data show a motion of a few cm a day in the North and East component, while the vertical component has a higher level of noise (fig. 3.2.15). In fig. 3.2.16 the comparison between 24hr average solution and 1 Hz solution is shown, revealing the same deformation pattern for the high frequency and daily solutions. The TERR site 1Hz solution is affected by multipath and sky-blockage, resulting in a corruption of the position estimate with long period signals (fig. 3.2.17) reflecting from the surrounding objects. In the next section, the spectral analysis of the track solutions will be discussed, as well as mitigation of the multipath through filtering of the 1Hz solution.

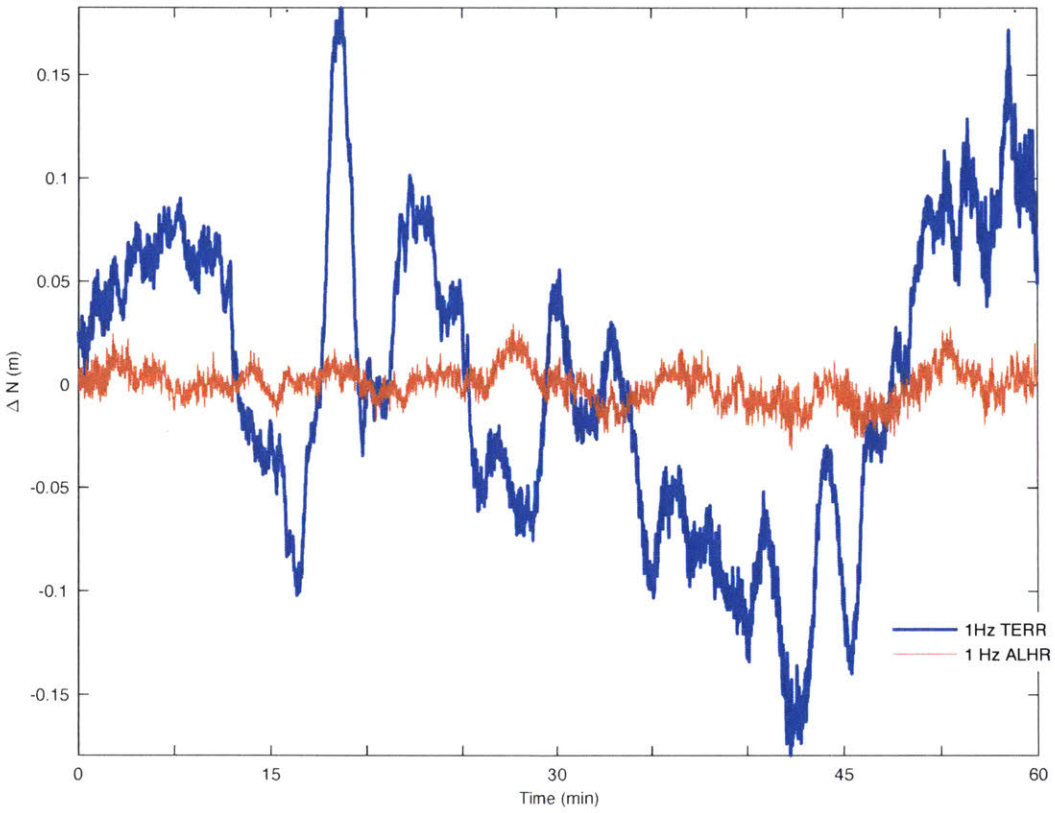

Figure 3.2.17: Comparison of the TERR (*blue*) and ALHR (*orange*) 1Hz solutions for the North component. The TERR estimate is affected by multipath as revealed by the presence of large long-period signals.

3.3 Multipath analysis and mitigation

3.3.1 Introduction

Although most of the error in GPS measurements are eliminated or minimized by differencing techniques (Leick 2004), multipath error still remains due to the highly-site specific nature of the reflection of GPS signals from nearby surfaces. Multipath is a distortion of the direct line-of-site satellite signal by localized reflected and/or diffracted signals (fig. 3.1.1). Multipath is characterized by:

- time delay relative to the LOS (additional propagation path)
- change in amplitude related to the reflecting surface
- phase rate of change related to the additional path length and the electrical properties of reflecting/diffracting surface
- change in the polarization of the signal

Multipath is often considered one of the most limiting factors in high rate GPS positioning (Axelrad et al. 1996): short term positions are subject to quasi-periodic errors with characteristic

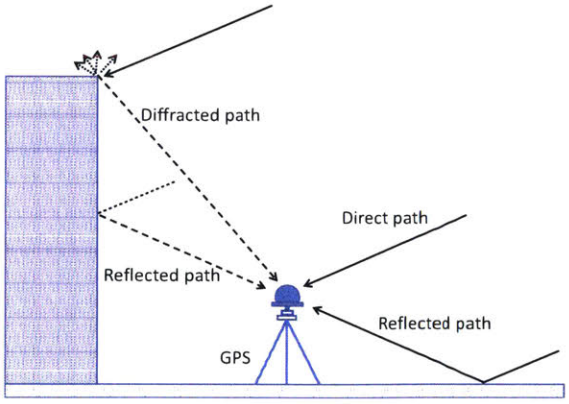

Figure 3.3.1 Multipath reflected and diffracted path

time-scales varying from seconds to minutes depending on the satellite-reflector geometry. Long-term positions can also be affected, where multipath can alias into periodic errors at annual and semi-annual periods (Penna and Stewart 2003).

When the reflector is close, the multipath will vary slowly; if it is distant, the multipath will rapidly change and will average to zero quickly.

Several techniques have been tested to reduce the effect of multipath on the GPS signal. The use of choke-ring antennas or special architecture receivers with built in multipath mitigation techniques eliminates much of the code multipath, leaving carrier-phase multipath still dominant, which is more embedded and harder to mitigate source of error (Van Dierendonck and Braasch 1997). More recent techniques have focused on post-processing stages through wavelet analysis, filtering or weighting data using signal-to-noise ratio (SNR) (Lau and Mok, 1999).

To recognize the multipath signature, several multipath unique features can be exploited. One of those is the repeatability of GPS constellations: they repeat themselves approximately 24 sidereal hours with adjustment for the precession of the nodes of satellite orbits (Herring et al., 2016). As the reflective surfaces causing the multipath effect are stationary, then if a particular satellite's transmission is reflected to produce a multipath effect, then that same long-period trend will reappear about 246 s earlier each day as that satellite passes by.

The first feature is the consistency of multipath frequency content in both the N–S and E–W displacements. The displacements of a structure in its local N–S and E–W coordinate system is determined by tracking the arrival time of transmissions from individual satellites (Kijewski-Correa et al., 2006b). When a transmission undergoes multipath reflection, both the original transmission and a delayed version are received by the GPS unit. The delay introduces a distortion that has a distinct periodicity, which infiltrates the displacement estimates along both of the local coordinate axes. Thus, any distinct harmonics that are well beneath the natural frequency of the structure and appear in both the N–S and E–W displacement estimates are likely associated with these multipath effects.

In our study, the 24 hours-averaged solution is somewhat affected by multipath and has been tested by comparing the solution with the new top site, ALHR (better geometry and far from reflectors) and by running tests on satellite constellation geometry changes.

For the sub-daily solution, multipath becomes prominent, corrupting the accuracy of the main terrace site solution. The effects of multipath have been investigated with the analysis of the estimated phase residuals.

We used a spectral analysis to recognize the repeatability of the multipath signal from a sidereal day to another and in a spatial sense between the two main terrace stations and to calculate the frequency content of the multipath signal. Once determined the nature of the multipath, the phase

changes were modeled in the antenna phase center models and included in the processing of the data.

3.3.2 Spectral analysis of GPS phase residuals

The phase residuals for the four GPS stations (TERR, TER2, KISR and KUWAIT) have been analyzed in order to understand the multipath effects on the signal. The signal showed different patterns and characteristics in each station (fig 3.3.2).

In particular, the two terrace sites show high frequency signals that are not present in the KISR and Kuwait sites where there are no major obstructions to the signal. Due to the vicinity of the reflecting objects on the roof of Al-Hamra tower, we expect the reflections and refractions to

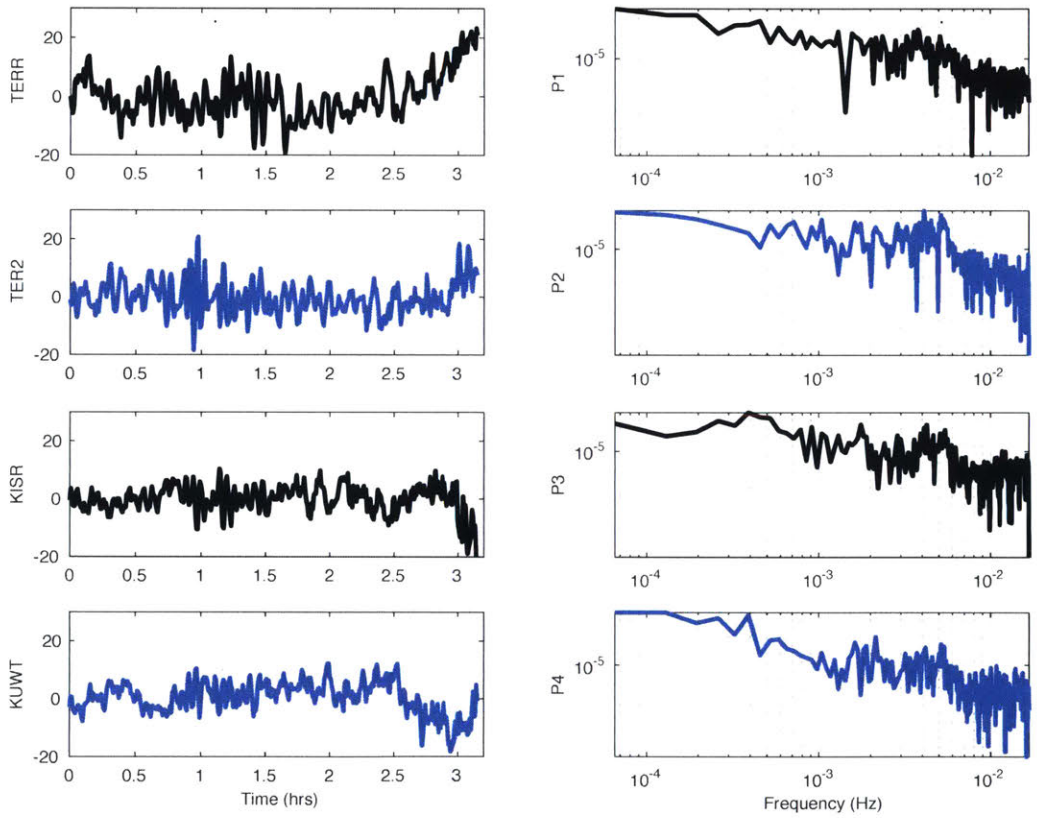

Figure 3.3.2 *On the left*: Phase residuals in mm for the TERR, TER2, KISR and KUWT sites for satellite PRN 24 on January 22nd, 2015. *On the right*: Power spectrum of the signals. In the TERR and TER2 most of the energy of the signal is in the 10-4 range.

produce high frequency signals that can also be complicated by atmospheric delay variation and

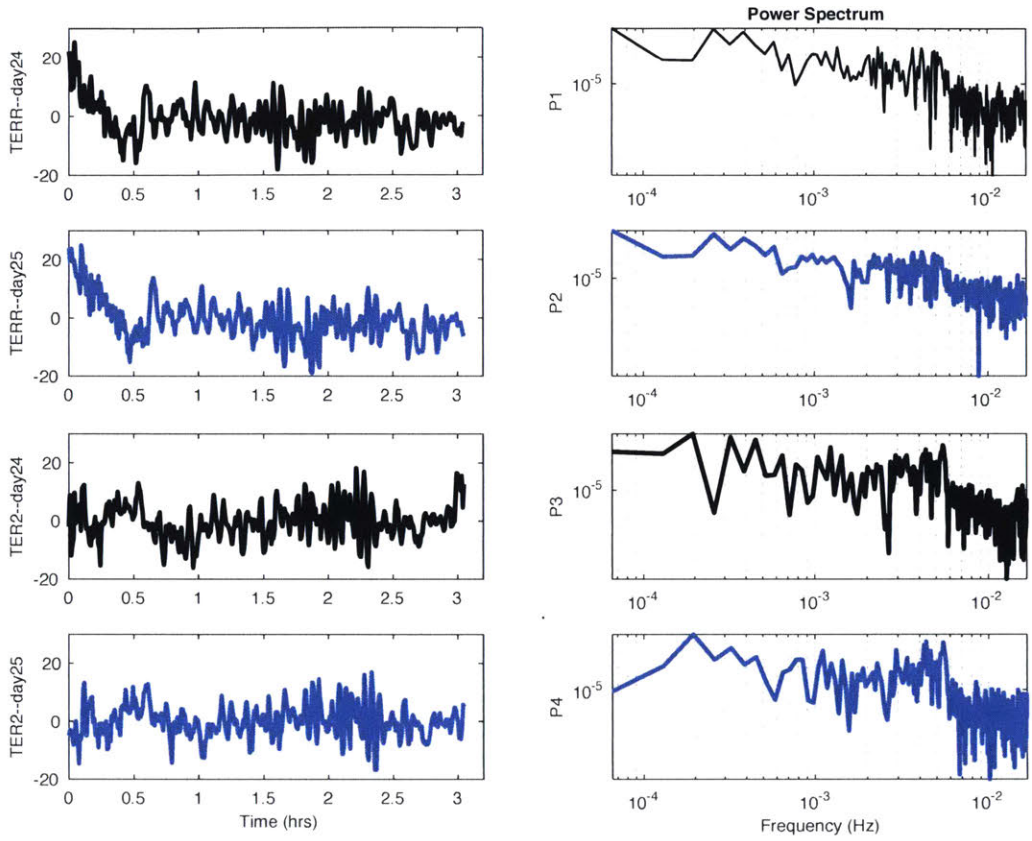

Figure 3.3.3: *On the left*: Phase residuals in mm for the TERR and TER2 for Jan, 24th 2015 and Jan, 25th 2015 for satellite PRN 24. *On the right*: Power spectrum of the signals. The signal for both TERR and TER2 repeats from a day to another with slight differences. In the spectra, we observed peaks at 3 and 4 min.

motion of building. However, if the environmental conditions don't change (meaning that the building doesn't move or the weather doesn't change), the multipath signal will repeat in the exact way from a day to another while the signal coming from the building or the atmosphere will change. In order to understand which part of the high frequency signal is due to multipath or to other sources (atmospheric effects, building motions), we analyzed the phase residuals for the two terrace stations for consecutive days (fig. 3.3.3 and fig. 3.3.4). For four consequent days, we found that the signal repeats with a time shift consistent with approximately the sidereal day shift, but there is a complexity associated with the atmospheric delay variation and possible motion of the building (fig. 3.3.5). The power spectrum reveals long period signals at ~1 hr, ~ 40 min and ~28 min at TERR sites for both Jan 24th and 25th, but stronger on the latter day (fig. 3.3.4). These signals are present also in TER2, but they are weaker and with a difference of 6-7 s (TER2 are

shorter). The shorter period signals are present in both stations with power spectrum of comparable magnitude. The peaks are at ~3 min, ~4 min and ~10 min (fig. 3.3.4).

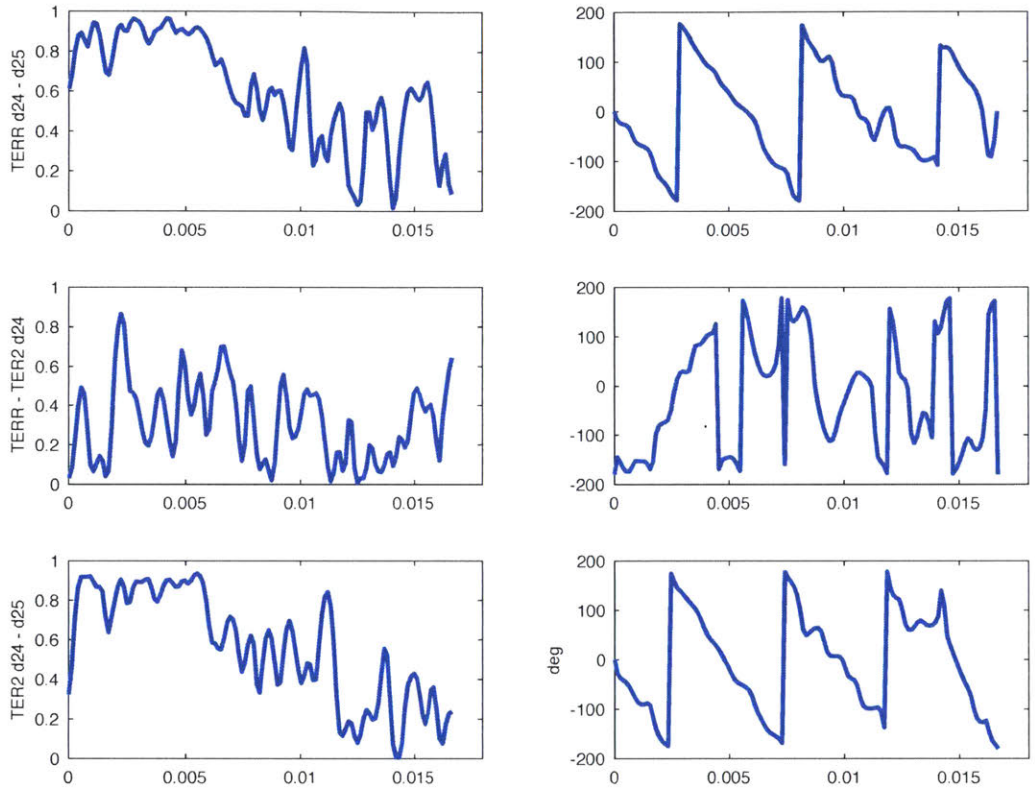

Figure 3.3.4 On the left: Coherence estimates for the TERR and TER2 for Jan, 24th 2015 and Jan, 25th 2015 for satellite PRN 24. On the right: Cross spectrum phase. The signals are highly coherent for different days at the same station, while the coherence between the two terrace sites for the same day is low. The cross spectrum for the same station at different days have steps due to the sidereal shift of the satellite

The coherence estimate for the TERR and TER2 on the two consecutive days reveals that the signals are highly coherent for different days at the same station but shifted of a time approximately equal to the sidereal day (~ 246 s difference), while the coherence between the two terrace sites for the same day is lower (fig. 3.3.4) with peaks at 7 min 4 min and 3 min.

The spectral analysis of the new site ALHR reveals that the high-amplitude/high-frequency signals characterizing the TERR site residuals are not present in the new site and the frequency content between the two station is very different. The signal for both ALHR and TERR repeats from a day

to another with slight differences. In the spectra, we observe long period signals in both sites at ~2 hours and short-period signals at 9 min, 4 min and 3 min for TERR site and 6 min for ALHR site. The power spectrum of TERR site is however one order of magnitude larger than ALHR site, with more energy at lower frequencies (fig 3.3.6). This suggests that the high-frequency/high-amplitude signals in the main terrace site are very likely to be related to multipath effects, that can therefore be partially removed through filtering and modeling of the phase residuals.

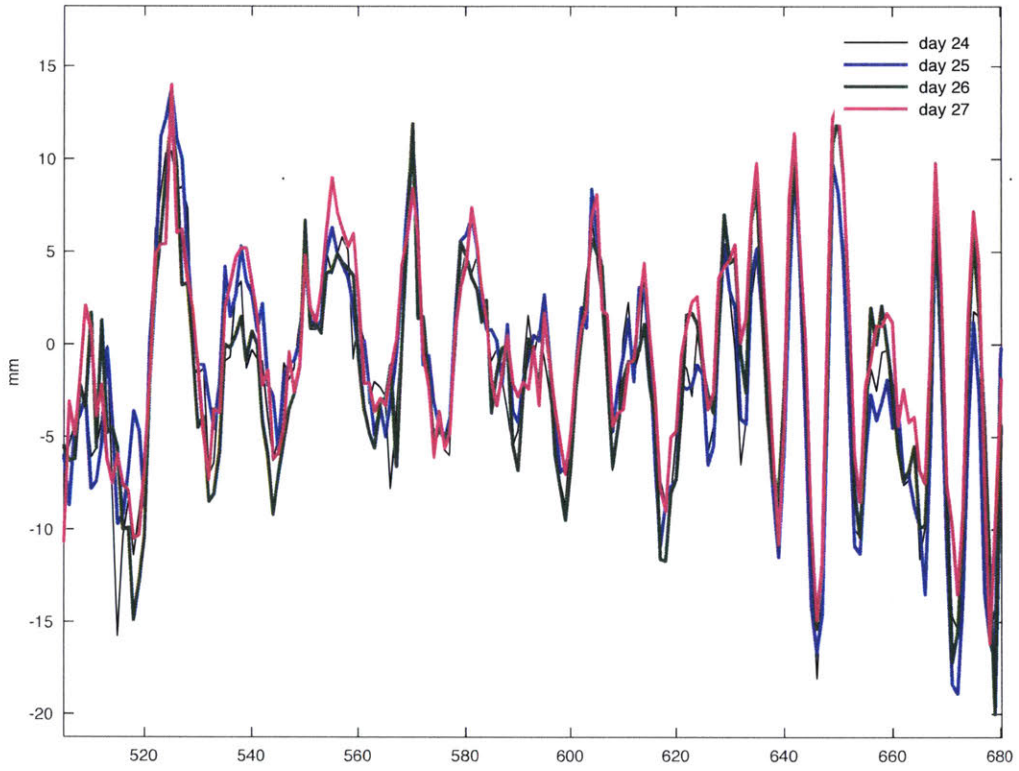

Figure 3.3.5 Overlapped phase residuals for four consecutive days for TERR site. The signals have been shifted for the sidereal day and show a good match from a day to another. However, there are subtle differences between the signals changing between the four days, possibly due to atmospheric delay variations and building motions

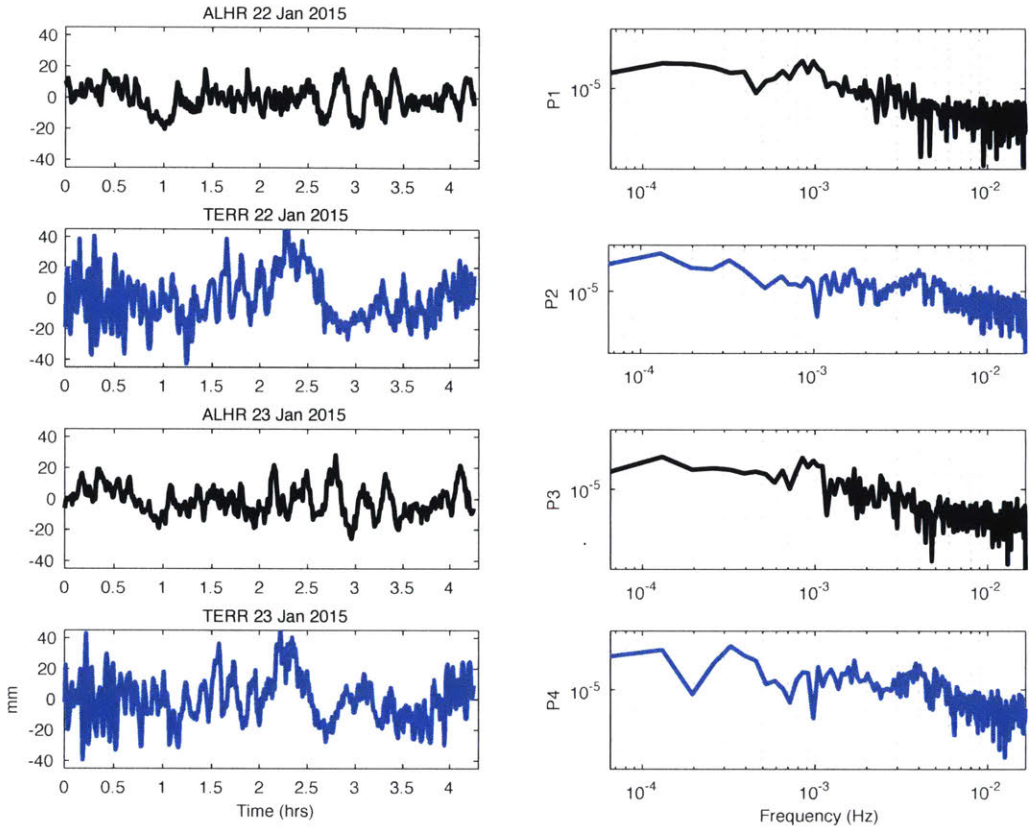

Figure 3.3.3: *On the left*: Phase residuals in mm for the ALHR and TERR sites for Jan, 22th 2015 and Jan, 23th 2015 for satellite PRN 24. *On the right*: Power spectrum of the signals. The signal for both ALHR and TERR repeats from a day to another with slight differences. In the spectra, we observed long period signals in both sites at ~2 hours and short-period signals at 9 min, 4 min and 3 min for TERR site and 6 min for ALHR site. The power spectrum of TERR site is however one order of magnitude larger than ALHR site.

3.3.3 Phase center Models

We developed a phase center model to reduce the effects of multipath on the phase residuals. The fit is performed in azimuth bins with a piecewise linear function in zenith angle and has been tested for a 1 and 0.5 degree grid. While the 1-degree function models reasonably well the phase residuals

for KUWT and KISR sites, the 0.5-degree function shows a better fit at the two Al-Hamra sites with high frequency signals. The RMS of the phase residuals drops of ~1.5 mm when the 0.5 grid is applied to KISR and KUWT stations and ~4-5 mm and ~ 3-4 mm when it is applied to TERR and TER2 respectively.

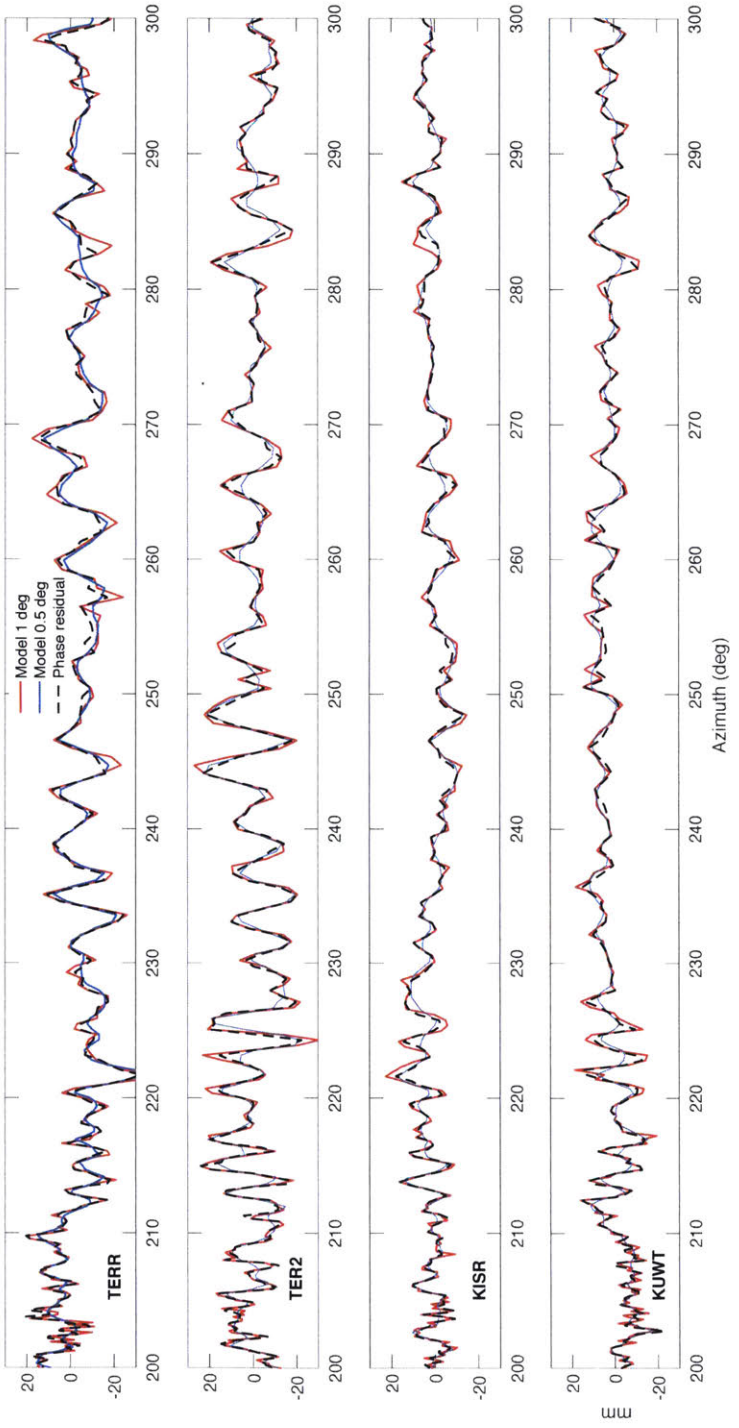

Figure 3.3.7: Phase residual models at 1 deg and 0.5 deg grid for (*from the top)* TERR, TER2, KISR and KUWT sites. The models are shown for satellite PRN 24. The RMS between the phase residual and the phase models drops of about 1.5-5 mm when a 0.5 deg model is applied.

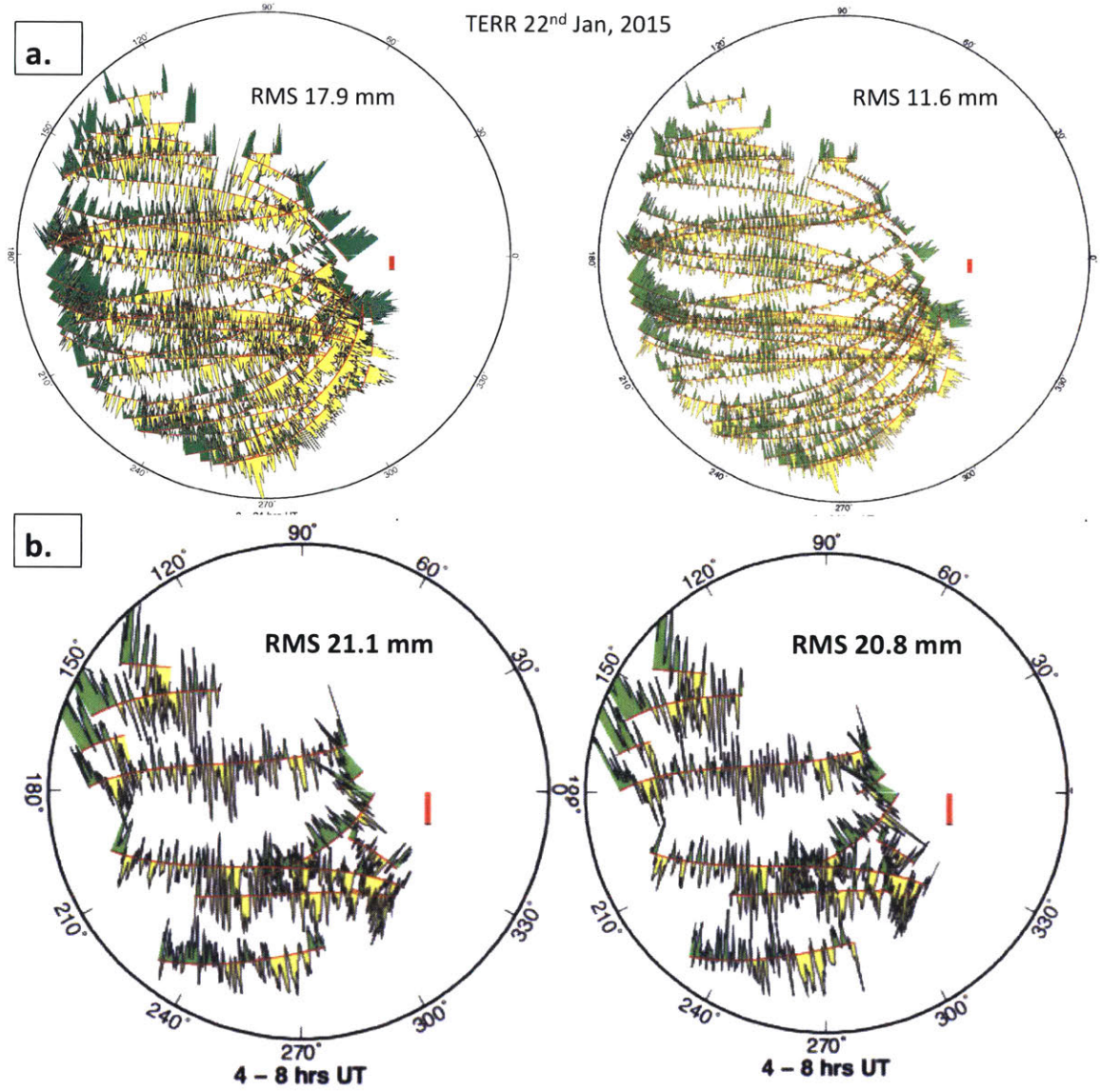

Figure 3.3.8: Sky plot before (*left*) and after (*right*) the application of 0.5 degree phase center model to the 24-hr averaged solution (*a)* and 6-hr averaged solution (*b*). *a.* Although the RMS drops from 17.9 to 11.6 mm, some of the higher frequency signals are still present in the phase residuals. *b.* The 6hr solution RMS only drops by 0.3 mm, when the phase antenna model is applied (*right*).

Preliminary results show that the phase models improve slightly the multipath on the terrace sites with a drop in the phase RMS of about 5 mm with a 5 degree model. However, the higher frequency components are still present in the signal (fig. 3.3.8).

The model is not as effective on the 6 hrs solution (fig.3.3.8-b): RMS of the phase residuals, in fact, only drops by 1 mm. As discuss previously, the 6 hr solution is also corrupted by poor sky configuration at certain time of the day.

3.3.4 Spectral analysis of kinematic solution

For the 1 Hz analysis, we used a wavelet analysis on a relatively short-duration response time history (of an hour or less). Since multipath effects have periods of several minutes to an hour, they would appear as constant harmonics in the analysis, while meaningful background response of the building (e.g. wind deformation) would display intermittent, broadband pockets of energy in the low-frequency range. The wavelet analyses were performed using the Short Time Fourier Transform (STFT) to the data. The TSFT is computed applying the Discrete Fourier Transform of continuous subset of the data and moving the window (range where the DTF is calculate) until the last subset of data is covered. Thus, the STFT is defined as:

$$A_k^t = \frac{1}{\sqrt{N}} \sum_{j=0}^{N-1} X_{j+t-N+1}\, \omega_N^{-jk}$$

The spectral analysis of the two Al-Hamra stations has been compared. As the top site is less

affected by multipath, the signal is expected to lack of the same low frequency content due to multipath, while the meaningful signal should appear in both stations. For the analysis, we selected a day with high winds in order to see the excitation of the building and detect its natural frequencies. The spectral analysis is carried with the matlab routine *periodogram*.

For the day 22 February 2016, a window of 3 hours data has been analyzed for the GPS sites on the building. In ALHR site (fig. 3.3.9), both the spectrogram and the PSD show a strong signal at 7.22 sec, 5.81 sec and 3.53 sec in the NS motion, 7.22 sec and 5.81 sec for the EW motion and 7.22 sec and 5.81 sec for the UP motion. In the TERR site (fig. 3.3.9) the 7.22 sec, 5.81 sec period are detected in both north-south and east-west components. These signals are more visible on windy days and more evident in the horizontal component. Due to their intermittent nature (associated with high wind) and the persistence in both ALHR and TERR stations, these signals are very likely to be the vibrations of the building to the wind stimulus and therefore represent the natural frequency of the building. To get a better insight on the lower frequency portion of the signals, we analyzed the two stations on an hour window at different time of the day (fig. 3.3.10). In particular, we picked the beginning of the day (30 minutes after midnight) and 10 o'clock when the winds started getting stronger reaching speeds of 28 mph with a SE direction. We concentrated on the lower part of the spectrum (<0.1 Hz) where we expect to see the energy associated with multipath.

The kinematic solutions for the two stations show different characteristics: the TERR signal has larger amplitude compared to ALHR, especially in the NS and EW components. The upper motion has instead comparable amplitudes.

A close-up of the spectrograms reveals high-energy signals below 0.1 Hz in the main terrace site at different times of the day. These signals are intermittent, although persistent in all the three

components and are not noticeable in ALHR site.

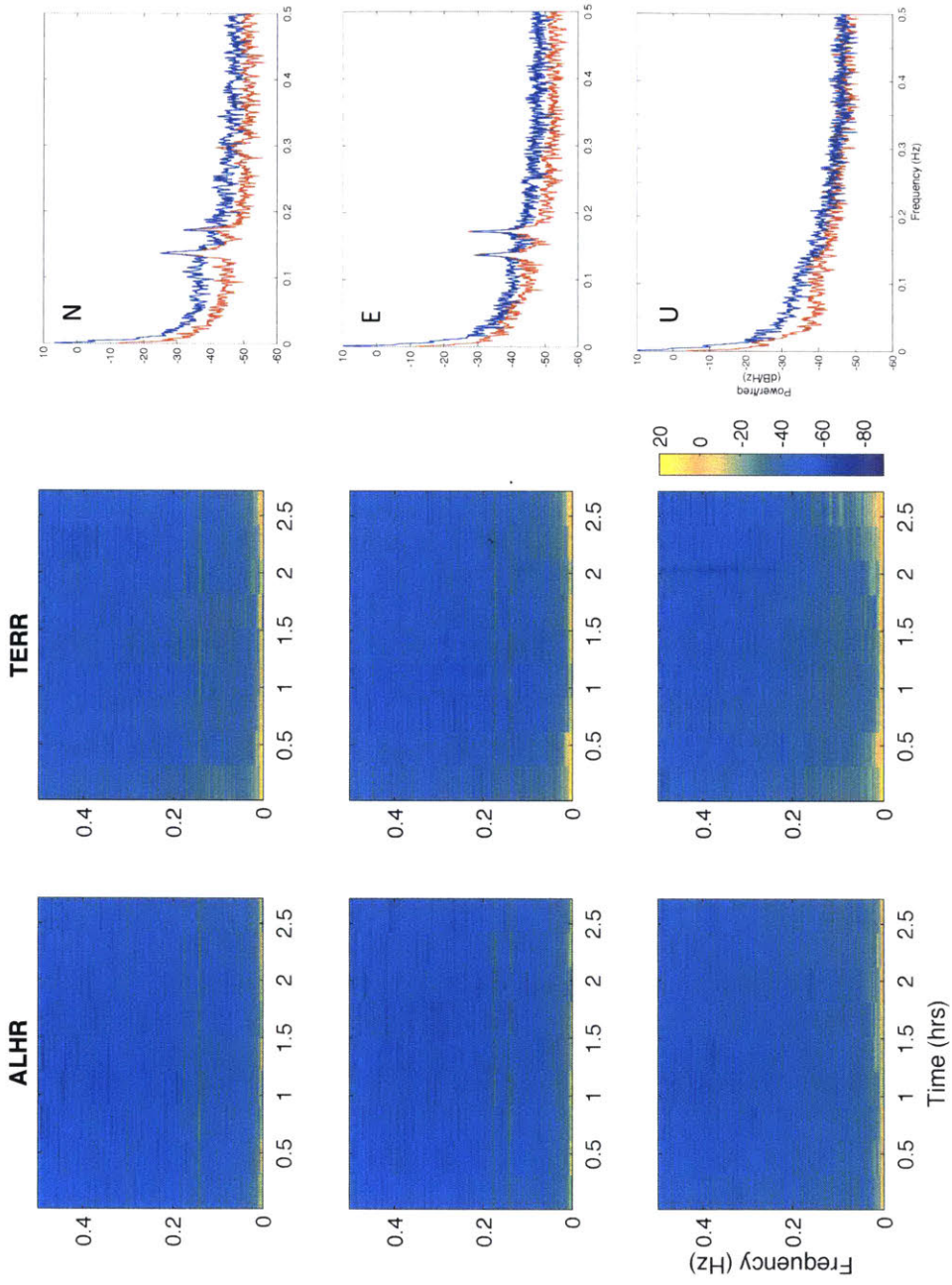

Figure 3.3.9. Spectrogram and PSD estimate for 3 hours window of the ALHR (*left*) and TERR (*right*) kinematic solution day Feb 20th, 2016.

Analyzing two different days at TERR site (20 February and 22 February), it is clear that the same low frequency signals are in the spectrogram and they are shifted by ~ 246 s seconds to approximately the length of the sidereal day. Correcting the spectrograms for the sidereal day, the pockets of energy at lower frequencies repeat on different days, as expected, with minor variation

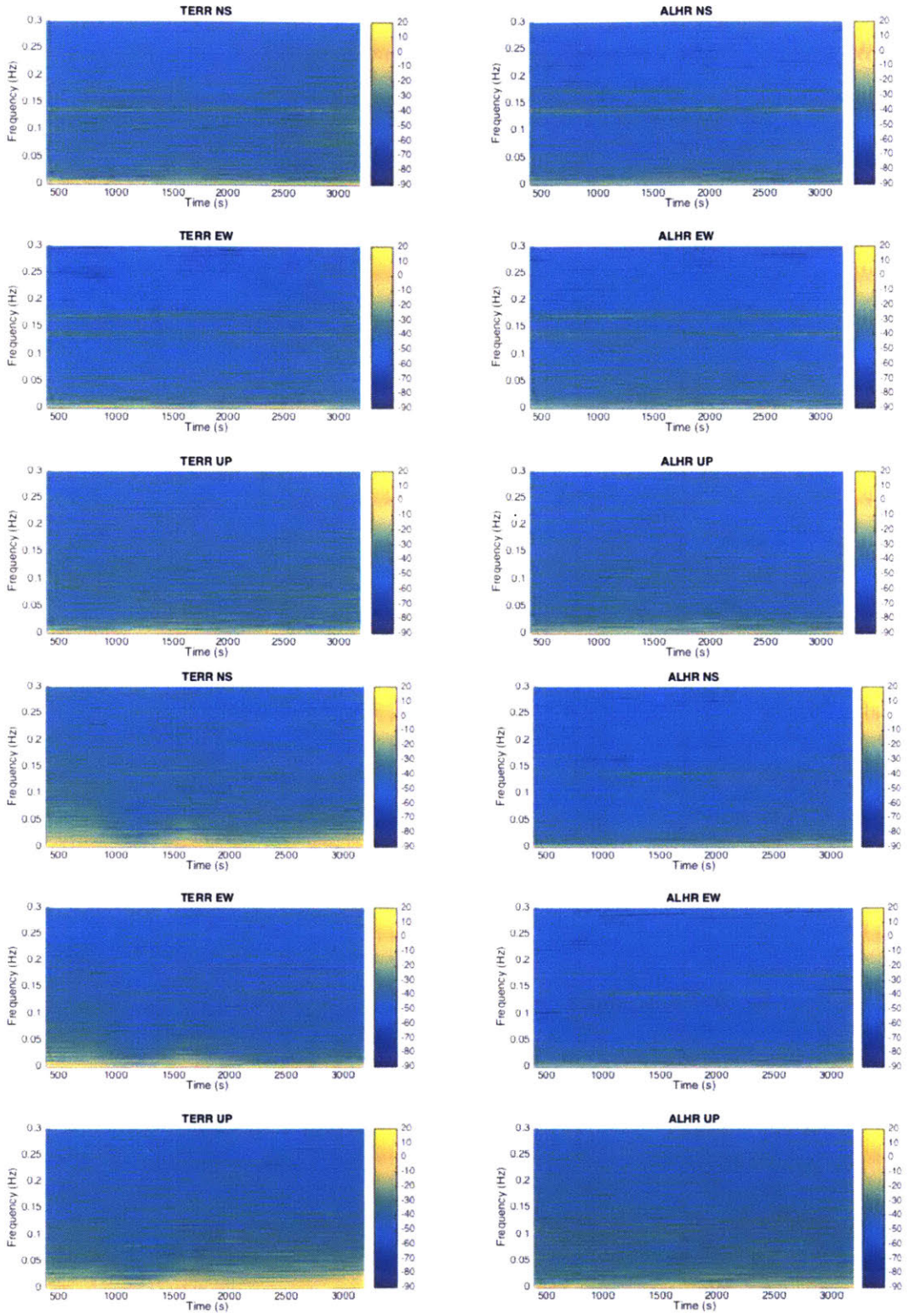

Figure 3.3.10 Spectrogram for TERR and ALHR on an hour window at 12:30 AM (*top*) and 10:00 AM (*bottom*) on day 51.

due to change in weather conditions between different days (fig. 3.3.11) or to different ambiguity

resolution. Due to the characteristics of these signals, we can conclude that TERR site has a clear multipath signature at lower frequency of the spectrum, in particular below 0.1 Hz.

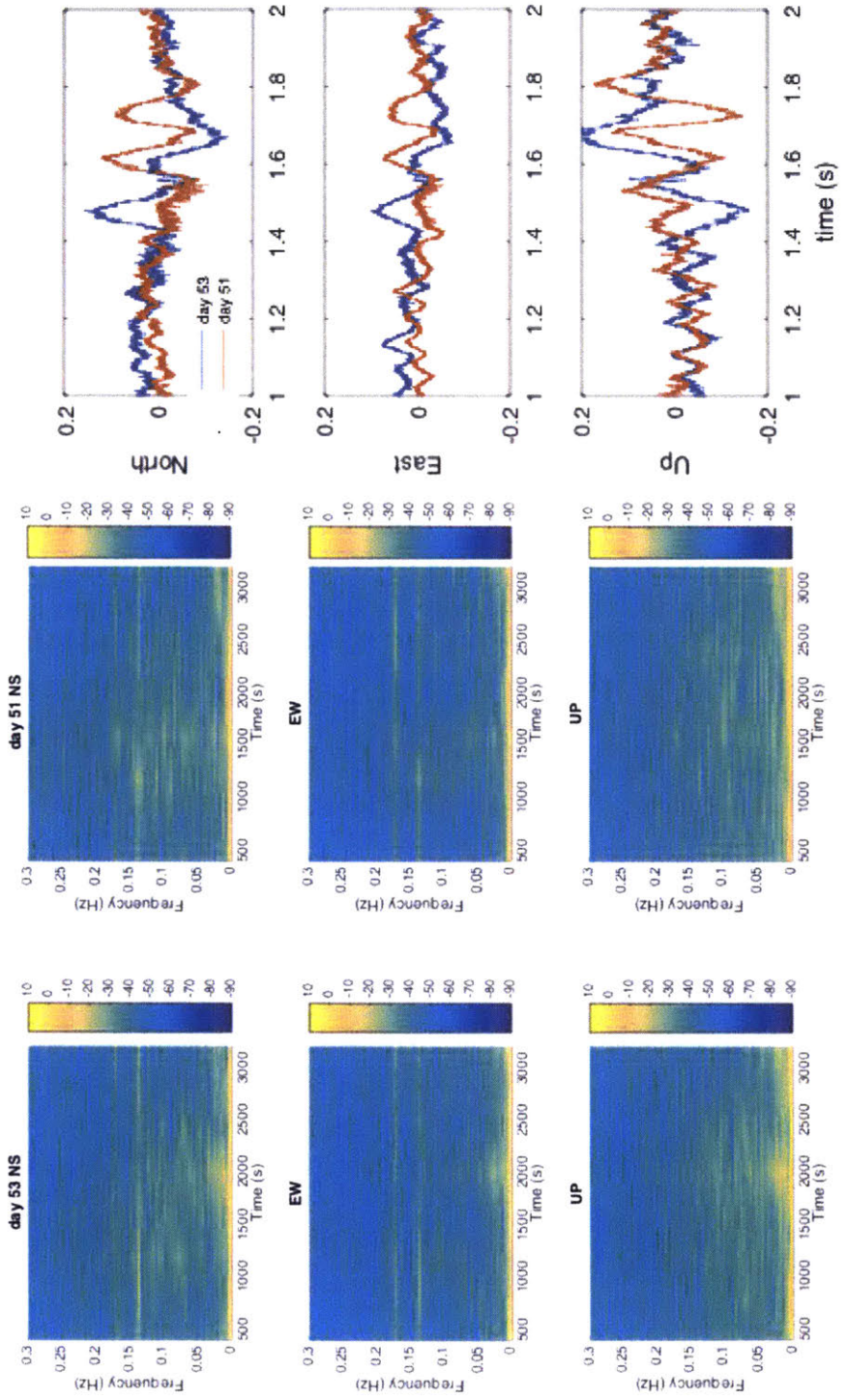

Figure 3.3.11 *Left and center:* Spectrogram of TERR site on day 53 and 51. The solution has been corrected for sidereal shift. *Right:* Kinematic solution for TERR station on days 53 (*blue*) and 53(*red*).

3.3.5 Filtering multipath

Once we recognized the characteristic of the multipath in TERR site, we designed a high pass filter in matlab to remove the unwanted signal at lower frequencies. We used a finite impulse response (FIR) filter, which is one of the most basic elements in a digital signal processing system, and it can guarantee a strict linear phase frequency characteristic with any kind of amplitude frequency characteristic. Besides, the unit impulse response is finite; therefore, FIR filters are stable system. The FIR filter has broad application in many fields, such as telecommunication, image processing, and so on. The system function of FIR is:

$$H(z) = \sum_{n=0}^{L-1} h[n]z^{-n}$$

where L is the length of the filter, and $h[n] = \begin{cases} b_n, & n = 0, \dots L-1 \\ 0, & otherwise \end{cases}$ is the impulse response. With a cut-off frequency of 0.03 Hz, the filtered signal of the main terrace matches better the signal at the ALHR site, as the large amplitude signal due to multipath are removed, and the spectrum of the filtered signal results visibly cleaner in the lower frequencies of all the three components. We show the comparison between the original and filtered signals and the related spectrograms at two different times during the day 22 Feb 2016 with different wind conditions.

Now the filtered signals can be analyzed for the wind response of the building. The PSD plots of the filtered signals at the ALHR and TERR sites show again a clear resonant peak at 7.22 sec, 5.81 sec and 3.53 sec in the NS motion, 7.22 sec and 5.81 sec for the EW motion and 7.22 sec and 5.81 sec for the UP motion at the ALHR and at 7.22 sec, 5.81 sec in the NS motion, 7.22 sec and 5.81 sec for the EW motion at the TERR site. In the spectrograms of the cleaned signals, it is now possible to detect the background component of the wind-induced response of the wind, as intermittent low-energy signals that are more consistent with the characteristics of wind signal. In fact, the background component is more evident in the NS signal round 6 AM and around 10 AM to 12 PM and that is consistent with the increasing in speed from 19 mph to 24-26 mph on average (fig 3.3.16). The peak and background components can be easily separated by filtering the clean signal and they will be discussed in the later section of modeling.

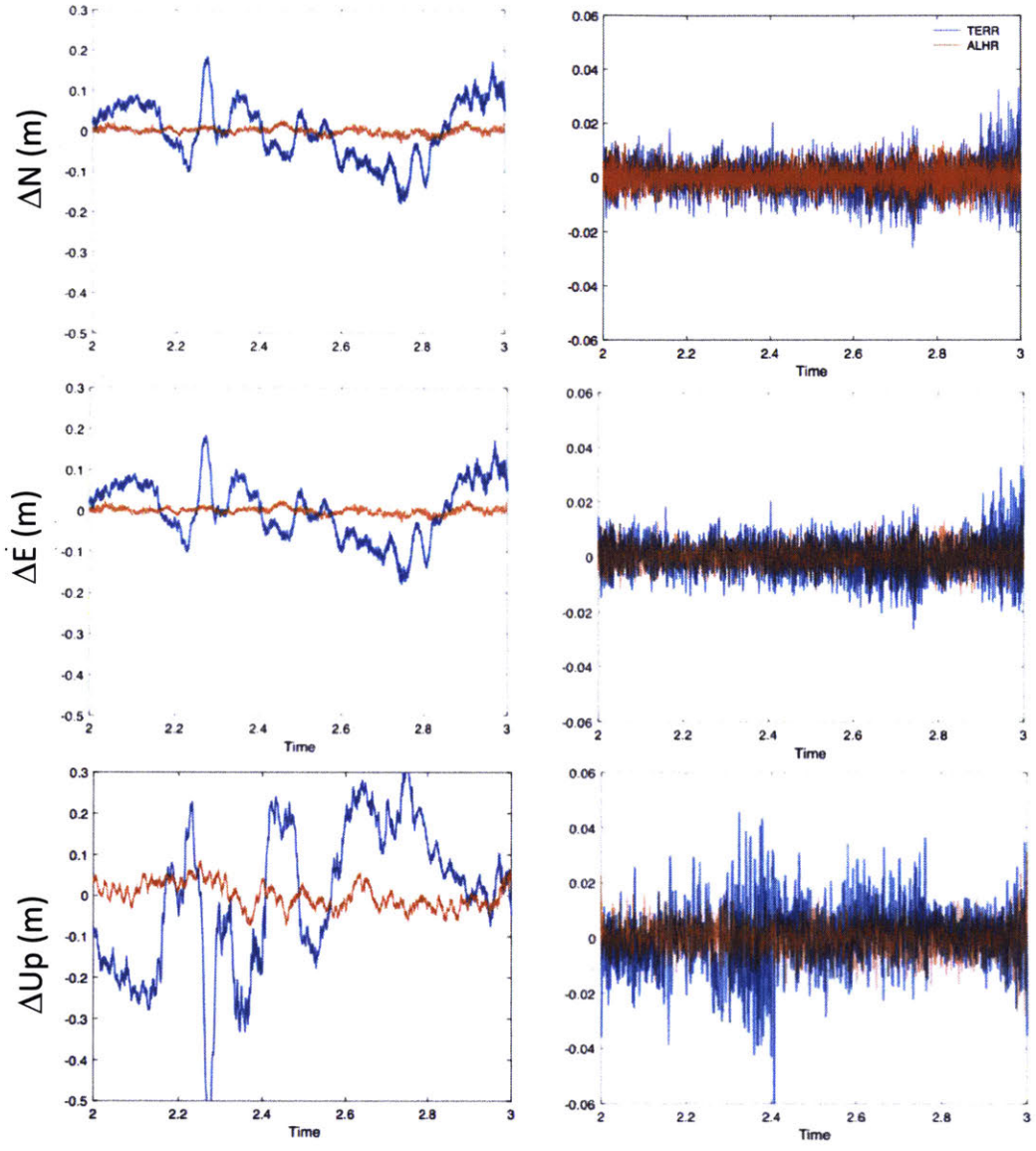

Figure 3.3.14 *Left:* N, E and Up component of the unfiltered signal for TERR and ALHR sites. *Right:* N, E and Up component of the filtered signal for TERR and ALHR sites. The multipath effects and noise on TERR site is significantly reduced.

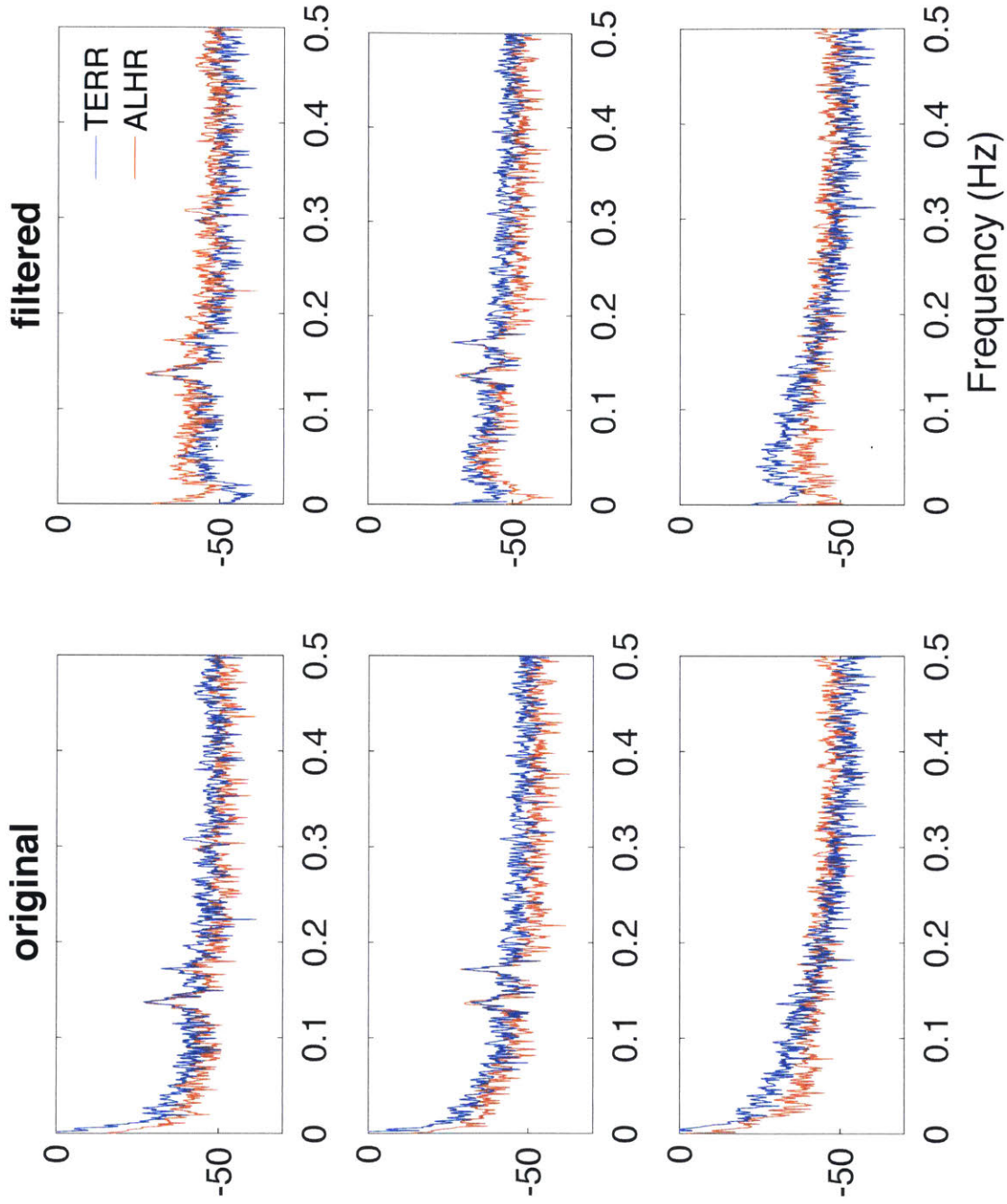

Figure 3.3.15 PSD in power/frequency of the NS (top), E (*center)* and Up (bottom) component of the original and filtered signals for ALHR and TERR sites at 2:00AM of February 22nd, 2016.

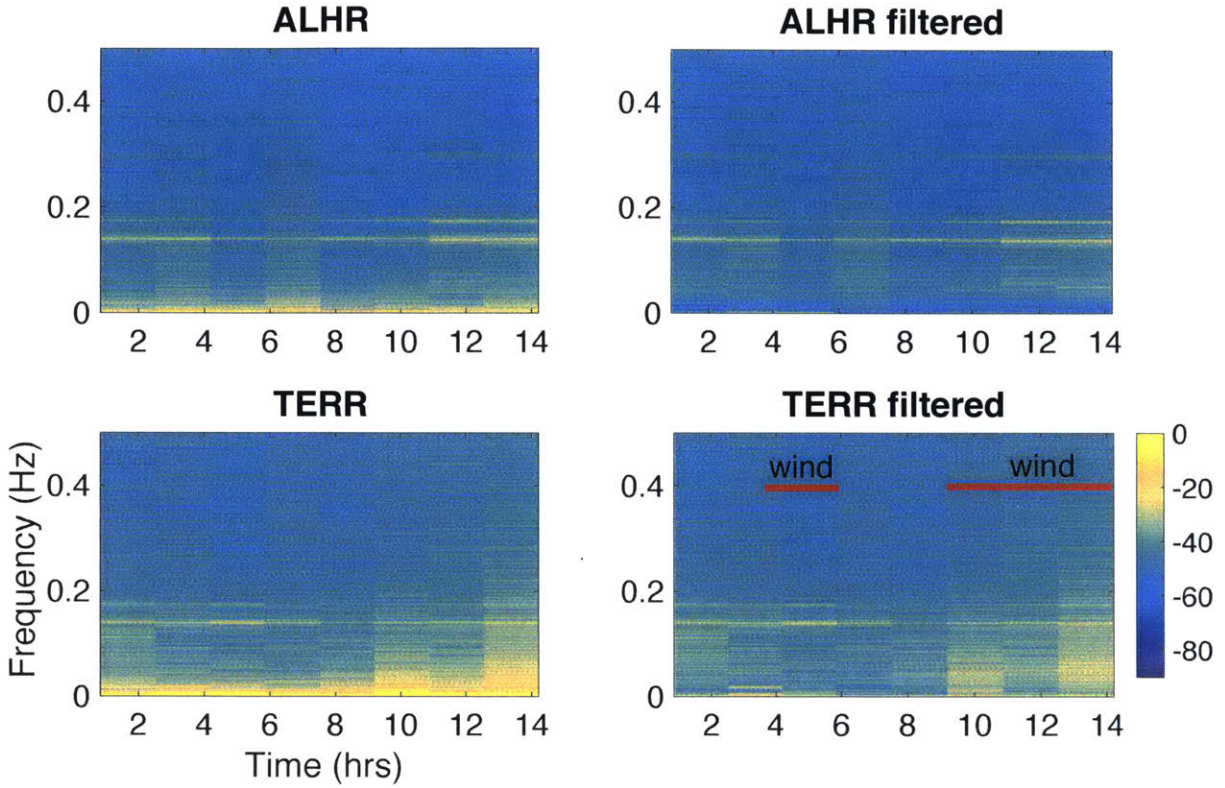

Figure 3.3.16 Spectrogram comparison of the unfiltered (*left*) and filtered (*right*) 1Hz solutions of the N component of ALHR (*top*) and TERR (*bottom*) site on February 22nd, 2016. Red bars (*bottom right*) indicate an increase in wind speed (24-26 mph).

3.3.7 Hilbert-Huang transform application

The Hilbert-Huang Transform method for spectral analysis has been successfully applied to other geophysical problems dealing with non-stationary and non-linear processes. This technique has the important advantage of separating the different contributions to the signal from multiple sources, happening in different time intervals. The normalized Hilbert–Huang transform consists of three steps: EMD (empirical mode decomposition) of the time series into IMFs (intrinsic mode function), normalization of the IMFs and extraction of instantaneous amplitudes, and finally extraction of instantaneous frequencies from the normalized IMFs using the Hilbert transform. The EMD begins by defining two cubic splines. One passes through all the local maxima of the data, and the other passes through all the local minima. The average of the two splines is considered the

local mean of the data, and is subtracted from the original time series. The result now has zero mean, but does not necessarily form an IMF since it can still contain introduced local extrema. The process is repeated until convergence is obtained, at which point it satisfies the conditions of being an IMF as defined by Huang et al. (1998). When the first IMF, $x_1(t)$, has been calculated using the above procedure, it is subtracted by the original signal:

$$U_1(t) = U(t) - x_1(t)$$

The signal $U_1(t)$ is the same as $U(t)$, but has had the highest-frequency fluctuations in it. The next IMF is then extracted from $U_1(t)$ using the same process, so that:

$$U_2(t) = U_1(t) - x_2(t)$$

When the signal, $U(t)$, has been decomposed into its constituent IMFs, $x_i(t)$, may be written as:

$$U(t) = \sum_{i=1}^{N} x_i(t) + \varepsilon(t)$$

where N is the number of IMFs that have been extracted from the signal and $\varepsilon(t)$ is the low-frequency trend, containing zero or one extrema. The IMFs are then normalized to avoid the problem that the spectrum of oscillation within the IMF and that of their low-frequency envelop overlap, then the instantaneous frequency will not be meaningful according to Bedroasian theorem (Huang and Wu, 2008). We chose this method to extract the wind contribution to the signal because of its ability to react quickly to changes in the time series, and because of its adaptive, nonparametric decomposition. This is especially true for the wind effects analysis, as this signal is known to contain complicated statistical structures, breakpoints, and periodicities. The hht (Hilbert-Huang transform) has been implemented in MATLAB using the Hilbert and peaks routines. We tested this analysis for the ALHR site on day 22nd February 2016 as the wind has different speeds throughout the day.

In figures from 3.3.17 to 3.3.19, the IMF decompositions for ALHR are shown. The wind bursts are visible in the GPS signal, especially in the north and up component. The amplitude of the oscillations caused by the wind are ~ 15 mm.

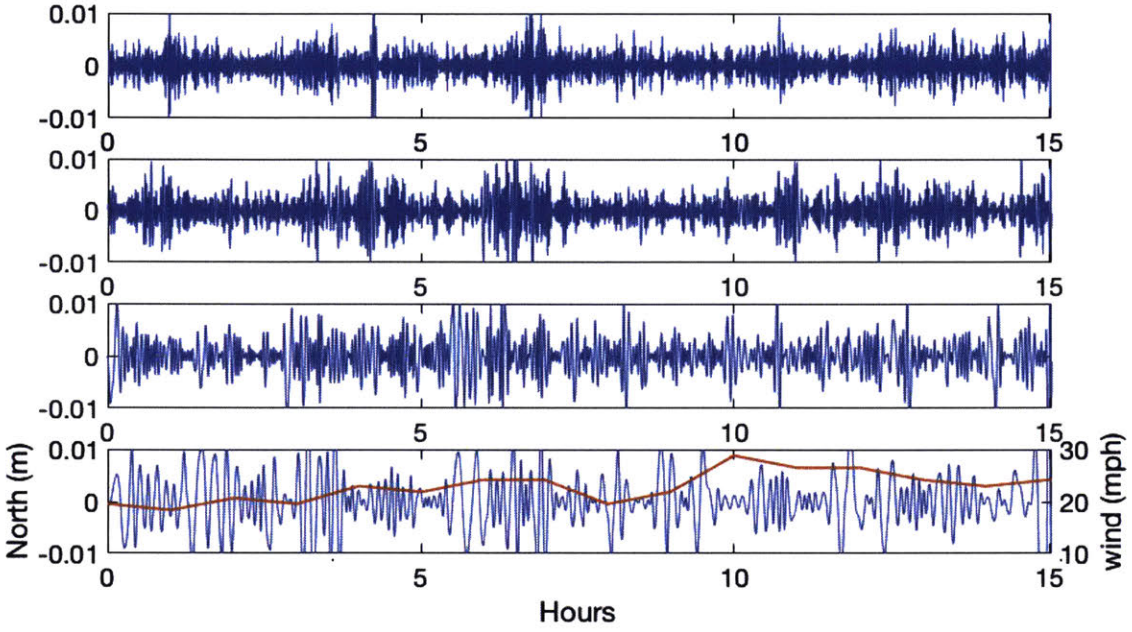

Figure 3.3.17 IMFs of the ALHR N-S component and wind speed variations (*bottom*). IMFs are starting from the top 0.7, 0.4, 0.2, 0.1 Hz.

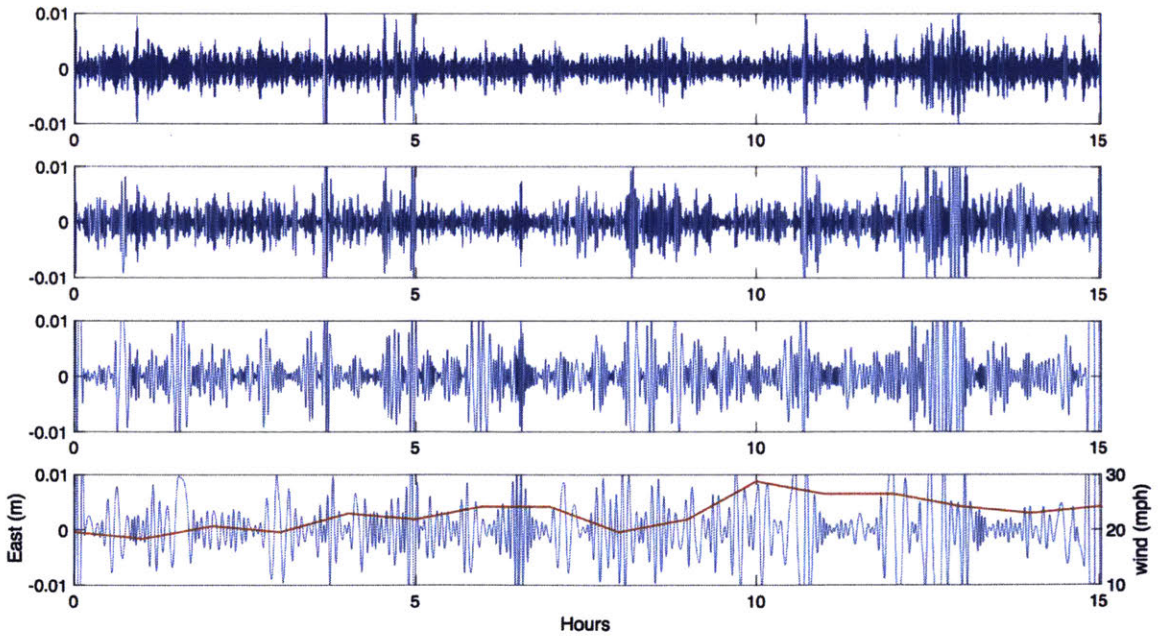

Figure 3.3.18 IMFs of the ALHR E-W component and wind speed variations (*bottom*). IMFs are starting from the top 0.7, 0.4, 0.2, 0.1 Hz.

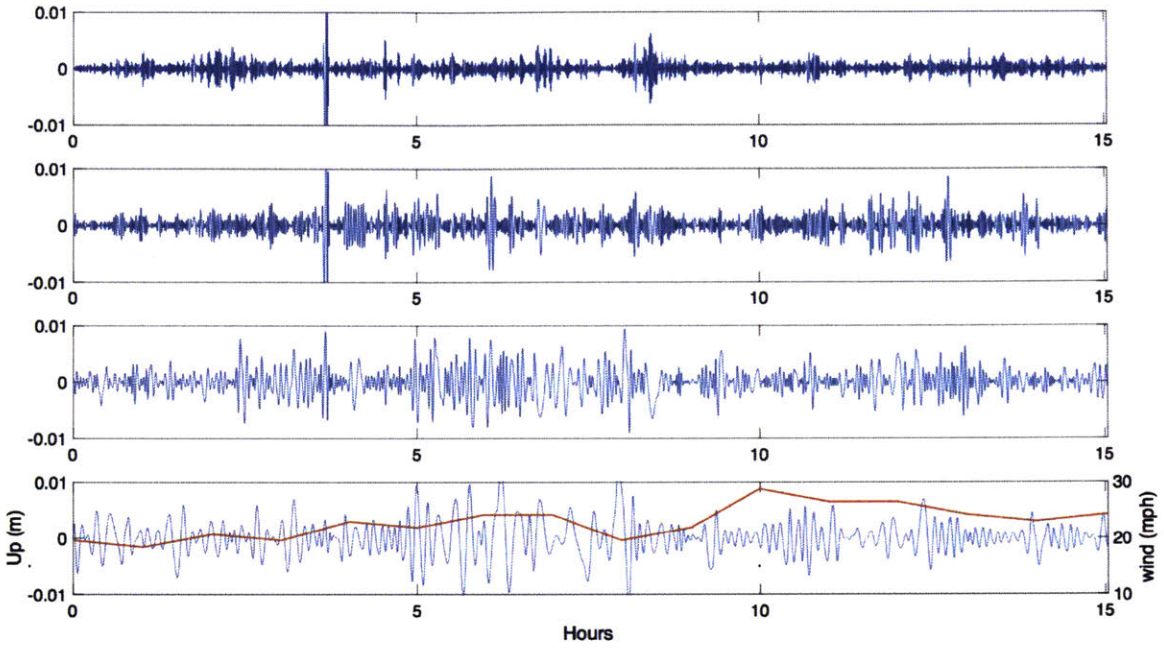

Figure 3.3.19 IMFs of the ALHR Up component and wind speed variations (*bottom*). IMFs are starting from the top 0.7, 0.4, 0.2, 0.1 Hz.

3.4 Al-Hamra deformation modeling

3.4.1 Introduction

The recent increase in construction of tall buildings with progressively more complicated structural designs has revealed the need for special performance based assessment. Traditional design codes, such as the Uniform Building Code (UBC) or International Building code (IBC) are widely used for different kind of hazard assessment and design, but lack of applicability to tall buildings. Also, the monitoring of these buildings is often inexistent, making it difficult to assess their structural behavior after construction.

Tall buildings structural assessments are mostly carried in the pre-construction phase through modeling, but very rarely is there a post-construction assessment to monitor the long-term behavior of these structures. The lack of assessment is partially due to the difficulties in instrumenting these high-rise buildings and also the possible outcomes of the deformation analysis on the existing buildings, as it might require very expensive modifications with economic consequences.

So, the objectives of the second part of this project are to assess the performance of Al-Hamra tower, through the modeling of the observed deformation in the GPS data.

Generally, the main sources of deformation for high-rise buildings are:

- structural loads
- creep and shrinkage
- earthquakes
- temperature
- wind

For this study, we focused on the latter three causes of deformation as they are related to post-construction phase.

3.4.2 Seismic Deformation

The effects of earthquake and ground motions on tall structures are already well known. The first

well-documented case is the measured displacements of the Trans America Building in San Francisco due to the 1989 Loma Prieta earthquake (MW = 6.9) at a distance of more than 100 km. Shown in figure 3.4.1 are the measured displacements of the different floors. The peak amplitude of ground displacement is about 1 cm at the basement, 10 cm at the 21st floor and 20 cm on the 49th floor. The duration of motions on higher floors is much longer than sixty seconds.

The primary hazard for Al-Hamra tower is therefore ground motion. In Kuwait, the primary sources of the potentially damaging ground vibrations are due to regional earthquakes, mostly in the Zagros Belt (Iran). In figure 3.4.2, locations of significant earthquakes in Zagros region and surrounding areas that occurred in the period 1997-2014 are shown. On average about one earthquake of magnitude 6 or greater occurs in the region per year.

The ground motion at a site in Kuwait depends on the earthquake magnitude, source mechanism, and crustal structure over which the seismic waves propagate.

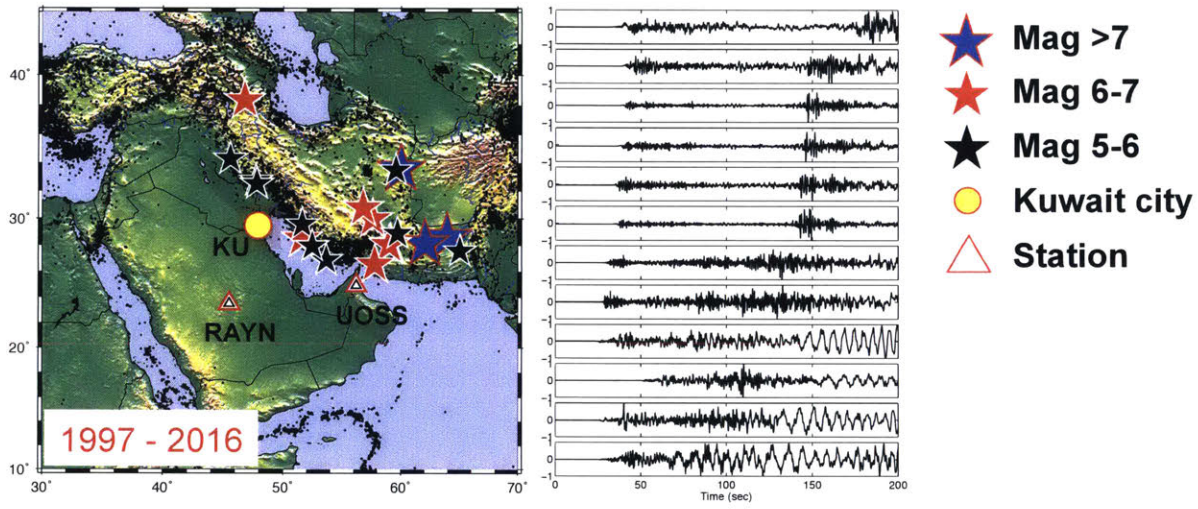

Figure 3.4.2 Significant regional earthquakes since 1997 that could affect tall buildings in Kuwait. Stars show locations (Blue: Mag>7, Red: 7>Mag>6, and Black: 6>Mag>5). Seismic records recorded by station "MIB" in Kuwait ("KU") are shown on the right. Duration of recording is limited to 200 seconds for each event (*Courtesy of Chen Gu, 2016*).

In 2015, three earthquakes (M=3.9, 4.1, 4.5) occurred in Kuwait. Most likely these occurred on pre-existing faults and were triggered by oil field activities.

The ground motion in Kuwait has been estimated for an earthquake of magnitude Mw=6.2 that occurred on 18 August 2014 near Iran-Iraq border 200 km NNE of Kuwait City (figures 3.4.2 and

3.4.3). The maximum displacements at Kuwait City were 0.3 cm. Maximum acceleration was 1.7 cm/sec^2. The duration of shaking was longer than 200 seconds. The motions were calculated for competent bedrock. However, the buildings in Kuwait City are mostly built on soft soils that can double the ground motion depending on geotechnical conditions and soil properties. The ground displacement calculated for such an earthquake could be as much as 5 to 10 cm.

3.4.3 Seasonal temperature variations

In several studies the thermal analysis on buildings has been primarily conducted to assess the cooling loads and natural heating and consequently to improve their thermal efficiency. However, the deformation effects of temperature variations on these building has not been investigated yet, as it is often minimal depending on the dimension and properties of the structures.

Kuwait has an arid climate with considerable temperature excursion between winter and summer. Rainfall in the nation varies from 75 to 150 millimeters (2.95 to 5.91 in) a year. In summer, average daily high temperatures range from 42 to 48 °C (107.6 to 118.4 °F), while in the winter daytime temperature is between 10–17 °C (50–63 °F). The sunshine hours are influenced by the sun path through the day and the year. Figure (25) shows the sun path at Al-Hamra Tower site, where the southern façade is the most exposed to the sun. The yearly average shine days in Kuwait City is 247 days.

Figure 3.4.4 Yearly motion of the sun around Al-Hamra tower. The yellow line shows the shortest path of the sun in the winter, while the upper boundary corresponds to the path of the sun in the summer.

The long-term motion of Al-Hamra tower processed over a year shows a strong seasonal signal that is highly correlated with temperature, especially for the NS component of the motion. Also at the sub-daily scale, the motion of the building follows the variation pattern of the air temperature. In both case, there is a delay of the response of the building to the temperature variations, as it would be expected. In particular, in the yearly motion, the building seems to bend towards south in the winter and towards North in the summer, while the height has a minimum in mid-winter. These seasonal motions might be related to the thermal deformation of the building. The concrete

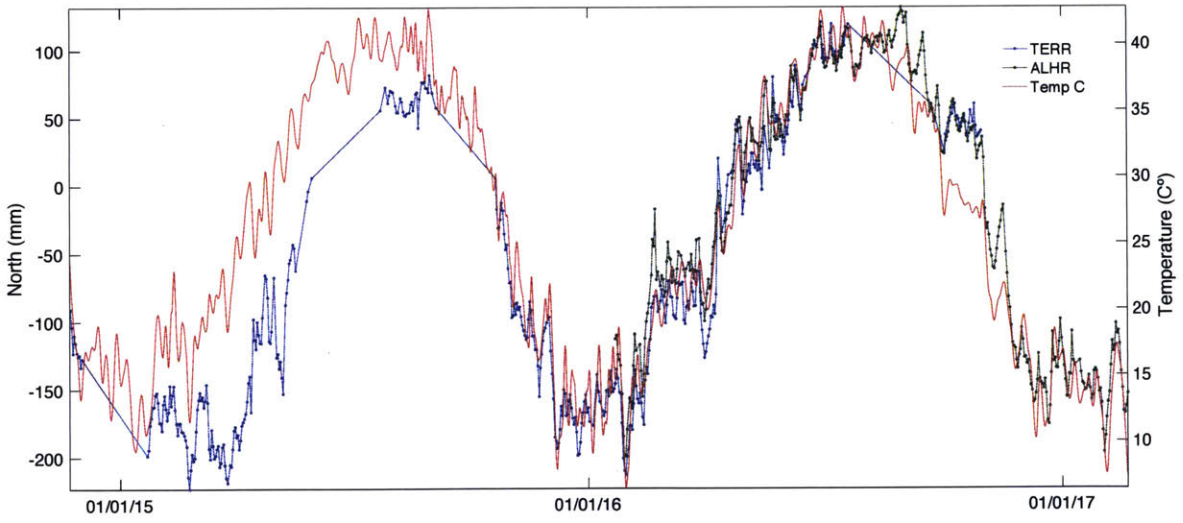

Figure 3.4.5 NS motion and temperature variations through the year. In red is the average temperature and in blue is the 24-hour averaged N solution for the main terrace site (TERR) and in green for 86th floor site (ALHR). The TERR site offsets in the data have been removed using ALHR site to estimate the seasonal signals of the building. The gaps in the GPS data are due to loss of power or antenna tipped over by the wind.

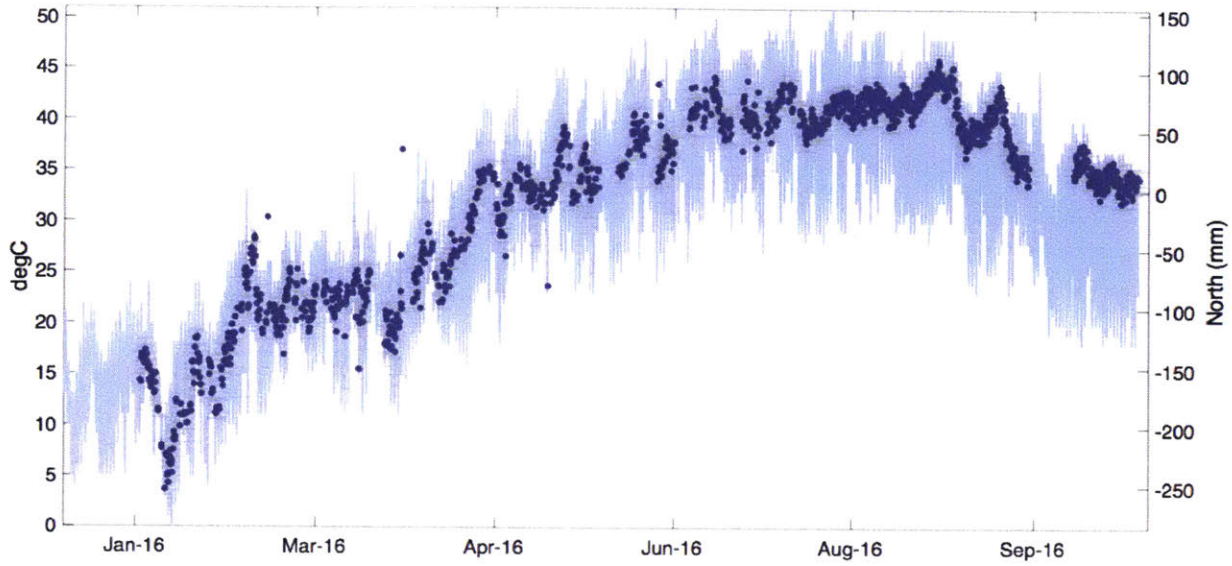

Figure 3.4.6 Sub-daily motion and temperature variations comparison. In light blue is the hourly temperature data and in blue is the 6-hour averaged NS solution for ALHR site.

side of the tower is in fact facing approximately south (8° off), while the glass wall is facing approximately north, suggesting that the two side of the building might be deforming differently under thermal stresses, causing the building to bend.

In order to study the thermal stress on the Al-Hamra tower, we conducted a thermal analysis, calculating the monthly solar radiation on the building using the software Diva (Reinhart et al., 2012). The software doesn't allow an hourly calculation, so the values are averaged over a day and month (fig. 3.4.7). Cumulatively on a year, the radiation reaches its highest values on the main terrace and on some area of the top wall, while the south façade has intermediate values. The north façade has instead the lower values as expected by the sun path analysis.

Figure 3.4.8 shows the monthly averaged variation of the solar radiation for the four walls and the roof of Al-Hamra tower. The solar radiation at the roof has the highest value among the external walls of the tower, reaching value of 250 kWh/m^2 in July and decreases to values of about 140 kWh/m^2 in the winter months.

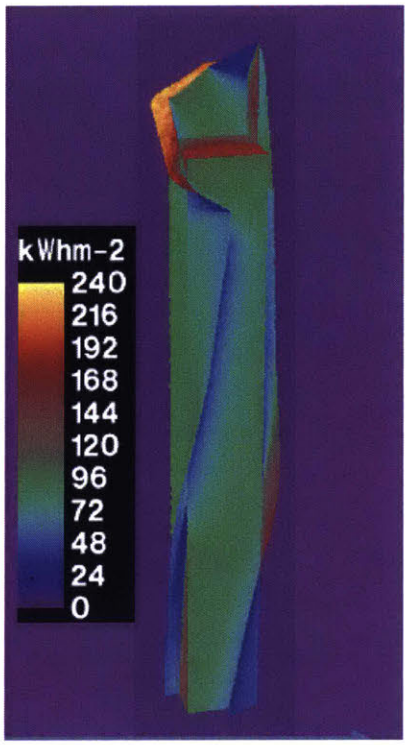

Figure 3.4.7 Distribution of the solar radiation over a year calculated with DIVA. The value of solar irradiation showed are averaged for each month. September solar radiation distribution is showed.

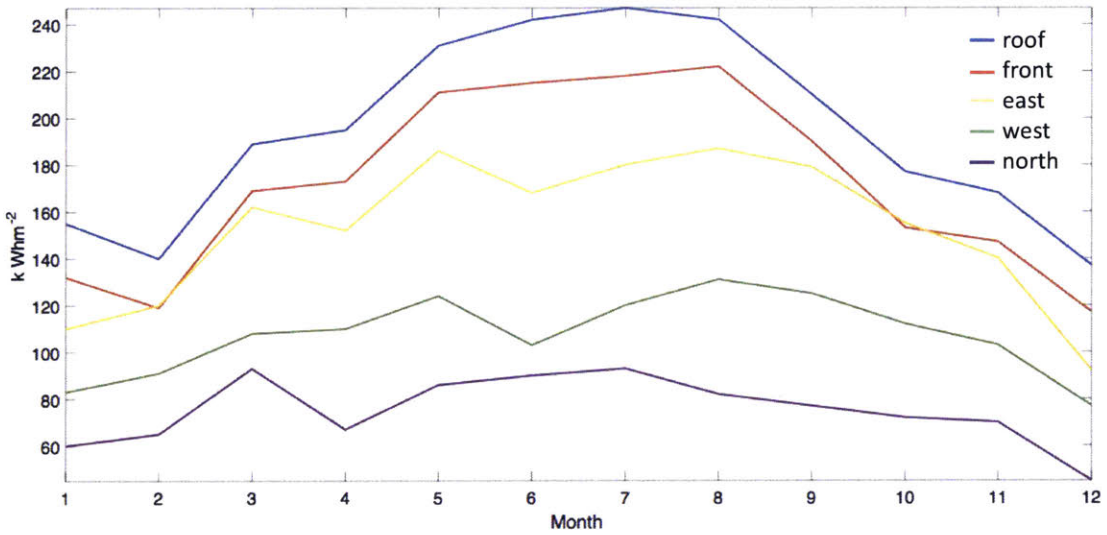

Figure 3.4.8 Averaged incident solar radiation on the wall throughout the year. West and wall solar radiation values are different as the curtain wall covers more surface on the west wall than the east wall, preventing the absorption of solar radiation.

We used the values of solar radiation and air temperature as inputs to estimate the heat gain through the walls of the buildings. As the solar radiation calculated doesn't consider hourly variations

during the day, I simulated the hourly values an interpolation of the peak values of solar radiation for the four walls at different time of the day (12pm for southern wall, roof and northern wall; 10 am for eastern wall and 3pm for western wall) and 0 solar radiation from sunset until sunrise (times are obtained from the weather data).

3.4.4 Solar-air temperature

The boundary conditions on the external walls of the building are given by the Solar-Air Temperature, which is a fictitious temperature equivalent to outside temperature that will cause the same rate of heat flow at the surface and the same temperature distribution through the material as current outdoor air temperature, in absence of all radiation changes (Stephenson, 1963). From ASHRAE (American Society of Heating, Refrigerating and Air-Conditioning Engineers) Fundamentals (1997), the heat balance at a sunlit surface gives the heat flux into the surface q/A as:

$$\frac{q}{A} = \alpha I_t + h_o(t_o - t_s) - \varepsilon\Delta\Re$$

where t_s is the surface temperature of the wall, t_o is the outdoor air temperature, ε is the hemispherical emittance of the surface, $\Delta\Re$ is the difference between long wave radiation incident on the surface from the sky and the surrounding radiation emitted by a black body at outdoor air temperature, α is the absorptivity of the surface for solar radiation, I_t is the total radiation incident on the surface and h_o is the coefficient of heat transfer by long wave radiation and convection and the outer surface. Expressing the rate of heat transfer in terms of solar-air temperature t_e, the rate of heat transfer will be:

$$\frac{q}{A} = h_o(t_e - t_s)$$

and therefore, the solar-air temperature will be:

$$t_e = t_o + \alpha I_t/h_o - \varepsilon\Delta\Re/h_o$$

AHSRAE Fundamentals suggests that the term $\varepsilon\Delta\Re/h_o$ for all type of horizontal surfaces equals 3.9 C°, with the limitation that the hemispherical admittance is considered constant (while it is

variable and depending on the temperature of the body according to Thankur, (1989). Tests by ASHRAE Fundamentals on different types of material and wall compositions suggests that the term α/h_o varies between 0.026 (for light colors) and 0.052 (for dark colors).

Several studies have pointed out some of the limitations of the solar-air calculation, as there is no differentiation between various climates, especially with regard to sky cover and air moisture content, pollution etc. that can influence the long-wave radiative exchange process. In particular Bliss (1963) suggested that values of the net long wave radiation exchange can account for up to 20% of uncertainty. Also, Al-Saud (2009) suggested that the solar-air temperature in hot-arid regions is often underestimate (up to 10 C°), suggesting that the term $\varepsilon\Delta\Re/h_o$ for horizontal surfaces is lower than the value suggested by ASHRAE.

For this study, I considered the solar-air temperature as an approximation of the real temperature of the external wall, under the limitations previously mentioned. I simulated the deformation for two short periods of 2016 (January 29-31st and August 3-5th) to test the sub-daily simulation and a month-long period (September 2016) to test the approximation of the external temperature of the walls with changing weather conditions. An example of solar-air temperature calculations for the

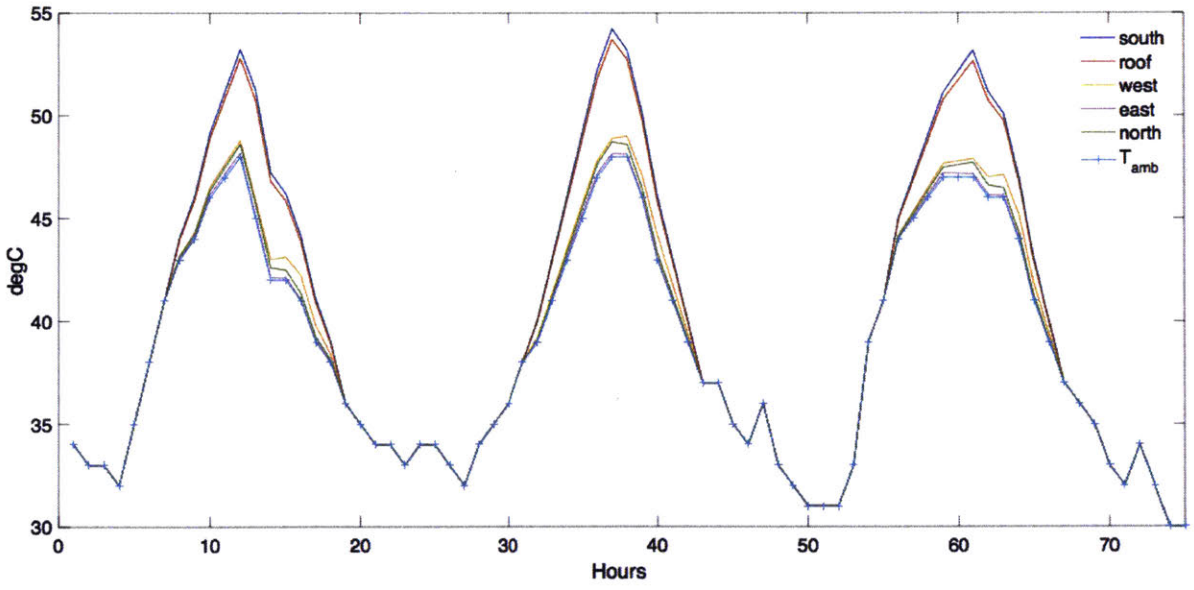

Figure 3.4.9 Solar air temperature for the 4 walls and the roof of al-Hamra tower for September 1st to 3rd, 2016. T_{amb} is the outside air temperature.

four external walls is shown in fig. 3.4.9.

The south wall and the roof reach the highest temperature during the day, with about 5 C° difference with the air temperature for the peak time of the day (noon), while the eastern and western walls only get 1-2 C° higher than air temperature and 1 C° for the northern wall.
One of the limitation of the solar air-temperature model is the effect of the wind of the surface temperature of buildings. Sustained winds can modify the surface temperature of the walls, increasing the rate of heat loss and reducing the effect of solar radiation on the surface. Moreover, the effect of wind can impact differently the walls depending on the direction of the wind. In order to take account of the effect of the wind on Al-Hamra tower, I built a preliminary finite element model with *COMSOL Multiphysics* software that simulates the surface temperature in windy conditions. The model is discussed in the following paragraph and the wind correction has been tested for September period, where some days are characterized by sustained wind with speeds up to 30 mph and North direction.

3.4.5 Wind model

The wind flux has been simulated using a coupled finite element model: turbolent fluid flow physics to model the flux of air around the building and solid heat transfers to estimate the heat exchange between the building and the air. Al-Hamra tower has been modeled as a concrete hollow square prism, with a base 40 m in length and a height of 400 m. The bottom layer has a fixed boundary condition while the external walls have a radiative surface boundary condition with a surface emissivity of 0.68. The domain for the laminar flow is represented by a prism of 2000x1000m area and a height of 800 m length. The inlet boundary condition on one side simulates the source of the incoming wind; the opposite boundary is set as outlet for the air with a pressure equal to atmospheric pressure; the side boundary have a symmetry condition to simulate an infinite plane in those directions. The velocity of the wind is set at 30 mph and air temperature of 20 C°, while the initial condition in the building is 24 C°. Figure 4.3.10 (*left*) show the preliminary result for the air flow around the building: the flow pattern is highly complex and characterized by a stagnation point and separated streams on the wind ward side. The outer flow displaced above the building reaches maximum speed of 36 mph, while on the lee side of the building, the flux is

separated in bubbles with internal vortex substructures. The temperature distribution resulting from thermal exchanges between surfaces and air flux is shown in figure 4.3.10.

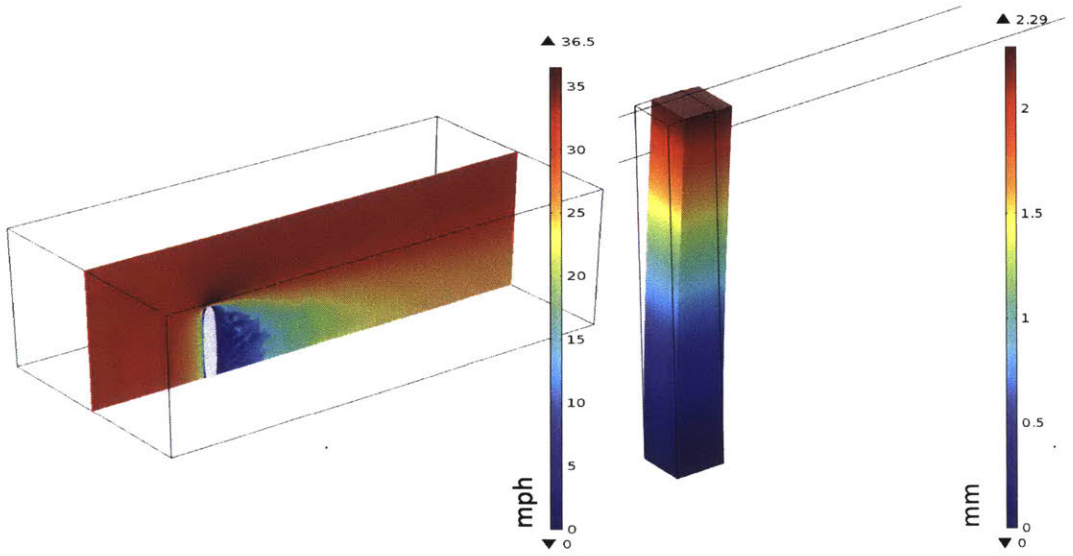

Figure 3.4.10 Wind model of Al-Hamra tower. *Left:* air flow for a wind speed of 36 mph and air temperature of 20 C°. *Right*: displacement in x-direction by wind action. In light gray, the tower is shown.

Generally, the surface temperatures are varied by the presence of wind, depending on the temperature of the air and the temperature of the building. In the model present, the temperature on the side walls, roof and back of the building are lowered by 2 °C, while the temperatures are lowered of about 4 °C on the wind ward side. The wind effect will be tested in the mechanical models, inputting the surface temperatures calculated in the wind simulation (fig. 4.3.11).

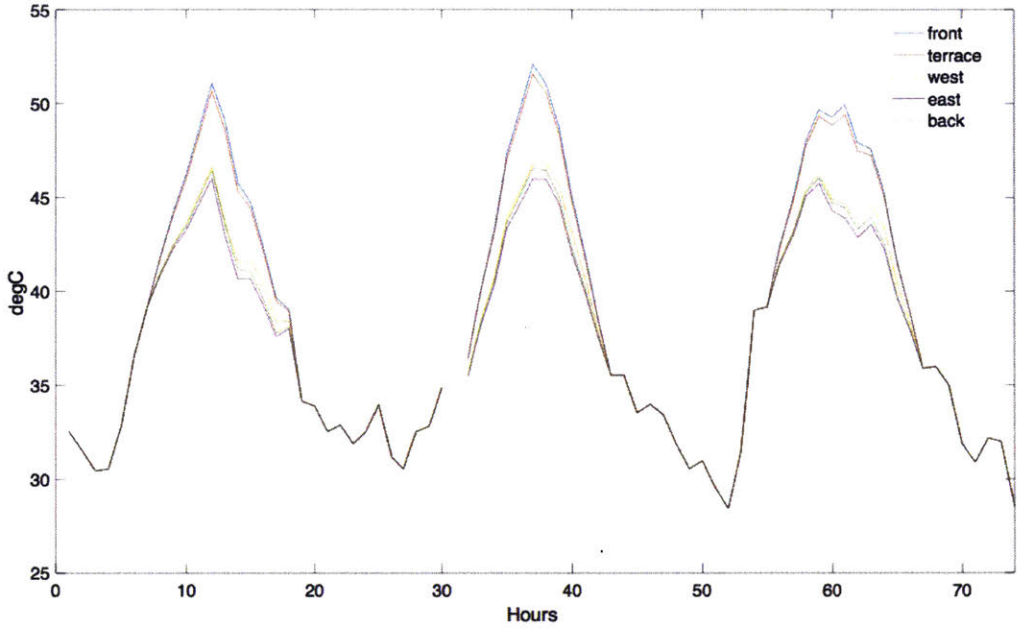

Figure 3.4.11 Solar air temperature for the 4 walls and the roof of al-Hamra tower for windy days in September. In windy days, the temperature of the front wall (*wind ward side*) is lowered by 3-4 C° compared to sunny days (fig. 3.4.9), while the temperatures of the side, back and roof walls are lowered by 2 C°.

3.4.6 Heat Gain through the walls

The estimation of the heat gain through the walls and the roofs has been widely performed to design energy-efficient buildings. Several techniques have been used to calculate the transient heat flow through the walls, using analytical or numerical calculations.

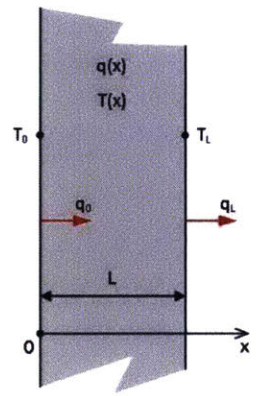

The heat flow through the walls is described by the Fourier's law of heat conduction:

$$q = -k \cdot \overline{\nabla} T,$$

that relates the heat fluxes to the temperature gradient and the 1st law of Thermodynamics (energy conservation):

$$\rho \cdot c_p \cdot \frac{\partial T}{\partial t} = -\overline{\nabla} q,$$

where ρ is the density, k is the thermal conductivity and c_p is the specific heat. I investigated the heat gain through the wall through a Finite Element Model, considering a slab with three material configurations and different boundary conditions. Typical values of thermal conductivity and specific heat for concrete are used for the modeling.

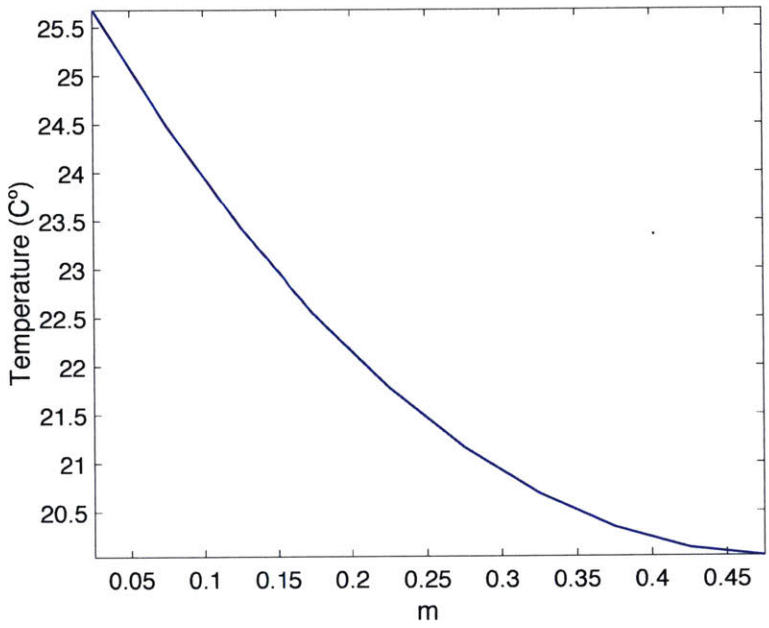

Figure 3.4.12 Distribution of temperatures inside the wall.

If a constant external temperature is applied on the external wall, the transmission of heat is not instantaneous but it will require several hours for the internal wall to reach the equilibrium temperature. In figure 4.3.12, the distribution of the temperature inside the wall is shown for an initial temperature of 15 °C and an external temperature of 21 °C.

If the external temperature varies during the day, as a sinusoidal function of time, the resulting temperature on the external wall will be a sinusoid with same frequency but different amplitude and phase. I tested two different wall settings: one has an isolated internal wall (no exchange of temperature with the internal room); the other has a constant internal temperature to simulate a constant A/C inside the room.

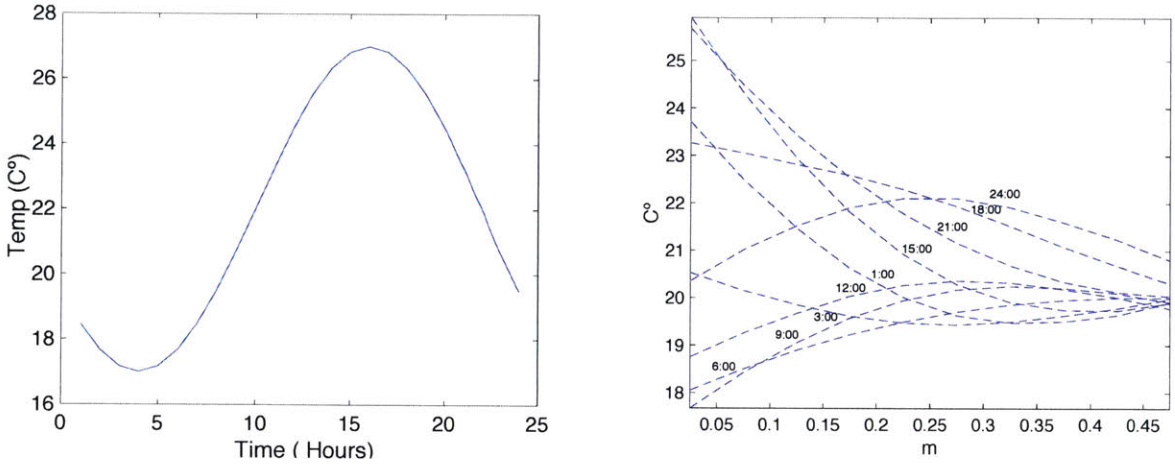

Figure 3.4.13 *Left:* sinusoidal input of external temperature. *Right*: cross section of the hourly temperature variations inside the wall with an insulated inner boundary.

In figure 4.3.13, cross section of the temperature variation inside the wall is shown at different hours for a varying temperature applied on the external wall. The inner wall is insulated in this case. Figure 4.3.14 show the distribution of temperatures for an insulated inner wall compared to inner wall at constant temperature (simulating A/C).

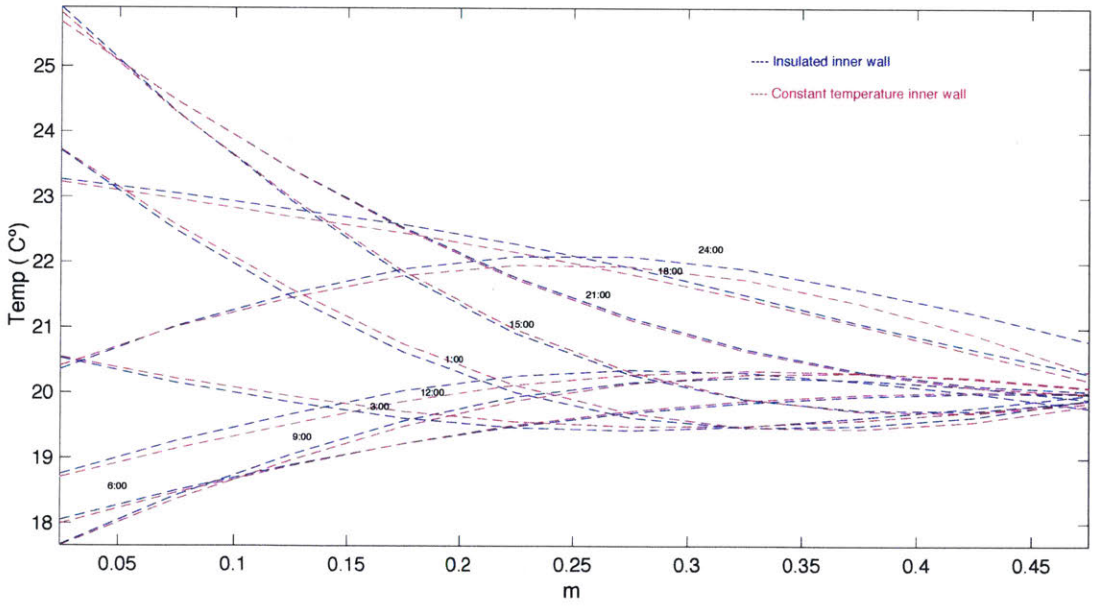

Figure 3.4.14 Comparison between the temperature variations for an insulated and a constant temperature inner boundary. The initial temperature is 20 °C

When the inner boundary is kept at the constant temperature, the temperature of the inner wall doesn't vary much, while it can vary few degrees from the initial temperature when the inner boundary is insulated. In a month-long simulation (fig. 4.3.15), the differences between the two type of boundary conditions are even more evident: the envelope of the temperatures for a simulated A/C is narrower, meaning less variation of temperatures inside the wall.

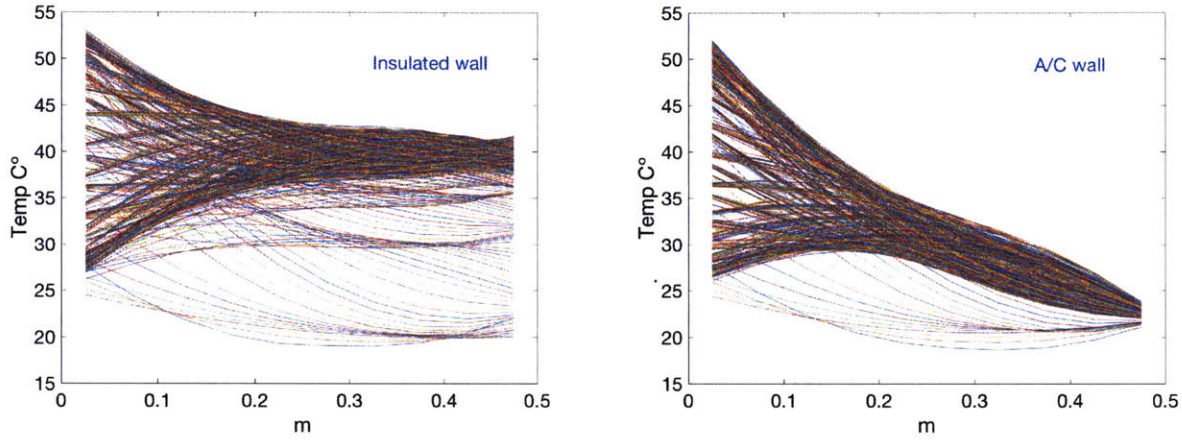

Figure 3.4.15 Comparison between the temperature variations for an insulated and a constant temperature inner boundary for a 30 days long simulation. The initial temperature is 20 C°

In figure 4.3.16 the variation of temperature for the external wall with the two boundaries condition is shown: the resulting inner wall temperature is a sinusoid with a smaller amplitude, reduced of about 7 degrees, and phase shift of about 8 hours for this type of wall. For the insulated boundary case, the overall temperature of the wall increase until the equilibrium is reached. The resulting sinusoid will be located at a temperature higher than the A/C case and the equilibrium temperature will depend on the initial conditions.

As the amplitude of the resulting sinusoid as well as the phase variation depend on the properties of the wall, I simulated the internal temperature changes for three different walls configurations. The inside temperature is kept at 22 °C throughout the day. The three walls have the same overall dimensions but they are made of different materials and the insulated layers are different thicknesses. The calculations are carried out with the real temperatures of February 22nd.

The first wall is made of ~ 20 m concrete layer and 2cm insulation material in the interior and exterior surfaces; the second wall is similar to the first wall, but with a mid-layer of brick instead of concrete; the third layer has the same materials of the first wall, but the insulation layers are 10 cm thick.

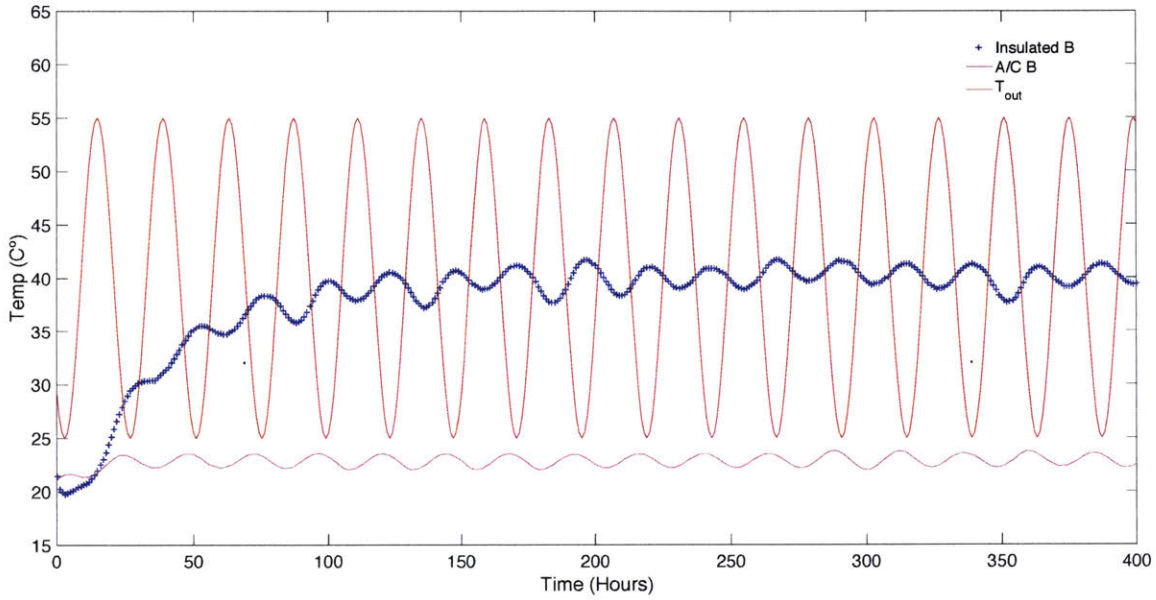

Figure 3.4.16 Input and output temperatures for insulated and constant temperature boundary conditions.

In the simulation, we observe that the outside temperature has 7 °C degrees of change throughout the day, while the inner temperature varies only of 2 °C degrees for the first two walls and doesn't change for the insulated wall. The only variation in the inside temperature is when there is a temperature difference between the inside and the outside of the time lag for the three walls is between 4 to 5 hours between the external temperature peak and the interior temperature peak. The different boundary conditions will be tested in the calculation of the mechanic stresses described in the next section.

3.2.7 Thermal stress at the Al-Hamra tower

For this preliminary analysis, I modeled the deformation of Al-Hamra tower, applying different temperatures to each side of the building, based on the annual solar radiation and temperature

variations. The finite element model was developed with two modules of *COMSOL Multiphysics* software: the heat transfer module to evaluate the distribution of temperature on the exterior of the building due to solar radiation and the structural mechanic module to calculate the mechanical expansion.

In the preliminary model, the geometric structure of the Al-Hamra tower has been simplified into a concrete hollow square prism, with a base 40 m in length and a height of 400 m and with 9 floors of 1 m thickness at 40m intervals. The thickness of the walls has been varied between 0.5 to 3m. The curtain wall hasn't been considered in the structural calculation. The bottom of the prism has a fixed boundary condition, while all the other surfaces of the building are free to move. On the external walls a time varying temperature, calculated as described in the previous paragraph, has been imposed. Two type of boundary conditions on the inner walls have been tested: an insulated boundary condition with no thermal exchange inside the building and a A/C boundary condition, simulated as a constant temperature, varying between 20 C° to 22 C°.

The value used for thermal conductivity was 1.6 W/$(m \cdot K)$, while specific heat and concrete density's values were 950 J/$(kg \cdot K)$ and 2400 kg/m^3, respectively. The surface emissivity was 0.85 and absorption coefficient was 0.5. The calculation has been carried for four different periods of the year: two short periods of 2016 (January 29-31st and August 3-5th) to simulate the sub-daily deformation, a month-long period (September 2016) to test the approximation of the external temperature of the walls with changing weather conditions and a full two year models with 1-day averaged temperatures. For all the models, the FEM NS component has been rotated of 8 degree to coincide with the NS component of the GPS estimates. I first tested the sensitivity of the model to different parameters, such as thickness of the wall and internal boundary conditions. In order to do that, I applied a temperature to the south wall, varying from 20 C° to 50 C° daily for a month-long simulation. The thickness of the wall influences the temperature distribution inside the wall, especially the temperature reached by the inner wall and the overall temperature of the building. Therefore, the resulting deformation will be different depending on the thickness of the wall. Figure 4.3.17 shows the simulation for different thicknesses for varying temperature between 20 C° and 50 C°. In a thinner wall the temperature of the inner walls reaches a higher temperature in a shorter time than in a thicker wall and the building reaches overall a higher temperature, resulting in an expansion of the building, rather than bending. The resulting hourly deformation is about 10 mm at mid-day for a wall of 0.5 m and about 30 mm for a wall of 3 m. The number of floors in the

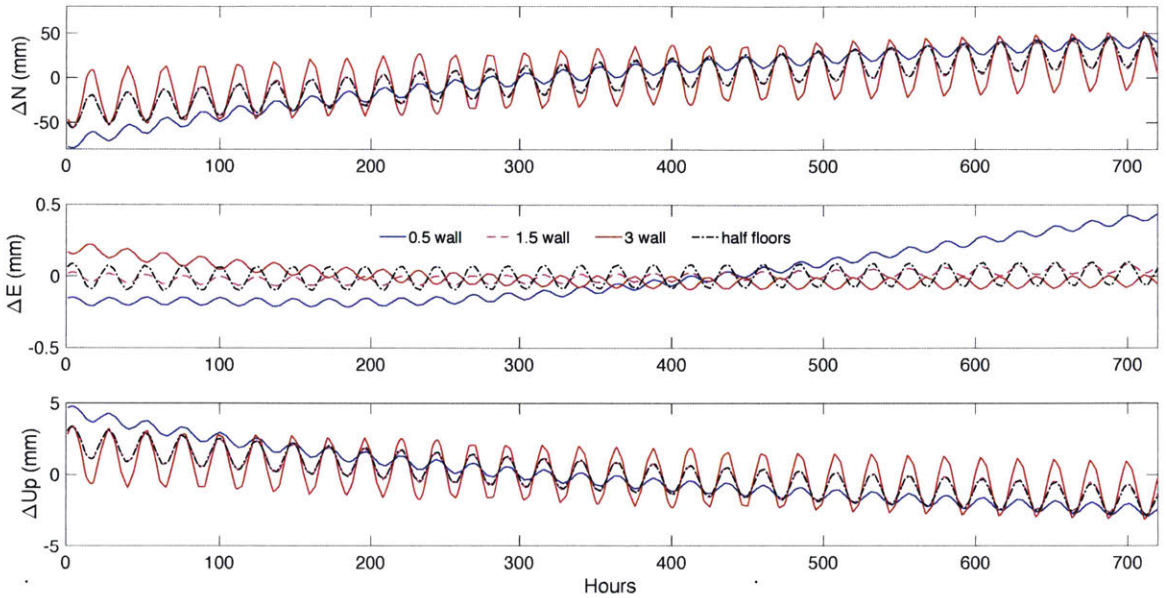

Figure 3.4.17 Comparison between different walls thickness and number of floors. The simulations show that a thicker wall has a larger sub daily motion variation, while a thinner wall has a higher monthly rate of deformation. Note the different scales on the displacement components.

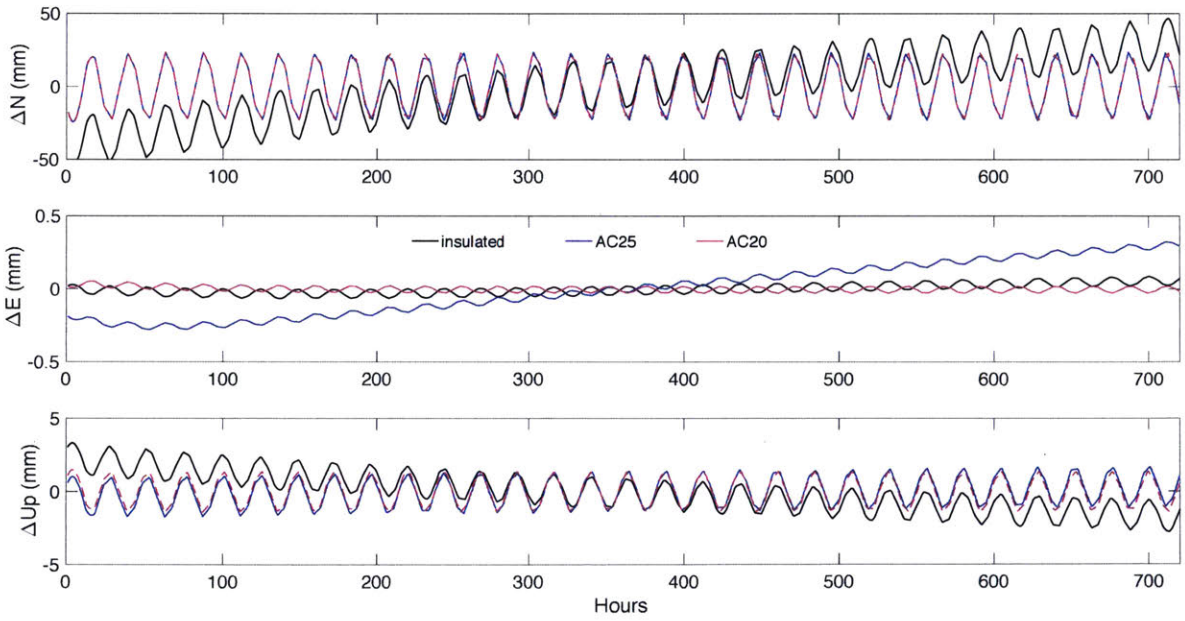

Figure 3.4.18 Comparison between inner walls models. The higher deformation is obtained with a simulated A/C on the inner walls with temperature of 20 and 22 C°. Note the different scales on the displacement components.

building also influences the distribution of temperatures inside the building and therefore the

deformation of the building. In particular, a larger number of floors results in a more stable lower temperature inside (that depends on the boundary conditions) and therefore the sub daily deformation is larger.

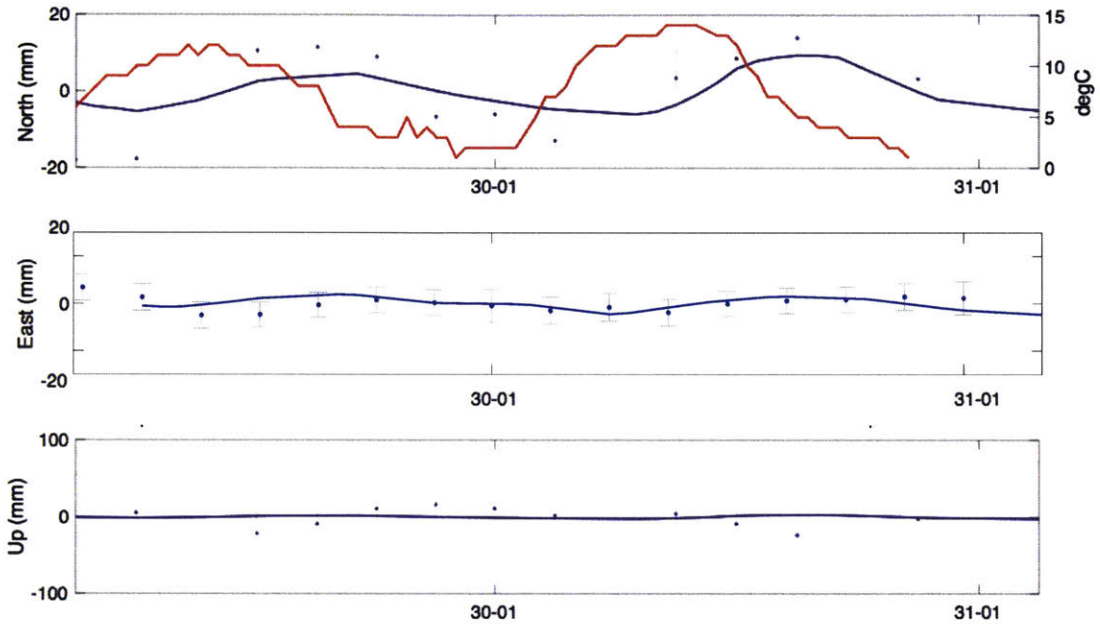

Figure 3.4.19 Comparison between the FEM model and GPS 6-hours solutions for January 29th-30th 2016 for the North (*top*), East (*middle*) and Up (*bottom*) component. *Top:* in red the hourly temperature is shown.

Different boundary conditions on the inner walls of the building have been tested: one model simulates A/C inside the building as a constant temperature inside the building; another model has an insulated layer on the inner walls. Different A/C temperatures have been modeled. The results are shown in figure 3.4.18. The two AC models have comparable daily motions, but different monthly rate for the E component. The insulated model shows a smaller daily variation and different monthly rate.

Preliminary results of 48 hours simulations at the end of January (fig 3.4.19) and the beginning of August (fig. 4.3.20) periods shows that the thermal model reproduces quite well the sub-daily motion by the GPS 6-hours solution, especially for the North and East components for a model with a 1.5 m thick wall and a mean solar radiation calculation. The time lag between the outside temperature and the surface temperature of the walls is about 3 hours.

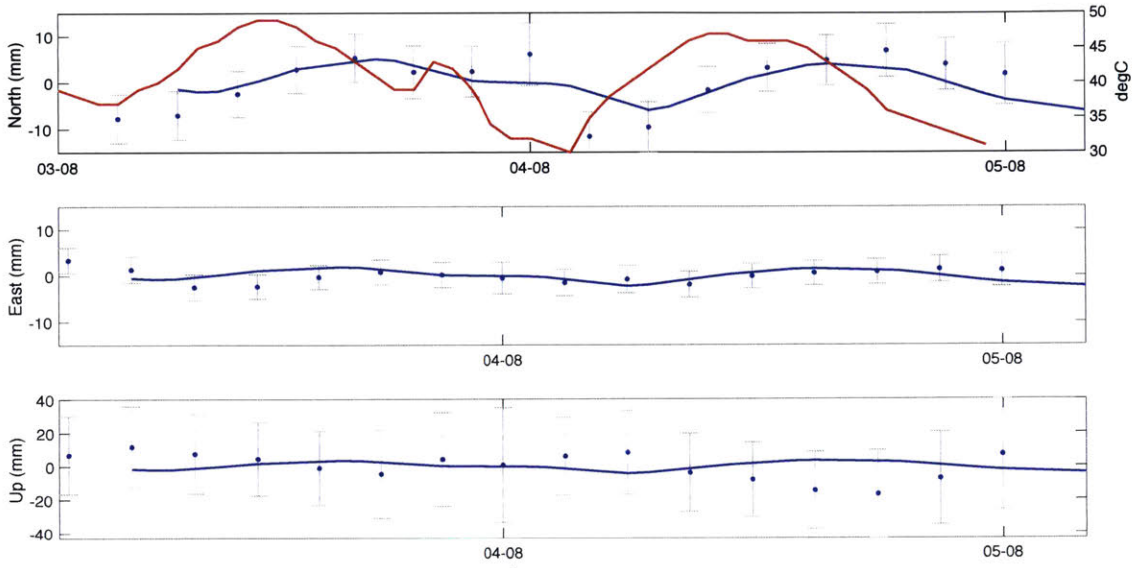

Figure 3.4.20 Comparison between the FEM model and GPS 6-hours solutions for August 3rd-5th 2016 for the North (*top*), East (*middle*) and Up (*bottom*) component. *Top:* in red the hourly temperature is shown.

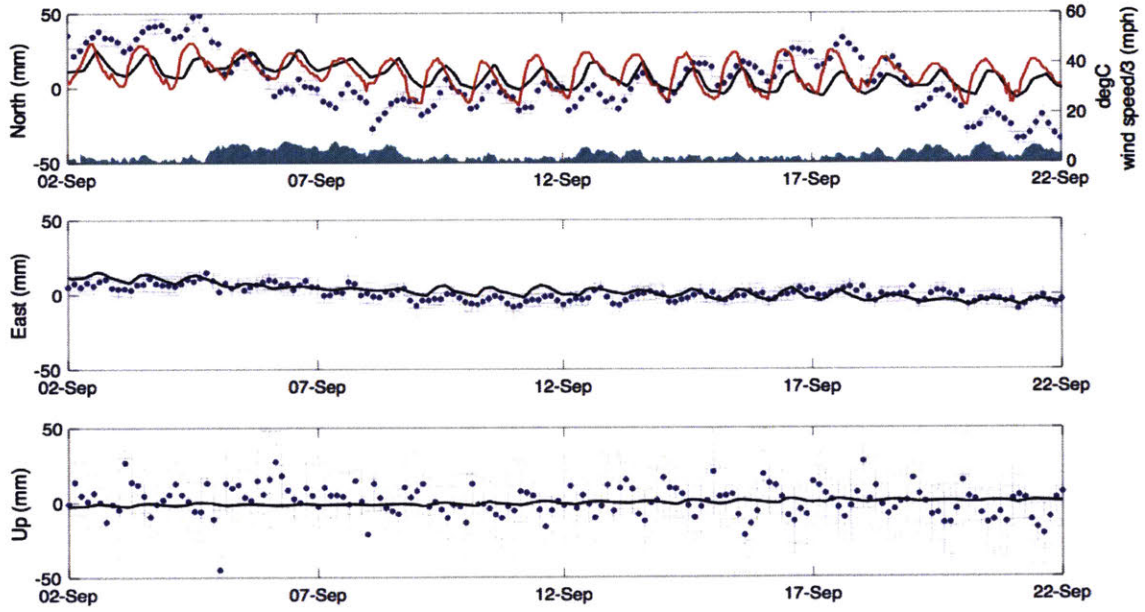

Figure 3.4.21 Comparison between the FEM model and GPS 6-hours solutions for September 2016 for the North (*top*), East (*middle*) and Up (*bottom*) component. *Top:* in red the hourly temperature is shown and in green the wind speed divided by 3. The time lag between the temperature and the deformation is about 3 hours.

The simulation for September month is shown in figure 3.4.21. The model fits very well the sub

daily motion of the east component, with few mm of deformation reached at mid-day. The deformation of the North component calculated by the model doesn't fit as well as the east component. In particular, for days with no wind, the displacement appears lower and for windy days, the displacement is overestimated. The result suggests that the temperatures used in the simulation are likely to be underestimated in days with good weather condition and overestimated in windy days. In the two year-long simulation (fig. 3.4.22), the displacement is estimated to be ~ 250 mm peak-to-peak for the N-S component, 10 mm for the EW component and 20 mm for the Up component. After the model reaches the equilibrium in the second half of 2014, the lag between the North component of the model and the daily temperature variation is ~14 days. The amplitude of the seasonal motion for the FEM model (~96.8 mm) is in agreement with the value estimated from the GPS data of the 86th floor site (~100.68 mm). However, there is a lag of about 6 days between the ALHR site North motion and the FEM model displacement. This can be due to different value of the admittance of the wall: in the FEM model, the perimeter wall has been simplified as a concrete slab of 0.5 m. However, the actual composition of the wall is more elaborated, with steal elements that can contribute to a faster heat exchange within the wall.
In table 3.4.1, the estimates of the periodic signals in the north position estimated, FEM model and temperature is reported. The GPS data are from the 86th floor site (ALHR) for the period Jan 22nd, 2016 - Jan 30th 2017.

Period (days)	North Amplitude GPS (mm)	North Amplitude FEM (mm)	Temperature Amplitude (C°)	Lag (days) GPS-Temp	Lag (days) FEM-Temp
1	12.82	8.15	6.23	-0.17	-0.13
30	2.69	1.9	0.4	-2.86	-3.6

Table 3.4.1. Estimates of the periodic signals in the north position estimated, FEM model and temperature is reported. The GPS data are from the 86th floor site (ALHR) for the period Jan 22nd, 2016 - Jan 30th 2017.

It can be concluded that a simple model of thermic stress due to differential temperatures on the outer walls of Al-Hamra tower can generally explain the daily and sub-daily motion observed in the GPS measurements. However, a more accurate analysis of the temperature, especially in

different weather conditions, is necessary to improve the fit of the finite element model with the observed deformation. In addition, including the curtain wall and a composite wall structure can improve the model, resulting a more realistic representation of the geometry of the tower.

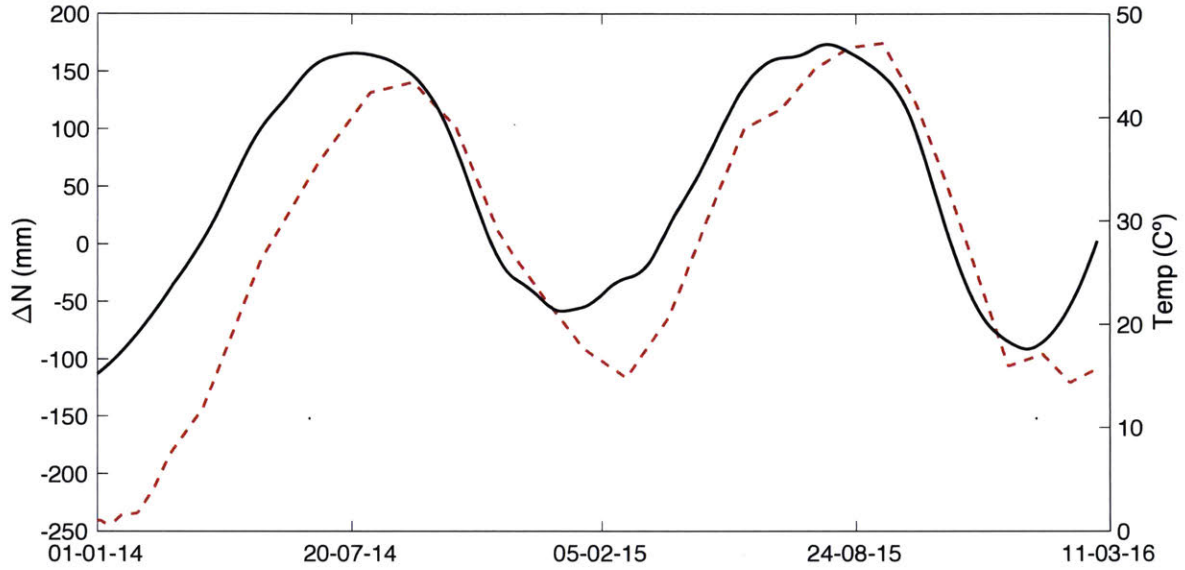

Figure 3.4.22 Comparison between the North component of the FEM model (*red*) and smoother temperature daily variation (*black*). The lag is 14 days.

3.2.8 Wind environment

Another cause of deformation of tall building on short periods is determined by sustained winds. The synoptic wind patterns in the gulf region are the result of the large-scale movement of air channeled along the north-westerly/south-easterly axis of the Persian Gulf. The wind climate is further affected by the local topography in each area around the Gulf. Very localized and short-term wind phenomena are known to exist in the Gulf region due to thunderstorms producing strong downbursts close to the ground. These downbursts form a cold air mass being deflected downward by a moving warm air mass, due to a strong temperature gradient. The incidence on the ground surface of the cold air mass generates short duration high intensity winds. Due to the presence of these strong winds, the structural design of the Al-Hamra tower was anticipated to be controlled by wind induced forces on the buildings and wind tunnel study model was developed.

While the thunderstorm wind profile could prove to be critical wind event for the structural system of a tower lower than 200m in height, the gross effect of the synoptic wind profile over the full height of the Al-Hamra tower controlled the design in all aspects.

The effects of the wind on the building have been carefully evaluated using the filtered 1-Hz data.

3.2.6 Wind-induced deformation of Al-Hamra tower

A full-scale finite element model of the Al-Hamra Tower was developed using ETABS by the Dept. of Civil Engineering team and by the KISR (Kuwait Institute for Scientific Research) team. Three types of elements were used in the model, namely, beam, frame and shell elements to describe beam, column, slab and shear walls, respectively. The preliminary results are shown in table 3.4.2.

The impulse response of the building has been also calculated through ambient vibration. The vibrations are recorded continuously at different levels and used to compute the impulse response of the building through interferometric approach. For ambient vibrations, it has been shown that,

Mode	FEM Period (sec)	Seismic data (sec)	GPS (sec)
North/South	7.87 (6.86)	7.09	7.27
East/West	5.78 (4.91)	5.65	5.82
Torsional	3.29 (3.23)	3.27	3.38

Table 3.4.2 Comparison between the modes of Al-Hamra tower, simulated by the KISR and MIT (*in parenthesis*) finite element models, calculated by ambient noise and calculated by GPS at the 86^{th} floor.

if the vibration sources are homogeneously distributed around and inside the building, the deconvolution between signals recorded at different floors will be the impulse response waveform of the portion of the building located between the two sensors. Preliminary results from the ambient vibration data calculations show resonant peaks at 7.09 s, 5.65 s and 3.29 s. These estimates come from a very short, temporary seismic deployment on the 80^{th} floor terrace.

The fundamental modes of Al-Hamra tower are detected by the high rate GPS with some variability due to the presence of a source of excitation for the building. In particular, in windy days, the three fundamental modes are visible at periods 7.22 s, 5.82 s and 3.38 s. In days where no source of excitation is present, only the first mode is visible (figure 3.4.25). In the table 3.4.2

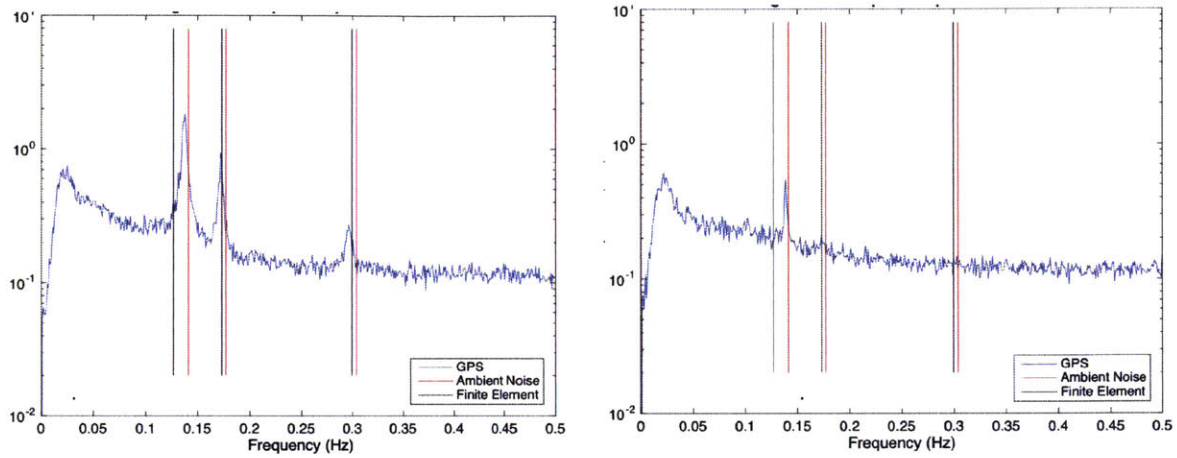

Figure 3.4.25 Example of mode excitations at the 86th floor GPS site. These averaged amplitude spectra are based on the averages of power-spectral density estimates from 20-minute, non-overlapping, data segments. A low pass filtered signal is removed first to reduce the longer period motions from noise, multipath, and temperature variations. The red and black lines are the expected mode frequencies from a very short, temporary seismic deployment (red) and from the finite element model.

are reported the preliminary results for the modes of Al-Hamra tower calculated by the FEM model and estimated by the GPS and ambient noise data.

The fundamental modes estimated by the FEM and measured by GPS and Ambient Noise differs due to the complexity of the vibrating structure as well as different sources of excitation.

3.3 Conclusions and future work

In this study, I analyzed the long- and short-term deformation of the Al-Hamra tower through GPS measurements and finite element modeling. Initially, two temporary GPS (TERR and TER2) sites are installed on the 80th floor of the building to measure the displacement of the tower. After running for about a year, one of the site (ALHR) is moved to the tip of the curtain walls where no obstructions are present and is mounted on the wall through a 4.5 m stainless steel pole. The new GPS site data shows a better quality as the station is less impacted by multipath.

Al-Hamra terrace sites (TERR and TER2) show a complex pattern of high frequency signals, due to reflecting signals from nearby objects. Short term position estimations at TERR stations are mostly affected by multipath and poor sky configuration. The characteristics of the multipath signature, assessed with a spectral analysis and comparison with other stations in not obstructed environments, are short term duration (up to 1 hour) and repeated pattern for different days with time shifts approximately consistent with sidereal day duration. Two methods to mitigate the effects of the multipath are proposed. For the 24-hr and 6-hour analysis, a phase center model is tested. The fit is performed in azimuth bins with a piecewise linear function in zenith angle and has been tested for a 1 and 0.5 degree grid. While the 1-degree function models reasonably well the phase residuals for KUWT and KISR sites, the 0.5-degree function shows a better fit at the two Al-Hamra sites with high frequency signals. In the 24hr solution, the RMS of the phase residuals drops of ~1.5 mm when the 0.5 grid is applied to KISR and KUWT stations and ~4-5 mm and ~ 3-4 mm for TERR and TER2 respectively. The model is not as effective on the 6-hrs solution: RMS of the phase residuals, in fact, only drops by 1 mm. As discuss previously, the 6-hrs solution is also corrupted by poor sky configuration at certain time of the day.

For 1Hz GPS solution, a finite impulse response (FIR) filter is used to filter multipath, once recognized the spectral characteristics. This filtering technique allows to reduce the multipath effect as well as the noise on TERR site.

GPS measurements have been made near the top of the Al-Hamra building for almost two years and during that time these measurements have shown predominately north-south (NS) motions of ±100 mm with an annual period and daily NS motion with an average amplitude of ±12 mm. These motions are highly correlated with local air temperature.

The temperature behavior is consistent with thermal straining of the building that results in it bending, due presumably, to differences in temperature between the south facing stone façade side of the building and the north, curtain-wall enclosed side of the building. A thermic stress finite element model was developed to estimate the deformation of the building due to differential temperature applied to the south and north walls. The different temperatures on the walls are modeled as effect of the solar radiation varying throughout the day and varying air temperature. The cooling effect of the wind is also tested using a fluid dynamic model to simulated the effect of the wind on the building. The preliminary results of the finite element model reproduce accurately the motion of the building in days with no wind, but the estimated displacement is higher in windy days compared to the measured motion in the GPS solutions.

We found similar amplitudes for the N-S seasonal daily and sub-daily signals: ~ 100 mm for 1-yr period, ~2.6 mm for 30-days period and ~12: 82 mm for 1-day period, estimated from the 86th floor GPS site (ALHR), and ~96 mm for 1-yr period, ~1.9 mm for 30-days period and ~ 8.15 mm, estimated from 1-day period for FEM model. The lags are respectively ~6 days, 2.8 days and ~4 hours for ALHR and ~14 days, 3.6 days and 3.8 hours for FEM model. The discrepancy in the time lags can be explained with the admittance value of the wall. In the FEM model, the perimeter wall has been simplified as a concrete slab of 0.5 m. However, the actual composition of the wall is more elaborate, with steal elements that can contribute to a faster heat exchange within the wall. It can be concluded that a simple model of thermic stress due to differential temperatures on the outer walls of Al-Hamra tower can generally explain the sub-daily motion observed in the GPS measurements. However, a more accurate analysis of the temperature, especially in different weather conditions, is necessary to improve the fit of the finite element model with the observed deformation. In addition, including the curtain wall and a composite wall structure can improve the model, resulting a more realistic representation of the geometry of the tower.

The effects of the wind on the building have been carefully evaluated using the filtered 1-Hz data. The amplitude of the displacement due to the wind varies from few mm to 15 mm.

The fundamental modes of Al-Hamra tower are detected by the high rate GPS solutions. In particular, in windy days, three fundamental modes are visible at periods 7.22 s, 5.82 s and 3.38 s. The wind-induced peak response has been compared to the modal analysis conducted through FE model and estimated from the seismic noise.

Future work will include a more accurate phase center models to be included in the GPS analysis software to reduce the effects of the high frequency components of the multipath; a more accurate model of Al-Hamra tower, including a more realistic temperature in different weather condition and a more accurate wall structure and geometry. Finally, a temporal analysis of the fundamental modes of Al-Hamra tower will improve the understanding of the long term structural behavior of the building.

Conclusions and future work

This doctoral thesis project focused on the application of geodetic techniques and finite element modeling to the studying crustal deformation and other processes. In particular, it focused on optimizing standard processing strategies, reducing the noise in the measurements and mitigating the effects of external processes in order to extract the signal of interest. Geodetic techniques, such GPS and InSAR, have improved tremendously in the recent years. Accuracies of few millimeters for ground displacement allow their application to the study of a wide variety of geophysical processes. However, their theoretical accuracy is not always achievable: processes such as multipath, atmospheric effects, snow, blockage of the signal by infrastructures can introduce a consistent amount of noise, making the detection of geophysical signal more difficult.

In this thesis, I analyzed three sets of data for which I used different approaches to estimate correctly the displacement and to investigate the sources of deformation that contribute to the signal.

The first project consisted in studying the deformation caused by seasonal cycle of injection/withdrawal of gas in a depleted gas reservoir using InSAR measurements and Finite Element modeling. I demonstrated that PS scatter technique used to process the InSAR data produce more coherent results compared to standard processing techniques presented in previous studies (Teatini et al. 2008). I presented a method to estimate noise covariance of InSAR data, taking into account the spatial correlation of noise between individual data points in the interferograms. The correlation length for each interferogram imaging the Beta gas field, calculated fitting a Gaussian curve, varies from 5 km to 10 km. The data were averaged and filtered InSAR data in order to reduce the numbers of points, reduce the noise in the data and remove regional signals. Comparison with the forward model have shown that the averaging with a grid size between 1 and 1.7 km has the best trade-off between noise reduction and retaining enough data points that contribute to the reservoir deformation.

The deformation was modeled through a Finite Element Model where pressures in the reservoir due to injection/withdrawal of gas was input to the geomechanical model. The modeled pressure variations inside the reservoir, provided by ENI-Stogit S.p.A. (2008), ranged between 105 kg/cm^2

and 140 kg/cm^2 and between 100 kg/cm^2 and 160 kg/cm^2 in the 107% and 120% scenarios respectively.

The simulated geomechanical response of the reservoir subject to fluid injection/production with a three-dimensional elastic model and vertical varying properties varied between 15 mm of subsidence and 5 mm of uplift. The comparison between the finite element model showed that InSAR time series are delayed in time respect to the model predictions. Deformation maps showed a complex spatial distribution of the deformations that was not reproduced by the FEM model. These patterns in the deformation are likely related perturbations of parameters in horizontal directions.

Future work will include the introduction of two-way coupling between the flow model and the geomechanical model to improve the fit with the InSAR measurements. Finally, I suggest the addition of GPS data to complement the InSAR measurement as they can be used to estimate the atmospheric contribution to the InSAR signal, which still represent a large source of uncertainty during the processing. The continuity of GPS data will also improve the time coverage of the geodetic data.

The second project analyzed the unrest of KATLA volcano in Iceland using GPS observables. GPS stations on top of the volcano register a complex signal, caused by the concurrence of different processes, such as snow on the antenna, multipath, earthquakes, volcanic deformation and hydrological events. In this project, I explored methods to model the effects of snow/ice on top of antennas and separate the different sources of the signal to extract the volcanic deformation component. The proposed snow detection algorithm, based on the spectral analysis of the signal-to-noise ratio (SNR), successfully detects spectral peaks variability throughout the year. The interpretation of these results is for now based on speculation on temporal and spatial characteristics of the spectral peaks (persistent in winter time), as snow data are unavailable at the location.

The second section of this project focused on the seasonal signal observed at AUST station on top of the volcano. The GPS motion at AUST station reveals a strong year-modulated signal, moving of about 2-2.5 cm on average in SW direction (toward the caldera) during the winter with the minimum value reached in March/April and it moves of about 2-2.5 cm in NE direction (away from the caldera) in the summer with maximum reached in August/September. The rate of

displacement in the summer is higher than the winter, meaning that the deformation measured by station is faster during the summer months. The vertical displacement of AUST station is about 4 cm on average in the up direction during the winter months with maximum value reached in November/December and about the same magnitude but in down direction during the summer months with the minimum reached in June.

I estimated the coherence of the seasonal deformation with different data and the analysis indicates that there is a correlation between the variation of air temperature, barometric pressure, precipitations (shorter periods) and gravity (longer period) and the observed deformation.

In section 3, I modeled the snow/ice loads as a possible source of deformation with depth varying properties of the crust and low-velocity magma chamber. To fit the observed deformation of 4 cm in the vertical and 2 cm in the horizontal components, as measured at AUST station, the loss of snow/ice from the ice-cap should be of about 40 m. The current estimates of mass balance at the Myrdalsjökull icecap only account for up to 6 meters in snow accumulation during the winter months and up to 65 cm/yr for the glacier retreat. I therefore concluded that ice/snow loading cannot explain the magnitude or phase of the deformation observed on the volcanic rim. I also suggested an alternative mechanism to explain the observed deformation: the freeze/melting cycles inside the pores and fractures of the rock beneath the volcano can cause change in pressure and ground deformation as well as reconfiguration of the hydrological system, with consequent circulation of geothermal gasses and fluids.

This study stresses the difficulties of interpreting the deformation of sub-glacial volcanoes, as different sources of deformation contribute to the measured signal. It then becomes necessary to carry out a thorough analysis of the observed deformation pattern at different time scales to separate different contributions and with a variety of measurements.

For future work, I recommend the installation of a camera and a meteorological station at the AUST station location to capture snow accumulation and measure weather data to compare with the spectral analysis of the SNR. And for the detection algorithm validation, I suggest this analysis to be applied to stations at different locations where similar behavior is observed.

I also suggest a poroelastic model to study the effects of melting/freezing of water inside the pores and fractures of the rocks beneath Katla volcano.

The third project involves the analysis long term deformation and determination of vibrations of the Al-Hamra tower in Kuwait, using 24-hours averaged, 6-hours averaged and 1Hz GPS measurements. The signals of GPS stations mounted on buildings are often affected by multipath due to reflective objects on the roof and by reduced accuracy due to the partial masking of the sky by infrastructures on the roof. I explore different ways to mitigate the multipath and loss of accuracy, assessing an optimal GPS processing strategy for building installation.

Al-Hamra terrace sites (TERR and TER2) show a complex pattern of high frequency signals, due to reflecting signals from nearby objects. Short term position estimations at TERR stations are mostly affected by multipath and poor sky configuration.

Two methods to mitigate the effects of the multipath are proposed. For the 24-hr and 6-hour analysis, a phase center model is tested. The fit is performed in azimuth bins with a piecewise linear function in zenith angle and has been tested for a 1 and 0.5 degree grid. While the 1-degree function models reasonably well the phase residuals for KUWT and KISR sites, the 0.5-degree function shows a better fit at the two Al-Hamra sites with high frequency signals. In the 24hr solution, the RMS of the phase residuals drops of ~1.5 mm when the 0.5 grid is applied to KISR and KUWT stations and ~4-5 mm and ~ 3-4 mm for TERR and TER2 respectively. The model is not as effective on the 6-hrs solution: RMS of the phase residuals, in fact, only drops by 1 mm. As discuss previously, the 6-hrs solution is also corrupted by poor sky configuration at certain time of the day.

For 1Hz GPS solution, a finite impulse response (FIR) filter is used to filter multipath, once recognized the spectral characteristics. This filtering technique allows to reduce the multipath effect as well as the noise on TERR site.

GPS measurements have been made near the top of the Al-Hamra building for almost two years and during that time these measurements have shown predominately north-south (NS) motions of ±100 mm with an annual period and daily NS motion with an average amplitude of ±12 mm. These motions are highly correlated with local air temperature.

The temperature behavior is consistent with thermal straining of the building that results in it bending, due presumably, to differences in temperature between the south facing stone façade side of the building and the north, curtain-wall enclosed side of the building. A thermic stress finite element model was developed to estimate the deformation of the building due to differential temperature applied to the south and north walls. The different temperatures on the walls are

modeled as effect of the solar radiation varying throughout the day and varying air temperature. The cooling effect of the wind is also tested using a fluid dynamic model to simulated the effect of the wind on the building. The preliminary results of the finite element model reproduce accurately the motion of the building in days with no wind, but the estimated displacement is higher in windy days compared to the measured motion in the GPS solutions.

We found similar amplitudes for the N-S seasonal daily and sub-daily signals: ~ 100 mm for 1-yr period, ~2.6 mm for 30-days period and ~12. 82 mm for 1-day period, estimated from the 86th floor GPS site (ALHR), and ~96 mm for 1-yr period, ~1.9 mm for 30-days period and ~ 8.15 mm, estimated from 1-day period for FEM model. The lags are respectively ~6 days, 2.8 days and ~4 hours for ALHR and ~14 days, 3.6 days and 3.8 hours for FEM model. The discrepancy in the time lags can be explained with the admittance value of the wall. In the FEM model, the perimeter wall has been simplified as a concrete slab of 0.5 m. However, the actual composition of the wall is more elaborated, with steel elements that can contribute to a faster heat exchange within the wall. It can be concluded that a simple model of thermic stress due to differential temperatures on the outer walls of Al-Hamra tower can generally explain the sub-daily motion observed in the GPS measurements. However, a more accurate analysis of the temperature, especially in different weather conditions, is necessary to improve the fit of the finite element model with the observed deformation. In addition, including the curtain wall and a composite wall structure can improve the model, resulting a more realistic representation of the geometry of the tower.

The effects of the wind on the building have been carefully evaluated using the filtered 1-Hz data. The amplitude of the displacement due to the wind varies from few mm to 15 mm.

The fundamental modes of Al-Hamra tower are detected by the high rate GPS solutions. In particular, in windy days, three fundamental modes are visible at periods 7.22 s, 5.82 s and 3.38 s. The wind-induced peak response has been compared to the modal analysis conducted through FE model and estimated from the seismic noise.

Future work will include a more accurate phase center models to be included in the GPS analysis software to reduce the effects of the high frequency components of the multipath; a more accurate model of Al-Hamra tower, including a more realistic temperature in different weather condition and a more accurate wall structure and geometry. Finally, a temporal analysis of the fundamental modes of Al-Hamra tower will improve the understanding of the long term structural behavior of the building.

Bibliography

Aagaard, B., C. Williams, M. Knepley (2008), PyLith: A finite-element code for modeling quasi-static and dynamic crustal deformation, *Eos Trans. AGU, 89(53),* Fall Meet. Suppl., Abstract T41A-1925.

Agarwal R., tari N., Hu L., Mathias N., Mazeika A., Sarkisian M., 2007, Sculpted High-rise, The Al-Hamra Tower, CTBUH technical Paper, Skidmore, Owings & Merrill LLP San Francisco, USA

Albino, F., V. Pinel, and F. Sigmundsson (2010), Influence of surface load variations on eruption likelihood: Application to two Icelandic subglacial volcanoes, Grímsvotn and Katla, *Geophys. J. Int.*, *181*, 1510–1524,

Árnadottir, Th. et al. Glacial rebound and plate spreading: results from the first countrywide GPS observations in Iceland. Geophys. *J. Int.*, 177, 691–716; DOI:10.1111/j.1365-246X.2008.04059.x (2009)

ASHRAE (American Society of Heating, Refrigerating and Air-Conditioning Engineers) Fundamentals,(1997), *ASHRAE Fundamentals* 28.5, Atlanta

Auriac, A., Spaans KH, Sigmundsson F, Hooper A, Schmidt P, Lund B, (2013). Iceland rising: Solid Earth response to ice retreat inferred from satellite radar interferometry and visco-elastic modeling. *J. Geophys. Res.-Sol. Ea., 118, 1331–1344; DOI:10.1002/jgrb.50082*

Axelrad, P., C. J. Comp, and P. F. Macdoran (1996), SNR-based multipath error correction for GPS differential phase, *IEEE Trans. Aerosp. Electron. Syst.*, 32, 650–660.

Beauducel F., Briole P., Froger J., 2000 Volcano-wide fringes in ERS synthetic aperture radar interferograms of Etna (1992-1998): Deformation or tropospheric effect?, JOURNAL OF GEOPHYSICAL RESEARCH, VOL. XX, NO. X,

Bilich, A., K. M. Larson, and P. Axelrad (2008), Modeling GPS phase multipath with SNR: Case study from the Salar de Uyuni, Boliva, J. Geophys. Res., 113, B04401, doi:10.1029/2007JB005194.

Biot, M. A. (1941), A general theory of three-dimensional consolidation, J. Appl. Phys., 12(2), 155–164.

Bishop, A. W. (1959), The principle of effective stress, Tek. Ukebl., 39, 859–863.

Bliss R.W. Jr, 1963, Atmospheric radiation near the surface of the ground: a summary for engineers. Solar Enenrgy 5:103-120.

Braasch, M. S. (1996), Multipath effects, in Global Positioning System: Theory and Applications, vol. 1, edited by B. W. Parkinson et al., chap. 14, Am. Inst. of Aeronaut. and Astronaut., Reston, Va.

Burgmann R. Rosen P.A. and Fielding E.J. (2000), Synthetic Aperture Radar Interferometry to measure Earth's surface topography and its deformation, Annu.Rev. Earth Planet. Sci., 169-209

Celebi M., 1998, The Loma Prieta, California earthquake of October 17, 1989- Building structures, U.S. Geological Survey, Professional Paper 1552-C.

Chen Gu, (2016). Ground Motions and Source Mechanisms of Earthquakes in Multiscale-Microseismicity to Macroseismicity, Doctoral thesis dissertation, MIT.

Comsol Multiphysics User's Guide, 2014, Comsol Multiphysics User's Guide, 466, 2016 Version 5.3, Comsol AB, Stockholm, Sweden.

Cubit User Manual v. 11.2 (2011), Sandia National Laboratories.

Delacourt C., Briole P., Achache J. (1998) Tropospheric corrections of SAR interferograms with strong topography: Application to Etna. Geophys. Res. Lett.;25:2849–2852

Delacourt C., Briole P., Achache J. (1998) Tropospheric corrections of SAR interferograms with strong topography: Application to Etna. Geophys. Res. Lett.;25:2849–2852

Doglioni, C., Some remarks on the origin of foredeeps, *Tectonophysics*, 228, 1–20, 1993.

Drouin V., Kosuke Heki, Freysteinn Sigmundsson, Sigrún Hreinsdóttir, Benedikt G. Ófeigsson (2016), Constraints on seasonal load variations and regional rigidity fromcontinuous GPS measurements in Iceland, *1997-2014*. Geophysical Journal International, 205:1843–1858. doi: 10.1093/gji/ggw122

Emardson, T. R., M. Simons, and F. H. Webb (2003), Neutral atmospheric delay in interferometric synthetic aperture radar applications: Statistical description and mitigation, J. Geophys. Res., 108(B5), 2231.

F. Onn, H. Zebker (2006), Correction for interferometric synthetic aperture radar atmospheric phase artifacts using time series of zenith wet delay observations from a GPS network, Journal of Geophysical Research, 111

Ferretti, A., C. Prati, and F. Rocca (2001), Permanent scatterers in SAR interferometry, IEEE Trans. Geosci. Remote Sens., 39(1), 8–20.

Ferretti, A., G. Savio, R. Barzaghi, A. Borghi, S. Musazzi, F. Novali, C. Prati, and F. Rocca (2007), Sub-millimeter accuracy of InSAR time series: Experimental validation, IEEE Trans. Geosci. Remote Sens., 45(5), 1142–1153.

Fialko, Y., M. Simons, and Y. Khazan (2001), Finite source modelling of magmatic unrest in Socorro, New Mexico, and Long Valley, California, Geophys. J. Int., 146(1), 191–200.

Gudmundsson, M. T. Thordason T, Hoskuldsson A, Larsen G, Bjornsson H, Prata FJ, Oddsson B., Magnusson E, Hognadottir T, Petersen GN, Hayward CL, Stevenson JA, Jonsdottir I, The Eyjafjallajökull eruption in April-May 2010; course of events, ash generation and ash dispersal. *Eos* 91(Fall meet. suppl.) (abstract V53F-01)

Gudmundsson, O., B. Brandsdottir, W. Menke, and G. Sigvaldason (1994), The crustal magma chamber of the Katla volcano in south Iceland revealed by 2-D seismic undershooting, *Geophys. J. Int.*, *119*(1), 277–296

Haney, G. (2009), Al Hamra Firdous Tower - Skidmore, Owings & Merrill. Archit Design, 79: 38–41. doi:10.1002/ad.848

Hanssen, R. A. (2001), Radar Interferometry: Data Interpretation and Error Analysis, Springer, New York.

Herring, T. A., King, R. W. & McClusky, S. C. *GLOBK Reference Manual, Global Kalman Filter VLBI and GPS Analysis Program, Release 10.3* (Technical report, MIT, 2012)

Herring, T. A., T. I. Melbourne, M. H. Murray, M. A. Floyd, W. M. Szeliga, R. W. King, D. A. Phillips, C. M. Puskas, M. Santillan, and L. Wang (2016), Plate Boundary Observatory and related networks: GPS data analysis methods and geodetic products, Rev. Geophys., 54, 759–808.

Hooper, A., H. Zebker, P. Segall, and B. Kampes (2004), A new method for measuring deformation on volcanoes and other natural terrains using InSAR persistent scatterers, Geophys. Res. Lett., 31, L23611, doi:10.1029/2004GL021737.

Huang, N. E., and Z. Wu (2008), A review on Hilbert-Huang transform: Method and its applications to geophysical studies, Rev. Geophys., 46, RG2006,

Jha, B., F. Bottazzi, R. Wojcik, M. Coccia, N. Bechor, D. McLaughlin, T. Herring, B. H. Hager, S. Mantica, and R. Juanes. (2015), Reservoir Characterization in an Underground Gas Storage Field Using Joint Inversion of Flow and Geodetic Data, International Journal for Numerical and Analytical Methods in Geomechanics 39, no. 14

Jonsdottir K., Roberts R., Pohjola V., Lund B., Shomal Z. H., Tryggvason A., Bodvarsson R., (2009), Glacial long period seismic events at Katla volcano, Iceland, *Geophys. J. Int, Vol. 36, L11402.*

Jonsson, S. (2002), Modeling volcano and earthquake defor- mation from satellite radar interferometric observations, Ph.D. thesis, Stanford Univ., Stanford, Calif.

Kijewski-Correa, T., J. Kilpatrick, A. Kareem, D. Kwon, R. Bashor, M. Kochly, B. S. Young, A. Abdelrazaq, J. Galsworthy, N. Isyumov and D. Morrish (2006), "Validating the Wind-Induced Response of Tall Buildings: A Synopsis of the Chicago Full-Scale Monitoring Program," Journal of Structural Engineering 132(10).

Lau and Mok, 1999, Improving of GPS relative positioning accuracy by using SNR, Journal of surveying engineering 125 (4), 185-202

Lohman, R. B., and M. Simons (2005), Some thoughts on the use of InSAR data to constrain models of surface deformation: Noise structure and data downsampling, Geochem. Geophys. Geosyst., 6, Q01007, doi:10.1029/2004GC000841.

M. Doin, C. Lasserre, G. Peltzer, O. Cavalié, C. Doubre, (2009), Corrections of stratified tropospheric delays in SAR interferometry: validation with global atmospheric models, Journal of Applied Geophysics, 69, pp. 35–5

Massonnet, D., P. Briole, and A. Arnaud (1995), Etna monitored by space- borne radar interferometry, Nature, 375, 567–570.

N.A. Al-Hemiddi, K.A.M. Al-Saud, The effect of a ventilated interior courtyard on the thermal performance of a house in hot-arid region, Renewable Energy, 24, pp. 581-595

Pedersen, R. & Sigmundsson, F. (2006), Temporal development of the 1999 intrusive episode in the Eyjafjallajökull volcano, Iceland, derived from InSAR images. *Bull. Volcanol.* 68, 377–393

Penna, N. T., and M. P. Stewart (2003), Aliased tidal signatures in continuous GPS height time series, Geophys. Res. Lett., 30, 2184, 23.

Pinel, V., C. Jaupart, and F. Albino (2010), On the relationship between cycles of eruptive activity and growth of a volcanic edifice, *J. Volcanol. Geotherm. Res.*, *194*, 150–164,

Puysségur, B., R. Michel, and J.-P. Avouac (2007), Tropospheric phase delay in interferometric synthetic aperture radar estimated from meteoro- logical model and multispectral imagery, J. Geophys. Res., 112, B05419, doi:10.1029/2006JB004352.

Reinhart, C.F.; Lagios, K.; Niemasz, J.; Jakubiec, A. Diva for Rhino; Solemma LLC: Cambridge, MA, USA, 2012. Available Online: http://diva4rhino.com/

Schlumberger (2007), Eclipse technical description, report, v. 2007.1, Abingdon, U. K.

Sigmundsson, F., Hreinsdottir S., Hopper A, Arnadottir T, Pedersen R, Roberts MJ, Oskarsson N, Auriac A, Decriem J., Einarsson P, Geirsson H., Hensch M, Ofeigsson B, Sturkell E, Hjorleifur S, Feigl K, (2010), Intrusion triggering of the 2010 Eyjafjallajökull explosive eruption, *Nature*, *468*, 426–432,

Sigmundsson, F., S. Hreinsdóttir, A. Hooper, Th. Árnadóttir, R. Pedersen, M. J. Roberts, Níels Óskarsson, Amandine Auriac, Judicael Decriem, Páll Einarsson, Halldór Geirsson, Martin Hensch, Benedikt G. Ófeigsson, Erik Sturkell, Hjörleifur Sveinbjörnsson, and Kurt L, Feigl, 2010, Intrusion triggering of the 2010 Eyjafjallajökull explosive eruption, Nature, 468, 426-430.

Simons, M., Y. Fialko, and L. Rivera (2002), Coseismic deformation from the 1999 Mw 7.1 Hector Mine, California, earthquake as inferred from InSAR and GPS observations, Bull. Seismol. Soc. Am., 92, 1390–1402.

Spaans, K. Hreinsdottir S., Hooper A., Ofeigsson B. G., (2015) Crustal movements due to Iceland's shrinking ice caps mimic magma inflow signal at Katla volcano. *Sci. Rep.* 5, 10285; doi: 10.1038/srep10285

Stancliffe R.P.W., van der Kooij M.W.A (2001). The use of satellite-based radar interferometry to monitor production activity at the Cold Lake heavy oil field, Alberta, Canada. AAPG Bull.;85:781–793.

Stephenson, D. "Extreme Temperatures at the Outer Surfaces of Buildings." *Canadian Building Digest*, CBD-47, (1963).

Sturkell, E., Einarsson P., Freysteinn S., Hooper A., Ofeigsson BG, Geirsson H, Olafsson H, (2010) Katla and Eyjafjallajökull Volcanoes. *Dev. Quat. Sci.* 13, 5–21

Tatarski, V. L. (1961), Wave Propagation in a Turbulent Medium, McGraw-Hill, New York.

Teatini, P., Castelletto N., Ferronato M., Gambolati G., Janna C., Cairo E., Marzorati D., Colombo D., Ferretti A, Bagliani A, Bottazzi F., (2011), Geomechanical response to seasonal gas storage in depleted reservoirs: A case study in the Po River basin, Italy, J. Geophys. Res., 116, F02002, doi:10.1029/2010JF001793.

Tregoning, P., and C. Watson (2009), Atmospheric effects and spurious signals in GPS analyses, J. Geophys. Res., 114, B09403.

Van Dierendonck, A.J., and M. Braasch (1997), Evaluation of GNSS Receiver Correlation Processing Technique for Multipath and Noise Mitigation, Proceedings of the US ION NTM (Santa Monica, CA, Jan. 14-16), pp. 207-215

Vasco D.W., Ferretti A., Novali F. (2008) Reservoir monitoring and characterization using satellite geodetic data: Interferometric synthetic aperture radar observations from the Krechba field, Algeria. Geophysics.;73:WA113–122.

Vasco, D. W., A. Rucci, A. Ferretti, F. Novali, R. C. Bissell, P. S. Ringrose, A. S. Mathieson, and I. W. Wright (2010), Satellite-based measurements of surface deformation reveal fluid flow associated with the geological storage of carbon dioxide, Geophys. Res. Lett., 37, L03303, doi:10.1029/2009GL041544.

Wadge G., Webley P.W., James I.N., Bingley R., Donson A., Waugh S., Veneboer T., Puglisi G., Mattia M., Baker D., Edwards S.C., Edwards S.C., Edwards S.J., Clarke P.J., (2002), Atmospheric models, GPS and InSAR measurements of the tropospheric water vapour field over Mount Etna, Geophys. Res. Lett., 29(19), 1905.

Webley, P. W., R. M. Bingley, A. H. Dodson, G. Wadge, S. J. Waugh, and I. N. James, 2002, Atmospheric water vapour correction to InSAR surface motion measurements on mountains: Results from a dense GPS network on Mount Etna, *Phys. Chem. Earth*, 27, 363–370.

Williams S., Boch Y., Fang P, (1998) Integrated satellite interferometry: tropospheric noise, GPS estimates and implications for interferometric synthetic aperture radar products. J. Geophys. Res,

Z. Li, E. Fielding, P. Cross, J. Muller (2006a) Interferometric synthetic aperture radar atmospheric correction: GPS topography-dependent turbulence model, Journal of Geophysical Research, 111

Zebker, H. A., P. A. Rosen, and S. Hensley (1997), Atmospheric effects in interferometric synthetic aperture radar sur- face deformation and topographic maps, J. Geophys. Res., 102, 7547–7563.